Bivalve shell microstructures - exploring a novel marine temperature proxy

Dissertation zur Erlangung des Grades "Doktor der Naturwissenschaften" im Promotionsfach Geowissenschaften/Paläontologie

Am Fachbereich 09 für Chemie, Pharmazie und Geowissenschaften der Johannes Gutenberg-Universität Mainz

Nils Höche

geb. 29.04.1992 in Duderstadt

Mainz, 2022

1. Berichterstatter: Removed for reasons of data protection
2. Berichterstatter: Removed for reasons of data protection

Tag der mündlichen Prüfung: Removed for reasons of data protection

Hiermit erkläre ich, dass ich die vorliegende Arbeit selbstständig verfasst und keine anderen als die angegebenen Quellen und Hilfsmittel benutzt habe.

Nils Höche

Abstract

Bivalve shells are unparalleled high-resolution climate archives. Not only can the environmental conditions prevailing during shell formation be stored in the physical, chemical, and, as recently shown, microstructural properties of the shells, but their paleoclimate records can also excellently be temporally contextualized by recurring growth lines, which form due to periodic shell growth. Nevertheless, most paleotemperature proxies employed in bivalve shells come with limitations. Temperature reconstructions based on the oxygen stable isotope ($\delta^{18}O_{shell}$) value of the shells, for example, also depend on the $\delta^{18}O_{water}$, which is often unknown. In addition, the $\delta^{18}O_{shell}$ values of the shells are prone to alteration during diagenesis. The trace elemental compositions of the shells, while correlating to the water temperature, were shown to be strongly affected by physiological processes such as variations in growth rate. The width of growth increments of the shells simultaneously inform about food conditions and temperature and are likewise strongly physiologically controlled. The microstructural properties of the shells, in contrast, might be less affected by factors other than temperature, and be preserved in fossil shells when geochemical signals such as the $\delta^{18}O_{shell}$ are already lost. However, a link between the shell microstructure and the ambient water temperature was hitherto only demonstrated in a few short-lived bivalve species. Before microstructural properties can confidently be used to infer paleotemperature, these proxies need to be adequately calibrated and tested.

This thesis examined whether an influence of temperature on microstructural properties such as the biomineral unit (BMU) size is a common phenomenon across long-lived bivalve taxa commonly used in sclerochronological paleoclimate reconstructions. In addition, it was evaluated whether food availability and quality, salinity, shell growth rate and ontogenetic age also affect the microstructural properties of the shells, possibly overprinting temperature signals. The results of this project comprise three manuscripts published in international, peer-reviewed scientific journals.

In the 1st manuscript, it is investigated whether the microstructure of the shells of *Glycymeris bimaculata*, a long-lived bivalve species broadly distributed in temperate coastal to brackish regions, is affected by changes in water temperature. *G. bimaculata* forms crossed-lamellar shells, a microstructure which occurs in over 90 % of all marine mollusks in some form. Novel image processing techniques applied to scanning electron microscopy images combined with stable oxygen isotope analysis revealed that the size, length and width of BMUs of *G. bimaculata* indeed correlate strongly with the water temperature. This link can be used to infer water tem-

peratures with up to 2.3 °C precision, introducing a promising new paleotemperature proxy that could potentially apply to a wide range of mollusk taxa which also form crossed-lamellar shells.

In Manuscript two, shells of *Arctica islandica*, a well-studied sclerochronological archive known for its extreme longevity and wide distribution across the northern North Atlantic, were analyzed. In order to study the effects of water temperature on the shells in isolation of other factors, specimens were analyzed that were raised in a lab under different temperature settings, while keeping salinity and food conditions constant. These experiments revealed a direct influence of water temperature on the size of the BMUs and the size of pores incorporated into the shells of *A. islandica*, suggesting that a microstructural response to temperature variations is a common phenonmenon across different bivalve taxa.

In Manuscript three, it was tested whether different environmental regimes can effectively be discriminated by the analysis of microstructural properties of *A. islandica* shells collected across multiple habitats. Analysis were also performed in different shell portions and across different ontogentic stages in order to determine physiological influences on the shell microstructure. This way, it could be revealed that temperature changes as small as approx. 1–2 °C trigger alterations of the microstructure. In naturally grown shells, however, temperature signals can be obstructed when unfavorable growth conditions prevail such as low and variable salinity or low dissolved oxygen content. In addition, the microstructural properties of the shells change strongly during ontogeny.

In summary, the experiments of this thesis revealed an influence of the water temperature on the microstructure of bivalve shells. However, the microstructural properties are also strongly coupled to the physiology of the bivalve and to its biomineralization processes, which complicates temperature reconstructions. The methods developed in this study strongly facilitate quantitative analysis of microstructural properties of carbonate shells and open up plenty of research applications not only in paleoclimatology but also in biomineralization research.

I carried out all laboratory work (oxygen stable isotope analysis, laser ablation–inductively coupled plasma–mass spectrometry measurements, growth pattern analysis, scanning electron microscopy and image analysis) of this thesis. I also developed the image analysis methods used for BMU morphometry, analyzed and interpreted the data and produced the figures. I wrote all text for manuscripts one and three and contributed substantially to the text of manuscript two. Contributions of other authors are stated at the beginning of each manuscript.

Zusammenfassung

Muschelschalen sind unvergleichliche hochauflösende Klimaarchive. Die während der Schalenbildung vorherrschenden Umweltbedingungen können nicht nur in den physikalischen, chemischen und, wie kürzlich gezeigt, auch mikrostrukturellen Eigenschaften der Muscheln gespeichert werden, sondern ihre Paläoklimaaufzeichnungen lassen sich auch hervorragend durch wiederkehrende Wachstumslinien, die sich aufgrund des periodischen Schalenwachstums bilden, zeitlich kontextualisieren. Dennoch sind die meisten Paläo-Temperaturproxies, die in Muschelschalen verwendet werden, mit Einschränkungen verbunden. Temperaturrekonstruktionen, die auf den stabilen Sauerstoffisotopenwerten ($\delta^{18}O_{shell}$) der Muscheln beruhen, hängen beispielsweise auch vom $\delta^{18}O_{water}$ ab, der oft unbekannt ist. Außerdem sind die $\delta^{18}O_{shell}$-Werte der Schalen anfällig für Veränderungen während der Diagenese. Die Spurenelementzusammensetzung der Schalen korreliert zwar mit der Wassertemperatur, wird aber auch stark von physiologischen Prozessen wie Schwankungen der Wachstumsrate beeinflusst. Die Breite der Wachstumsinkremente der Schalen gibt gleichzeitig Auskunft über die Nahrungsbedingungen und die Temperatur und ist ebenfalls stark physiologisch beeinflusst. Die mikrostrukturellen Eigenschaften der Schalen dagegen könnten weniger von anderen Faktoren als der Temperatur beeinflusst sein und in fossilen Schalen erhalten bleiben, selbst wenn geochemische Signale wie $\delta^{18}O_{shell}$ bereits verloren sind. Ein Zusammenhang zwischen der Schalenmikrostruktur und der Umgebungstemperatur des Wassers wurde jedoch bisher nur bei einigen kurzlebigen Muschelarten nachgewiesen. Bevor mikrostrukturelle Eigenschaften zuverlässig zur Abschätzung von Paläo-Temperaturen verwendet werden können, müssen diese Proxies angemessen kalibriert und getestet werden.

In dieser Arbeit wurde untersucht, ob ein Einfluss der Temperatur auf mikrostrukturelle Eigenschaften wie die BMU-Größe ein allgemeines Phänomen bei langlebigen Muscheltaxa ist, die üblicherweise in sklerochronologischen Paläoklima-Rekonstruktionen verwendet werden. Darüber hinaus wurde untersucht, ob die Verfügbarkeit und Qualität der Nahrung, der Salzgehalt, die Wachstumsrate der Muschel und das ontogenetische Alter ebenfalls die mikrostrukturellen Eigenschaften der Muscheln beeinflussen und möglicherweise Temperatursignale überlagern. Die Ergebnisse dieses Projekts umfassen drei Manuskripte, die in internationalen, begutachteten Fachzeitschriften veröffentlicht wurden.

In ersten Manuskript wurde untersucht, ob die Mikrostruktur der Schalen von *Glycymeris bimaculata*, einer langlebigen Muschelart, die in Küsten- und Brackwasserregionen mittlerer

Breiten häufig vorkommt, durch Veränderungen der Wassertemperatur beeinflusst wird. *G. bimaculata* bildet kreuz-lamellare Schalen – eine Mikrostruktur, die in mehr als 90 Prozent aller marinen Mollusken in der einen oder anderen Form vorkommt. Die Anwendung neuartiger Bildverarbeitungstechniken auf Rasterelektronenmikroskopie-Bilder in Verbindung mit der Analyse stabiler Sauerstoffisotope hat gezeigt, dass die Größe, Länge und Breite der BMUs von *G. bimaculata* tatsächlich stark mit der Wassertemperatur korreliert. Dieser Zusammenhang kann genutzt werden, um Wassertemperaturen mit einer Genauigkeit von bis zu 2.3 °C zu rekonstruieren, was einen vielversprechenden neuen Paläo-Temperatur-Proxy einführt, der potenziell für eine Vielzahl von Mollusken-Taxa gelten könnte, die ebenfalls kreuz-lamellare Schalen bilden.

Im zweiten Manuskript wurden die Schalen von *Arctica islandica*, einem gut untersuchten sklerochronologischen Archiv, das für seine extreme Langlebigkeit und weite Verbreitung im nördlichen Nordatlantik bekannt ist, analysiert. Um die Auswirkungen der Wassertemperatur auf die Schalen unabhängig von anderen Faktoren zu untersuchen, wurden Individuen analysiert, die in einem Labor unter verschiedenen Temperaturbedingungen aufgezogen wurden, während der Salzgehalt und die Nahrungsbedingungen konstant gehalten wurden. Diese Experimente zeigten einen direkten Einfluss der Wassertemperatur auf die Größe der BMUs und die Größe der in den Schalen von *A. islandica* eingebauten Poren, was darauf hindeutet, dass mikrostrukturelle Veränderungen in Reaktion auf Temperaturschwankungen in vielen Muscheltaxa weit verbreitet sind.

Im dritten Manuskript wurde getestet, ob verschiedene Umweltregime durch die Analyse der mikrostrukturellen Eigenschaften von *A. islandica*-Schalen aus verschiedenen Lebensräumen effektiv unterschieden werden können. Die Analysen wurden auch in verschiedenen Schalenabschnitten und verschiedenen ontogentischen Stadien durchgeführt, um physiologische Einflüsse auf die Schalenmikrostruktur zu bestimmen. Auf diese Weise konnte gezeigt werden, dass bereits Temperaturänderungen im Bereich von ca. 1–2 °C Veränderungen der Mikrostruktur auslösen. In natürlich gewachsenen Schalen können die Temperatursignale jedoch verschleiert werden, wenn ungünstige Wachstumsbedingungen herrschen, wie z. B. geringer und variabler Salzgehalt oder niedriger Gehalt an gelöstem Sauerstoff. Darüber hinaus ändern sich die mikrostrukturellen Eigenschaften der Schalen während der Ontogenese stark.

Insgesamt haben alle Experimente dieser Arbeit einen Einfluss der Wassertemperatur auf die Mikrostruktur von Muschelschalen gezeigt. Die mikrostrukturellen Eigenschaften sind jedoch auch stark an die Physiologie der Muschel und an ihre Biomineralisierungsprozesse gekoppelt, was Temperaturrekonstruktionen erschwert.

Ich habe alle Laborarbeiten (Analyse stabiler Sauerstoffisotope, Laser Ablation-induktiv gekoppelte Plasma-Massenspektrometrie, Wachstumsmusteranalyse, Rasterelektronenmikroskopie und Bildanalyse) dieser Arbeit durchgeführt. Außerdem habe ich die für die BMU Morphometrie verwendeten Bildanalysemethoden entwickelt, die Daten analysiert und interpretiert und die Abbildungen erstellt. Ich habe den gesamten Text für die Manuskripte eins und drei geschrieben und wesentlich zum Text von Manuskript zwei beigetragen. Die Beiträge anderer Autoren sind zu Beginn jedes Manuskripts angegeben.

Contents

Acknowledgements

Removed for reasons of data protection

List of abbreviations

ACC amorphous calcium carbonate

BMU biomineral unit

CA crossed-acicular

DO dissolved oxygen

EBSD electron backscatter diffraction analysis

E/Ca trace element-to-calcium

EPF extrapallial fluid

FA factor analysis

FCCL fine compex-crossed lamellar

FP fibrous prismatic

HOM homogeneous

ISL inner shell layer

iOSL inner portion of the outer shell layer

ISP irregular simple prismatic

LA-ICP-MS laser ablation–inductively coupled plasma–mass spectrometry

oOSL outer portion of the outer shell layer

OSL outer shell layer

POM particulate organic matter

QCM quality control material

ROI region of interest

SEM scanning electron microscopy

SphP spherulitic prismatic

List of Figures

List of Tables

1 Introduction

1.1 Climate and its reconstruction via proxy archives

Climate change and anthropogenic greenhouse warming pose the biggest socio-economical threats of the 21st century (Houghton et al., 1990; Hansen and Sato, 2012; Masson-Delmotte et al., 2021). Accordingly, substantial research efforts are underway to predict future climate trends and to mitigate associated damages (e.g., Schellnhuber et al., 2006). It is now possible to detect, model and predict complex climate feedback mechanisms (Cess et al., 1990; Curry et al., 1995; Gedney et al., 2004), latitudinal gradients (Rind, 1998) and oscillations on multiple timescales (Scholz et al., 2012; Vavrus et al., 2020). Obtaining such knowledge requires the analysis of climatological data that span long time periods, i.e., hundreds of years, and come with sufficient temporal resolution and spatial coverage. However, continuous instrumental temperature records are only available since the mid 19th century (e.g., Jones et al., 1999; Houghton et al., 2001; Smith and Reynolds, 2003). The extension of high-resolution instrumental temperature records into more distant time is thus one of the most pressing tasks to quantify anthropogenic influence on the climate system and to advance understanding about natural high-frequency (e.g., annual, decadal) climate oscillations. Paleoclimate data provide a means to test, verify and constrain climate simulations predicting future climate change (Schmidt et al., 2014; Cauquoin et al., 2019; Asami et al., 2020).

Oceans represent a major part of the climate system because they interact with the atmosphere by sequestration of CO_2 and storage and transport of heat via circulating water masses (e.g., Levitus et al., 2000; Bigg et al., 2003; Sabine et al., 2004). High-resolution (annually and better resolved) marine paleotemperature records are even more limited than terrestrial temperature records (e.g., Vose et al., 1992; Jones et al., 1999; Houghton et al., 2001). Hence, reconstruction of marine paleoclimate is of utmost importance to confidently assess climate trends.

Instrumental temperature records can be extended further back in time by the analysis of proxy values (i.e., physical or geochemical properties that reflect climate variables) in climate

archives — natural (abiogenic or biogenic) objects which record climate information. Proxy-derived temperature approximations from climate archives can provide paleoclimate records spanning hundreds to millions of years (e.g., Krantz, 1990; Cheddadi and Rossignol-Strick, 1995; Burns et al., 1998; Johnson et al., 2002). Such paleoclimate data facilitated climate research and made it possible to distinguish climate oscillations from anthropogenic warming trends.

Ideally, climate archives should fulfill a range of quality criteria. (i) Since the age model is one of the largest sources of uncertainty in paleoclimatology (Breitenbach et al., 2012; Huntley, 2012), climate archives should be easily and absolutely datable so that the obtained proxy records can be accurately put into temporal context. Most climate archives are sequentially formed deposits and contain growth structures due to variable speed of growth or changes in material composition. The growth lines or layers mark fixed points in time and can thus be used for dating purposes (Marchitto et al., 2000; Comboul et al., 2014). If growth structures are absent, geochemical techniques such as radiocarbon (^{14}C) or U – Th dating can be used to temporally align the paleoclimate records (Andree et al., 1986; Wendt et al., 2021). (ii) Another large source of uncertainty arises from the fact that most proxy systems are influenced by environmental parameters at the same time (e.g., Huntley, 2012; Hiebenthal et al., 2013; Ballesta-Artero et al., 2018a). In case of biogenic climate archives, proxies can additionally be affected by physiological processes (Gillikin et al., 2005; Schöne, 2008). Thus, in order to produce accurate climate reconstructions, climate archives should provide well-constrained and calibrated proxies that ideally relate to only one environmental parameter (Villalba et al., 2009; Trofimova et al., 2020). In addition, uncertainty can be minimized by employing multi-proxy approaches (Li et al., 2010; Woelders et al., 2018; Reynolds et al., 2019). (iii) Climate archives from fossil environments should be well-preserved, as diagenesis can alter geochemical signals (Casella et al., 2017; Ritter et al., 2017) leading to a loss of environmental information. The geographical and temporal availability of a climate archive in the fossil record also determines the extent to which climate reconstructions can be generated. To be able to assess high-frequency climate variations (e.g., annual or seasonal), however, high temporal resolution is required.

Both terrestrial and marine environments offer a large variety of climate archives. On the continents, valuable climate archives are, e.g., lake sediments (Conroy et al., 2008; Stansell et al., 2013; Zhang et al., 2014), peat (Wooller et al., 2007), ice cores (Dansgaard et al., 1982, 1993; Petit et al., 1999) or speloethems (Fairchild et al., 2006; Vollweiler et al., 2006; Drysdale et al., 2007; Scholz et al., 2012). In addition, trees record air temperature information in their density (Conkey, 1979; Briffa et al., 1986; Schweingruber and Briffa, 1996), width of tree rings (Briffa et al., 1986; Esper

et al., 2002; Martinelli, 2004; Sheppard, 2010), or in changes of pollen assemblages contained in sedimentological successions (Cheddadi and Rossignol-Strick, 1995; Burns et al., 1998). Marine paleoclimate records, in contrast, can be provided by deep sea sediment cores (e.g. Martinson et al., 1987), or by layered carbonate deposits on the continental shelves. Marine climate archives are usually biogenic such as skeletal remains of corals (Beck et al., 1992; Mitsuguchi et al., 1996; Shen et al., 1996; Alpert et al., 2016), bivalves (Jones et al., 2009; Butler et al., 2013; Reynolds et al., 2013), brachiopods (Wang et al., 2020), or coralline red algae (Halfar et al., 2008; Kamenos et al., 2008; Chan et al., 2019). The remains of these marine organisms are abundantly preserved in the fossil record (Oschmann, 2018). In addition, the skeletal hard parts grow periodically and hence contain growth structures which establish precise temporal context. Biogenic marine archives thus provide highly-resolved, long-term records of ocean climate.

Each climate archive comes with individual qualities in respect to geographic and temporal coverage, resolution and datability. Abiogenic archives usually cover long time periods but have a low temporal resolution. Biogenic proxy records, on the other hand, have limited temporal coverage (depending on the longevity of the organism and state of preservation) but are precisely datable and potentially record annual, seasonal or even daily environmental variation. The physical and chemical properties of different climate archives also respond differently to environmental triggers, resulting in different proxy systems. Often, trade-offs need to be made between temporal resolution and coverage in the selection of appropriate paleoclimate archives. Ultimately, proxy records from various different climate archives should be considered in combination in order to gain a comprehensive and holistic view on paleoclimate.

1.2 Reconstruction of marine climate using mollusk shells

Bivalve shells are outstanding high-resolution climate archives. They not only record climate information in their physical and chemical properties, but also perfectly fulfill all other proxy archive quality criteria mentioned above. Firstly, bivalves grow their shells periodically, forming internal growth bands and lines (Clark, 1968; Jones, 1980), usually at annual periodicity (Clark, 1974; Jones, 1980; Thompson et al., 1980a; Ropes et al., 1984a). Hence, the calendar year corresponding to each growth increment can be determined, and multiple coeval specimens can easily be cross-dated (Scourse et al., 2006). In addition, bivalves often form finer, sub-annual growth lines in their shells (in, e.g., fortnightly, daily or tidal frequency), which allows for pre-

cise intra-annual alignment of the growth record (Clark, 1968; Schöne et al., 2005a; Höche et al., 2020). Secondly, bivalves occur nearly all over the world, including brackish and freshwater systems, coastal regions and the entire neritic zone (Jablonski et al., 2013). Bivalve shell proxy records thus cover a broad geographic area, whereas records provided by other organisms (e.g., corals, which predominantly live in shallow, warm and clear water; Goreau et al., 1979) are more geographically limited. Lastly, bivalves can attain lifespans of several hundred years (Thompson et al., 1980a; Schöne et al., 2005b; Wanamaker et al., 2008) and have a rich fossil record: they exist since the Cambrian explosion and became dominant after the Permian-Triassic extinction event (Sepkoski, 1981; Fraiser and Bottjer, 2007). Since fossil shells are often well-preserved (Harper, 1998; Casella et al., 2017; Vendrasco et al., 2019), derived proxy records come with a high temporal coverage. All these properties make the shells of bivalves unprecedented as high-resolution climate archives and enabled researchers to generate century-long proxy records of marine paleoclimate (Butler et al., 2010, 2013; Reynolds et al., 2013).

Bivalve shells offer a wide array of proxy values that provide climate information. Currently, the most robust and most commonly employed paleotemperature proxy for bivalve shells is their oxygen stable isotope signature ($\delta^{18}O_{shell}$, i.e., the ratio of heavy to light oxygen isotopes in a shell sample compared to that of a known standard). The $\delta^{18}O_{shell}$ value of bivalve shell carbonates, which forms near isotopic equilibrium with the seawater (Epstein et al., 1953; Mook and Vogel, 1968; Hickson et al., 1999), changes with the water temperature due to temperature-dependent fractionation of the oxygen stable isotopes. Using the equation by Grossman and Ku (1986) in combination with possibly required correction factors for different scales and standards (SMOW, PDB, V-SMOW and V-PDB; Gonfiantini et al., 1995; Dettman et al., 1999), paleotemperatures can be reconstructed using $\delta^{18}O_{shell}$:

$$T = 20.6 - 4.34 \times \left(\delta^{18}O_{shell(V-PDB)} - (\delta^{18}O_{water(SMOW)} - 0.27)\right) \tag{1.1}$$

However, as shown in Eq. 1.1 (Grossman and Ku, 1986; Gonfiantini et al., 1995), temperature reconstructions also require knowledge of the stable oxygen isotope signature of the water ($\delta^{18}O_{water}$), which is often missing. Salinity data can be used to overcome the lack of knowledge of the $\delta^{18}O_{water}$ to some extent, because waters with differing $\delta^{18}O_{water}$ (e.g. freshwater vs. marine water) also have different salinity, the link between the two being almost linear (Torgersen, 1979; Strain and Tan, 1993; Rohling and Bigg, 1998).

Apart from the $\delta^{18}O_{shell}$, also the proportion of bonds between two heavy isotopes ($^{13}C-{}^{18}O$;

so-called 'clumps') relative to those bonds involving lighter isotopes, is sensitive to the water temperature, giving rise to the Δ_{47} proxy value (Eiler, 2007, 2011; de Winter et al., 2021). The clumped isotope paleoclimate proxy does not require knowledge of the $\delta^{18}O_{water}$ and does not depend on the absolute partitioning of heavy versus light isotopes in the carbonate samples (Eiler, 2011), eliminating the biggest drawbacks of the $\delta^{18}O_{shell}$ value. Δ_{47}-based temperature reconstructions, however, have limited precision (Fiebig et al., 2016; Fernandez et al., 2017), usually require large amount of sample material (Eiler, 2011; Fernandez et al., 2017), and are strongly affected by diagenetic alteration of the sample material (Winkelstern and Lohmann, 2016; Leutert et al., 2019; Guo et al., 2021).

In addition to isotope-based proxies, the shell growth patterns, specifically the width of growth increments can be used to gain paleoenvironmental information (Schöne et al., 2002; Butler et al., 2013; Edge et al., 2021). Although timing and rate of shell formation are strongly biologically controlled (Clark, 1975; Richardson et al., 1980; Kim et al., 1999) and change throughout ontogeny (e.g., Jones, 1980; Thompson et al., 1980a), environmental parameters still significantly influence the shell growth rate (Schöne et al., 2005c; Miyaji et al., 2007). In most cases, shell growth rates correlate strongly with the water temperature and/or food availability, so that analysis of growth increment widths can provide paleoclimate or paleoproductivity information (e.g., Witbaard, 1997; Schöne et al., 2005c; Wanamaker et al., 2009; Reynolds et al., 2017).

The trace elemental composition of the shells, i.e. their trace element-to-calcium (E/Ca) ratios, can also provide information about environmental variables of climatic importance (Füllenbach et al., 2015; Markulin et al., 2019). Most notably, Sr/Ca ratios of shell carbonate correlate with the water temperature (Schöne et al., 2011b; Yan et al., 2013), whereas Ba/Ca ratios seem to be controlled by primary productivity (Marali et al., 2017; Justine et al., 2020). However, element signatures were shown to be strongly affected by physiological processes of the animal (e.g., Gillikin et al., 2005; Wanamaker and Gillikin, 2019) and do not always provide reliable temperature estimates. Furthermore, all geochemical signals such as the $\delta^{18}O_{shell}$ and E/Ca can easily be lost in fossil specimens due to diagenesis (Killingley, 1983; Knoll et al., 2016; Leutert et al., 2019).

Recently it was shown that also the microstructure of the shells changes with temperature (Kennish and Olsson, 1974; Tan Tiu, 1988; Olson et al., 2012). Specifically, the size of individual BMUs increases in warmer waters (Gilbert et al., 2017; Milano et al., 2017b). Microstructural proxies might still provide valid paleoclimate information even when the original geochemical (e.g., $\delta^{18}O_{shell}$ and E/Ca) signals are lost due to diagenesis or when they are obstructed by influences of other environmental variables (e.g., $\delta^{18}O_{water}$ or salinity) or animal physiology. A link

between the microstructure and the water temperature was, however, only determined in a few short-lived bivalve species (Gilbert et al., 2017; Milano et al., 2017b) so far, and many other open questions remain before this emerging proxy can be confidently applied. It is therefore highly promising to further develop microstructural temperature proxies.

1.3 Bivalve biomineralization and shell architecture

Bivalves shells consist mainly of calcite, aragonite, or a composite of the two polymorphs (Bøggild, 1930; Carter, 1980) but can also incorporate small amounts of amorphous calcium carbonate (ACC) and vaterite (Jacob et al., 2008; Spann et al., 2010; Wehrmeister et al., 2011; Nehrke et al., 2012). In addition, the shells contain up to 5 wt% organic components (Agbaje et al., 2017b; Clark et al., 2020). The organics play a significant role in the production of the different microstructures during biomineralization (Weiner et al., 1984; Kobayashi and Samata, 2006). The shells are divided into inner shell layer (ISL) and outer shell layer (OSL), each of which might be further subdivided into microstructurally distinct sub-layers, and covered by an organic periostracum (Bøggild, 1930). Both aragonite and calcite occur in an astounding variety of different microstructures resulting from the spatial organization of the individual BMU and organic components (Bøggild, 1930). Before introducing these microstructures, the concept of bivalve biomineralization will be briefly described.

1.3.1 Biomineralization and ion transport pathways

Many aspects of bivalve biomineralization still remain elusive. According to the currently accepted model, calcification occurs extracellularly in the extrapallial fluid (EPF). The EPF fills the approx. 100 nm-thin extrapallial cavity between preexisting shell and mantle (Harper, 1997; Checa, 2000; Checa et al., 2014; Stemmer et al., 2019). The chemical composition of the EPF at the outer mantle edge is actively maintained by the bivalve to foster carbonate precipitation (Stemmer et al., 2019). The EPF is divided into an inner and outer portion, in which the ISL and OSL form, respectively (Wilbur and Saleuddin, 1983). Between the inner and outer EPF, at the pallial line, the mantle is attached secreting the thin myostracum that separates ISL and OSL (Carter et al., 2012).

To build the shell, carbonate ($CaCO_3$) and organic material need to be acquired or synthesized by the bivalve and transported to the EPF. The carbonate precursors, i.e. Ca^{2+} and HCO_3^-

or CO_3^{2-} ions, are acquired from food or seawater by filtration (Carré et al., 2006; Marin et al., 2012). HCO_3^- can also be synthesized by the animal itself using respiratory CO_2 (Marin et al., 2012). These precursor ions are transported to the site of biomineralization either through the haemolymph or intercellularly across the cell membranes (Carré et al., 2006; Clark et al., 2020). Haemolymphatic transport occurs passively via diffusion, whereas transmembrane transport can occur both passively, through Ca^{2+}-channels, or actively (using metabolic energy), through Ca^{2+}-ATPase-pumps (Carré et al., 2006; Marin et al., 2012; Clark et al., 2020). There is an ongoing debate whether in addition to ionic transport to the biomineralization site, carbonate precursors can also be transported as ACC granules (Weiss et al., 2002; Nassif et al., 2005; Jacob et al., 2008). If they are indeed involved in shell formation, ACC granules would destabilize in the EPF, transforming into shell aragonite or calcite by interaction with the present organic components (Jacob et al., 2008; Macías-Sánchez et al., 2017).

The organic shell components are produced using organic material acquired via food uptake (Marin et al., 2012). Organic secretion requires a whole array of specialized protein-encoding genes which vary greatly in expression among mollusk taxa (Le Roy et al., 2012, 2014; Kong et al., 2019; Clark et al., 2020). However, most mollusks share an evolutionally conserved 'mineralization toolbox' (e.g., carbonic anhydrase, tyrosinase and chitin-binding proteins), which serve important functions during biomineralization and aid in acid-base regulation (Le Roy et al., 2014; Clark et al., 2020). Organic secretion is bound to a significant energy expenditure (Palmer, 1983; Clark et al., 2020). The organic material serves several functions during shell formation. Thick layers of chitineous and/or silk-like proteins delineate calcification compartments during biomineralization (Bevelander and Nakahara, 1969, 1980; Levi-Kalisman et al., 2001). In contrast, more finely distributed, partially polar polysaccharide compounds promote crystal nucleation (Clark, 1980). The type of organic material exerts great influence on the shape of the shell microstructure through this intimate interaction between organic and mineral phase during biomineralization (Nudelman et al., 2006; Marin et al., 2012; Clark et al., 2020).

1.3.2 Shell microstructure

Bivalves form multiple microstructurally distinct shell layers (Bøggild, 1930; Kennedy et al., 1969), which contribute to the extraordinary fracture toughness and flexibility of the shells (Li et al., 2017). Hundreds of different terms were introduced to describe the diverse microstructural appearances (e.g., Bøggild, 1930; Carter et al., 2012). The microstructures and types of carbonate

polymorphs formed by each bivalve species depends on its phylogeny (Kobayashi and Samata, 2006). Yet, each microstructure type was invented independently multiple times during bivalve evolution (Clark et al., 2020). The shell microstructure also depends on its mineralogy: prismatic structures occur in both calicitic and aragonitic shells, fibrous, foliated and chalky microstructures occur mostly within calcitic shells, and nacre and crossed-lamellar microstructures occur exclusively in aragonitic shells (Checa, 2018). As this thesis focuses on aragonitic bivalve shells, only the four main aragonitic microstructure types will be introduced in the following.

(A) **Prismatic** microstructures are composed of prisms of tens of µm in diameter, aligned perpendicularly or obliquely to the shell surface and enveloped by organic matrices (Fig. 1.1A; Bøggild, 1930; Checa, 2018). These prisms grow continuously in length over hundreds of µm (Cuif et al., 2020). Internally, prisms either come with a uniform crystallographic orientation (i.e., normal or simple prismatic), have a central optical axis, with crystallographic orientation diverging to the sides (i.e., complex prismatic), or are composed of smaller, 2^{nd} order prisms arranged in a feather-like pattern (i.e., composite prismatic; Bøggild, 1930; Kennedy et al., 1969; Carter et al., 2012). In nearly all bivalve species, a special form of prismatic microstructures, irregular simple prismatic (ISP), constitutes the annual growth lines as well as the myostracal layer which separates the ISL and OSL (e.g., Jones, 1980; Thompson et al., 1980a; Ropes et al., 1984a).

(B) **Nacre** or mother-of-pearl is composed of sub-µm sized aragonite tablets, arranged in a brick-and-mortar like fashion, and separated by sheets of silk-like organics (Fig. 1.1B; Cartwright and Checa, 2007). Nacre composes the ISL of many shells and is commonly overlain by prismatic microstructures in the OSL (Checa et al., 2014). Due to its well-organized spatial structure, extraordinary mechanical properties and involvement in pearl formation (and thus economic importance), nacre is of the best-studied microstructures and often represented in models of shell formation (Nudelman et al., 2006; Nudelman, 2015; Cuif et al., 2018).

(C) **Crossed-lamellar** microstructures are hierarchically organized into lamellae of several orders (Fig. 1.1C; Bøggild, 1930; Böhm et al., 2016; Checa, 2018). The 1^{st} order lamellae are composed of stacks of mineral sheets (i.e., 2^{nd} order lamellae) of uniform spatial orientation (Carter et al., 2012). These sheets are, in turn, composed of elongated rods of sub-µm diameter, so-called 3^{rd} order lamellae (Böhm et al., 2016; Agbaje et al., 2017a). Several

variations of crossed-lamellar microstructures exist, which mainly differ in the organization of 1st order lamellae. Simple crossed-lamellar microstructures have two dominant dip directions that alternate in each 1st order lamella, which appear as zebra stripes running perpendicular to the growth front. In the simple crossed-lamellar microstructures of *Glycymeris*, for example, the angles of incidence of the BMU (i.e., 3rd roder lamellae) of each approx. 10 µm-wide 1st order lamella are tilted towards neighboring ones by approx. 90° (Agbaje et al., 2017a). Complex crossed-lamellar microstructures, in contrast, possess 1st order lamellae with three or more dominant dip directions that appear as chaotically arranged, discontinuous blocks (Carter et al., 2012). Over 90 % of all bivalve taxa incorporate crossed-lamellar microstructures in some form (Almagro et al., 2016).

(D) **Homogeneous (HOM)** microstructures are labelled as such because they appear not to have any structure in optical microscopy (Fig. 1.1D; Carter et al., 2012). HOM consists of rounded, equally-sized BMUs which are only visible in SEM. For this reason HOM microstructures are sometimes called aragonitic granular microstructures. Any hierarchical organization into larger structural units is missing (Bøggild, 1930; Carter et al., 2012). Each homogeneous BMU internally consists of smaller, needle-shaped aragonite crystallites (possibly twins) which share the same orientation (Kennedy et al., 1969; Dunca et al., 2009). Due to this feature, some authors attribute HOM to be a simplified and miniaturized version of the crossed-lamellar microstructure (Taylor, 1973; Ropes et al., 1984a). Other authors, however, described HOM as a prismatic structure with extraordinarily short prisms (Harper et al., 2009), due to the partially angular, polyhedral form of its BMUs. Since homogeneous microstructures of different taxa also differ drastically in organic content and BMU size (Harper et al., 2009; Agbaje et al., 2017b; Milano et al., 2017a), it is possible that several forms of homogeneous microstructures exist, all of which representing simplified variations of more complex microstructures.

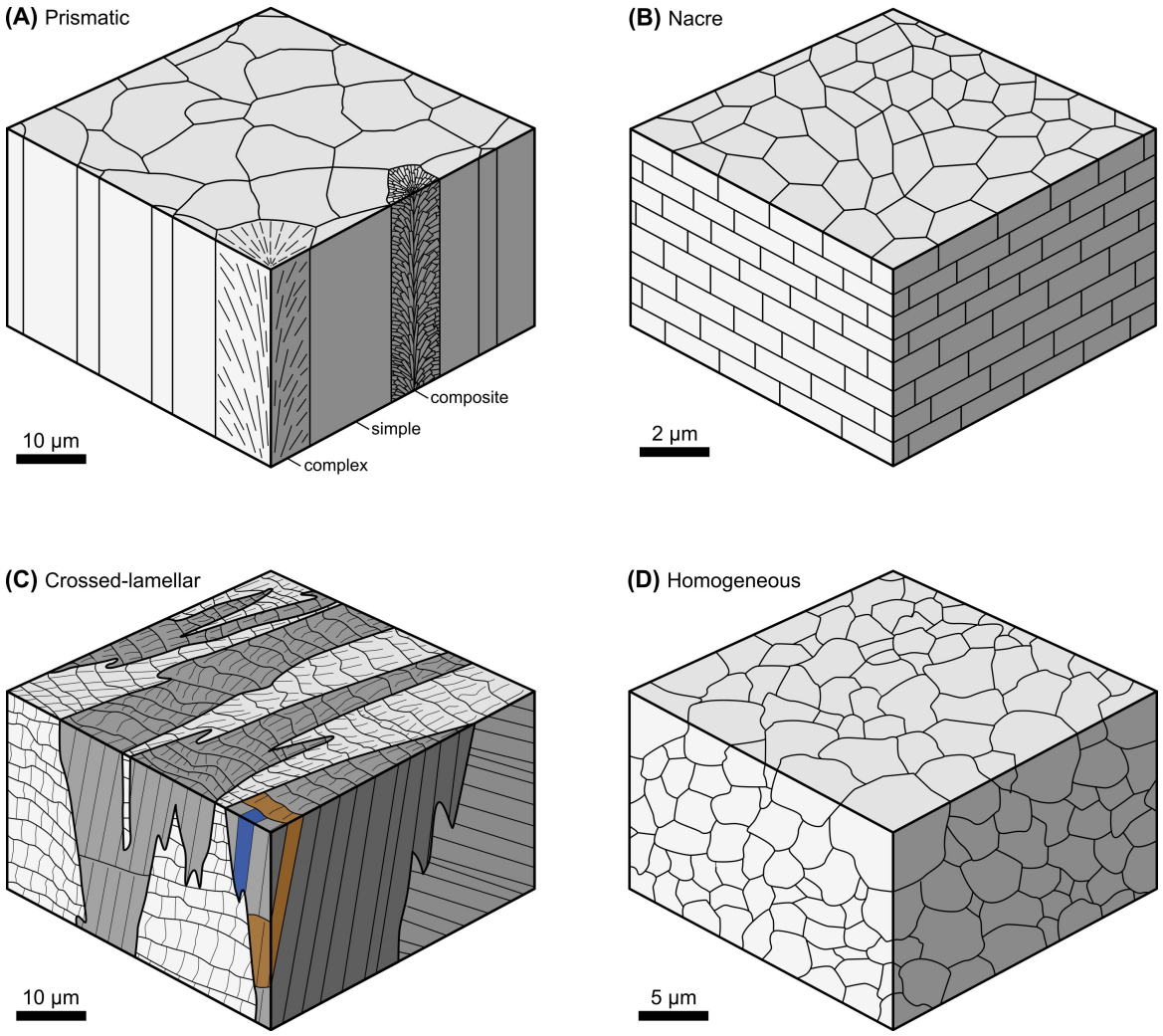

Figure 1.1 Sketches of blocks of common aragonitic shell microstructures (A) Prismatic microstructure consisting of prisms of tens of µm diameter aligned perpendicularly or obliquely to the sell surface. Prisms are either of uniform crystallographic orientation (= simple), are internally twinned and have diverging crystallographical axes (= complex), or consist of smaller 2nd order prisms diverging sideways in orientation away from the main prism axis (= composite). The prisms can grow several hundreds of µm in length. (B) Nacre. Sub-µm-sized aragonite tablets arranged in a brick and mortar like fashion and separated by sheets of silk-like organics. While bivalves mostly form sheet nacre (as shown here), gastropods often build shells of columnar nacre. (C) Simple crossed lamellar microstructure. Approx. 10 µm-wide 1stst order lamellae (light and dark gray) consisting of stacked sheets (2nd order lamellae; orange) of aragonitic rods (3rd order lamellae; blue). Adjacent 1st order lamellae alternate between two dominant directions of incidence of the long axis of their mineral rods, here tilted at an angle of about 80°. (D) Homogeneous microstructure consisting of rounded to angular and polyhedral, equidimensional biomineral units of roughly 1–20 µm^2 size. (A-C) modified after Kennedy et al. (1969). Note difference in scale between the panels.

1.4 Motivation and aims of the research

This thesis studies whether bivalve shells can record temperature information in their microstructural properties and calibrates potential microstructural paleotemperature proxies. While bivalve shell microstructures are well-studied for taxonomic and phylogenic purposes (Bøggild, 1930; Taylor, 1973; Carter et al., 2012), only few authors demonstrated that the microstructural properties might change in response to environmental forcing and thus store paleotemperature information (Kennish and Olsson, 1974; Tan Tiu and Prezant, 1989; Nishida et al., 2012; Olson et al., 2012). Even fewer publications demonstrated such a link quantitatively, in a correlation between the size of individual BMUs of the shells and the ambient water temperature (Gilbert et al., 2017; Milano et al., 2017b). Furthermore, relatively short-lived bivalves were investigated in these publications (i.e., *Cerastoderma edule* in Milano et al., 2017b; *Pinna nobilis*, *Pinna cornea* and *Atrina rigida* in Gilbert et al., 2017), which is why microstructural proxies were not tested in longer time series so far. Furthermore, only relatively rare microstructures (i.e. non-denticular composite prismatic microstructure in Milano et al., 2017b) or such that occur in the inner layers of the shells (i.e., nacre in Gilbert et al., 2017) were hitherto studied. These layers are largely unsuitable for paleotemperature reconstructions because they can dissolve repeatedly during anaerobiosis (Crenshaw, 1980) and only provide incomplete, highly condensed growth records. Clearly, further research is needed before temperature-dependent microstructural changes can be used to infer climate information.

Thus, the microstructural properties of the long-lived bivalve species *Glycymeris bimaculata* and *Arctica islandica* shells were investigated quantitatively and in great detail within this thesis in order to resolve some of the most pressing research questions that need to be answered in order to faithfully reconstruct paleotemperature using bivalve shell microstructures. Microstructural analyses were performed mainly via SEM and temporal alignment of the growth records was accomplished by growth pattern analysis, stable oxygen isotope analysis, and trace element analysis. The results of this thesis were published as three manuscripts in international, peer-reviewed journals, each of which tackling different research questions:

In Manuscript 1 it is studied whether temperature-dependent alterations of the microstructural properties also occur in shells of long-lived bivalve taxa and in common microstructure types. The crossed-lamellar shells of *Glycymeris bimaculata* from the Adriatic Sea were investigated, a bivalve genus which attains lifespans of up to 200 years (Reynolds et al., 2013) and occurs in brackish and nearshore environments of mid-latitudes. *Glycymeris* has a rich fossil record ex-

tending back to the Cretaceaous (Casey, 1961; Squires, 2010; Crippa, 2013). The shells of *G. bimaculata* are composed entirely of crossed-lamellar microstructures, which are widespread in many mollusk taxa (Almagro et al., 2016). Thus, temperature proxies that are potentially discovered in *G. bimaculata* promise to be broadly applicable. The shape of the sub-µm-sized BMU of the crossed-lamellar shells was measured in sub-seasonal resolution and compared to the ambient temperature, salinity and chlorophyll a concentration. A customized image processing algorithm based on established methods was generated to facilitate extraction of such morphological data from SEM images of crossed-lamellar shells.

In Manuscript 2, the effects of water temperature on the shell microstructure were studied in juvenile specimens of *Arctica islandica* without additional environmental influences. Specimens were raised in aquaria at different temperature settings (1, 3, 5, 6, 9, 12 and 15 °C) with salinity and food conditions kept constant (Witbaard et al., 1997). Such experiments are prerequisite to determine causality between the water temperature and the observed microstructural changes and potentially infer paleothermometry transfer functions. *A. islandica* is a bivalve taxon that occurs at higher latitudes than *G. bimaculata* and forms different microstructures (i.e., HOM, crossed-acicular, and fine compex-crossed lamellar). *A. islandica* is also extremely long-lived, well-studied, and routinely used as a sclerochronological climate archive (Scourse et al., 2006; Wanamaker et al., 2009; Schöne, 2013). This study thus covers an additional important bivalve species and several microstructure types.

In Manuscript 3, the microstructure of *A. islandica* from different temperature regimes (Northeast Iceland, E'Viking Bank, Norwegian Trench, and Baltic Sea) was studied to assess how accurately the temperature-induced BMU size changes determined in the laboratory can be recovered from naturally grown shells. Additionally, 'vital effects' on the shell microstructure were studied by comparing the microstructures of shells grown under hostile growth conditions (i.e. the episodically hypoxic and lowly saline habitat of the Baltic Sea), with such grown at ideal conditions in open marine habitats. Ontogenetic effects on the shell microstructure were studied. Different microstructures were compared by performing analysis in various shell portions.

References

Agbaje, O. B. A., Thomas, D. E., McInerney, B. V., Molloy, M. P., and Jacob, D. E., 2017a. Organic macromolecules in shells of *Arctica islandica*: comparison with nacroprismatic bivalve shells. Mar. Biol. 164, 208.

Agbaje, O. B. A., Wirth, R., Morales, L. F. G., Shirai, K., Kosnik, M., Watanabe, T., and Jacob, D. E., 2017b. Architecture of crossed-lamellar bivalve shells: the southern giant clam (*Tridacna derasa*, Röding, 1798). R. Soc. Open Sci. 4, 170622.

Almagro, I., Drzymala, P., Berent, K., Ignacio Sainz-Diaz, C., Willinger, M. G., Bonarski, J., and Checa, A. G., 2016. New crystallographic relationships in biogenic aragonite: the crossed-lamellar microstructures of mollusks. Cryst. Growth Des. 16, 2083–2093.

Alpert, A. E., Cohen, A. L., Oppo, D. W., DeCarlo, T. M., Gove, J. M., and Young, C. W., 2016. Comparison of equatorial Pacific sea surface temperature variability and trends with Sr/Ca records from multiple corals. Paleoceanography 31, 252–265.

Andree, M., Oeschger, H., Siegenthaler, U., Riesen, T., Moell, M., Ammann, B., and Tobolski, K., 1986. ^{14}C dating of plant macrofossils in lake sediment. Radiocarbon 28, 411–416.

Asami, R., Yoshimura, N., Toriyabe, H., Minei, S., Shinjo, R., Hongo, C., Sakamaki, T., and Fujita, K., 2020. High-resolution evidence for Middle Holocene East Asian winter and summer monsoon variations: snapshots of fossil coral records. Geophys. Res. Lett. 47, e2020GL088509.

Ballesta-Artero, I., Janssen, R., van der Meer, J., and Witbaard, R., 2018a. Interactive effects of temperature and food availability on the growth of *Arctica islandica* (Bivalvia) juveniles. Mar. Environ. Res. 133, 67–77.

Beck, J. W., Edwards, R. L., Ito, E., Taylor, F. W., Recy, J., Rougerie, F., Joannot, P., and Henin, C., 1992. Sea-surface temperature from coral skeletal strontium/calcium ratios. Science 257, 644–647.

Bevelander, G. and Nakahara, H., 1969. An electron microscope study of the formation of the nacreous layer in the shell of certain bivalve molluscs. Calc. Tiss. Res. 3, 84–92.

Bevelander, G. and Nakahara, H., 1980. Compartment and envelope formation in the process of biological mineralization. In: The mechanisms of biomineralization in animals and plants. Ed. by M. Ōmori and N. Watabe. Tokai University Press, 19–27.

Bigg, G. R., Jickells, T. D., Liss, P. S., and Osborn, T. J., 2003. The role of the oceans in climate. Int. J. Climatol. 23, 1127–1159.

Bøggild, O. B., 1930. The shell structure of the molluscs. Vol. 9.2. Raekke 9 2. Copenhagen, Denmark: Det Kongelige Danske Videnskabernes Selskabs Skrifter. Naturvidenskabelig og Mathematisk Afdeling. 231-326.

Böhm, C. F., Demmert, B., Harris, J., Fey, T., Marin, F., and Wolf, S. E., 2016. Structural commonalities and deviations in the hierarchical organization of crossed-lamellar shells: a case study on the shell of the bivalve *Glycymeris glycymeris*. J. Mater. Res. 31, 536–546.

Breitenbach, S. F. M., Rehfeld, K., Goswami, B., Baldini, J. U. L., Ridley, H. E., Kennett, D. J., Prufer, K. M., Aquino, V. V., Asmerom, Y., Polyak, V. J., Cheng, H., Kurths, J., and Marwan, N., 2012. COnstructing Proxy Records from Age models (COPRA). Clim. Past 8, 1765–1779.

Briffa, K. R., Jones, P. D., Wigley, T. M. L., Pilcher, J. R., and Baillie, M. G. L., 1986. Climate reconstruction from tree rings: Part 2, spatial reconstruction of summer mean sea-level pressure patterns over Great Britain. J. Climatol. 6, 1–15.

Burns, S. J., Matter, A., Frank, N., and Mangini, A., 1998. Speleothem-based paleoclimate record from northern Oman. Geology 26, 499–502.

Butler, P. G., Richardson, C. A., Scourse, J. D., Wanamaker, A. D., Shammon, T. M., and Bennell, J. D., 2010. Marine climate in the Irish Sea: analysis of a 489-year marine master chronology derived from growth increments in the shell of the clam *Arctica islandica*. Quat. Sci. Rev. 29, 1614–1632.

Butler, P. G., Wanamaker, A. D., Scourse, J. D., Richardson, C. A., and Reynolds, D. J., 2013. Variability of marine climate on the North Icelandic Shelf in a 1357-year proxy archive based on growth increments in the bivalve *Arctica islandica*. Palaeogeogr. Palaeoclimatol. Palaeoecol. Unraveling environmental histories from skeletal diaries - advances in sclerochronology 373, 141–151.

Carré, M., Bentaleb, I., Bruguier, O., Ordinola, E., Barrett, N. T., and Fontugne, M., 2006. Calcification rate influence on trace element concentrations in aragonitic bivalve shells: evidences and mechanisms. Geochim. Cosmochim. Acta 70, 4906–4920.

Carter, J. G., 1980. Selected mineralogical data for the Bivalvia. In: Skeletal growth of aquatic organisms. Ed. by D. C. Rhoads and R. A. Lutz. Appendix 2, 627–631.

Carter, J. G., Harries, P. J., Malchus, N., Sartori, A. F., Anderson, L. C., Bieler, R., Bogan, A. E., Coan, E. V., Cope, J. C. W., Cragg, S. M., García-March, J. R., Hylleberg, J., Kelley, P., Kleemann, K., Kříž, J., McRoberts, C. A., Mikkelsen, P. M., Pojeta Jr., J., Tëmkin, I., Yancey, T., and Zieritz, A., 2012. Part N: Illustrated glossary of the Bivalvia. In: Treatise on Invertebrate Paleontology no. 48, Revised. Vol. 1. Chapter 31. Kansas: University of Kansas, 1–209.

Cartwright, J. H. and Checa, A. G., 2007. The dynamics of nacre self-assembly. J. R. Soc. Interface 4, 491–504.

Casella, L. A., Griesshaber, E., Yin, X., Ziegler, A., Mavromatis, V., Müller, D., Ritter, A.-C., Hippler, D., Harper, E. M., Dietzel, M., Immenhauser, A., Schöne, B. R., Angiolini, L., and Schmahl, W. W., 2017. Experimental diagenesis: insights into aragonite to calcite transformation of *Arctica islandica* shells by hydrothermal treatment. Biogeosciences 14, 1461–1492.

Casey, R., 1961. The stratigraphical palaeontology of the Lower Greensand. Palaeontology 3, 487–621.

Cauquoin, A., Werner, M., and Lohmann, G., 2019. Water isotopes - climate relationships for the mid-Holocene and preindustrial period simulated with an isotope-enabled version of MPI-ESM. Clim. Past 15, 1913–1937.

Cess, R. D., Potter, G. L., Blanchet, J. P., Boer, G. J., Del Genio, A. D., Déqué, M., Dymnikov, V., Galin, V., Gates, W. L., Ghan, S. J., Kiehl, J. T., Lacis, A. A., Le Treut, H., Li, Z.-X., Liang, X.-Z., McAvaney, B. J., Meleshko, V. P., Mitchell, J. F. B., Morcrette, J.-J., Randall, D. A., Rikus, L., Roeckner, E., Royer, J. F., Schlese, U., Sheinin, D. A., Slingo, A., Sokolov, A. P., Taylor, K. E., Washington, W. M., Wetherald, R. T., Yagai, I., and Zhang, M.-H., 1990. Intercomparison and interpretation of climate feedback processes in 19 atmospheric general circulation models. J. Geophys. Res. Atmospheres 95, 16601–16615.

Chan, P., Halfar, J., Adey, W., Lebednik, P., Steneck, R., Norley, C., and Holdsworth, D., 2019. Recent density decline in wild-collected subarctic crustose coralline algae reveals climate change signature. Geology 48, 226–230.

Checa, A., 2000. A new model for periostracum and shell formation in Unionidae (Bivalvia, Mollusca). Tissue Cell 32, 405–416.

Checa, A. G., 2018. Physical and biological determinants of the fabrication of molluscan shell microstructures. Front. Mar. Sci. 5, 353.

Checa, A. G., Salas, C., Harper, E. M., and Bueno-Pérez, J. d. D., 2014. Early Stage Biomineralization in the Periostracum of the 'Living Fossil' Bivalve *Neotrigonia*. PLOS ONE 9, e90033.

Cheddadi, R. and Rossignol-Strick, M., 1995. Eastern Mediterranean Quaternary paleoclimates from pollen and isotope records of marine cores in the Nile Cone Area. Paleoceanography 10, 291–300.

Clark, G. R., 1974. Growth lines in invertebrate skeletons. Annu. Rev. Earth Planet. Sci. 2, 77–99.

Clark, G. R., 1968. Mollusk shell: daily growth lines. Science 161, 800–802.

Clark, G. R., 1975. Periodic growth and biological rhythms in experimentally grown bivalves. In: Growth rhythms and the history of the Earth's rotation. Ed. by G. D. Rosenberg and S. K. Runcorn. London: John Wiley & Sons, 103–117.

Clark, G. R., 1980. Study of Molluscan Shell Structure and Growth Lines Using Thin Sections. In: Lutz, R. A. and Rhoads, D. C. Skeletal growth of aquatic organisms. Biological records of environmental change, 603–606.

Clark, M., Peck, L., Arivalagan Immanuel, J., Backeljau, T., Berland, S., Cardoso, J., Caurcel, C., Chapelle, G., De Noia, M., Dupont, S., Gharbi, K., Hoffman, J., Last, K., Marie, A., Melzner, F., Michalek, K., Morris, J., Power, D., Ramesh, K., and Harper, E., 2020. Deciphering mollusc shell production: the roles of genetic mechanisms through to ecology, aquaculture and biomimetics. Biol. Rev.

Comboul, M., Emile-Geay, J., Evans, M. N., Mirnateghi, N., Cobb, K. M., and Thompson, D. M., 2014. A probabilistic model of chronological errors in layer-counted climate proxies: applications to annually banded coral archives. Clim. Past 10, 825–841.

Conkey, L. E., 1979. Response of Tree-Ring Density to Climate in Maine, U.S.A. Tree-Ring Bull. 39, 29–38.

Conroy, J. L., Overpeck, J. T., Cole, J. E., Shanahan, T. M., and Steinitz-Kannan, M., 2008. Holocene changes in eastern tropical Pacific climate inferred from a Galápagos lake sediment record. Quat. Sci. Rev. 27, 1166–1180.

Crenshaw, M. A., 1980. Mechanisms of Shell Formation and Dissolution. In: Skeletal growth of aquatic organisms. Ed. by D. C. Rhoads and R. A. Lutz. Red. by F. G. Stehli. Topics in Geobiology. Boston, MA: Springer US, 115–132.

Crippa, G., 2013. The shell ultrastructure of the genus *Glycymeris* DA COSTA, 1778: A comparison between fossil and recent specimens. Riv. Ital. Paleontol. E Stratigr. 119, 387–399.

Cuif, J.-P., Belhadj, O., Borensztajn, S., Gèze, M., Trigos-Santos, S., Prado, P., and Dauphin, Y., 2020. Prism substructures in the shell of *Pinna nobilis* (Linnaeus, 1758), Mollusca – Evidence for a three-dimensional pulsed-growth model. Heliyon 6, e04513.

Cuif, J.-P., Dauphin, Y., Luquet, G., Medjoubi, K., Somogyi, A., and Perez-Huerta, A., 2018. Revisiting the organic template model through the microstructural study of shell development in *Pinctada margaritifera*, the Polynesian Pearl Oyster. Minerals 8, 370.

Curry, J. A., Schramm, J. L., and Ebert, E. E., 1995. Sea ice-albedo climate feedback mechanism. J. Clim. 8, 240–247.

Dansgaard, W., Clausen, H. B., Gundestrup, N., Hammer, C. U., Johnsen, S. F., Kristinsdottir, P. M., and Reeh, N., 1982. A new Greenland deep ice core. Science 218, 1273–1277.

Dansgaard, W., Johnsen, S. J., Clausen, H. B., Dahl-Jensen, D., Gundestrup, N. S., Hammer, C. U., Hvidberg, C. S., Steffensen, J. P., Sveinbjörnsdottir, A. E., Jouzel, J., and Bond, G., 1993. Evidence for general instability of past climate from a 250-kyr ice-core record. Nature 364, 218–220.

Dettman, D. L., Reische, A. K., and Lohmann, K. C., 1999. Controls on the stable isotope composition of seasonal growth bands in aragonitic fresh-water bivalves (unionidae). Geochim. Cosmochim. Acta 63, 1049–1057.

De Winter, N., Müller, I., Kocken, I., Thibault, N., Ullmann, C., Farnsworth, A., Lunt, D., Claeys, P., and Ziegler, M., 2021. Absolute seasonal temperature estimates from clumped isotopes in

bivalve shells suggest warm and variable greenhouse climate. Commun. Earth Environ. 2, 121.

Drysdale, R. N., Zanchetta, G., Hellstrom, J. C., Fallick, A. E., McDonald, J., and Cartwright, I., 2007. Stalagmite evidence for the precise timing of North Atlantic cold events during the early last glacial. Geology 35, 77–80.

Dunca, E., Mutvei, H., Goransson, P., Morth, C.-M., Schone, B. R., Whitehouse, M. J., Elfman, M., and Baden, S. P., 2009. Using ocean quahog (*Arctica islandica*) shells to reconstruct palaeoenvironment in Öresund, Kattegat and Skagerrak, Sweden. Int. J. Earth Sci. 15.

Edge, D. C., Reynolds, D. J., Wanamaker, A. D., Griffin, D., Bureau, D., Outridge, C., Stevick, B. C., Weng, R., and Black, B. A., 2021. A multicentennial proxy record of Northeast Pacific sea surface temperatures from the annual growth increments of *Panopea generosa*. Paleoceanogr. Paleoclimatology n/a, e2021PA004291.

Eiler, J. M., 2007. "Clumped-isotope" geochemistry—The study of naturally-occurring, multiply-substituted isotopologues. Earth Planet. Sci. Lett. 262, 309–327.

Eiler, J. M., 2011. Paleoclimate reconstruction using carbonate clumped isotope thermometry. Quat. Sci. Rev. 30, 3575–3588.

Epstein, S., Buchsbaum, R., Lowenstam, H. A., and Urey, H. C., 1953. Revised carbonate-water isotopic temperature scale. GSA Bull. 64, 1315–1326.

Esper, J., Cook, E. R., and Schweingruber, F. H., 2002. Low-Frequency Signals in Long Tree-Ring Chronologies for Reconstructing Past Temperature Variability. Science 295, 2250–2253.

Fairchild, I. J., Smith, C. L., Baker, A., Fuller, L., Spötl, C., Mattey, D., McDermott, F., and E.i.m.f., 2006. Modification and preservation of environmental signals in speleothems. Earth-Sci. Rev. ISOtopes in PALaeoenvironmental reconstruction (ISOPAL) 75, 105–153.

Fernandez, A., Müller, I. A., Rodríguez-Sanz, L., van Dijk, J., Looser, N., and Bernasconi, S. M., 2017. A reassessment of the precision of carbonate clumped isotope measurements: implications for calibrations and paleoclimate reconstructions. Geochem. Geophys. Geosystems 18, 4375–4386.

Fiebig, J., Hofmann, S., Löffler, N., Lüdecke, T., Methner, K., and Wacker, U., 2016. Slight pressure imbalances can affect accuracy and precision of dual inlet-based clumped isotope analysis. Isotopes Environ. Health Stud. 52, 12–28.

Fraiser, M. L. and Bottjer, D. J., 2007. When bivalves took over the world. Paleobiology 33, 397–413.

Füllenbach, C. S., Schöne, B. R., and Mertz-Kraus, R., 2015. Strontium/lithium ratio in aragonitic shells of *Cerastoderma edule* (Bivalvia) — A new potential temperature proxy for brackish environments. Chem. Geol. 417, 341–355.

Gedney, N., Cox, P. M., and Huntingford, C., 2004. Climate feedback from wetland methane emissions. Geophys. Res. Lett. 31.

Gilbert, P. U., Bergmann, K. D., Myers, C. E., Marcus, M. A., DeVol, R. T., Sun, C.-Y., Blonsky, A. Z., Tamre, E., Zhao, J., Karan, E. A., Tamura, N., Lemer, S., Giuffre, A. J., Giribet, G., Eiler, J. M., and Knoll, A. H., 2017. Nacre tablet thickness records formation temperature in modern and fossil shells. Earth Planet. Sci. Lett. 460, 281–292.

Gillikin, D. P., Lorrain, A., Navez, J., Taylor, J. W., André, L., Keppens, E., Baeyens, W., and Dehairs, F., 2005. Strong biological controls on Sr/Ca ratios in aragonitic marine bivalve shells. Geochem. Geophys. Geosystems 6.

Gonfiantini, R., Stichler, W., and Rozanski, K., 1995. Standards and intercomparison materials distributed by the International Atomic Energy Agency for stable isotope measurements (IAEA-TECDOC–825). IAEA.

Goreau, T. F., Goreau, N. I., and Goreau, T. J., 1979. Corals and coral reefs. Sci. Am. 241, 124–137.

Grossman, E. L. and Ku, T.-L., 1986. Oxygen and carbon isotope fractionation in biogenic aragonite: Temperature effects. Chem. Geol. Iso Geosc Sec 59, 59–74.

Guo, Y., Deng, W., Liu, X., Kong, K., Yan, W., and Wei, G., 2021. Clumped isotope geochemistry of island carbonates in the South China Sea: Implications for early diagenesis and dolomitization. Mar. Geol. 437, 106513.

Halfar, J., Steneck, R., Joachimski, M., Kronz, A., and Wanamaker Jr., A., 2008. Coralline red algae as high-resolution climate recorders. Geology 36, 463–466.

Hansen, J. E. and Sato, M., 2012. Paleoclimate implications for human-made climate change. In: Climate change. Ed. by A. Berger, F. Mesinger, and D. Sijacki. Vienna: Springer, 21–47.

Harper, E. M., 1997. The molluscan periostracum: an important cnstraint in bivalve evolution. Paleontology 40, 71–91.

Harper, E. M., 1998. The fossil record of bivalve molluscs. In: The adequacy of the fossil record. Ed. by S. K. Donovan and C. R. C. Paul. Chichester, UK: John Wiley & Sons, 243–267.

Harper, E. M., Checa, A. G., and Rodríguez-Navarro, A. B., 2009. Organization and mode of secretion of the granular prismatic microstructure of *Entodesma navicula* (Bivalvia: Mollusca). Acta Zool. 90, 132–141.

Hickson, J. A., Johnson, A. L. A., Heaton, T. H. E., and Balson, P. S., 1999. The shell of the Queen Scallop *Aequipecten opercularis* (L.) as a promising tool for palaeoenvironmental reconstruction: evidence and reasons for equilibrium stable-isotope incorporation. Palaeogeogr. Palaeoclimatol. Palaeoecol. 154, 325–337.

Hiebenthal, C., Philipp, E. E. R., Eisenhauer, A., and Wahl, M., 2013. Effects of seawater pCO_2 and temperature on shell growth, shell stability, condition and cellular stress of Western Baltic Sea *Mytilus edulis* (L.) and *Arctica islandica* (L.) Mar. Biol. 160, 2073–2087.

Höche, N., Peharda, M., Walliser, E. O., and Schöne, B. R., 2020. Morphological variations of crossed-lamellar ultrastructures of *Glycymeris bimaculata* (Bivalvia) serve as a marine temperature proxy. Estuar. Coast. Shelf Sci. 237, 106658.

Houghton, J. T., Ding, Y., Griggs, D. J., Noguer, M., Linden, P. J. van der, Dai, X., Maskell, K., and Johnson, C. A., 2001. Climate change 2001: The scientific basis: contribution of working group I to the third assessment report of the Intergovernmental Panel on Climate Change. Cambridge University Press. 1038 pp.

Houghton, J. T., Jenkins, G. J., and Ephraums, J. J., 1990. Climate change. United Kingdom. 404 pp.

Huntley, B., 2012. Reconstructing palaeoclimates from biological proxies: Some often overlooked sources of uncertainty. Quat. Sci. Rev. 31, 1–16.

Jablonski, D., Belanger, C. L., Berke, S. K., Huang, S., Krug, A. Z., Roy, K., Tomasovych, A., and Valentine, J. W., 2013. Out of the tropics, but how? Fossils, bridge species, and thermal ranges in the dynamics of the marine latitudinal diversity gradient. PNAS 110, 10487–10494.

Jacob, D. E., Soldati, A. L., Wirth, R., Huth, J., Wehrmeister, U., and Hofmeister, W., 2008. Nanostructure, composition and mechanisms of bivalve shell growth. Geochim. Cosmochim. Acta 72, 5401–5415.

Johnson, T. C., Brown, E. T., McManus, J., Barry, S., Barker, P., and Gasse, F., 2002. A high-resolution paleoclimate record spanning the past 25,000 years in southern East Africa. Science 296, 113–132.

Jones, D. S., 1980. Annual cycle of shell growth increment formation in two continental shelf bivalves and its paleoecologic significance. Paleobiology 6, 331–340.

Jones, P. D., Briffa, K. R., Osborn, T. J., Lough, J. M., van Ommen, T. D., Vinther, B., Luterbacher, J., Wahl, E., Zwiers, F., Mann, M., Schmidt, G., Ammann, C., Buckley, B., Cobb, K., Esper, J., Goosse, H., Graham, N., Jansen, E., Kiefer, T., Kull, C., Küttel, M., Mosley-Thompson, E., Overpeck, J., Riedwyl, N., Schulz, M., Tudhope, A., Villalba, R., Wanner, H., Wolff, E., and Xoplaki, E., 2009. High-resolution palaeoclimatology of the last millennium: a review of current status and future prospects. The Holocene 19, 3–49.

Jones, P. D., New, M., Parker, D. E., Martin, S., and Rigor, I. G., 1999. Surface air temperature and its changes over the past 150 years. Rev. Geophys. 37, 173–199.

Justine, D., Gwénaëlle, C., Pierre, P., Pascal, L., André, P., Laurent, C., Philippe, A., and Julien, T., 2020. Assessment of Ba/Ca in *Arctica islandica* shells as a proxy for phytoplankton dynamics in the Northwestern Atlantic Ocean. Estuar. Coast. Shelf Sci. 237, 106628.

Kamenos, N. A., Cusack, M., and Moore, P. G., 2008. Coralline algae are global palaeothermometers with bi-weekly resolution. Geochim. Cosmochim. Acta 72, 771–779.

Kennedy, W. J., Taylor, J. D., and Hall, A., 1969. Environmental and biological controls on bivalve shell mineralogy. Biol. Rev. 44, 499–530.

Kennish, M. J. and Olsson, R. K., 1974. Effects of thermal discharges on the microstructural growth of *Mercenaria mercenaria*. Environ. Geol. 1, 44–64.

Killingley, J. S., 1983. Effects of diagenetic recrystallization on $^{18}O/^{16}O$ values of deep-sea sediments. Nature 301, 594–597.

Kim, W. S., Huh, H. T., Lee, J.-H., Rumohr, H., and Koh, C. H., 1999. Endogenous circatidal rhythm in the Manila clam *Ruditapes philippinarum* (Bivalvia: Veneridae). Mar. Biol. 134, 107–112.

Knoll, K., Landman, N. H., Cochran, J. K., Macleod, K. G., and Sessa, J. A., 2016. Microstructural preservation and the effects of diagenesis on the carbon and oxygen isotope composi-

tion of Late Cretaceous aragonitic mollusks from the Gulf Coastal Plain and the Western Interior Seaway. Am. J. Sci. 316, 591–613.

Kobayashi, I. and Samata, T., 2006. Bivalve shell structure and organic matrix. Mater. Sci. Eng. C 26, 692–698.

Kong, J., Liu, C., Yang, D., Yan, Y., Chen, Y., Liu, Y., Zheng, G., Xie, L., and Zhang, R., 2019. A novel basic matrix protein of *Pinctada fucata*, PNU9, functions as inhibitor during crystallization of aragonite. CrystEngComm 21, 1250–1261.

Krantz, D. E., 1990. Mollusk-isotope records of Plio-Pleistocene marine paleoclimate, U. S. Middle Atlantic Coastal Plain. PALAIOS 5, 317–335.

Le Roy, N., Jackson, D. J., Marie, B., Ramos-Silva, P., and Marin, F., 2014. The evolution of metazoan α-carbonic anhydrases and their roles in calcium carbonate biomineralization. Front. Zool. 11, 75.

Le Roy, N., Marie, B., Gaume, B., Guichard, N., Delgado, S., Zanella-Cleon, I., Becchi, M., Auzoux-Bordenave, S., Sire, J.-Y., and Marin, F., 2012. Identification of two carbonic anhydrases in the mantle of the european abalone *Haliotis tuberculata* (Gastropoda, Haliotidae): Phylogenetic implications. J. Exp. Zool. Part B 318B, 353–367.

Leutert, T. J., Sexton, P. F., Tripati, A., Piasecki, A., Ho, S. L., and Meckler, A. N., 2019. Sensitivity of clumped isotope temperatures in fossil benthic and planktic foraminifera to diagenetic alteration. Geochim. Cosmochim. Acta 257, 354–372.

Levi-Kalisman, Y., Falini, G., Addadi, L., and Weiner, S., 2001. Structure of the nacreous organic matrix of a bivalve mollusk shell examined in the hydrated state using cryo-TEM. J. Struct. Biol. 135, 8–17.

Levitus, S., Antonov, J. I., Boyer, T. P., and Stephens, C., 2000. Warming of the world ocean. Science 287, 2225–2229.

Li, B., Nychka, D. W., and Ammann, C. M., 2010. The value of multiproxy reconstruction of past climate. J. Am. Stat. Assoc. 105, 883–895.

Li, X. W., Ji, H. M., Yang, W., Zhang, G. P., and Chen, D. L., 2017. Mechanical properties of crossed-lamellar structures in biological shells: A review. J. Mech. Behav. Biomed. Mater. 74, 54–71.

Macías-Sánchez, E., Willinger, M. G., Pina, C., and Checa, A., 2017. Transformation of ACC into aragonite and the origin of the nanogranular structure of nacre. Sci. Rep. 7.

Marali, S., Schoene, B. R., Mertz-Kraus, R., Griffin, S. M., Wanamaker, A. D., Butler, P. G., Holland, H. A., and Jochum, K. P., 2017. Reproducibility of trace element time-series (Na/Ca, Mg/Ca, Mn/Ca, Sr/Ca, and Ba/Ca) within and between specimens of the bivalve *Arctica islandica* - A LA-ICP-MS line scan study. Paleogeogr. Paleoclimatol. Paleoecol. 484, 109–128.

Marchitto, T. M., Jones, G. A., Goodfriend, G. A., and Weidman, C. R., 2000. Precise temporal correlation of Holocene mollusk shells using sclerochronology. Quat. Res. 53, 236–246.

Marin, F., Le Roy, N., and Marie, B., 2012. The formation and mineralization of mollusk shell. Front. Biosci. S4, 1099–1125.

Markulin, K., Peharda, M., Mertz-Kraus, R., Schöne, B. R., Uvanović, H., Kovač, Ž., and Janeković, I., 2019. Trace and minor element records in aragonitic bivalve shells as environmental proxies. Chem. Geol. 507, 120–133.

Martinelli, N., 2004. Climate from dendrochronology: latest developments and results. Glob. Planet. Change. Global Climate Changes during the Late Quaternary 40, 129–139.

Martinson, D. G., Pisias, N. G., Hays, J. D., Imbrie, J., Moore, T. C., and Shackleton, N. J., 1987. Age dating and the orbital theory of the Ice Ages: development of a high-resolution 0 to 300,000-year chronostratigraphy 1. Quat. Res. 27, 1–29.

Masson-Delmotte, V., Zhai, P., Pirani, A., Connors, S. L., Péan, C., Berger, S., Caud, N., Chen, Y., Goldfarb, L., Gomis, M. I., Huang, M., Leitzell, K., Lonnoy, E., Matthews, J. B. R., Maycock, T. K., Waterfield, T., Yelekçi, Ö., Yu, R., and Zhou, B., eds., 2021. Climate change 2021: The physical science basis. Contribution of working group I to the sixth assessment report of the Intergovernmental Panel on Climate Change. Cambridge University Press.

Milano, S., Nehrke, G., Wanamaker, A. D., Ballesta-Artero, I., Brey, T., and Schöne, B. R., 2017a. The effects of environment on *Arctica islandica* shell formation and architecture. Biogeosciences 14, 1577–1591.

Milano, S., Schöne, B. R., and Witbaard, R., 2017b. Changes of shell microstructural characteristics of *Cerastoderma edule* (Bivalvia) — A novel proxy for water temperature. Palaeogeogr. Palaeoclimatol. Palaeoecol. 465, 395–406.

Mitsuguchi, T., Matsumoto, E., Abe, O., Uchida, T., and Isdale, P. J., 1996. Mg/Ca thermometry in coral skeletons. Science 274, 961–963.

Miyaji, T., Tanabe, K., and Schöne, B. R., 2007. Environmental controls on daily shell growth of *Phacosoma japonicum* (Bivalvia: Veneridae) from Japan. Mar. Ecol. Prog. Ser. 336, 141–150.

Mook, W. G. and Vogel, J. C., 1968. Isotopic equilibrium between shells and their environment. Science 159, 874–875.

Nassif, N., Pinna, N., Gehrke, N., Antonietti, M., Jäger, C., and Cölfen, H., 2005. Amorphous layer around aragonite platelets in nacre. Proc. Natl. Acad. Sci. 102, 12653–12655.

Nehrke, G., Poigner, H., Wilhelms-Dick, D., Brey, T., and Abele, D., 2012. Coexistence of three calcium carbonate polymorphs in the shell of the Antarctic clam *Laternula elliptica*. Geochem. Geophys. Geosystems 13.

Nishida, K., Ishimura, T., Suzuki, A., and Sasaki, T., 2012. Seasonal changes in the shell microstructure of the bloody clam, *Scapharca broughtonii* (Mollusca: Bivalvia: Arcidae). Palaeogeogr. Palaeoclimatol. Palaeoecol. 363–364, 99–108.

Nudelman, F., 2015. Nacre biomineralisation: A review on the mechanisms of crystal nucleation. Semin. Cell Dev. Biol. Biomineralisation & Motorisation of pathogens 46, 2–10.

Nudelman, F., Gotliv, B. A., Addadi, L., and Weiner, S., 2006. Mollusk shell formation: Mapping the distribution of organic matrix components underlying a single aragonitic tablet in nacre. J. Struct. Biol. 153, 176–187.

Olson, I. C., Kozdon, R., Valley, J. W., and Gilbert, P. U. P. A., 2012. Mollusk shell nacre ultrastructure correlates with environmental temperature and pressure. J. Am. Chem. Soc. 134, 7351–7358.

Oschmann, W., 2018. Leben der Vorzeit: Grundlagen der Allgemeinen und Speziellen Paläontologie. 1. Auflage. UTB Paläontologie, Geowissenschaften. Bern: Haupt Verlag. 400 pp.

Palmer, A. R., 1983. Relative cost of producing skeletal organic matrix versus calcification: evidence from marine gastropods. Mar. Biol. 75, 287–292.

Petit, J. R., Jouzel, J., Raynaud, D., Barkov, N. I., Barnola, J.-M., Basile, I., Bender, M., Chappellaz, J., Davis, M., Delaygue, G., Delmotte, M., Kotlyakov, V. M., Legrand, M., Lipenkov, V. Y., Lorius,

C., PÉpin, L., Ritz, C., Saltzman, E., and Stievenard, M., 1999. Climate and atmospheric history of the past 420,000 years from the Vostok ice core, Antarctica. Nature 399, 429–436.

Reynolds, D. J., Butler, P., Williams, S., Scourse, J., Richardson, C., Wanamaker, A., Austin, W., Cage, A., and Sayer, M., 2013. A multiproxy reconstruction of Hebridean (NW Scotland) spring sea surface temperatures between AD 1805 and 2010. Palaeogeogr. Palaeoclimatol. Palaeoecol. 386, 275–285.

Reynolds, D. J., Hall, I. R., Slater, S. M., Scourse, J. D., Halloran, P. R., and Sayer, M. D. J., 2017. Reconstructing past seasonal to multicentennial-scale variability in the NE Atlantic Ocean using the long-lived marine bivalve mollusk *Glycymeris glycymeris*. Paleoceanography 32, 1153–1173.

Reynolds, D. J., Hall, I. R., and Slater, S. M., 2019. An integrated carbon and oxygen isotope approach to reconstructing past environmental variability in the northeast Atlantic Ocean. Paleogeogr. Paleoclimatol. Paleoecol. 523, 48–61.

Richardson, C. A., Crisp, D. J., and Runham, N. W., 1980. An endogenous rhythm in shell deposition in *Cerastoderma edule*. J. Mar. Biol. Assoc. U. K. 60, 991–1004.

Rind, D., 1998. Latitudinal temperature gradients and climate change. J. Geophys. Res. Atmospheres 103, 5943–5971.

Ritter, A.-C., Mavromatis, V., Dietzel, M., Kwiecien, O., Wiethoff, F., Griesshaber, E., Casella, L. A., Schmahl, W. W., Koelen, J., Neuser, R. D., Leis, A., Buhl, D., Niedermayr, A., Breitenbach, S. F. M., Bernasconi, S. M., and Immenhauser, A., 2017. Exploring the impact of diagenesis on (isotope) geochemical and microstructural alteration features in biogenic aragonite. Sedimentology 64, 1354–1380.

Rohling, E. J. and Bigg, G. R., 1998. Paleosalinity and $\delta^{18}O$: A critical assessment. J. Geophys. Res. Oceans 103, 1307–1318.

Ropes, J. W., Jones, D., Murawski, S., Serchuk, F., and Jearld, A., 1984a. Documentation of annual growth lines in ocean quahogs, *Arctica islandica* Linné. Fish. Bull. 82, 1–19.

Sabine, C. L., Feely, R. A., Gruber, N., Key, R. M., Lee, K., Bullister, J. L., Wanninkhof, R., Wong, C. S., Wallace, D. W. R., Tilbrook, B., Millero, F. J., Peng, T.-H., Kozyr, A., Ono, T., and Rios, A. F., 2004. The oceanic sink for anthropogenic CO_2. Science 305, 367–371.

Schellnhuber, H. J., Cramer, W., Cramer, W. P., Nakicenovic, N., Wigley, T., and Yohe, G., 2006. Avoiding dangerous climate change. United Kingdom: Cambridge University Press. 407 pp.

Schmidt, G. A., Annan, J. D., Bartlein, P. J., Cook, B. I., Guilyardi, E., Hargreaves, J. C., Harrison, S. P., Kageyama, M., LeGrande, A. N., Konecky, B., Lovejoy, S., Mann, M. E., Masson-Delmotte, V., Risi, C., Thompson, D., Timmermann, A., Tremblay, L.-B., and Yiou, P., 2014. Using palaeoclimate comparisons to constrain future projections in CMIP5. Clim. Past 10, 221–250.

Scholz, D., Frisia, S., Borsato, A., Spötl, C., Fohlmeister, J., Mudelsee, M., Miorandi, R., and Mangini, A., 2012. Holocene climate variability in north-eastern Italy: potential influence of the NAO and solar activity recorded by speleothem data. Clim. Past 8, 1367–1383.

Schöne, B. R., 2008. The curse of physiology - challenges and opportunities in the interpretation of geochemical data from mollusk shells. Geo-Mar. Lett. 28, 269–285.

Schöne, B. R., 2013. *Arctica islandica* (Bivalvia): A unique paleoenvironmental archive of the northern North Atlantic Ocean. Glob. Planet. Change 111, 199–225.

Schöne, B. R., Dunca, E., Fiebig, J., and Pfeiffer, M., 2005a. Mutvei's solution: An ideal agent for resolving microgrowth structures of biogenic carbonates. Palaeogeogr. Palaeoclimatol. Palaeoecol. 228, 149–166.

Schöne, B. R., Fiebig, J., Pfeiffer, M., Gleβ, R., Hickson, J., Johnson, A. L., Dreyer, W., and Oschmann, W., 2005b. Climate records from a bivalved Methuselah (*Arctica islandica*, Mollusca; Iceland). Palaeogeogr. Palaeoclimatol. Palaeoecol. 228, 130–148.

Schöne, B. R., Goodwin, D. H., Flessa, K. W., Dettman, D. L., and Roopnarine, P. D., 2002. Sclerochronology and growth of the bivalve mollusks *Chione* (Chionista) *fluctifraga* and *C.* (Chionista) *cortezi* in the northern Gulf of California, Mexico. Veliger 45, 45–54.

Schöne, B. R., Houk, S. D., Freyre Castro, A. D., Fiebig, J., Oschmann, W., Kröncke, I., Dreyer, W., and Gosselck, F., 2005c. Daily growth rates in shells of *Arctica islandica*: Assessing subseasonal environmental controls on a long-lived bivalve mollusk. PALAIOS 20, 78–92.

Schöne, B. R., Zhang, Z., Radermacher, P., Thébault, J., Jacob, D. E., Nunn, E. V., and Maurer, A.-F., 2011b. Sr/Ca and Mg/Ca ratios of ontogenetically old, long-lived bivalve shells (*Arctica islandica*) and their function as paleotemperature proxies. Palaeogeogr. Palaeoclimatol. Palaeoecol. Reconstructing mid- to high-latitude marine climate and ocean variability us-

ing bivalves, coralline algae, and marine sediment cores from the Northern Hemisphere 302, 52–64.

Schweingruber, F. H. and Briffa, K. R., 1996. Tree-ring density networks for climate reconstruction. In: Climatic variations and forcing mechanisms of the last 2000 years. Ed. by P. D. Jones, R. S. Bradley, and J. Jouzel. NATO ASI Series. Berlin, Heidelberg: Springer, 43–66.

Scourse, J., Richardson, C., Forsythe, G., Harris, I., Heinemeier, J., Fraser, N., Briffa, K., and Jones, P., 2006. First cross-matched floating chronology from the marine fossil record: data from growth lines of the long-lived bivalve mollusc *Arctica islandica*. Holocene 16, 967–974.

Sepkoski, J. J., 1981. A factor analytic description of the Phanerozoic marine fossil record. Paleobiology 7, 36–53.

Shen, C.-C., Lee, T., Chen, C.-Y., Wang, C.-H., Dai, C.-F., and Li, L.-A., 1996. The calibration of D[Sr/Ca] versus sea surface temperature relationship for Porites corals. Geochim. Cosmochim. Acta 60, 3849–3858.

Sheppard, P. R., 2010. Dendroclimatology: extracting climate from trees. WIREs Clim. Change 1, 343–352.

Smith, T. M. and Reynolds, R. W., 2003. Extended reconstruction of global sea surface temperatures based on COADS data (1854–1997). J. Clim. 16, 1495–1510.

Spann, N., Harper, E. M., and Aldridge, D. C., 2010. The unusual mineral vaterite in shells of the freshwater bivalve *Corbicula fluminea* from the UK. Naturwissenschaften 97, 743–751.

Squires, R. L., 2010. Northeast Pacific Upper Cretaceous and Paleocene glycymeridid bivalves. J. Paleontol. 84, 895–917.

Stansell, N. D., Rodbell, D. T., Abbott, M. B., and Mark, B. G., 2013. Proglacial lake sediment records of Holocene climate change in the western Cordillera of Peru. Quat. Sci. Rev. 70, 1–14.

Stemmer, K., Brey, T., Gutbrod, M. S., Beutler, M., Schalkhausser, B., and De Beer, D., 2019. in situ measurements of pH, Ca^{2+} and DIC dynamics within the extrapallial fluid of the ocean quahog *Arctica islandica*. J. Shellfish Res. 38, 71–78.

Strain, P. M. and Tan, F. C., 1993. Seasonal evolution of oxygen isotope-salinity relationships in high-latitude surface waters. J. Geophys. Res. Oceans 98, 14589–14598.

Tan Tiu, A., 1988. Temporal and spatial variation of shell microstructure of *Polydesmoda carolini-ana* (Bivalvia: Heterodonta). Am. Malacol. Bull. 6, 199–206.

Tan Tiu, A. and Prezant, R. S., 1989. Temporal variation in microstructure of the inner shell surface of *Corbicula fluminea* (Bivalvia: Heterodonta). Am. Malacol. Bull. 7, 65–71.

Taylor, J. D., 1973. The structural evolution of the bivalve shell. Paleontology 16, 519–534.

Thompson, I., Jones, D. S., and Dreibelis, D., 1980a. Annual internal growth banding and life history of the Ocean Quahog *Arctica islandica* (Mollusca: Bivalvia). Mar. Biol. 57, 25–34.

Torgersen, T., 1979. Isotopic composition of river runoff on the U.S. east coast: Evaluation of stable isotope versus salinity plots for coastal water mass identification. J. Geophys. Res. Oceans 84, 3773–3775.

Trofimova, T., Alexandroff, S. J., Mette, M. J., Tray, E., Butler, P. G., Campana, S. E., Harper, E. M., Johnson, A. L., Morrongiello, J. R., Peharda, M., Schöne, B. R., Andersson, C., Andrus, C. F. T., Black, B. A., Burchell, M., Carroll, M. L., DeLong, K. L., Gillanders, B. M., Grønkjær, P., Killam, D., Prendergast, A. L., Reynolds, D. J., Scourse, J. D., Shirai, K., Thébault, J., Trueman, C., and de Winter, N., 2020. Fundamental questions and applications of sclerochronology: Community-defined research priorities. Estuar. Coast. Shelf Sci. 245, 106977.

Vavrus, S. J., He, F., Kutzbach, J. E., and Ruddiman, W. F., 2020. Rapid neoglaciation on Ellesmere Island promoted by enhanced summer snowfall in a transient climate model simulation of the middle-late-Holocene. The Holocene 30, 1474–1480.

Vendrasco, M. J., Checa, A. G., and Heimbrock, W. P., 2019. Remarkable preservation of shell microstructures from the Late Ordovician of the Cincinnati Arch region, USA, and the success of nacre among Ordovician mollusks. J. Paleontol. 93, 658–672.

Villalba, R., Grosjean, M., and Kiefer, T., 2009. Long-term multi-proxy climate reconstructions and dynamics in South America (LOTRED-SA): State of the art and perspectives. Palaeogeogr. Palaeoclimatol. Palaeoecol. Long-term multi-proxy climate reconstructions and dynamics in South America (LOTRED-SA): State of the art and perspectives 281, 175–179.

Vollweiler, N., Scholz, D., Mühlinghaus, C., Mangini, A., and Spötl, C., 2006. A precisely dated climate record for the last 9 kyr from three high alpine stalagmites, Spannagel Cave, Austria. Geophys. Res. Lett. 33.

Vose, R. S., Schmoyer, R. L., Steurer, P. M., Peterson, T. C., Heim, R., Karl, T. R., and Eischeid, J. K., 1992. The global historical climatology network: Long-term monthly temperature, precipitation, sea level pressure, and station pressure data. Technical Report. Oak Ridge National Lab., TN (United States). Carbon Dioxide Information Analysis Center.

Wanamaker, A. D. and Gillikin, D. P., 2019. Strontium, magnesium, and barium incorporation in aragonitic shells of juvenile *Arctica islandica*: Insights from temperature controlled experiments. Chem. Geol. Chemical sclerochronology 526, 117–129.

Wanamaker, A. D., Heinemeier, J., Scourse, J. D., Richardson, C. A., Butler, P. G., Eiríksson, J., and Knudsen, K. L., 2008. Very long-lived mollusks confirm 17th century AD tephra-based radiocarbon reservoir ages for North Icelandic shelf waters. Radiocarbon 50, 399–412.

Wanamaker, A. D., Kreutz, K. J., Schöne, B. R., Maasch, K. A., Pershing, A. J., Borns, H. W., Introne, D. S., and Feindel, S., 2009. A late Holocene paleo-productivity record in the western Gulf of Maine, USA, inferred from growth histories of the long-lived ocean quahog (*Arctica islandica*). Int. J. Earth Sci. 98, 19.

Wang, W.-q., Garbelli, C., Zhang, F.-f., Zheng, Q.-f., Zhang, Y.-c., Yuan, D.-x., Shi, Y.-k., Chen, B., and Shen, S.-z., 2020. A high-resolution Middle to Late Permian paleotemperature curve reconstructed using oxygen isotopes of well-preserved brachiopod shells. Earth Planet. Sci. Lett. 540, 116245.

Wehrmeister, U., Jacob, D. E., Soldati, A. L., Loges, N., Häger, T., and Hofmeister, W., 2011. Amorphous, nanocrystalline and crystalline calcium carbonates in biological materials. J. Raman Spectrosc. 42, 926–935.

Weiner, S., Traub, W., Miller, A., Phillips, D. C., and Williams, R. J. P., 1984. Macromolecules in mollusc shells and their functions in biomineralization. Philos. Trans. R. Soc. Lond. B Biol. Sci. 304, 425–434.

Weiss, I. M., Tuross, N., Addadi, L., and Weiner, S., 2002. Mollusc larval shell formation: amorphous calcium carbonate is a precursor phase for aragonite. J. Exp. Zool. 293, 478–491.

Wendt, K. A., Li, X., and Edwards, R. L., 2021. Uranium–thorium dating of speleothems. Elements 17, 87–92.

Wilbur, K. M. and Saleuddin, A. S. M., 1983. 6 - Shell Formation. In: The Mollusca. Ed. by A. S. M. Saleuddin and K. M. Wilbur. Academic Press, 235–287.

Winkelstern, I. Z. and Lohmann, K. C., 2016. Shallow burial alteration of dolomite and limestone clumped isotope geochemistry. Geology 44, 467–470.

Witbaard, R., Franken, R., and Visser, B., 1997. Growth of juvenile *Arctica islandica* under experimental conditions. Helgoländer Meeresunters. 51, 417–431.

Witbaard, R., 1997. Tree of the sea: The use of the internal growth lines in the shell of *Arctica islandica* (Bivalvia, Mollusca) for the retrospective assessment of marine environmental change. Groningen, The Netherlands: University of Groningen.

Woelders, L., Vellekoop, J., Weltje, G. J., de Nooijer, L., Reichart, G.-J., Peterse, F., Claeys, P., and Speijer, R. P., 2018. Robust multi-proxy data integration, using late Cretaceous paleotemperature records as a case study. Earth Planet. Sci. Lett. 500, 215–224.

Wooller, M. J., Morgan, R., Fowell, S., Behling, H., and Fogel, M., 2007. A multiproxy peat record of Holocene mangrove palaeoecology from Twin Cays, Belize. The Holocene 17, 1129–1139.

Yan, H., Shao, D., Wang, Y., and Sun, L., 2013. Sr/Ca profile of long-lived *Tridacna gigas* bivalves from South China Sea: A new high-resolution SST proxy. Geochim. Cosmochim. Acta 112, 52–65.

Zhang, W., Ming, Q., Shi, Z., Chen, G., Niu, J., Lei, G., Chang, F., and Zhang, H., 2014. Lake sediment records on climate change and human activities in the Xingyun Lake catchment, SW China. PLOS ONE 9, e102167.

2 Morphological variations of crossed-lamellar ultrastructures of *Glycymeris bimaculata* (Bivalvia) serve as a marine temperature proxy

Nils Höche[1], Melita Peharda[2], Eric O. Walliser[1], Bernd R. Schöne[1]

1. *Johannes Gutenberg-University, Mainz, Germany*
2. *Institute of Oceanography and Fisheries, Split, Croatia*

N. Höche, M. Peharda, E. O. Walliser, and B. R. Schöne, 2020. Morphological variations of crossed-lamellar ultrastructures of *Glycymeris bimaculata* (Bivalvia) serve as a marine temperature proxy. Estuar. Coast. Shelf Sci. 237, 106658

In this chapter, methods were established to measure the morphology of the BMUs of bivalve shells in SEM images. It was possible to demonstrate a strong effect of the water temperature on the BMU length, width and size in shells of *Glycymeris bimaculata*. This manuscript was

published in the journal "Estuarine Coastal and Shelf Science". I contributed to the conceptualization, formal analysis, investigation, methodology, software, visualization, writing-original draft and writing-review and editing of the manuscript. This work was supported by the DFG grant [SCHO794/20] to BRS and the SCOOL project to MP; Samples were collected within the framework of the ARAMACC project.

Author contributions:

NH Conceptualization, Formal analysis, Investigation, Methodology, Software, Visualization, Writing-original draft, Writing review and editing.

MP Investigation, Resources, Validation, Writing-review and editing.

EOW Investigation, Validation, Writing-review and editing.

BRS Conceptualization, Formal analysis, Funding acquisition, Investigation, Resources, Supervision, Validation, Writing-original draft, Writing-review and editing.

Abstract

Bivalve shells are among the most promising archives for high-resolution seawater temperature reconstructions. However, despite major research advances in bivalve sclerochronology over the past decades, estimating water temperature from shells remains a challenging task. This is largely because the most frequently used and widely accepted temperature proxy in bivalves, i.e., the shell oxygen isotope ($\delta^{18}O_{shell}$) value, also requires knowledge of changes in $\delta^{18}O$ of the water ($\delta^{18}O_{water}$) in which the bivalve lived, which is rarely available for ancient environments. According to a few recent studies, the size and shape of individual biomineral units (BMUs) of the shell ultrastructure may serve as an independent temperature proxy that is also less vulnerable to diagenetic changes than isotope chemical proxies. However, the crossed-lamellar ultrastructure, which occurs in ca. 90 % of all mollusk species, has hitherto not been investigated. Here, we evaluate the potential use of morphological properties of the BMUs in *Glycymeris bimaculata* as a proxy for water temperature. For this purpose we introduce a suitable preparation technique (immersion for 2 min in 0.001 vol% formic acid followed by 20–30 min in 3.5 vol% H_2O_2) and an automated image processing technique that tremendously speed up ultrastructure analysis (five seconds versus one to two hours image processing time with automated and manual methods, respectively) and increase the robustness of BMU measurements. *Glycymeris* is a particularly useful target taxon, because it is a cosmopolitan genus with evolutionary roots in the Upper Cretaceous, and some species of *Glycymeris* can attain a lifespan of more than two hundred years, which allows for long-term high-resolution paleoclimate reconstructions. As in other previously studied ultrastructures, larger and more elongated BMUs formed in warmer water permitting temperature estimates with an error of 2.3 °C (1σ). Since the new temperature proxy is unaffected by other environmental variables, including salinity, it can potentially be applied to (modern and fossil) specimens from brackish environments.

For reasons of copyright protection, the main text of this chapter is available at http://www.doi.org/10.1016/j.ecss.2020.106658.

3 Temperature-induced microstructural changes in shells of laboratory-grown *Arctica islandica* (Bivalvia)

Nils Höche[1], Eric O. Walliser[1], Niels J. de Winter[2,3], Rob Witbaard[4], Bernd R. Schöne[1]

1. *Johannes Gutenberg-University, Mainz, Germany*
2. *Department of Earth Sciences, Faculty of Geosciences, Utrecht University, Utrecht, The Netherlands*
3. *AMGC Research Group, Vrije Universiteit Brussel, Brussels, Belgium*
4. *Department of Estuarine & Delta Systems, NIOZ Royal Institute for Sea Research, Yerseke, The Netherlands*

N. Höche, E. O. Walliser, N. J. de Winter, R. Witbaard, and B. R. Schöne, 2021b. Temperature-induced microstructural changes in shells of laboratory-grown *Arctica islandica* (Bivalvia). PLOS ONE 16.2, e0247968

In this chapter, the effects of water temperature on the microstructure of shells of *Arctica*

islandica raised under controlled laboratory conditions were studied. The investigated specimens were grown under different temperature settings (1, 3, 6, 9, 12 and 15 °C) while keeping other parameters constant. It could be demonstrated that in warmer temperatures, the BMUs occupy more space in the SEM images, individual BMUs grow larger, and the size of pores between BMUs of the shells also increases. This chapter was published as a manuscript in the journal "PLOS ONE". My contributions to this manuscript consisted of data curation, formal analysis, investigation, methodology, validation, visualization, and writing-review and editing. Financial support for this work came from a DFG grant to BRS [SCHO793/20-1], and a Marie Curie Fellowship [UNBIAS 83011] and a junior postdoc grant of the Flemish Research Council [12ZB220N] to NdW.

Author contributions:

NH Data Curation, Formal analysis, Investigation, Methodology, Validation, Visualization, Writing-review and editing.

EOW Supervision, Project administration, Supervision, Validation, Visualization, Writing-original draft, Writing-review and editing.

NdW Investigation, Resources, Writing-review and editing

RW Resources, Validation, Writing-review and editing

BRS Conceptualization, Funding acquisition, Project administration, Resources, Supervision, Validation, Visualization, Writing-original draft, Writing-review and editing.

Abstract

Bivalve shells are increasingly used as archives for high-resolution paleoclimate analyses. However, there is still an urgent need for quantitative temperature proxies that work without knowledge of the water chemistry as is required for ^{18}O-based paleothermometry and can better withstand diagenetic overprint. Recently, microstructural properties have been identified as a potential candidate fulfilling these requirements. So far, only few different microstructure categories (nacreous, prismatic and crossed-lamellar) of some short-lived species have been studied in detail, and in all such studies, the size and/or shape of individual biomineral units was found to increase with water temperature. Here, we explore whether the same applies to properties of the crossed-acicular microstructure in the hinge plate of *Arctica islandica*, the microstructurally most uniform shell portion in this species. In order to focus solely on the effect of temperature on microstructural properties, this study uses bivalves that grew their shells under controlled temperature conditions (1, 3, 6, 9, 12 and 15 °C) in the laboratory. With increasing temperature, the size of the largest individual biomineral units and the relative proportion of shell occupied by the crystalline phase increased. The size of the largest pores, a specific microstructural feature of *A. islandica*, whose potential role in biomineralization is discussed here, increased exponentially with culturing temperature. This study employs scanning electron microscopy in combination with automated image processing software, including an innovative machine learning–based image segmentation method. The new method greatly facilitates the recognition of microstructural entities and enables a faster and more reliable microstructural analysis than previously used techniques. Results of this study establish the new microstructural temperature proxy in the crossed-acicular microstructures of *A. islandica* and point to an overarching control mechanism of temperature on the micrometer-scale architecture of bivalve shells across species boundaries.

3.1 Introduction

Seasonally to annually resolved past ocean temperature data are crucial to better understand feedbacks in the global climate system and constrain climate simulations (Schmidt et al., 2014; Cauquoin et al., 2019; Asami et al., 2020). This type of information is increasingly reconstructed from bivalve shells (Butler et al., 2013; Reynolds et al., 2013; Justine et al., 2020), specifically stable oxygen isotope ($^{18}O_{shell}$) values (Schöne et al., 2004; von Leesen et al., 2017; Featherstone et al., 2019). Given known limitations of this paleothermometer, i.e., vulnerability to diagenetic overprint (Casella et al., 2018) and difficulties to obtain $^{18}O_{water}$ signatures of ancient and/or coastal water bodies, the search for alternative temperature proxies is in full swing (Δ^{47}: Eiler, 2011; de Winter et al., 2020; Δ^{48}: Fiebig et al., 2019; Mg, Sr: Schöne et al., 2013). A highly promising candidate is the shell microstructure (Tan Tiu, 1988; Tan Tiu and Prezant, 1989; Nishida et al., 2012; Olson et al., 2012). It cannot only provide sub-seasonally resolved temperature data, but is also much less susceptible to diagenetic overprint than geochemical properties of shells (Brand and Morrison, 1987; Morrison and Brand, 1988) and, contrary to the incorporation of trace and minor elements into the shells (Shirai et al., 2014; Füllenbach et al., 2015; Wanamaker and Gillikin, 2019), appears to be unaffected by kinetic and vital effects (Gilbert et al., 2017; Milano et al., 2017b).

As demonstrated by existing studies, increasingly larger and/or more elongated BMUs are formed when temperature rises. This applies to bivalves with nacreous (*Pinna* sp. and *Atrina* sp.: Gilbert et al., 2017), prismatic (*Cerastoderma edule*: Milano et al., 2017b) and crossed-lamellar microstructures (*Glycymeris bimaculata*: Höche et al., 2020). However, in the long-lived ocean quahog, *Arctica islandica*, Milano et al. (2017a) were unable to identify temperature-related morphological changes of individual BMUs. The reservation must be made that these authors only evaluated the microstructures in the ventral margin by visual assessment, while placing the focus of their study on the relationship between the crystallographic orientation of BMUs and environmental variables. Due to the enormous microstructural diversity – in particular in shell portions of the ventral margin – morphometric analysis of BMUs in *A. islandica* is a particularly challenging task. For example, the HOM microstructure in the outer portion of the outer shell layer of *A. islandica* gradually merges intocrossed-acicular (CA) microstructure toward the myostracum

(Fig. 3.1A-D; Ropes et al., 1984a; Milano et al., 2017a). In addition, the thickness of the HOM portion increases with ontogenetic age (Trofimova et al., 2018). Yet, fine compex-crossed lamellar (FCCL) microstructure occurs in the inner portion of the outer shell layer and in the ISL (Ropes et al., 1984a; Dunca et al., 2009). As in almost all other mollusks, the annual growth lines are dominated by ISP microstructures (Ropes et al., 1984a; Karney et al., 2011; Füllenbach et al., 2017). The only region in *A. islandica* which is microstructurally relatively uniform is the hinge (growth increments: predominantly CA; annual growth lines: ISP; Ropes et al., 1984a; Karney et al., 2012; Schöne, 2013). Given the important role of the ocean quahog in sclerochronology-based paleoclimate reconstructions (Wanamaker et al., 2009; Butler et al., 2010, 2013; Lohmann and Schöne, 2013) including the more distant past (Walliser et al., 2016), the known limitations of geochemical proxies outlined above and promising results in recent BMU studies, a more detailed assessment of the shell microstructure of *A. islandica* as a possible recorder of water temperature seems overdue.

Here we investigate possible effects of temperature on microstructural properties in the hinge plate of young *A. islandica* specimens. To minimize interferences with other environmental variables and thus following the rationale of Milano et al. (2017a), we studied shell portions that grew under controlled laboratory conditions. Our study is based on 17 specimens that were cultured for 95 days at six different temperature regimes (1–15 °C; Table 3.1). Machine learning–assisted image segmentation was used to (reproducibly and objectively) identify individual BMUs and µm-sized pores, a characteristic feature in *A. islandica* (Ehrenbaum, 1884; Ropes et al., 1984a; Dunca et al., 2009), in SEM images of polished shell cross-sections after immersion in H_2O_2. The size (area) of individual BMUs and pores was automatically determined by means of image processing software. Since the individual BMUs of the CA microstructure are often challenging to distinguish, even for currently available user-trained artificial intelligence software, the proportion covered by the BMUs (= BMU coverage) was also determined. The new technique presented herein not only provides more robust data than manual microstructure analyses and visual inspection, but also vastly accelerates the measurements compared with previously used image processing techniques. Our approach can pave the way toward improved high-resolution paleotemperature estimates from bivalve shells, specifically *A. islandica*.

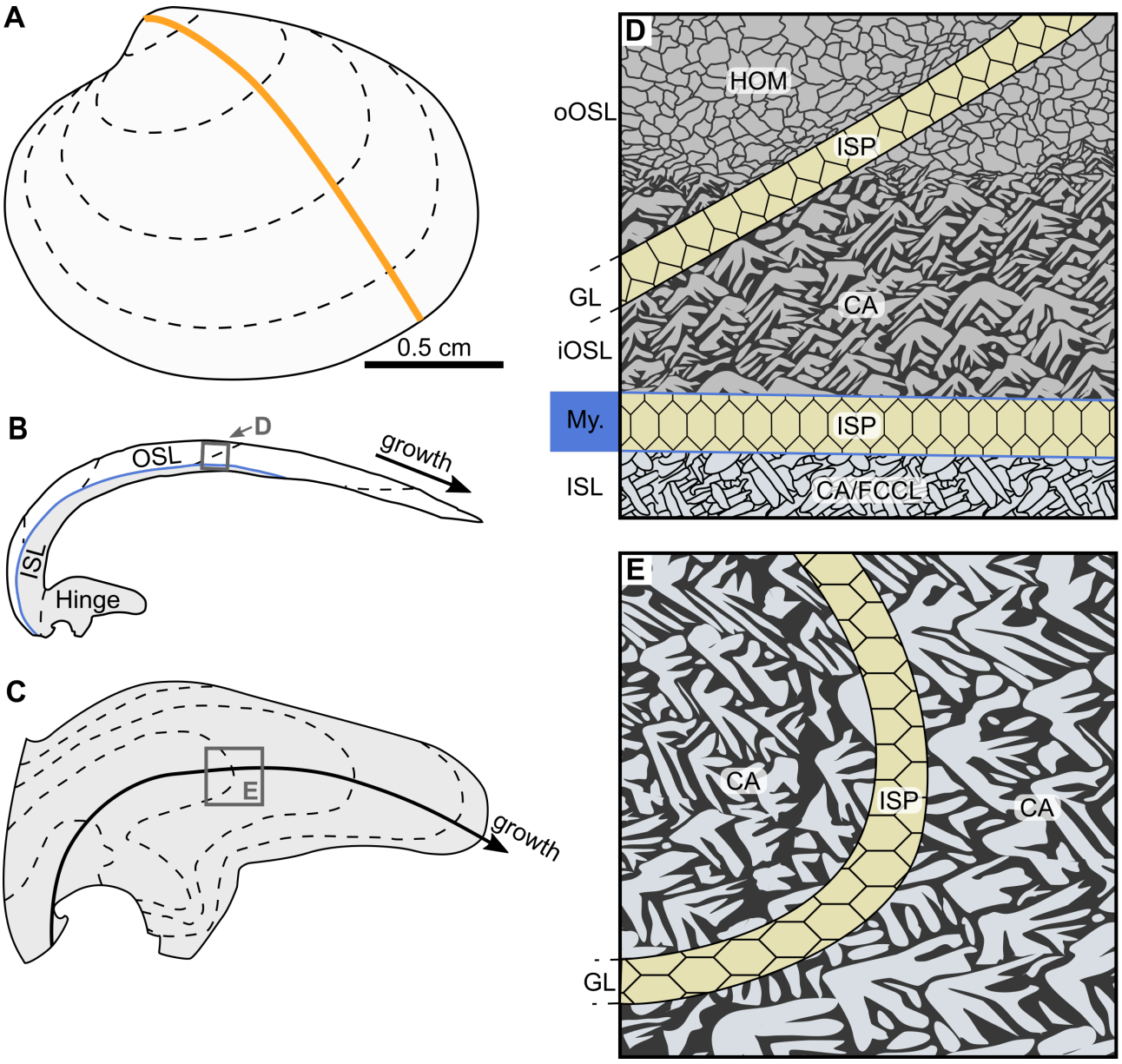

Figure 3.1 Shell growth patterns and microstructure of *Arctica islandica*. (A) Sketch of the left valve of a juvenile specimen. Cutting axis is indicated as orange line. (B) Radial shell section of the valve. The shell is divided into an outer shell layer (OSL; white) and inner shell layer (ISL; gray), separated by the pallial myostracum (blue line). (C) Magnified sketch of the hinge plate showing annual growth lines (dashed) and axis of maximum growth (black line with arrow). (D) Sketch of the microstructures of the ventral shell portion. The outer portion of the outer shell layer (oOSL) consists of homogeneous (HOM) microstructure, which gradually merge into crossed-acicular (CA) microstructure toward the inner portion of the outer shell layer (iOSL). Transitional fine compex-crossed lamellar (FCCL) and CA microstructures are formed in the ISL. Annual growth lines (GL) and pallial myostracum (My.) consist of irregular simple prismatic (ISP) microstructure. (E) Sketch of the microstructures in the hinge plate. Growth increments and lines are composed of CA and ISP microstructures, respectively. Dashed black lines represent annual growth lines. Boxes in B and C show the extent of the microstructure sketches portrayed in D and E, respectively.

Table 3.1 Shells of *Arctica islandica* used in the present study.

Specimen ID: "Nioz-TC-…"	Specimen ID in original culturing study[1]	# LA-ICP-MS measurements	BMU morphometry (μm^2)	Pore morphometry (μm^2)
01-A1R	89	16	7,320	2,455
01-A2R[2]	71	19	1,220	720
03-A1R	69	19	13,420	10,977
03-A2R	36	23	3,660	22,555
03-A3R	20	-	10,980	20,590
06-A1R	55	29	14,640	23,274
06-A2R	32	23	3,660	39,836
06-A3R	21	22	10,980	33,764
09-A1R	113	-	13,420	6,501
09-A2R	98	21	6,100	10,541
09-A3R	58	22	4,880	9,797
12-A1R	149	-	1,220	13,505
12-A2R	70	24	8,540	47,779
12-A3R	44	21	10,980	27,566
15-A1R	99	-	12,200	46,883
15-A2R	93	-	1,220	36,789
15-A3R	12	-	4,880	47,422

[1] Consecutive numbers were assigned to each shell in the original culturing study (Witbaard et al., 1997). Here, new specimen IDs were assigned (given in leftmost column, all starting with "Nioz-TC-…") to ease identification.

[2] Due to the very limited number of samples remaining from this culturing experiment, only two specimens cultured at 1 °C could be used.

3.2 Material and methods

Shells of seventeen juvenile (five years-old) *A. islandica* specimens were used in the present study. Bivalves were collected alive on 8 February 1993 from the trawl site 'Süderfahrt/Millionenviertel', Kiel Bay, Germany, western Baltic Sea (54° 52′ 59″ N, 10° 8′ 0″ E), at a water depth of 20 m using a "Kieler Kinderwagen" dredge and subsequently used in a culturing experiment (Witbaard et al., 1997). After collection, bivalves were cooled, aerated and transferred to the Royal Netherlands Institute for Sea Research, Texel (The Netherlands), where they were distributed over different sand-filled containers supplied with filtered, constantly aerated seawater and acclimatized to North Sea conditions. After four weeks, the experimental aquaria were adjusted to constant temperature regimes (1, 3, 6, 9, 12 and 15 °C; Table **??**) for 95 days. Food availability was kept ad libitum by supplying a (freshly cultured) phytoplankton mixture of *Isochrysis galbana* and *Dunaliella marina* with cell densities maintained in the optimum range of 10–20 × 10^6 cells per liter (Winter, 1969; Witbaard et al., 1997).

3.2.1 Shell preparation

The right valve of each specimen was affixed to acrylic glass cubes with a quick-drying plastic welder (WIKO Multi Power 03) and all surfaces along the axis of growth from the umbo to the ventral margin covered with a ca. 1 cm broad and several mm-thick protective layer of metal epoxy resin (WIKO 05 epoxy). After curing, each valve was cut along the axis of maximum growth using a low-speed saw (Buehler IsoMet 1000) operated at 250 rpm and equipped with a diamond-coated wafering thin blade (Buehler 15LC 11-4255, 0.4 mm thickness, low-diamond concentration). From that axis, two shell slabs (2.5–3.0 mm-thick) were obtained and embedded in Araldite 2020 mixed with conductive filler (Buehler 20-8500). All slabs were ground successively with P800, P1200 and P2500 grit SiC paper and then polished with 1.0 and 0.3 µm Al_2O_3 suspension using polishing cloths (Buehler MasterTex) on a rotating lap (Buehler MetaServ 2000) at 100 rpm. After each grinding and polishing step, samples were ultrasonically rinsed in tap water for two minutes. The final rinsing step was conducted with demineralized water to avoid precipitation of calcium carbonate impurities on the cross-sectioned surfaces. One shell slab of each specimen was used for trace element and growth pattern analyses and the other one for SEM studies.

3.2.2 Identification of laboratory-grown shell portions

The laboratory grown shell portions appeared to be separated from the remainder of the shell by a distinct growth check (accompanied by a change of periostracum color) that was visible at first glance in marginal shell portions on the external surfaces of all shells. In order to confirm which shell portions of the hinge plates formed under controlled laboratory conditions, a combined geochemical, microstructural and growth pattern analysis was applied. The trace and minor element composition of bivalve shells can serve as a provenance indicator, because the water chemistry of the environment is partially reflected in the shells (Pitts and Wallace, 1994; Price and Pearce, 1997; Markich et al., 2002; Liehr et al., 2005). In particular, as experimentally demonstrated multiple times, elevated levels of dissolved manganese in the water are mirrored in the shell (e.g., Jeffree et al., 1995; Barbin et al., 2008). Since Mn is a redox-sensitive element, whose concentration increases with decreasing content of dissolved oxygen (Kremling and Petersen, 1978; Kremling, 1983; van de Velde et al., 2020), bivalves living in low-oxygen environments such as settings below the seasonal halocline in the Baltic Sea (e.g., Bonsdorff, 2006; Conley et al., 2011; Hansson and Gustafsson, 2011; Carstensen et al., 2014) show higher Mn concentrations than specimens from well-oxygenated waters (own observation). Shell portions formed in tanks supplied with oxygen-rich North Sea water are thus expected to show significantly lower Mn/Ca values than those grown in the Baltic Sea.

To determine the Mn content in situ, LA-ICP-MS analysis was carried out on one polished slab of 11 of the studied specimens (Table 3.1). Equally spaced LA spots (midpoints: 85 µm apart; 65 µm diameter) were placed along the axis of maximum growth in the hinge plates. Analyses were performed with an Agilent 7500ce quadrupole ICP-MS coupled to an ESI NWR193 ArF excimer laser ablation system equipped with a TwoVol2 ablation cell. Pulse rate was set to 10 Hz at an energy density of 3 J m^{-2}. For each measurement, pre-ablation was set to 15 seconds followed by 25 seconds ablation time and 10 seconds wash-out time. NIST SRM 610 and 612 were used as calibration material (Jochum et al., 2011) and accuracy and precision of the analyses were assessed by measuring the quality control materials (QCMs) USGS MACS-3, JCt-1 and USGS BCR-2G. The raw data were processed using the "LAtools" module (Branson et al., 2019) for python. For data reduction, ^{43}Ca was used as the internal standard, applying the preferred values reported in the GeoReM database (http://georem.mpch-mainz.gwdg.de/, application version 27; Jochum et al., 2007, 2011) for the QCMs and calibration material. Element concentrations determined for the QCMs are given in Supplement 3A. In all QCMs, the average relative Mn/Ca precision

(standard deviation / mean) based on repeated measurements (n = 25) was better than 3.2 %. Note that no measurements could be performed on the specimens cultured at 15 °C (Table 3.1), because the hinge plates were contaminated by epoxy, which penetrated small cracks during preparation.

In addition to the microstructural analysis (see below) and the manganese method, growth patterns, i.e., growth increments and growth lines (periodic growth lines and disturbance lines) were studied in order to distinguish shell portions that formed in the field and under controlled laboratory conditions (e.g., presence or absence of annual growth lines). For this purpose, the polished section that was used for LA-ICP-MS analysis was immersed in Mutvei's solution (Schöne et al., 2005a) for 7 min at 38 °C under constant stirring. After rinsing in deionized water and air-drying, stained specimens were photographed using a Canon EOS 600D DLSR camera mounted to a Leica Stemi 508 stereomicroscope with sectoral dark-field illumination.

3.2.3 Scanning electron microscopy and automated image analysis

The remaining polished shell slab of each specimen was analyzed by means of SEM (Phenom Pro Desktop SEM, 3rd generation, equipped with a CeB_6 source and backscatter electron detector). To assess the microstructural properties of the laboratory-grown shell portions of the hinge plates, images were taken near the axis of maximum growth and calibrated for brightness and contrast. In these images, BMU size, elongation (ratio between the longest and shortest BMU axes) and coverage and pore size, were determined. Since the bivalves added variable amounts of shell material at the different temperature regimes (Witbaard et al., 1997), the regions selected for automated morphometric analyses varied in area between 1218 and 47 479 µm^2 (Table 3.1). SEM imaging for pore morphometry was conducted on non-sputtered, polished shell portions at 5 keV and 1550 × magnification. Qualitative images of the pores were taken on a fractured hinge plate of a specimen that was not used in the quantitative analyses (# 109).

To properly identify individual BMUs, specimens were immersed in 10.5 vol% H_2O_2 solution for 20 min to (superficially) remove the inter-crystalline organic matrix leaving behind empty spaces between the microstructural entities (Crippa et al., 2016). Note, since hydrogen peroxide is slightly acidic, this treatment also slightly attacked the BMUs and thus produced a three-dimensional relief (Supplement 3B) with shell portions more resistant against H_2O_2 standing out of the surface (cores of BMUs) and less resistant shell portions forming depressions (inter-crystalline organics, pores and rims of BMUs). Thereafter, the samples were rinsed with dem-

ineralized water, gently dried with compressed air and sputter-coated with a 5 nm-thick platinum layer. Stitched overviews were generated from individual photographs taken at 5 keV and 3200 × magnification. Morphometric analyses of BMU size and coverage were conducted in SEM images taken at 10 keV and 7700× magnification, which represented a compromise between sufficient resolution to discern individual BMUs and extensive image processing times.

The BMU coverage-approach is based on intensity differences of the SEM backscatter images, which result from both the sample topography and the sample material. Removal of the inter-crystalline organic matrix by H_2O_2 oxidation eliminated material contrast and left behind a topographical gradient (visualized in SEM images as shadings of gray) between the BMUs (highest points) and the inter-crystalline space (lowest points). The mean intensity (i.e., mean gray value) of the images was set as a threshold value to better distinguish between the mineral phase (white) and inter-crystalline space (black) and generate black-and-white images (binarization; Fig. 3.22B,D). The relative amount of white pixels in an image times 100 represents the (minimum) area in percent covered by crystalline phases (BMUs). It should be noted that the actual area occupied by the BMUs is larger than calculated here, because of the sample topography and the selected threshold value of the gray scale spectrum. Thus, black pixels represent inter-crystalline space as well as a proportion of BMU edges (Fig. S3.2 in Supplement 3C).

The automated measurement of the size (= area) of BMUs and pores as well as the elongation of BMUs required binary images, in which individual objects of interest were discretized and distinguished from the surrounding material. Recognition of these two phases (black = inter-crystalline spaces, pores and/or BMU rims; white = BMUs) was accomplished via machine learning–assisted image segmentation using the computer program Ilastik (Berg et al., 2019). Performance of the machine learning method was evaluated by comparing the segmentation results to manually generated 'ground truth' segmentations (Supplement 3E). Subsequently, the area of pores and BMUs as well as the elongation were automatically measured in the segmented binary images using the image processing software ImageJ (Schneider et al., 2012; Schindelin et al., 2015; Rueden et al., 2017). Where necessary, artifacts (e.g., fractures in the shell, dirt particles and scratches on the sample surface) were manually excluded from morphometric analyses and only particles larger than two pixels were used for analysis.

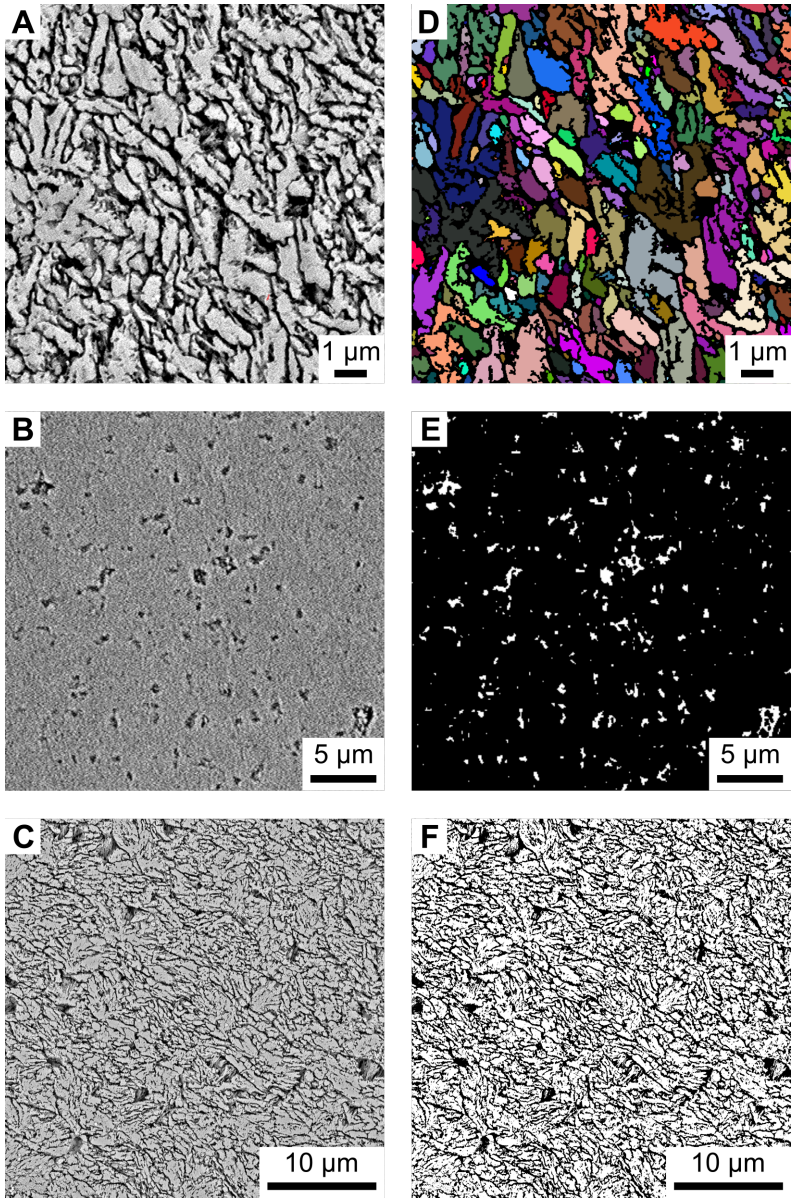

Figure 3.2 Image segmentation of hinge plate SEM backscatter images. (A-C) Morphological analyses were conducted on SEM backscatter images. BMU size and coverage were analyzed in the same image (A,C), taken after oxidation of the organic matrix by immersion in 10.5 vol% H_2O_2 for 20 minutes (image A magnified for visual clarity). Images for pore morphometry (B), in contrast, were taken in a polished and chemically untreated shell slab. (D-F) Binary images (objects of interest = white; remainder = black) used for the automated image segmentation process. Individual BMUs (D; here shown in various colors to allow discrimination of the individual entities) and pores (E, white) were recognized by the machine learning–based image segmentation process and separated from the remainder of the images (black). (F) For the calculation of BMU coverage a threshold based on the average gray value of the image series was applied. Values above this threshold were assigned to the crystalline (white) phase, those below the threshold to the inter-crystalline phase (black).

3.2.4 Machine learning–based image segmentation

In order to perform automatized recognition of BMUs and pores in the SEM images of etched and chemically untreated shell portions, respectively, we used the (bio)image analytical software Ilastik (Berg et al., 2019). This program utilizes supervised machine learning (Geurts et al., 2009) to sort image portions into certain categories (i.e., image segmentation) based on user-supplied training data. Ilastik was successfully applied in two- and three-dimensional pore space reconstructions of sedimentary rocks (Lei et al., 2018; Jacob et al., 2020). In the present study, we employed the toolkit to classify each pixel of the SEM images by backscatter electron categories, whereby bright pixels reflected high-density mineral phases and black pixels empty spaces. In other words, the gray values of the SEM images were used as height indicators of the studied shell surfaces. The Ilastik workflow was supplied with training images (Fig. 3.2A,C) and user-defined 'labels' ($n \geq 10$ per image), with areas that belong to the class of interest (e.g., BMU, pore). The machine learning-based classifier also considers the image texture, gradients and edges (Berg et al., 2019) and thus has the potential to outperform solely intensity-based approaches. It produced binary images, where objects of interest (mineral phases and pores) were assigned the value 1 (white) and the remainder 0 (black; Fig. 3.2D,E; BMUs shown in various colors instead of white to allow discrimination of the individual entities).

3.3 Results

3.3.1 Naturally and laboratory-grown shell portions

All samples showed a prominent growth band (ca. 84.5 ± 32.2 µm-broad) that divided the hinge plates into two zones which formed under natural and laboratory conditions, respectively. This growth band was also visible on external shell surfaces after the specimens were transferred to controlled-temperature tanks, but had not developed previously when collected in the field, confirming the assumption that the band formed during the one-month acclimatization phase. The two zones that were separated by this 'acclimatization growth band' were characterized by unique shell growth patterns and microstructural features (Fig. 3.3A-C). The ontogenetically younger zone before the acclimatization band, which formed in the Baltic Sea, occupied the

largest proportion of the studied hinge plates (Fig. 3.3A). In all studied specimens, this shell portion revealed four annual growth increments (predominantly crossed-acicular (CA) microstructure; Fig. 3.3C) which were delimited by distinct annual growth lines (irregular simple prismatic (ISP)) with strong backscatter intensity and thus bright appearance (Fig. 3.4A). The annual lines were in most cases followed by ca. 10–20 µm broad fine compex-crossed lamellar (FCCL) fringes composed of small acute crystallites that gradually increased in size along the growth direction (Fig. 3.4B). We also observed several, erratically distributed, fainter growth lines, aka disturbance lines (reflecting physiologically stressful conditions (Clark, 1968; Palmer, 1980; Sato and Chiba, 2016)), consisting of spherulitic prismatic (SphP) and fibrous prismatic (FP) microstructures (Fig. 3.4A). These growth lines thus differ microstructurally from periodic growth lines (made of ISP) such as annual growth lines (Ropes et al., 1984b; Karney et al., 2011).

The acclimatization band was developed shortly after the most recent annual growth line (Fig. 3.3A,B). In Mutvei-stained specimens, it showed an internal color gradient from dark to light blue in the direction of growth (Fig. 3.3A). At higher magnification, two – potentially fortnightly – growth increments became apparent within this growth band which were further subdivided into even narrower, up to 6.5 µm broad microgrowth increments (Fig. 3.3B), likely resembling daily or circalunidian (lunar daily) growth increments. Considering that the bivalves were supplied with North Sea water during the acclimatization phase, the presence of tide-controlled growth patterns was expected.

Under the SEM, the acclimatization band appeared as a protruding ridge composed of FCCL microstructure which was delimited by a disturbance line made of SphP microstructure. The aforementioned color change in Mutvei-stained sections was associated with a gradually rising gray value (i.e., increasing backscatter electron intensity, brighter) in the SEM images resulting from increasingly larger FCCL BMUs that progressively merged into triangular patches (Fig. 3.3C). Overall, the acclimatization band consisted of very thin, highly elongated, needle shaped BMUs that were aligned in two predominant dip directions (open angle in the direction of growth; Fig. 3.4C,D). In growth direction, the acclimatization band ended with another disturbance line followed by a shell portion (representing the 95 days under controlled temperature conditions) composed of CA microstructure. The CA microstructure precipitated during the experimental phase differed from that in ontogenetically younger portions preceding the acclimatization band by more equally sized and rounder BMUs (Fig. 3.4E,F). This more uniform CA microstructure dominated the remainder of shell up to the margin of the hinge plate, i.e., the date of death of the animals (Fig. 3.3A-C). Individual BMUs of the CA microstructure typically consisted of (two

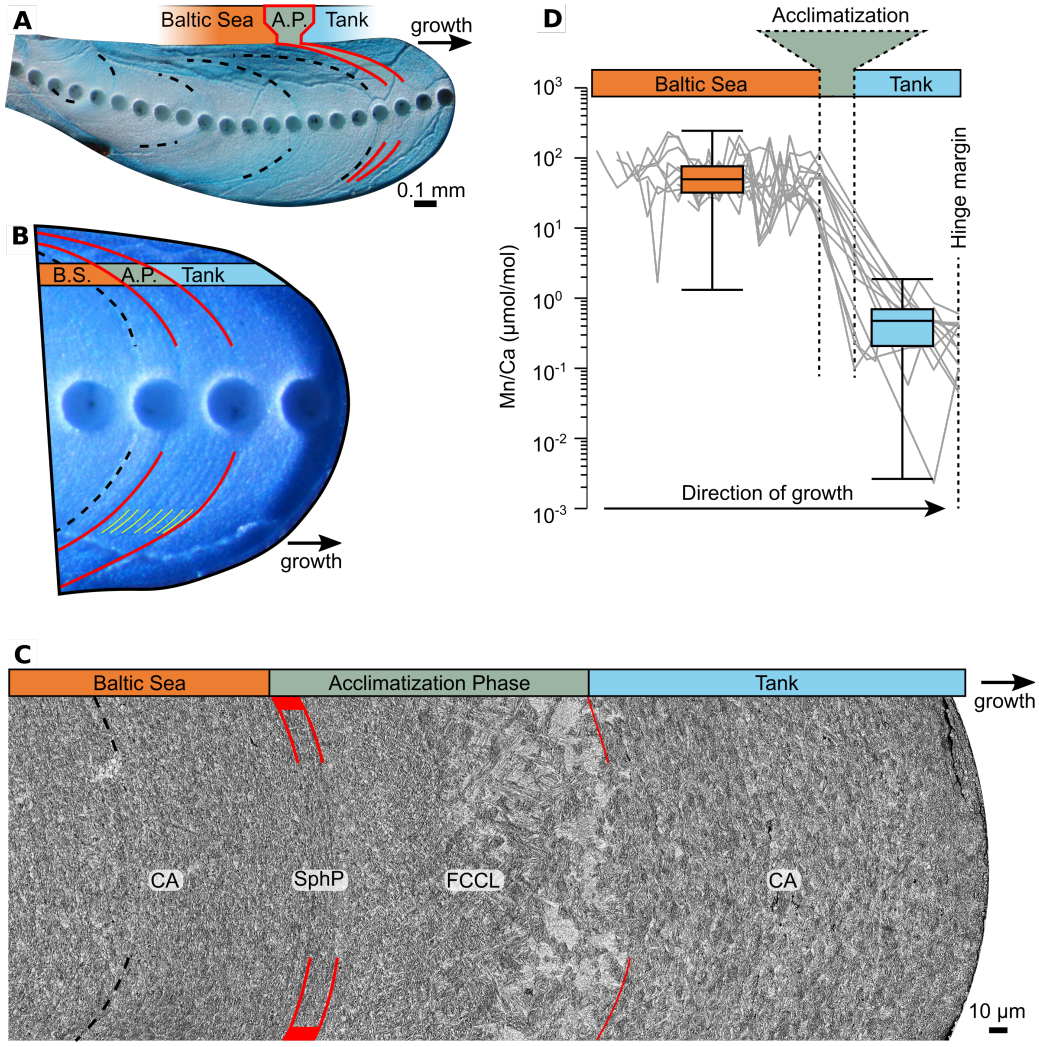

Figure 3.3 Growth patterns, Mn/Ca values and microstructures in the hinge plate of the studied *Arctica islandica*. (A) Mutvei-stained hinge plate of specimen Nioz-TC-12-A2R when viewed under a stereomicroscope with sectoral dark-field illumination. LA-ICP-MS analysis was conducted prior to the immersion in Mutvei's solution. Black dashed lines denote annual growth lines. Red solid lines = disturbance lines. These lines reflect handling stress (collection in the Baltic Sea, transferral to NIOZ, transferal to experimental tanks) and delimit the growth band that formed during the 4-week acclimatization phase. (B+C) Magnifications of (A): light microscopy (B) and SEM (C). (B) Portions formed during the acclimatization phase showed faint microgrowth patterns (the most defined ones indicated in yellow) possibly corresponding to circatidal or circalunidian increments and lines. Portion formed in tank was devoid of annual or disturbance lines. (C) Shell microstructures. Shell portions formed in the Baltic Sea consisted predominantly of crossed-acicular (CA) microstructure and exhibited variable sizes of the BMUs. The beginning of the experimental period is marked by a prominent SphP disturbance line (red) followed by a zone of fine complex crossed-lamellar (FCCL) microstructure during the acclimatization phase. After another disturbance line, uniform CA microstructure is visible which formed in the experimental aquaria. (D) Ontogenetic changes of shell Mn/Ca ratios. Gray lines denote the different studied specimens; boxplots show distribution of manganese in shell portions formed in nature and during artificial tank environments.

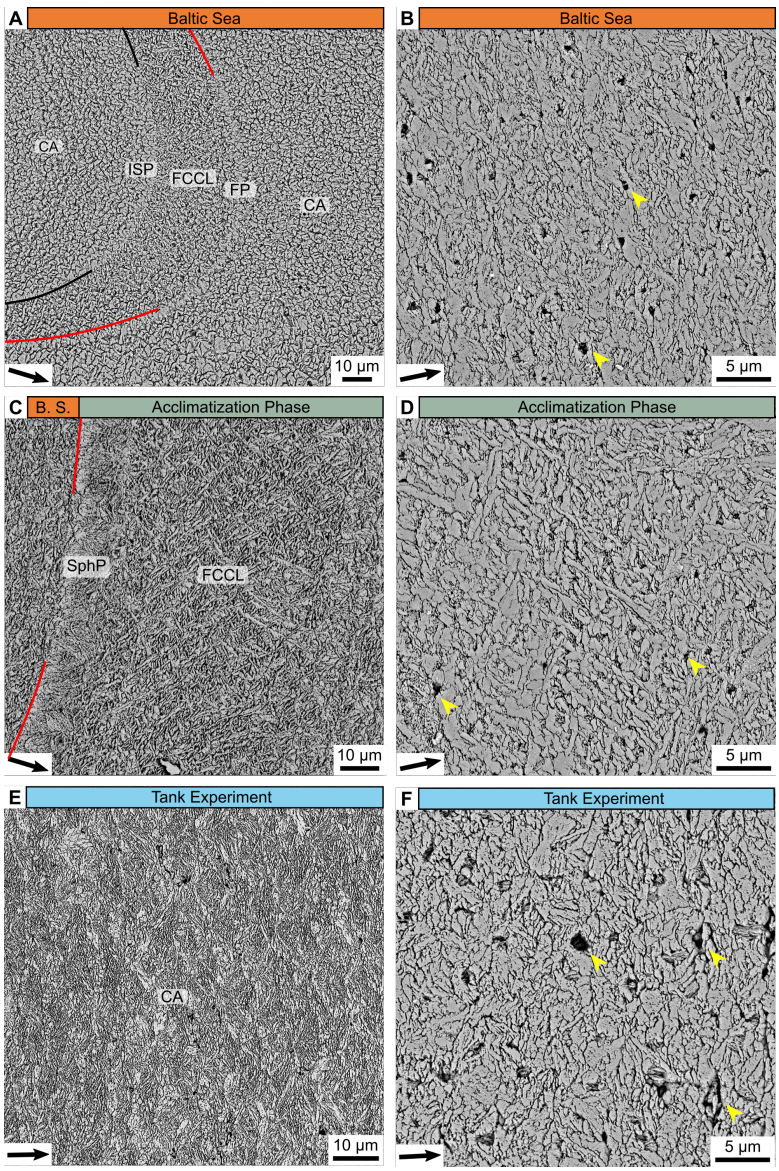

Figure 3.4 Microstructures in the hinge plate of the studied *Arctica islandica* specimens. (A) Hinge portions formed in the Baltic Sea predominantly exhibited crossed-acicular (crossed-acicular (CA)) microstructure. Annual growth lines (black line) consisted of irregular simple prismatic (ISP), often followed by 10–20 µm-broad fine compex-crossed lamellar (FCCL) fringes, as shown here. Numerous faintly visible disturbance lines (red line) consisted of fibrous prismatic (FP) or spherulitic prismatic (SphP) microstructures. (B) Magnified image of the CA microstructures formed in the Baltic Sea. biomineral unit (BMU) consist of a few elongated crystallites, which merged with each other and were loosely aligned in two predominant directions (open angles in direction of growth). (C) Microstructures of shell portions formed in the Baltic Sea (B.S.; leftmost image portion) and the early acclimatization phase (rightmost image portion). A prominent disturbance line (red) composed of SphP microstructure delimits the two shell portions. During the acclimatization phase, FCCL microstructures were produced. (D) Magnified image of the FCCL microstructures formed during the acclimatization phase. Compared to CA microstructures, the FCCL BMUs are even more elongated, strictly aligned in two dip directions and intersect with their neighboring units. (E-F) The CA microstructures formed under controlled temperature in the laboratory exhibited a rather uniform appearance along the growth axis. Dip directions of the needle shaped BMUs varied more strongly than those formed in the Baltic Sea, leading to a looser arrangement and a less organized appearance. All microstructures – except ISP – contained nm- to µm-sized pores (yellow arrows). Black arrows indicate direction of growth.

to four) fused needles (Fig. 3.4F). Like the naturally formed shell portion, the laboratory-grown zone contained a considerable number of µm-sized pores that were often filled with granular (Fig. 3.5E) and/or fibrous (Fig. 3.5F,G) crystallites. Fractured shell portions demonstrated that the pores were originally coated by and infilled with organic material (Fig. 3.5A-C).

The change in microstructure in the direction of growth was accompanied by a marked change in shell Mn/Ca values. Within the acclimatization band, Mn/Ca ratios abruptly decreased in all specimens, from 502.39 ± 377.24 µmol mol^{-1} to merely 4.26 ± 2.40 µmol mol^{-1} (median ± 1 inner quartile range; Fig. 3.3D, Supplement 3A). Mn/Ca provided additional evidence for which shell portions formed in the Baltic Sea and during the 95 days spent under temperature-controlled conditions in laboratory tanks.

3.3.2 Microstructure morphometrics of shell portions grown at constant temperature regimes

BMU and pore sizes exhibited logarithmic distributions with a distinct predominance of very small entities (99.9 % of values fell below 3.13 and 2.79 µm^2, respectively; Fig. 3.6). The size of the BMUs ranged from 0.0005 to 18.70 µm (Fig. 3.6A), while that of the pores varied between 0.003 and 14.04 µm (Fig. 3.6B, Supplement 3C). Distribution curves of BMU and pore sizes revealed statistically significant differences between culturing temperatures in all cases, except for pore sizes between 1 and 3 °C (two sample Kolmogorov-Smirnov tests, $p < 0.05$; Fig. 3.6, Supplement 3C). Thereby, the largest BMU and pore size values increased most strongly with culturing temperature, whereas the large amount of smaller BMUs and pores remained largely invariant. In other words, when considering increasingly large data subsets of the largest pores and BMUs, the correlation to water temperature decreases (Supplement 3D). To balance between explanatory power and sufficient sample size, a subset of the 15 largest BMUs and pores of each temperature setting was considered for the construction of the predictive models. These data subsets revealed statistically significant positive correlations to culturing temperature (Fig. 3.7, Supplement 3C). The size of the 15 largest BMUs increased from 2.79 ± 0.74 µm^2 at 1 °C to 10.42 ± 2.74 µm^2 at 15 °C (Spearman's $r = 0.82$, $r^2 = 0.67$, $p < 0.05$; Fig. 3.7A). Linear and exponential models between BMU size and temperature exhibited a near complete overlap. Therefore, linear models were chosen (Fig. S3.4 in Supplement 3D). The size of the 15 largest pores, in contrast, increased exponentially from 0.68 ± 0.09 µm at 1 °C to 10.13 ± 2.41 µm at 15 °C ($r = 0.92$, $r^2 = 0.77$, $p < 0.05$; Fig. 3.7D). Here, linear models produced negative values and non-randomly distributed residu-

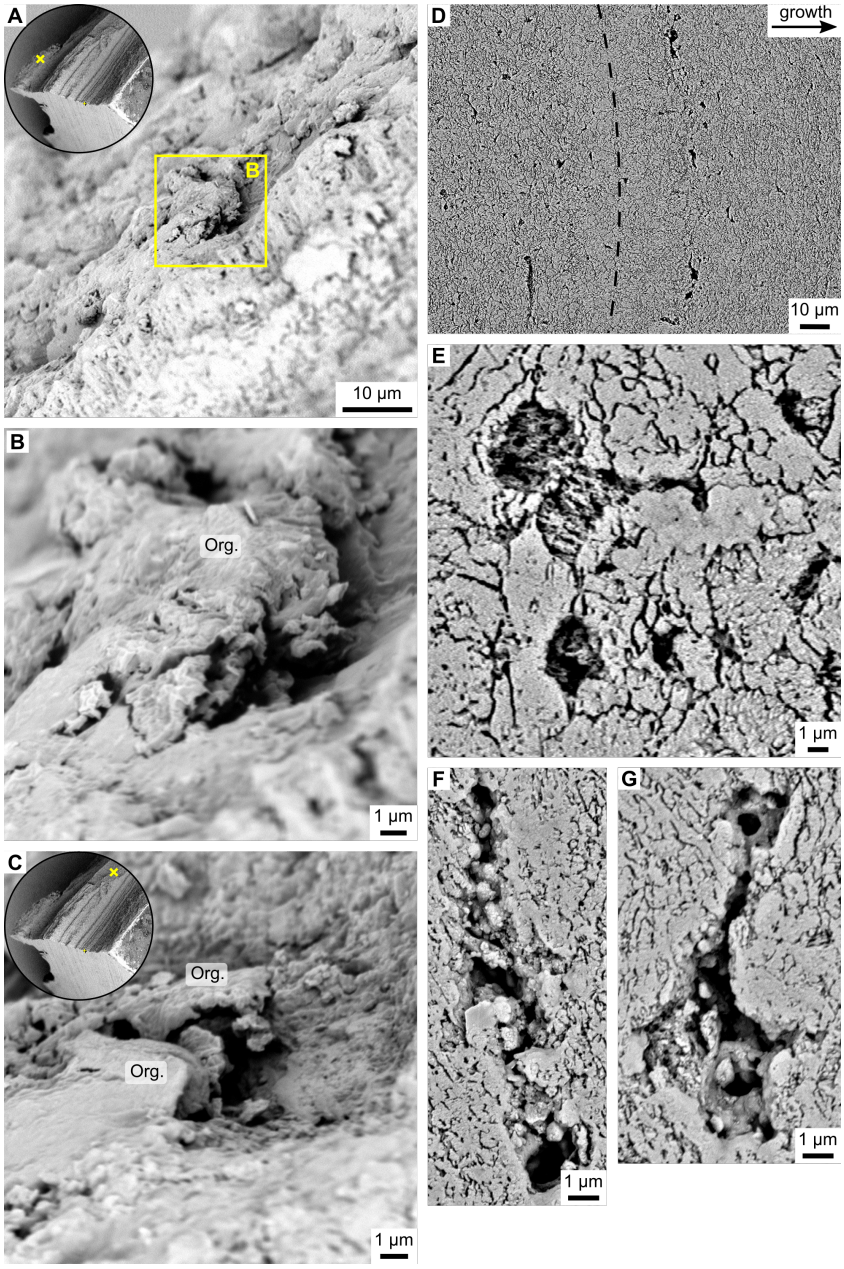

Figure 3.5 Pores of *Arctica islandica* shells. (A-C) Pores viewed on an untreated, fractured surface of a hinge plate. Insets in (A) and (C) depict an overview of the fractured shell. Yellow crosses within the insets denote the location of the respective images. (B,C) Higher magnification reveals the presence of shriveled organic envelopes (Org.) surrounding the partially void pores. (D-G) Pores viewed in a polished hinge surface after oxidation of the organic matter by immersion in 10.5 H2O2 for 20 min. Direction of growth is to the right. (D) Pores were aligned with their longest axis parallel to the growth front, as shown here near an annual growth line (black dashed line). (E) A pore filled with co-aligned, fibrous particles facing the same direction. (F,G) Pores partially filled with granular, spherical particles and remnants of organics

als. These problems did not occur when exponential regressions were computed (see Fig. S3.4 in Supplement 3D). Although BMU coverage did not require thresholding, respective data showed the same trend as BMU size, i.e., a statistically significant positive linear coupling with water temperature ($r = 0.78$, $r^2 = 0.54$, $p < 0.05$; Fig. 3.7B). The area covered by BMUs increased linearly from 55.4 ± 0.5 % at 1 °C to 63.0 ± 1.7 % at 15 °C. No correlation was found between the elongation of the 15 largest BMU and temperature (Fig. 3.7C).

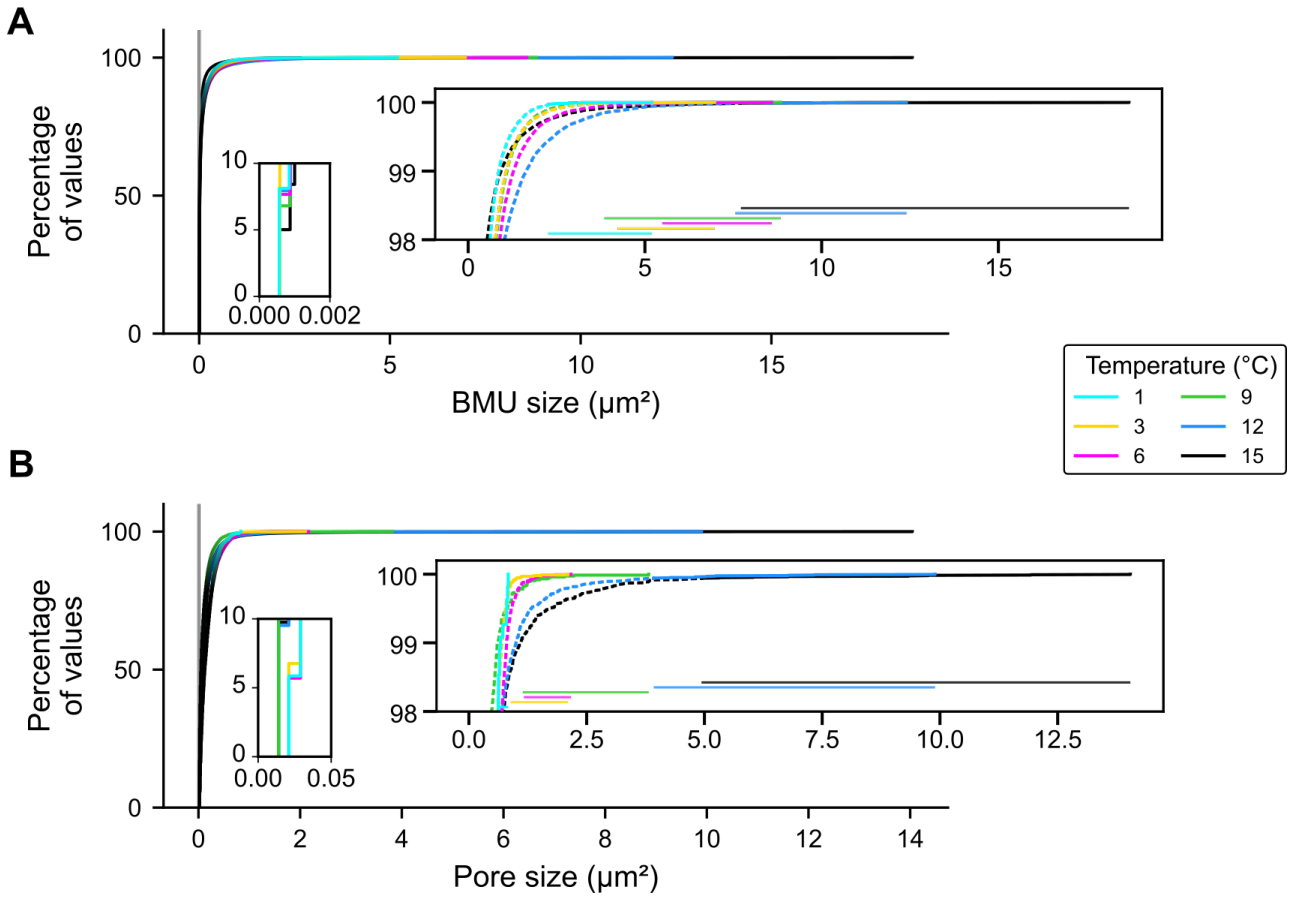

Figure 3.6 Empirical cumulative distribution functions of (A) BMU size and (B) pore size. The majority of BMUs and pores incorporated in the shells were small, whereas only few large entities existed. Small insets depict magnifications of the smallest 1 % of the values and the large insets depict the largest 2 % of the values (dashed lines). Ranges of the 15 largest values (solid lines) are shown as horizontal lines. The maximum size of pores and BMUs increased with culturing temperature. Detection limit of the analytical method (2 pixels) is indicated represented by vertical gray line.

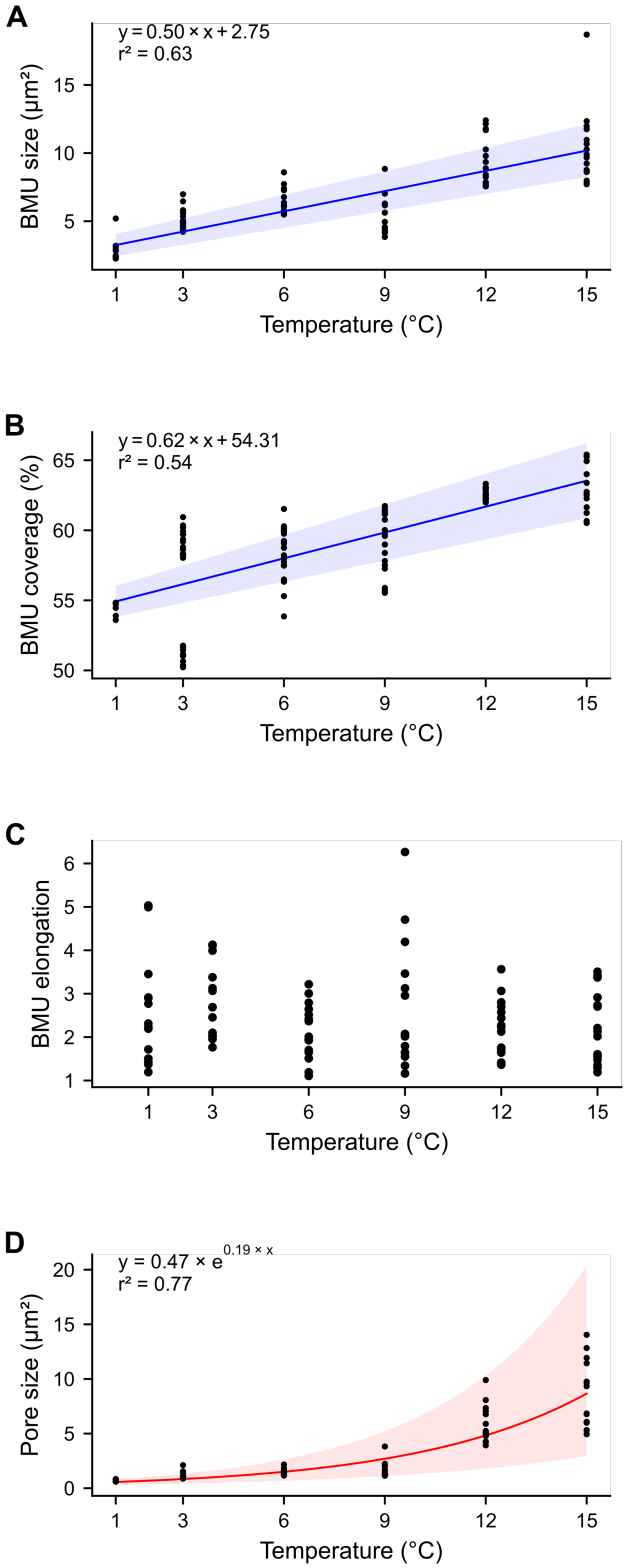

Figure 3.7 Quantitative microstructural data of hinge plate grown under temperature-controlled conditions. (A) The size of the 15 largest BMUs of each temperature treatment and (B) the space occupied by crystalline phase (BMU coverage) displayed a statistically significant linear increase with culturing temperature. Note, the relationship between BMU size and temperature was stronger than that of the BMU coverage values (r^2 = 0.67 vs. 0.54). Large inter-individual variability was observed among the BMU coverage values of specimen cultured at 3 °C. (C) BMU elongation did not exhibit any significant link with culturing temperature. (D) The size of the largest 15 pores increased exponentially with rising temperature. Shaded areas represent ± 2 standard errors of each parameter of the respective models. Model equations and r^2 goodness-of-fit values are annotated in the graphs. For justification of the choice of sample size (15 largest values) and type of model see Supplement 3D.

3.4 Discussion

3.4.1 Water temperature control on microstructural properties

As revealed by the findings of this study, several microstructural properties in the hinge plate of laboratory grown *Arctica islandica* specimens were statistically significantly linked to water temperature. Specifically, the size of the largest BMUs and pores as well as the relative proportion of the shell occupied by biominerals increased with temperature (Fig. 3.7). The correlation between BMU size and temperature was also highlighted in other existing studies on biominerals of mollusks (Olson et al., 2012; Gilbert et al., 2017; Milano et al., 2017b; Höche et al., 2020) pointing to an overarching control mechanism. Such a concept was recently outlined by Milano et al. 2017 and will be briefly rehearsed in the following. As in abiogenic systems (e.g., Mejri et al., 2014), rising water temperature can promote the amount and rate of $CaCO_3$ precipitation. This requires sufficient availability of calcium and bicarbonate ions. In bivalves, these building materials are transported from seawater across epithelial membranes to the site of biomineralization, for example, via passive diffusion through ion channels and actively via ion pumps (Carré et al., 2006; Marin et al., 2012). Both transport mechanisms proceed faster at higher temperature (Carré et al., 2006; Marin et al., 2012). If species-specific optimum growth temperatures are exceeded, the rate of transmembrane ion transport via ATPase Ca^{2+}-pumps (Carré et al., 2006) decreases and can potentially result in reduced biomineralization rates.

However, this model does not seem to be directly applicable to the CA microstructural entities in *A. islandica* shells. Actually, the overwhelming majority of BMUs and pores seemed to remain largely unaffected by the prevailing temperature regime (Fig. 3.6). One possible explanation for this surprising observation is the morphology of the BMUs. The majority of angles at which the long, needle shaped (acicular) objects of CA microstructure can be sectioned produce cutting patterns with small areas. This cut-effect bias explains the shape of the size distribution curve in Figure 3.6. Significant correlation existed also between the size of (more elongated) BMUs which were cut parallel to the longest axes, but fell below the selected threshold (15 largest BMUs of each temperature regime; Fig. S3.3 in Supplement 3D). Respective cutting planes may be identified through a study of the crystallographic orientation, since electron backscatter diffraction analysis (EBSD) results demonstrated that the a- and b-axes of the BMUs can assume multiple orientations (Karney et al., 2012) and do not always coincide with the same morphological axis Future studies should implement EBSD analyses.

The reservation must be made that the elongation of the 15 largest BMUs of each temperature setting was uncoupled from temperature, i.e., in the studied specimens of *A. islandica*, higher temperature did not favor the growth of more elongated CA needles. It is therefore likely that the same applies to the remaining BMUs and elongation is not tied to temperature. Since this observation contradicts previous observations by Milano et al. (2017b) on BMUs in the nondenticular composite prismatic microstructure of naturally-grown *Cerastoderma edule*, it is hypothesized here that the shape of BMUs, at least the largest ones, is more strongly affected by other environmental variables which were successfully precluded in controlled laboratory conditions. Perhaps, the temperature control on BMU shape is also species-specific and/or microstructure-specific. More detailed investigation of this matter would certainly be useful.

An alternative, more likely explanation for the relationship between temperature and microstructural properties in studied shell portions of *A. islandica* is that the growth of most BMUs was strongly biologically limited, whereas only a few entities were allowed to grow larger. These few BMUs were governed to a larger degree by thermodynamic processes and thus carried a stronger temperature signal than the smaller ones. Perhaps, a clear dominance of small BMUs was required for biomechanical reasons, because the hardness of shell material decreases with increasing BMU size (Milano et al., 2016). Interestingly, the size of the smallest BMUs (represented by the lower end of the size distribution curve; magnified portion in Figure 3.6) remained close to the detection limit of two pixels, irrespective of different growth temperatures. This either suggests that the number of BMUs in a given area of the growth front remained unchanged, or that noise in the SEM backscatter images was erroneously detected as tiny BMUs. In case of the latter, the effect could be counteracted by using longer pixel integration times during SEM imagery, or, as in our case, by applying an analysis threshold (Supplement 3B).

A strong biological control also appears to have limited the size of pores. As in the case of BMUs, the relationship between pore size and water temperature was most pronounced when only a few of the largest pores were considered (Fig. 3.7D, Fig. S3.3 in Supplement 3D). In order to interpret why temperature dependence amplifies at larger pore sizes, more investigation is needed on the function of the pores, which as yet remains unresolved (Ropes et al., 1984b; Dunca et al., 2009; Karney et al., 2011). The exponential nature of the temperature relationship of pore size (Fig. S3.4 in Supplement 3D) possibly suggests a strong influence of metabolic processes, because these also accelerate exponentially in warmer temperatures (Gillooly et al., 2001). Furthermore, the orientation of the pores' long axes along the growth front (Fig. 3.5D) might indicate an interrelation with biomineralization processes. In accordance with previous studies

(Karney et al., 2012), the pores were coated and filled with organic components and contained mineral precipitates. Other than the tubules in, e.g., arcoid bivalves (Shibata, 1979; Waller, 1980; Malchus, 2010), the pores in *A. islandica* shells were only a few micrometers in size, irregular in shape and often elongated, but spatially highly confined. Although many pores were cross-cut at arbitrary angles, none was observed that showed a tube-like morphology. Hence, the pores are not tubular channels (as stated in Ehrenbaum, 1884; Dunca et al., 2009), precluding a sensory function.

It appears unlikely that the pores represent dump sites for organic matrices that were produced in excess of demand during biomineralization, because the production of organics is very energy-consumptive (Palmer, 1983). However, the pores could represent the remains of failed attempts to form BMUs. This hypothesis would take up the ACC-mediated biomineralization hypothesis according to which organic envelopes (compartments) are produced, which are subsequently filled with amorphous carbonate that later transforms into a crystalline phase (Bevelander and Nakahara, 1980; Gotliv et al., 2003; Cuif et al., 2018). However, this type of biomineralization occurs in mollusks with nacro-prismatic shells (Xiang et al., 2014; Cuif et al., 2018) with high organic content (ca. 3.5 wt%; Agbaje et al., 2017a) and likely does not play a major role in *A. islandica* shells with much lower amounts of organics (1.65 wt%, Agbaje et al., 2017a). Furthermore, nacro-prismatic shells contain sheets of β-chitin and silk-like proteins (Levi-Kalisman et al., 2001), which are required for the building of such organic envelopes. Shell organics of *A. islandica*, on the contrary, contain less of these compartment-forming molecules, but more polar and soluble organic components, which closely resemble the composition of the organic matter in the crossed-lamellar microstructure (Agbaje et al., 2017a, 2019). Actually, the nucleation of crossed microstructures has been shown to be largely unaffected by organic scaffolding (Bevelander and Nakahara, 1980). Presumably, organic compounds of *A. islandica* shells predominantly provide the nucleation sites for the shell carbonate, control the biomineral precipitation rate, and the trace metal composition. In conclusion, the function of pores in *A. islandica* remains enigmatic, but a role in biomineralization appears likely. As such, their sizes are largely governed by biological processes and partly by thermodynamic processes.

3.4.2 Data quality and method evaluation

Given the novel analytical approaches used in the current study to assess the link between temperature and microstructural properties, an appraisal of the working principles and image pro-

cessing techniques seems justified.

At the outset we wish to emphasize the importance of conducting controlled laboratory experiments when it comes to assess new proxies for environmental variables. Only under such conditions it is possible to study the link between a specific environmental variable and microstructural properties because growth conditions can be selectively modified. On the other hand, an artificial growth environment may evoke the formation of untypical microstructural patterns (Grefsrud et al., 2008). As demonstrated here, shell portions in the hinge plate formed under laboratory conditions deviated from those grown in nature. The CA microstructure of the laboratory-grown shell portions appeared more uniform with rounder and more equally sized BMUs than in the shell portion that formed in the Baltic Sea (Fig. **??**). Therefore, the results achieved herein need to be tested in the future using field-grown specimens. Obviously, this requires detailed and high-resolution monitoring of a variety of environmental properties, which were not available in the present study for the shell portions produced in the Baltic Sea.

In this study, the discrimination and recognition of microstructural entities was based on gentle variations in surface topography and as such intensity variations caused by electrons backscattered by the shells. Because of the fixed position of the backscatter electron detectors, such variations depend on the orientation of the studied surface in the SEM. The largest number of backscatter electrons is detected when the sample surface is in horizontal position, and values progressively decrease with increasing sample tilt (Goldstein et al., 2017). Accordingly, backscatter intensity in a mineralogically uniform material, e.g., an aragonitic shell, can be used to trace changes in surface height. Thereby, polished surfaces of individual BMUs form elevations that emit high backscatter intensity (high gray values, light gray to white), whereas depressions (such as the pores or the inter-crystalline space; here produced by immersion in H_2O_2) are detected as areas of reduced to zero emission (low gray values, dark gray to black) (Fig. 3.2, Supplement 3B). Such topographic principles are well understood (Soreghan and Francus, 2004) and have been employed in several existing studies to assess the microstructural properties of bivalve (Höche et al., 2020) and gastropod shells (Füllenbach et al., 2014) as well as other calcium carbonate materials (Faÿ-Gomord et al., 2017).

A reliable automated image segmentation process represents a fundamental step to identify individual BMUs and pores and subsequently conduct morphometric analyses. Because of the large gray value contrast between the polished shell surface and the pores, segmentation of these microstructural entities did not require intensive image pretreatment or training of the (bio)image software Ilastik. The precise identification of pore boundaries was occasionally com-

plicated by the presence of particles inside the pores (Figs. 3.2 and 3.5E-G). However, when supplied with additional training data to segment these structures, the classification algorithm overcame such bias and produced reliable pore space reconstructions (Fig. 3.2). The automated segmentation process of the pores allowed use of a lower magnification (1550 ×) than required for the BMUs, which considerably reduced the acquisition and processing time while maintaining an adequate spatial resolution. On the contrary, training of the software for BMU recognition turned out more challenging. A major prerequisite to use automatized image segmentation is that all images have uniform characteristics, e.g., comparable surface topography generated by etching (of the mineral phase) or oxidation (of the organic phases) and comparable image resolution. To assess the BMU size and coverage, the polished shell surfaces were immersed in H_2O_2 to reveal boundaries between the microstructural units. We decided to treat the sample with an oxidative agent to remove organic matrices located between the BMUs (inter-crystalline organics) without completely dissolving the mineral phase of the shell. In preparation for the present study, however, we experimented with different chemical treatments of *A. islandica* shells to identify the most suitable method. Among others, different types and concentrations of acids and oxidation agents were explored (Fig. S3.1 in Supplement 3C). According to these tests, immersion in formic or hydrochloric acid, even at very low concentration (<0.01 vol%), resulted in micrometer-scale to nanometer-scale dissolution of the polished BMU surfaces. These areas were then erroneously detected by the segmentation software as BMU boundaries. Furthermore, the etching affected the individual BMUs differently, probably related to minute variations in density and/or intra-crystalline organic content. The degree of etching also varied considerably among specimens. A solution of 10.5 vol% H_2O_2 for 20 min turned out to provide the best results for the scope of the present study. Hydrogen peroxide solution has been used in the past to remove organic matter from biogenic carbonates (Penkman et al., 2008; Krause-Nehring et al., 2011; Crippa et al., 2016). It reacted well with the organic matrices of the shell, which consist mostly of non-acidic, polar proteinaceous materials (Agbaje et al., 2017a). According to high-resolution images, BMUs remained largely unaltered by treatment with H_2O_2 (Fig. 3.2A), except for the rims (Fig. S3.2 in Supplement 3C), and consistent results were achieved within and among specimens. These assets were prerequisite for a reproducible segmentation process. Note, that the large inter-individual variability observed in the BMU coverage values of specimens cultured at 3 °C (Fig. 3.7) does likely not result from the chosen preparation and etching method, because those specimens were embedded in the same batch of epoxy and thus prepared in exactly the same manner.

Through the use of novel analytical techniques, we were able to automate the recognition of microstructural entities as well as the morphometric analyses, which hitherto had to be performed manually or semi-automatically with manual corrections (Nishida et al., 2011; Füllenbach et al., 2014). Previous morphometric studies of BMUs included only few SEM images representing relatively small shell areas (e.g., 19 images in Milano et al., 2017b; 64 images in Ballesta-Artero et al., 2018a) in order to compensate for the excessively long analytical times. With such reduced sample sizes, the chances of finding relevant relationships between microstructural properties and environmental variables diminish, as shown by the extraordinarily high threshold that had to be chosen in the present study in conjunction with the logarithmic particle size distributions (Fig. S3.3 in Supplement 3D; Fig. 3.6). The technique used here, however, reduced the time for measurement significantly and facilitated the analysis of large shell regions (Table 3.1) without sacrificing analytical precision or requiring manual intervention (S5 Supporting information). Accordingly, the sample size and spatial coverage (total number of BMUs = 699 587) substantially exceeded those of previous studies (e.g., ca. 2170 BMUs in Milano et al., 2017b). These large sample sizes enabled us to detect subtle temperature-induced variability of the shell microstructural properties that previously remained unnoticed, emphasizing the importance of comprehensive shell imaging and highlighting the potential of automated image processing techniques combined with machine learning algorithms.

Focusing on a specific subset (thresholding) can serve as an efficient means to detect unnoticed signals in large datasets. This approach has been successfully applied in a previous study of the crossed-lamellar microstructure of *Glcymeris bimaculata* (Höche et al., 2020), in which only the largest 10 % of the biominerals were taken into consideration. The appropriate threshold value most certainly varies among different microstructures due to differences in the degree of hierarchical organization, complexity, the morphology of individual BMUs and fusing of discrete BMUs to larger units. For example, in the crossed-lamellar microstructure, stacks of the smallest building blocks, elongated rods of a few hundred nm diameter, so-called 3rd order lamellae, form 2nd order lamellae, which are assembled into 1st order lamellae. The latter can attain widths of ca. 28 µm and are alternatingly arranged in a rustic fence-like manner (Carter, 1990; Füllenbach et al., 2014; Böhm et al., 2016). The CA microstructure, in contrast, lacks such a hierarchical organization into larger structural units. Their BMUs consist of acicular units, which are only co-aligned morphologically in two dominant dip directions (ca. 30–40° off the growth surface) and fused together in platelets (Carter, 1990; Carter et al., 2012). EBSD experiments performed on shell hinges of *Arctica islandica* confirmed that the morphologically co-aligned

acicular units also share a common crystallographic orientation (thus forming a BMU; Karney et al., 2012). The crystallographic c-axes of all BMUs are aligned roughly parallel to the direction of growth, but other than that, no overarching crystallographic alignment seems to persist (Karney et al., 2012). In conclusion, the BMUs of the CA microstructure are much smaller and less complexly arranged than the BMUs of the crossed-lamellar microstructure. Cross-sections of the CA microstructure reveal more irregularly shaped BMUs than those of other microstructures (i.e., nacre tablets, Gilbert et al., 2017; prisms, Milano et al., 2017b; 3rd order lamellae of the cross-lamellar microstructure Höche et al., 2020). Therefore, a much higher size threshold was required than in previous analyses (Supplement 3D). The same issue arose in the case of pores, which were likewise irregular in shape.

The BMU coverage analysis followed a more simplistic approach than the segmentation analysis and was based on the proportion of shell covered by crystalline phases relative to such largely occupied by organic phases plus downward dipping edges of BMUs. The gray value of each pixel of the binarized image indirectly provided height information over an area of ca. 0.0003 µm^2 (= the same resolution as used for BMU size analysis), spanning a total topographical height of ca. 6 µm. The production of binary images depended strongly on the uniformity of the gray scale balance among all studied SEM images. The latter is a measure of the emitted backscatter electrons during acquisition and can strongly vary between specimens, depending on subtle differences in thickness of the platinum coating, orientation of the studied surface or density of the aragonite. Since the individual images used in this study exhibited similar gray value distributions, the average gray value of all studied images was chosen as the threshold to distinguish BMUs from the inter-crystalline space. In other words, the BMU coverage serves as a measure of surface area above the average height of all samples, inferred from backscatter intensities (gray values; Fig. S3.2 in Supplement 3C). In turn, this means that the BMU coverage value is no exact measure of the actual proportion occupied by BMUs (see section 3.2.3). The BMUs stand out from the surface as plateaus, but the angle at which their rims dip downward is shallower than 90°. Due to the selected gray value threshold, some portions of these gently descending BMU edges were assigned to the depression zones and became black in the binarized image. Hence the BMU coverage values cannot be used to quantify the actual proportion of inter-crystalline space or BMUs. However, it can be used to rapidly detect differences in the relative proportion of crystalline phase in different shell portions. BMU coverage results agreed with that obtained from segmented BMU analysis documenting the validity of the method.

3.5 Conclusions

Variations in water temperature resulted in subtle microstructural changes in the hinge plate of *A. islandica* grown under controlled laboratory conditions. The size of the largest biomineral units and pores as well as the relative proportion of crystalline components in the crossed-acicular microstructure increased with water temperature. Since only a very small proportion of the microstructural units was affected, the subtle changes would have remained unnoticed without the use of automated image processing techniques and machine learning–assisted object recognition. While it may be challenging to reliably reconstruct small (1 °C) changes of long-term ocean climate from these minute microstructural variations, they can prove useful to assess seasonal temperature variations and extremes or serve as a source of temperature information when geochemical proxy signals have vanished due to diagenetic overprint. Further, using fossil shells collected from different localities and environmental regimes will shed light on the applicability and sensitivity of the new microstructure-based temperature proxies.

3.6 Supplementary material

Supplement 3A - Mn/Ca data (LA-ICP-MS) of the studied bivalve shells

Table S3.1 Mn/Ca data (LA-ICP-MS) of the studied bivalve shells

Sample	Measurement	$^{55}Mn/^{4}3Ca$ (mmol mol^{-1})	1σ $^{55}Mn/^{4}3Ca$ (mmol mol^{-1})
BCR-2G	0	22.3535	1.2650
BCR-2G	1	22.5589	1.1686
BCR-2G	2	22.6689	1.4515
BCR-2G	3	21.8598	1.4925
BCR-2G	4	21.7571	1.4496
BCR-2G	5	21.9488	1.5108
BCR-2G	6	21.9751	1.8394
BCR-2G	7	21.8618	1.2969
BCR-2G	8	22.0196	1.2309
BCR-2G	9	21.6921	1.0793
BCR-2G	10	22.1196	1.3991
BCR-2G	11	22.1544	1.4276
BCR-2G	12	21.6897	1.3237
BCR-2G	13	21.9671	1.3728
BCR-2G	14	21.9974	1.4449
BCR-2G	15	22.3005	1.6065
BCR-2G	16	22.7183	1.5945
BCR-2G	17	22.0568	1.2317
BCR-2G	18	22.0533	1.6955
BCR-2G	19	22.4496	1.6008
BCR-2G	20	22.3156	1.5563
BCR-2G	21	21.7162	1.5196
BCR-2G	22	21.9714	1.2575
BCR-2G	23	21.9194	1.3710
BCR-2G	24	22.1085	1.3974
BCR-2G	25	22.3718	1.6685

BCR-2G	26	22.3939	1.3327
JcT-1	0	0.0002	0.0007
JcT-1	1	0.0002	0.0008
JcT-1	2	0.0044	0.0047
JcT-1	3	-0.0002	0.0008
JcT-1	4	0.0010	0.0041
JcT-1	5	0.0013	0.0046
JcT-1	6	0.0002	0.0006
JcT-1	7	0.0003	0.0008
JcT-1	8	0.0004	0.0006
JcT-1	9	0.0006	0.0009
JcT-1	10	0.0005	0.0007
JcT-1	11	0.0002	0.0007
JcT-1	12	0.0004	0.0007
JcT-1	13	0.0004	0.0007
JcT-1	14	0.0004	0.0006
JcT-1	15	0.0001	0.0008
JcT-1	16	0.0003	0.0007
JcT-1	17	0.0005	0.0008
JcT-1	18	0.0005	0.0008
JcT-1	19	0.0004	0.0010
JcT-1	20	0.0004	0.0009
JcT-1	21	0.0002	0.0009
JcT-1	22	0.0002	0.0007
JcT-1	23	0.0005	0.0008
JcT-1	24	0.0003	0.0007
JcT-1	25	0.0004	0.0008
JcT-1	26	0.0000	0.0008
MACS-3	0	1.0441	0.0520
MACS-3	1	0.9856	0.0542
MACS-3	2	1.0110	0.0483
MACS-3	3	1.0360	0.0844
MACS-3	4	0.9874	0.0606

MACS-3	5	0.9873	0.0579
MACS-3	6	1.0162	0.0658
MACS-3	7	0.9944	0.0530
MACS-3	8	0.9827	0.0596
MACS-3	9	1.0101	0.0598
MACS-3	10	0.9968	0.0455
MACS-3	11	0.9992	0.0402
MACS-3	12	0.9700	0.0593
MACS-3	13	1.0029	0.0511
MACS-3	14	0.9945	0.0513
MACS-3	15	1.0222	0.0603
MACS-3	16	1.0150	0.0779
MACS-3	17	1.0293	0.0523
MACS-3	18	1.0080	0.0494
MACS-3	19	0.9907	0.0516
MACS-3	20	1.0097	0.0448
MACS-3	21	1.0176	0.0573
MACS-3	22	1.0018	0.0604
MACS-3	23	1.0077	0.0485
MACS-3	24	1.0196	0.0485
MACS-3	25	0.9906	0.0515
MACS-3	26	1.0113	0.0487
Nioz-TC-01-A1R	0	-0.0004	0.0008
Nioz-TC-01-A1R	1	0.0002	0.0009
Nioz-TC-01-A1R	2	0.0150	0.0023
Nioz-TC-01-A1R	3	0.0248	0.0029
Nioz-TC-01-A1R	4	0.0321	0.0034
Nioz-TC-01-A1R	5	0.0431	0.0039
Nioz-TC-01-A1R	6	0.0427	0.0034
Nioz-TC-01-A1R	7	0.0112	0.0020
Nioz-TC-01-A1R	8	0.0068	0.0015
Nioz-TC-01-A1R	9	0.1208	0.0069
Nioz-TC-01-A1R	10	0.0683	0.0051

Nioz-TC-01-A1R	11	0.0606	0.0068
Nioz-TC-01-A1R	12	0.0343	0.0060
Nioz-TC-01-A1R	13	0.0311	0.0034
Nioz-TC-01-A1R	14	0.0568	0.0110
Nioz-TC-01-A1R	15	0.0495	0.0046
Nioz-TC-01-A2R	0	0.0001	0.0008
Nioz-TC-01-A2R	1	0.0000	0.0008
Nioz-TC-01-A2R	2	0.0092	0.0018
Nioz-TC-01-A2R	3	0.0265	0.0031
Nioz-TC-01-A2R	4	0.0164	0.0028
Nioz-TC-01-A2R	5	0.0075	0.0015
Nioz-TC-01-A2R	6	0.0943	0.0056
Nioz-TC-01-A2R	7	0.0379	0.0035
Nioz-TC-01-A2R	8	0.0362	0.0039
Nioz-TC-01-A2R	9	0.0711	0.0057
Nioz-TC-01-A2R	10	0.1509	0.0106
Nioz-TC-01-A2R	11	0.0479	0.0046
Nioz-TC-01-A2R	12	0.0231	0.0027
Nioz-TC-01-A2R	13	0.0399	0.0044
Nioz-TC-01-A2R	14	0.0908	0.0239
Nioz-TC-01-A2R	15	0.0518	0.0100
Nioz-TC-01-A2R	16	0.0703	0.0086
Nioz-TC-01-A2R	17	0.0508	0.0076
Nioz-TC-01-A2R	18	0.0722	0.0084
Nioz-TC-03-A1R	0	0.0004	0.0009
Nioz-TC-03-A1R	1	0.0001	0.0006
Nioz-TC-03-A1R	2	0.0005	0.0016
Nioz-TC-03-A1R	3	0.0000	0.0008
Nioz-TC-03-A1R	4	0.0112	0.0021
Nioz-TC-03-A1R	5	0.0222	0.0024
Nioz-TC-03-A1R	6	0.0316	0.0032
Nioz-TC-03-A1R	7	0.0287	0.0028
Nioz-TC-03-A1R	8	0.0202	0.0029

Nioz-TC-03-A1R	9	0.0089	0.0017
Nioz-TC-03-A1R	10	0.0263	0.0027
Nioz-TC-03-A1R	11	0.1269	0.0073
Nioz-TC-03-A1R	12	0.2162	0.0103
Nioz-TC-03-A1R	13	0.0947	0.0066
Nioz-TC-03-A1R	14	0.0273	0.0030
Nioz-TC-03-A1R	15	0.0288	0.0032
Nioz-TC-03-A1R	16	0.0211	0.0032
Nioz-TC-03-A1R	17	0.0481	0.0038
Nioz-TC-03-A1R	18	0.0304	0.0030
Nioz-TC-03-A2R	0	0.0005	0.0006
Nioz-TC-03-A2R	1	0.0002	0.0006
Nioz-TC-03-A2R	2	0.0002	0.0008
Nioz-TC-03-A2R	3	0.0001	0.0007
Nioz-TC-03-A2R	4	0.0003	0.0006
Nioz-TC-03-A2R	5	0.0119	0.0019
Nioz-TC-03-A2R	6	0.0236	0.0027
Nioz-TC-03-A2R	7	0.0323	0.0033
Nioz-TC-03-A2R	8	0.0310	0.0038
Nioz-TC-03-A2R	9	0.0298	0.0027
Nioz-TC-03-A2R	10	0.0099	0.0016
Nioz-TC-03-A2R	11	0.0058	0.0017
Nioz-TC-03-A2R	12	0.0799	0.0067
Nioz-TC-03-A2R	13	0.0821	0.0182
Nioz-TC-03-A2R	14	0.0342	0.0094
Nioz-TC-03-A2R	15	0.0543	0.0041
Nioz-TC-03-A2R	16	0.0516	0.0033
Nioz-TC-03-A2R	17	0.0323	0.0035
Nioz-TC-03-A2R	18	0.0387	0.0036
Nioz-TC-03-A2R	19	0.0367	0.0035
Nioz-TC-03-A2R	20	0.0344	0.0054
Nioz-TC-03-A2R	21	0.0407	0.0055
Nioz-TC-03-A2R	22	0.0153	0.0032

Nioz-TC-03-A2R	23	0.0708	0.0086
Nioz-TC-06-A1R	0	0.0006	0.0009
Nioz-TC-06-A1R	1	0.0009	0.0010
Nioz-TC-06-A1R	2	0.0019	0.0011
Nioz-TC-06-A1R	3	0.0009	0.0010
Nioz-TC-06-A1R	4	0.0004	0.0009
Nioz-TC-06-A1R	5	0.0001	0.0010
Nioz-TC-06-A1R	6	0.0198	0.0031
Nioz-TC-06-A1R	7	0.0290	0.0028
Nioz-TC-06-A1R	8	0.0420	0.0042
Nioz-TC-06-A1R	9	0.0324	0.0034
Nioz-TC-06-A1R	10	0.0195	0.0026
Nioz-TC-06-A1R	11	0.0314	0.0031
Nioz-TC-06-A1R	12	0.0451	0.0040
Nioz-TC-06-A1R	13	0.0527	0.0043
Nioz-TC-06-A1R	14	0.0688	0.0063
Nioz-TC-06-A1R	15	0.0526	0.0042
Nioz-TC-06-A1R	16	0.0438	0.0045
Nioz-TC-06-A1R	17	0.0966	0.0071
Nioz-TC-06-A1R	18	0.0676	0.0059
Nioz-TC-06-A1R	19	0.1023	0.0077
Nioz-TC-06-A1R	20	0.1963	0.0181
Nioz-TC-06-A1R	21	0.2446	0.0121
Nioz-TC-06-A1R	22	0.1312	0.0079
Nioz-TC-06-A1R	23	0.0764	0.0071
Nioz-TC-06-A1R	24	0.0824	0.0068
Nioz-TC-06-A1R	25	0.0506	0.0085
Nioz-TC-06-A1R	26	0.0391	0.0042
Nioz-TC-06-A1R	27	0.0682	0.0065
Nioz-TC-06-A1R	28	0.1295	0.0083
Nioz-TC-06-A2R	0	0.0033	0.0012
Nioz-TC-06-A2R	1	0.0030	0.0011
Nioz-TC-06-A2R	2	0.0019	0.0011

Nioz-TC-06-A2R	3	0.0007	0.0009
Nioz-TC-06-A2R	4	0.0002	0.0008
Nioz-TC-06-A2R	5	0.0002	0.0010
Nioz-TC-06-A2R	6	0.0000	0.0009
Nioz-TC-06-A2R	7	0.0013	0.0011
Nioz-TC-06-A2R	8	0.0333	0.0033
Nioz-TC-06-A2R	9	0.0346	0.0040
Nioz-TC-06-A2R	10	0.0647	0.0054
Nioz-TC-06-A2R	11	0.0362	0.0042
Nioz-TC-06-A2R	12	0.0404	0.0036
Nioz-TC-06-A2R	13	0.0160	0.0024
Nioz-TC-06-A2R	14	0.0899	0.0064
Nioz-TC-06-A2R	15	0.1447	0.0096
Nioz-TC-06-A2R	16	0.1461	0.0081
Nioz-TC-06-A2R	17	0.0628	0.0188
Nioz-TC-06-A2R	18	0.0402	0.0038
Nioz-TC-06-A2R	19	0.0720	0.0125
Nioz-TC-06-A2R	20	0.0415	0.0104
Nioz-TC-06-A2R	21	0.1323	0.0113
Nioz-TC-06-A2R	22	0.0524	0.0065
Nioz-TC-06-A3R	0	0.0004	0.0009
Nioz-TC-06-A3R	1	0.0005	0.0009
Nioz-TC-06-A3R	2	0.0006	0.0007
Nioz-TC-06-A3R	3	0.0005	0.0010
Nioz-TC-06-A3R	4	0.0001	0.0007
Nioz-TC-06-A3R	5	0.0002	0.0007
Nioz-TC-06-A3R	6	0.0087	0.0019
Nioz-TC-06-A3R	7	0.0275	0.0028
Nioz-TC-06-A3R	8	0.0562	0.0056
Nioz-TC-06-A3R	9	0.0360	0.0039
Nioz-TC-06-A3R	10	0.0356	0.0043
Nioz-TC-06-A3R	11	0.0197	0.0032
Nioz-TC-06-A3R	12	0.0072	0.0019

Nioz-TC-06-A3R	13	0.1171	0.0081
Nioz-TC-06-A3R	14	0.1143	0.0069
Nioz-TC-06-A3R	15	0.2044	0.0169
Nioz-TC-06-A3R	16	0.0398	0.0035
Nioz-TC-06-A3R	17	0.0390	0.0057
Nioz-TC-06-A3R	18	0.0469	0.0046
Nioz-TC-06-A3R	19	0.0498	0.0054
Nioz-TC-06-A3R	20	0.0545	0.0041
Nioz-TC-06-A3R	21	0.0399	0.0041
Nioz-TC-09-A2R	0	0.0002	0.0007
Nioz-TC-09-A2R	1	-0.0002	0.0009
Nioz-TC-09-A2R	2	0.1303	0.0081
Nioz-TC-09-A2R	3	0.0776	0.0053
Nioz-TC-09-A2R	4	0.0432	0.0040
Nioz-TC-09-A2R	5	0.0271	0.0027
Nioz-TC-09-A2R	6	0.0456	0.0043
Nioz-TC-09-A2R	7	0.1834	0.0094
Nioz-TC-09-A2R	8	0.0119	0.0019
Nioz-TC-09-A2R	9	0.0363	0.0031
Nioz-TC-09-A2R	10	0.0285	0.0033
Nioz-TC-09-A2R	11	0.0538	0.0052
Nioz-TC-09-A2R	12	0.0688	0.0051
Nioz-TC-09-A2R	13	0.0425	0.0033
Nioz-TC-09-A2R	14	0.0235	0.0029
Nioz-TC-09-A2R	15	0.0568	0.0065
Nioz-TC-09-A2R	16	0.0250	0.0026
Nioz-TC-09-A2R	17	0.0443	0.0043
Nioz-TC-09-A2R	18	0.0824	0.0064
Nioz-TC-09-A2R	19	0.0786	0.0110
Nioz-TC-09-A2R	20	0.0511	0.0110
Nioz-TC-09-A3R	0	0.0000	0.0008
Nioz-TC-09-A3R	1	0.0001	0.0007
Nioz-TC-09-A3R	2	0.0716	0.0048

Nioz-TC-09-A3R	3	0.1284	0.0074
Nioz-TC-09-A3R	4	0.1120	0.0061
Nioz-TC-09-A3R	5	0.1230	0.0079
Nioz-TC-09-A3R	6	0.0414	0.0036
Nioz-TC-09-A3R	7	0.1308	0.0095
Nioz-TC-09-A3R	8	0.1478	0.0089
Nioz-TC-09-A3R	9	0.1289	0.0078
Nioz-TC-09-A3R	10	0.0166	0.0025
Nioz-TC-09-A3R	11	0.0296	0.0035
Nioz-TC-09-A3R	12	0.0671	0.0045
Nioz-TC-09-A3R	13	0.0610	0.0042
Nioz-TC-09-A3R	14	0.0972	0.0055
Nioz-TC-09-A3R	15	0.1009	0.0068
Nioz-TC-09-A3R	16	0.1471	0.0065
Nioz-TC-09-A3R	17	0.1305	0.0080
Nioz-TC-09-A3R	18	0.0855	0.0060
Nioz-TC-09-A3R	19	0.1453	0.0080
Nioz-TC-09-A3R	20	0.0581	0.0057
Nioz-TC-09-A3R	21	0.1258	0.0072
Nioz-TC-12-A2R	0	0.0000	0.0008
Nioz-TC-12-A2R	1	0.0008	0.0007
Nioz-TC-12-A2R	2	0.0000	0.0006
Nioz-TC-12-A2R	3	0.0596	0.0059
Nioz-TC-12-A2R	4	0.0699	0.0048
Nioz-TC-12-A2R	5	0.0797	0.0050
Nioz-TC-12-A2R	6	0.0247	0.0032
Nioz-TC-12-A2R	7	0.0364	0.0036
Nioz-TC-12-A2R	8	0.2028	0.0085
Nioz-TC-12-A2R	9	0.0631	0.0058
Nioz-TC-12-A2R	10	0.0262	0.0025
Nioz-TC-12-A2R	11	0.0543	0.0043
Nioz-TC-12-A2R	12	0.0596	0.0042
Nioz-TC-12-A2R	13	0.0935	0.0055

Nioz-TC-12-A2R	14	0.0535	0.0047
Nioz-TC-12-A2R	15	0.0235	0.0027
Nioz-TC-12-A2R	16	0.0903	0.0055
Nioz-TC-12-A2R	17	0.2105	0.0102
Nioz-TC-12-A2R	18	0.2090	0.0122
Nioz-TC-12-A2R	19	0.0887	0.0113
Nioz-TC-12-A2R	20	0.0824	0.0060
Nioz-TC-12-A2R	21	0.0646	0.0050
Nioz-TC-12-A2R	22	0.0537	0.0037
Nioz-TC-12-A2R	23	0.1252	0.0065
Nioz-TC-12-A3R	0	0.0003	0.0008
Nioz-TC-12-A3R	1	0.0005	0.0008
Nioz-TC-12-A3R	2	0.0003	0.0008
Nioz-TC-12-A3R	3	0.0602	0.0047
Nioz-TC-12-A3R	4	0.0648	0.0076
Nioz-TC-12-A3R	5	0.0667	0.0050
Nioz-TC-12-A3R	6	0.2157	0.0139
Nioz-TC-12-A3R	7	0.0183	0.0024
Nioz-TC-12-A3R	8	0.0579	0.0046
Nioz-TC-12-A3R	9	0.0378	0.0039
Nioz-TC-12-A3R	10	0.0479	0.0080
Nioz-TC-12-A3R	11	0.0431	0.0096
Nioz-TC-12-A3R	12	0.0756	0.0257
Nioz-TC-12-A3R	13	0.0532	0.0207
Nioz-TC-12-A3R	14	0.0440	0.0047
Nioz-TC-12-A3R	15	0.0472	0.0085
Nioz-TC-12-A3R	16	0.0604	0.0053
Nioz-TC-12-A3R	17	0.0694	0.0087
Nioz-TC-12-A3R	18	0.0886	0.0152
Nioz-TC-12-A3R	19	0.0018	0.0012
Nioz-TC-12-A3R	20	0.0485	0.0290

Supplement 3B - Morphological data of the BMUs and pores

Table S3.2 Morphological data of the BMUs and pores.

Specimen ID	Pore size (μm^2)	Specimen ID	Image #	BMU size (μm^2)	BMU elongation
Nioz-TC-01-A1R	0.835	Nioz-TC-01-A1R	7	2.838	1.193
Nioz-TC-01-A1R	0.821	Nioz-TC-01-A1R	9	2.260	1.426
Nioz-TC-01-A1R	0.806	Nioz-TC-01-A1R	9	2.374	1.503
Nioz-TC-01-A1R	0.799	Nioz-TC-01-A1R	9	2.841	4.992
Nioz-TC-01-A1R	0.721	Nioz-TC-01-A1R	11	2.266	2.313
Nioz-TC-01-A1R	0.671	Nioz-TC-01-A1R	11	2.361	2.239
Nioz-TC-01-A1R	0.649	Nioz-TC-01-A1R	11	2.424	1.505
Nioz-TC-01-A2R	0.649	Nioz-TC-01-A1R	11	2.472	1.718
Nioz-TC-01-A1R	0.628	Nioz-TC-01-A1R	11	2.923	5.032
Nioz-TC-01-A1R	0.628	Nioz-TC-01-A1R	13	2.357	2.914
Nioz-TC-01-A1R	0.621	Nioz-TC-01-A1R	13	2.841	2.771
Nioz-TC-01-A1R	0.621	Nioz-TC-01-A1R	13	3.145	3.453
Nioz-TC-01-A1R	0.614	Nioz-TC-01-A1R	13	3.195	1.370
Nioz-TC-01-A1R	0.599	Nioz-TC-01-A1R	13	5.199	2.898
Nioz-TC-01-A1R	0.599	Nioz-TC-01-A1R	17	2.289	2.193
Nioz-TC-03-A3R	2.105	Nioz-TC-03-A1R	18	5.343	2.100
Nioz-TC-03-A1R	1.534	Nioz-TC-03-A1R	20	6.976	3.992
Nioz-TC-03-A3R	1.370	Nioz-TC-03-A1R	24	4.925	1.765
Nioz-TC-03-A2R	1.113	Nioz-TC-03-A1R	24	5.577	4.129
Nioz-TC-03-A1R	1.092	Nioz-TC-03-A1R	26	4.474	2.036
Nioz-TC-03-A3R	1.013	Nioz-TC-03-A1R	26	5.657	2.691
Nioz-TC-03-A3R	1.006	Nioz-TC-03-A1R	26	6.459	1.956
Nioz-TC-03-A3R	0.978	Nioz-TC-03-A1R	28	5.033	2.687
Nioz-TC-03-A2R	0.942	Nioz-TC-03-A1R	30	4.364	2.030
Nioz-TC-03-A3R	0.942	Nioz-TC-03-A1R	30	5.808	1.956
Nioz-TC-03-A1R	0.935	Nioz-TC-03-A1R	32	4.284	2.454

Nioz-TC-03-A1R	0.892	Nioz-TC-03-A1R	32	4.702	4.105
Nioz-TC-03-A3R	0.892	Nioz-TC-03-A1R	36	4.225	3.066
Nioz-TC-03-A3R	0.885	Nioz-TC-03-A2R	25	4.592	3.127
Nioz-TC-03-A3R	0.885	Nioz-TC-03-A2R	30	4.846	3.379
Nioz-TC-06-A1R	2.169	Nioz-TC-06-A1R	13	6.165	1.925
Nioz-TC-06-A3R	1.825	Nioz-TC-06-A1R	17	7.727	1.649
Nioz-TC-06-A3R	1.683	Nioz-TC-06-A1R	19	5.527	1.191
Nioz-TC-06-A3R	1.489	Nioz-TC-06-A1R	19	5.802	1.510
Nioz-TC-06-A1R	1.477	Nioz-TC-06-A1R	19	7.273	2.416
Nioz-TC-06-A1R	1.434	Nioz-TC-06-A1R	21	6.074	2.367
Nioz-TC-06-A1R	1.391	Nioz-TC-06-A1R	25	5.528	2.518
Nioz-TC-06-A1R	1.363	Nioz-TC-06-A1R	25	5.540	2.792
Nioz-TC-06-A3R	1.346	Nioz-TC-06-A1R	25	8.586	1.105
Nioz-TC-06-A3R	1.320	Nioz-TC-06-A1R	29	5.677	1.946
Nioz-TC-06-A3R	1.307	Nioz-TC-06-A1R	31	5.551	1.702
Nioz-TC-06-A2R	1.284	Nioz-TC-06-A2R	29	5.488	3.218
Nioz-TC-06-A3R	1.243	Nioz-TC-06-A2R	31	6.770	3.004
Nioz-TC-06-A3R	1.243	Nioz-TC-06-A3R	20	6.356	2.009
Nioz-TC-06-A3R	1.165	Nioz-TC-06-A3R	20	7.394	2.643
Nioz-TC-09-A2R	3.818	Nioz-TC-09-A1R	7	4.273	3.125
Nioz-TC-09-A3R	2.233	Nioz-TC-09-A1R	11	6.169	1.645
Nioz-TC-09-A2R	2.034	Nioz-TC-09-A1R	11	7.027	1.341
Nioz-TC-09-A2R	1.720	Nioz-TC-09-A1R	15	4.197	2.957
Nioz-TC-09-A2R	1.677	Nioz-TC-09-A1R	19	6.296	1.161
Nioz-TC-09-A2R	1.506	Nioz-TC-09-A1R	21	4.215	1.792
Nioz-TC-09-A3R	1.406	Nioz-TC-09-A1R	21	4.450	3.463
Nioz-TC-09-A2R	1.299	Nioz-TC-09-A1R	21	4.574	2.016
Nioz-TC-09-A2R	1.242	Nioz-TC-09-A1R	21	8.843	4.194
Nioz-TC-09-A2R	1.234	Nioz-TC-09-A1R	23	4.286	2.050
Nioz-TC-09-A2R	1.234	Nioz-TC-09-A1R	23	5.627	1.551
Nioz-TC-09-A3R	1.234	Nioz-TC-09-A1R	27	4.144	1.645
Nioz-TC-09-A2R	1.199	Nioz-TC-09-A2R	12	3.847	4.706
Nioz-TC-09-A2R	1.149	Nioz-TC-09-A2R	12	4.952	6.264

Nioz-TC-09-A3R	1.142	Nioz-TC-09-A3R	10	4.205	2.073
Nioz-TC-12-A1R	9.897	Nioz-TC-12-A2R	3	7.868	2.440
Nioz-TC-12-A1R	8.070	Nioz-TC-12-A2R	3	9.348	1.364
Nioz-TC-12-A2R	7.335	Nioz-TC-12-A2R	5	11.784	3.064
Nioz-TC-12-A3R	7.071	Nioz-TC-12-A2R	7	9.790	2.126
Nioz-TC-12-A2R	6.772	Nioz-TC-12-A2R	7	10.264	1.642
Nioz-TC-12-A1R	5.887	Nioz-TC-12-A2R	7	12.402	2.700
Nioz-TC-12-A2R	5.238	Nioz-TC-12-A2R	10	8.262	1.758
Nioz-TC-12-A2R	5.088	Nioz-TC-12-A3R	19	8.881	2.271
Nioz-TC-12-A1R	5.038	Nioz-TC-12-A3R	21	7.829	1.666
Nioz-TC-12-A1R	5.031	Nioz-TC-12-A3R	21	11.686	2.801
Nioz-TC-12-A2R	4.795	Nioz-TC-12-A3R	23	7.585	2.573
Nioz-TC-12-A2R	4.795	Nioz-TC-12-A3R	23	7.722	1.731
Nioz-TC-12-A3R	4.274	Nioz-TC-12-A3R	23	8.407	2.227
Nioz-TC-12-A2R	4.217	Nioz-TC-12-A3R	29	7.555	1.414
Nioz-TC-12-A2R	3.925	Nioz-TC-12-A3R	29	12.152	3.564
Nioz-TC-15-A2R	14.043	Nioz-TC-15-A1R	10	7.977	1.557
Nioz-TC-15-A2R	11.931	Nioz-TC-15-A1R	25	7.714	2.914
Nioz-TC-15-A2R	11.438	Nioz-TC-15-A1R	25	9.674	2.733
Nioz-TC-15-A2R	9.754	Nioz-TC-15-A1R	27	10.670	1.605
Nioz-TC-15-A2R	9.626	Nioz-TC-15-A1R	27	11.981	1.479
Nioz-TC-15-A2R	9.333	Nioz-TC-15-A3R	5	9.232	3.374
Nioz-TC-15-A2R	6.779	Nioz-TC-15-A3R	7	8.757	2.209
Nioz-TC-15-A3R	6.072	Nioz-TC-15-A3R	7	10.266	2.128
Nioz-TC-15-A3R	6.037	Nioz-TC-15-A3R	7	10.971	1.354
Nioz-TC-15-A2R	5.987	Nioz-TC-15-A3R	9	7.833	3.507
Nioz-TC-15-A3R	5.316	Nioz-TC-15-A3R	9	8.607	3.415
Nioz-TC-15-A2R	5.295	Nioz-TC-15-A3R	9	9.898	1.293
Nioz-TC-15-A2R	4.938	Nioz-TC-15-A3R	9	11.752	2.018
Nioz-TC-15-A2R	4.702	Nioz-TC-15-A3R	9	12.340	1.191
Nioz-TC-15-A2R	4.681	Nioz-TC-15-A3R	9	18.695	2.703

Table S3.3 p-values for two-sided t-tests for the means of BMU and pore size data of pairs of different temperature settings

BMU area significance levels (p)

Using all values

	1 °C	3 °C	6 °C	9 °C	12 °C	15 °C
1 °C	1.000	0.000	0.000	0.000	0.000	0.000
3 °C	0.000	1.000	0.000	0.000	0.000	0.000
6 °C	0.000	0.000	1.000	0.038	0.000	0.000
9 °C	0.000	0.000	0.038	1.000	0.000	0.000
12 °C	0.000	0.000	0.000	0.000	1.000	0.001
15 °C	0.000	0.000	0.000	0.000	0.001	1.000

Pore area significance levels (p)

Using all values

	1 °C	3 °C	6 °C	9 °C	12 °C	15 °C
1 °C	1.000	0.634	0.453	0.000	0.000	0.000
3 °C	0.634	1.000	0.386	0.000	0.000	0.000
6 °C	0.453	0.386	1.000	0.000	0.000	0.000
9 °C	0.000	0.000	0.000	1.000	0.000	0.000
12 °C	0.000	0.000	0.000	0.000	1.000	0.031
15 °C	0.000	0.000	0.000	0.000	0.031	1.000

Using the 15 largest values

	1 °C	3 °C	6 °C	9 °C	12 °C	15 °C
1 °C	1.000	0.009	0.000	0.017	0.000	0.000
3 °C	0.009	1.000	0.146	0.818	0.000	0.000
6 °C	0.000	0.146	1.000	0.092	0.010	0.003
9 °C	0.017	0.818	0.092	1.000	0.000	0.000
12 °C	0.000	0.000	0.010	0.000	1.000	0.670
15 °C	0.000	0.000	0.003	0.000	0.670	1.000

Using the 15 largest values

	1 °C	3 °C	6 °C	9 °C	12 °C	15 °C
1 °C	1.000	0.043	0.000	0.000	0.000	0.000
3 °C	0.043	1.000	0.078	0.111	0.000	0.000
6 °C	0.000	0.078	1.000	0.867	0.005	0.000
9 °C	0.000	0.111	0.867	1.000	0.003	0.000
12 °C	0.000	0.000	0.005	0.003	1.000	0.367
15 °C	0.000	0.000	0.000	0.000	0.367	1.000

Supplement 3C - Sample preparation for morphometric analyses

Bivalve shells are typically immersed in acids or oxidation agents (Dunca et al., 2009; Crippa et al., 2016; Milano et al., 2017b) to reveal microstructures and their individual constituents (i.e., BMUs), which are otherwise not distinguishable in SEM. The choice of the chemical agent, the concentration and the duration of immersion determine the degree of etching of the individual BMUs and the overall sample appearance under the SEM. For automated microstructure morphometry, an optimal preparation method should I) outline the boundaries of individual objects of interest as accurately and uniformly as possible, II) keep the topographical relief (= gray value contrast) at a minimum and III) retain the pristine shapes of the individual components to be measured.

In preparation for this study, we tested different acids (HCl, HCOOH) and oxidation agents (NaOCl, H_2O_2) in various concentrations and for various immersion times (results summarized in Fig. S3.1). Acid treatments inevitably resulted in microscale dissolution of the individual BMUs, which substantially altered their shape and generated strong topographical relief. In addition, incomplete removal of the organic matrix results only in a partial separation of adjoining BMUs. Acid-based shell preparation was therefore not suitable for automatic BMU size measurements. Weak oxidation agents (NaOCl), in contrast, did not affect the BMU morphology. However, treatment with NaOCl did not completely remove the organic matrices and, thus, did not resolve the BMU boundaries. Hydrogen peroxide turned out to be the most suitable preparation agent, because it retained the polished state of the sample surface (low topographical relief; Fig. S3.2), removed the superficial organic components thoroughly, and only slightly affected the BMU edges (Figs. 3.2-3.4 in the main text). A concentration of 10.5 % at an immersion time of 20 minutes provided the most distinct results in the studied bivalve species (*A. islandica*).

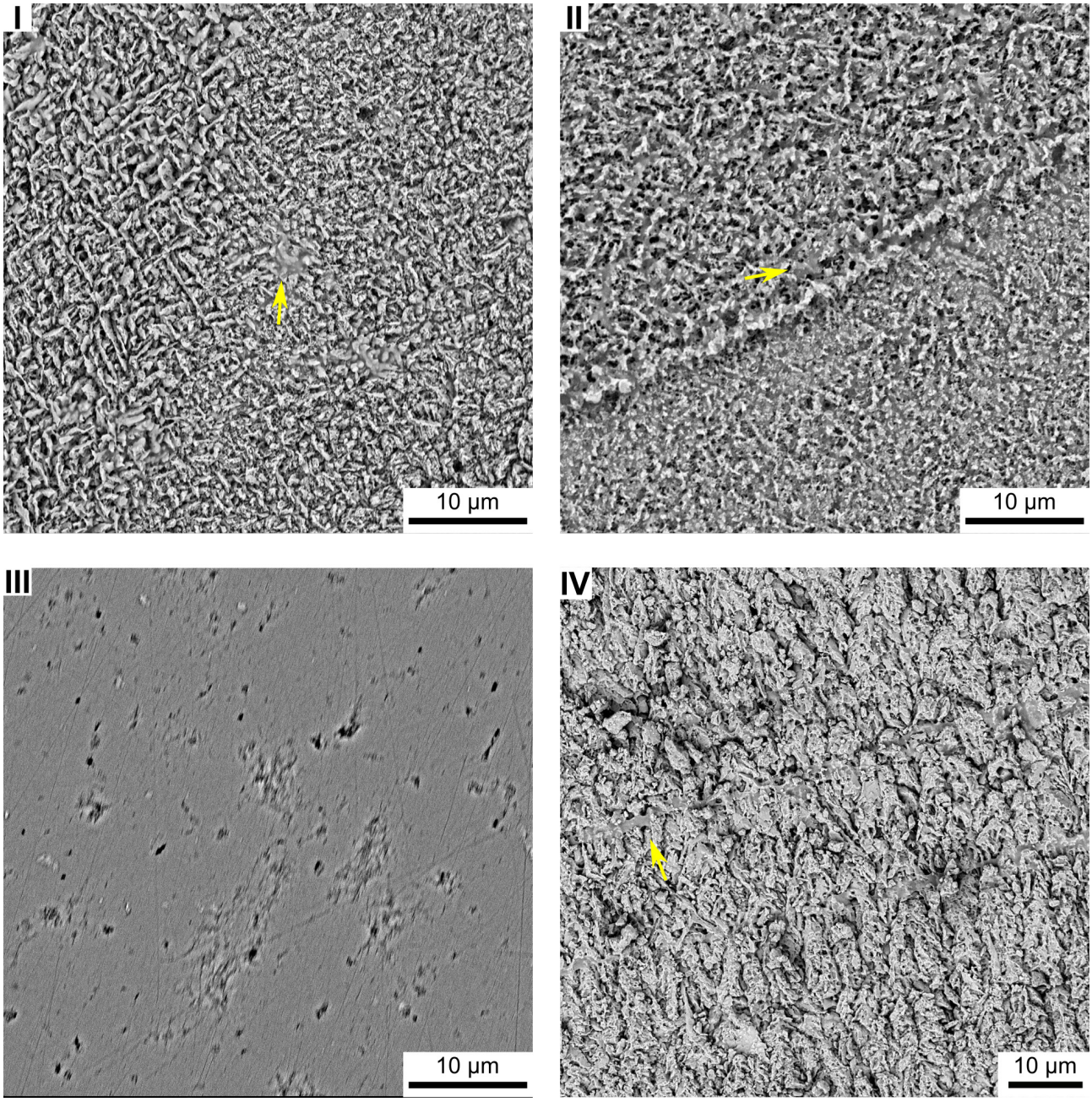

Figure S3.1 SEM micrographs of shell slabs of *A. islandica* after various chemical treatments. (I) Immersion in 8 % HCl for one second generated a strong topographical relief (= highly variable backscatter intensity) and only incompletely removed interstitial organic components (yellow arrow). (II) Treatment with weaker acids at lower concentration (0.1 % formic acid for 20 minutes) led to partial dissolution of the mineral phase and only marginally removed the organic matrices. (III) Weak oxidation agents (12 % NaOCl for 20 minutes) left the sample surface substantially unaltered. (IV) Immersion in a mixture of 1 % HCl and 5 % commercial bleach for 20 minutes carved out the biomineral morphology reasonably well, but still left behind organic inclusions. Loose mineral grains were scattered on the surface. All samples were sputter-coated with 5 nm Pt and imaged at 10 keV.

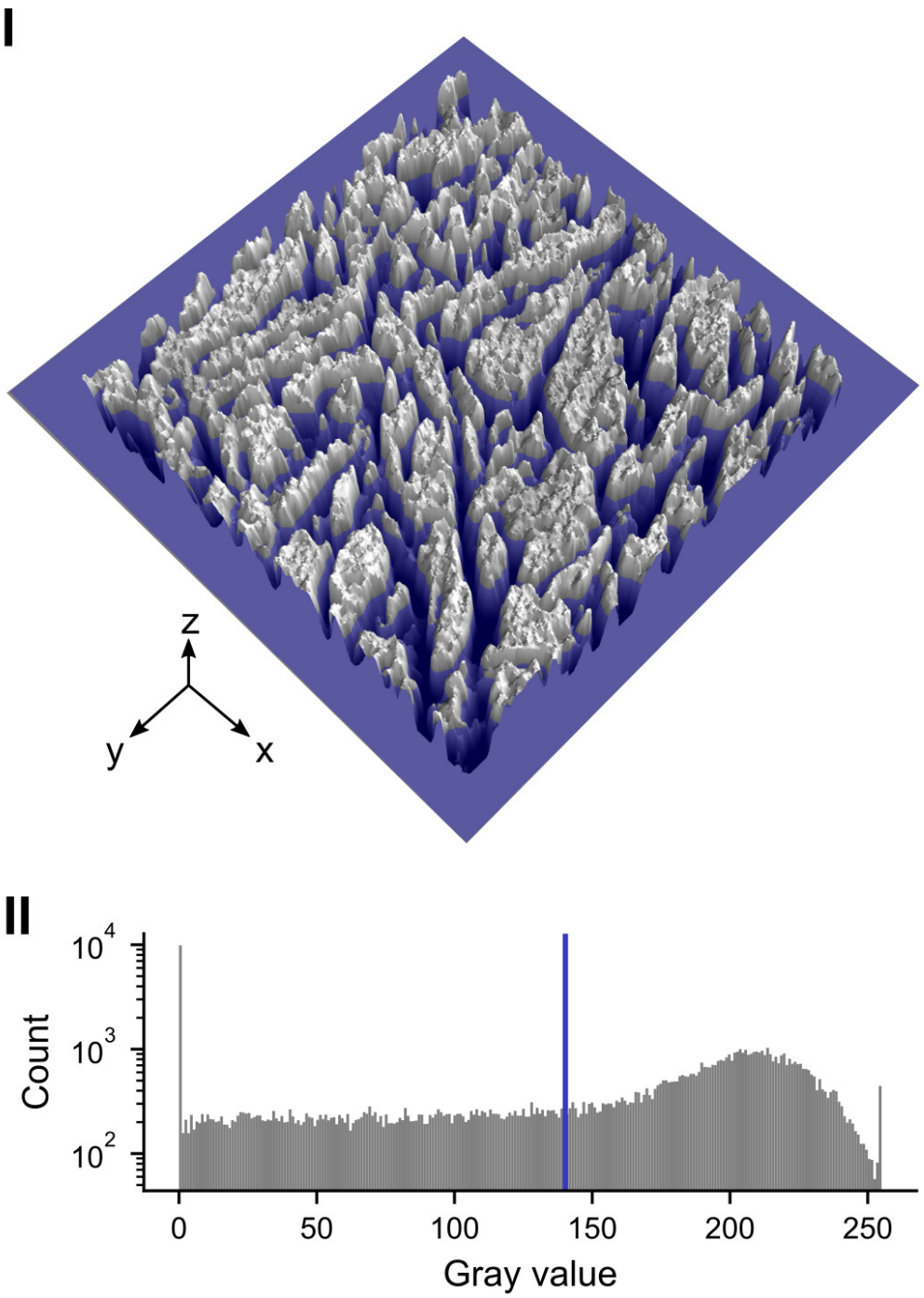

Figure S3.2 Three-dimensional visualization of a polished and oxidized shell slab surface. (I) The gray value of each pixel of a SEM image was used as a height reference. Biominerals (= bright gray values) appeared as hills, depressions and voids (= dark gray values and black) as valleys. The blue plane represents the average gray value of the image (z = 140), which was used as a threshold value to assess the spatial coverage of the mineral phase in the SEM images. Model was generated using the 3D visualizer mayavi (Ramachandran and Varoquaux, 2011). (II) Gray value histogram of the SEM image used in the 3D visualization. Threshold value for BMU coverage analysis is indicated as vertical blue line.

Supplement 3D - Statistical analyses of morphometric data

Since the temperature dependence of BMU and pore size data was most evident in the largest values of the respective datasets, small values were filtered out by applying a threshold. The suitable threshold value was determined by calculating linear regressions for increasingly larger sample sets incorporating the n largest BMU and pore size values, respectively (Fig. S3.3). The slope of regression lines for both BMU and pore size decreased with increasing sample size. Correlation coefficients (r), coefficients of determination (r^2) and standard errors of the models attained maximum values at the lowest sample sizes and asymptotically decreased with increasing n. All computed regressions (except that for n = 1) were statistically significant ($p < 0.05$). As a compromise between strong predictive power (i.e., high r, r^2) of the model and an adequate sample size, the 15 largest values of each temperature setting were incorporated in the regression analyses.

To determine which type of regression model fits the data, we calculated exponential and linear regressions for each microstructural parameter measured in the study, i.e., BMU size and coverage and pore size (Fig. S3.4). In case of BMU size and coverage, the two models exhibited only marginal differences (Fig. S3.4I+II). Hence, the more simple linear models were used for BMU size and coverage in the manuscript. In case of pore size, however, linear regressions predicted negative BMU size values for temperatures below ca. 2 °C, which is physically impossible (Figs. S3.3II, S3.4III). Use of the exponential regression model prevented this effect. In addition, the residuals of the exponential model were more randomly distributed than those of the linear model, eliminating a systematic prediction bias that otherwise would have been introduced (Fig. S3.4VI).

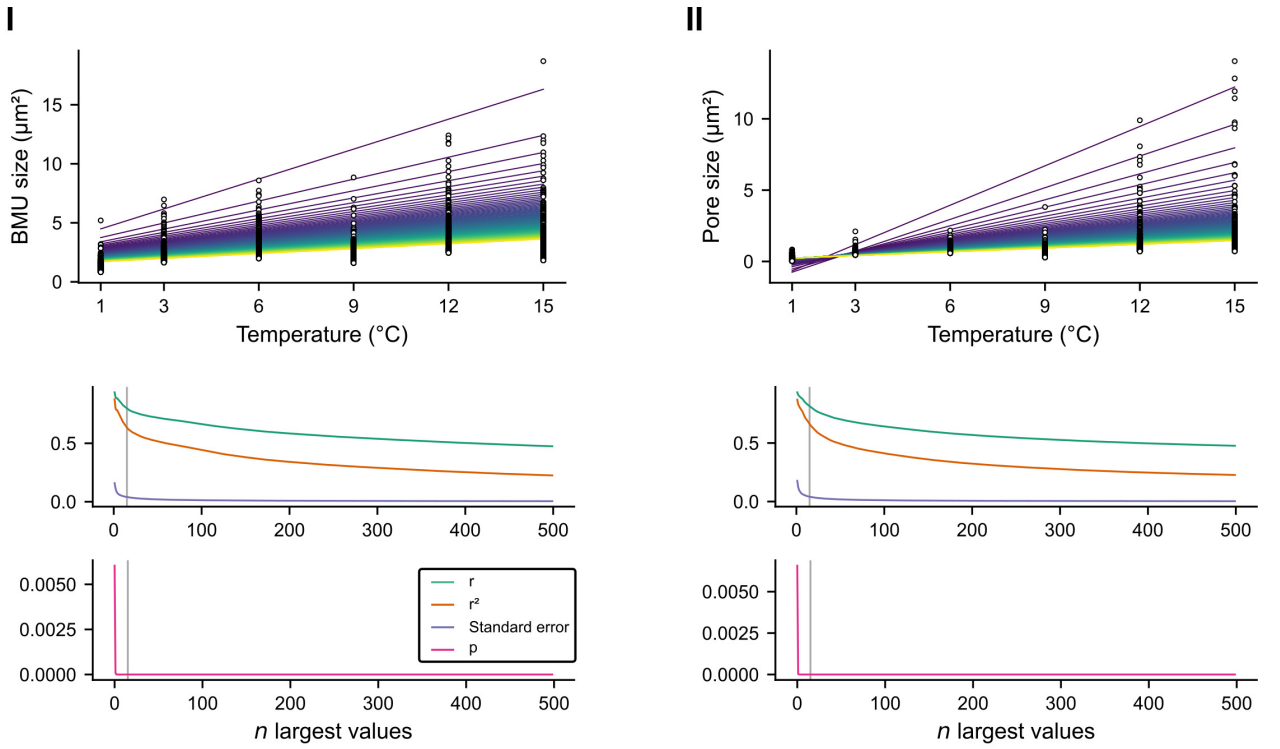

Figure S3.3 Linear models and their corresponding statistics for (I) BMU size and (II) pore size computed for different thresholds. Top row: Linear regressions were computed for the n (1–500, step size = 5) largest BMUs and pores of each temperature setting. Each line represents one regression; Line color shifts from purple to yellow with increasing n. White circles represent the 500 largest values of each temperature setting. Bottom rows: Correlation coefficients (r), coefficients of determination (r^2), standard errors and p-values for regressions computed with increasing n. Threshold used in this study (n = 15) is indicated as vertical gray line.

Supplement 3E - Evaluation of the image segmentation process

The reproducibility of machine learning–based image processing was assessed by comparing the segmentation results of four SEM images to their manually generated 'ground truth' or 'gold standard' segmentations (Fig. S3.5I-III). Of the four images, two were taken in shell portions grown under controlled temperature conditions (1 and 15 °C, 34.9 × 34.9 µm) and two images (17.45 × 17.45 µm) in shell portions grown in the Baltic Sea under natural conditions, which show CA and FCCL microstructures. The binary images resulting from manual and automated workflows were compared visually and by means of classification metrics, namely the Jaccard index (JI; Jaccard, 1912) and the variation of information (VI; Meilă, 2007). The JI represents a

similarity measure between two sets ranging from 0–100 %. The VI assesses the entropy of both under-segmentation and over-segmentation. The entropy of under-segmentation refers to the uncertainty at which BMUs were interpreted as one entity, despite representing multiple ones (false merges; x-axis in Fig. S3.5IV). Over-segmentation, in turn, describes splitting a BMU into multiple ones, despite representing a single entity in the manually generated 'ground truth' segmentation (false splits; y-axis in Fig. S3.5IV). The scale of this metric is standardized with smaller values implying better segmentation performance. Zero indicates no uncertainty and identity with the ground truth, whereas a value of 1 implies a chance of 50 % to correctly split or merge an element (= BMU) when two phases are to be considered (= BMU and inter-crystalline space).

For images of shell portions grown under controlled temperature conditions, comparisons of manual and automated image segmentations (Fig. S3.5) yielded JI values of 84.8 and 83 %, respectively. The entropy of over- and under-segmentation were relatively small (0.46–0.50 and 0.46–0.47, respectively). Comparable values were attained for automatic segmentation processes of similar studies (Höche et al., 2020; Ilett et al., 2020), demonstrating the reliability of the machine-learning based method applied here. Microstructures grown in the Baltic Sea yielded JI values of 85.7 % and 90.9 % for CA and FCCL microstructures, respectively. VI values were even lower than in the temperature-controlled portions, attaining values of 0.41 and 0.45 for CA, and 0.22 and 0.28 for FCCL, respectively (Fig. S3.5IV). These results suggest that BMUs of environmentally grown shell portions can also be faithfully determined by the automated image segmentation process. FCCL microstructures can be detected with even more confidence given their lower VI values compared to all other investigated images. This might be due to the increased co-alignment of adjoining BMUs and the increased spatial regularity.

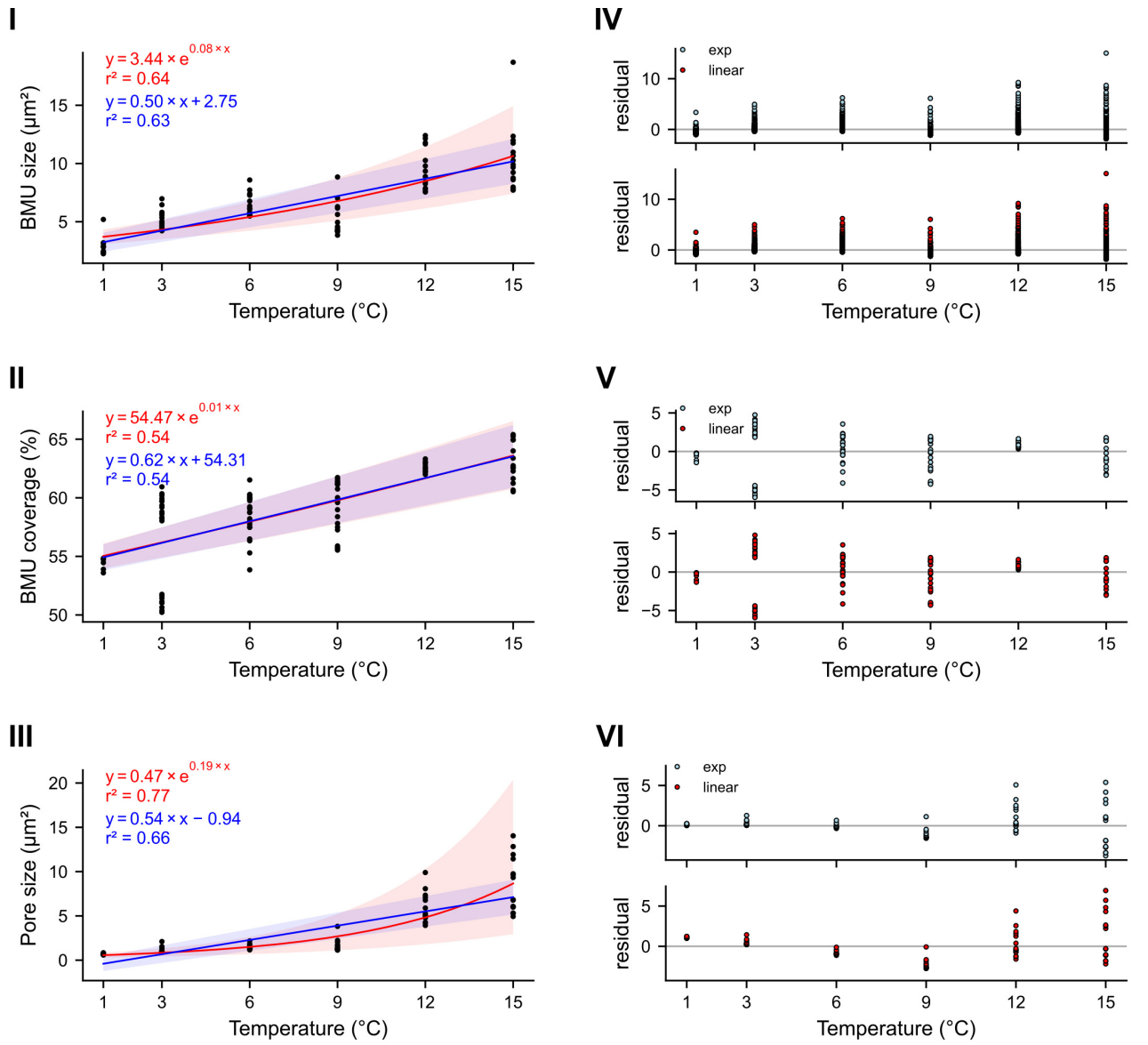

Figure S3.4 Comparison of exponential and linear models fitted to each of the measured microstructural parameters. (I-III) Exponential and linear models fitted to microstructural data. In case of the size of the 15 largest BMUs (I) and the BMU coverage (II), models exhibited a near complete overlap. In case of the size of the 15 largest pores (III), in contrast, models overlapped to a lesser degree. (IV-VI) Residuals ($y - y_{pred.}$) of the model functions presented in I-III. In the case of BMU size (IV) and coverage (V), residuals of both models were randomly distributed and showed only minor differences in their values. Residuals of pore size (VI), in contrast, displayed non-random distributions for the linear model, leading to a bias toward large pore sizes at low and high temperatures (1–3 and 12–15 °C), and toward small values in the intermediate temperature range (6–9 °C). An exponential fit successfully eliminated this effect and produced more randomly distributed residuals with a smaller average value.

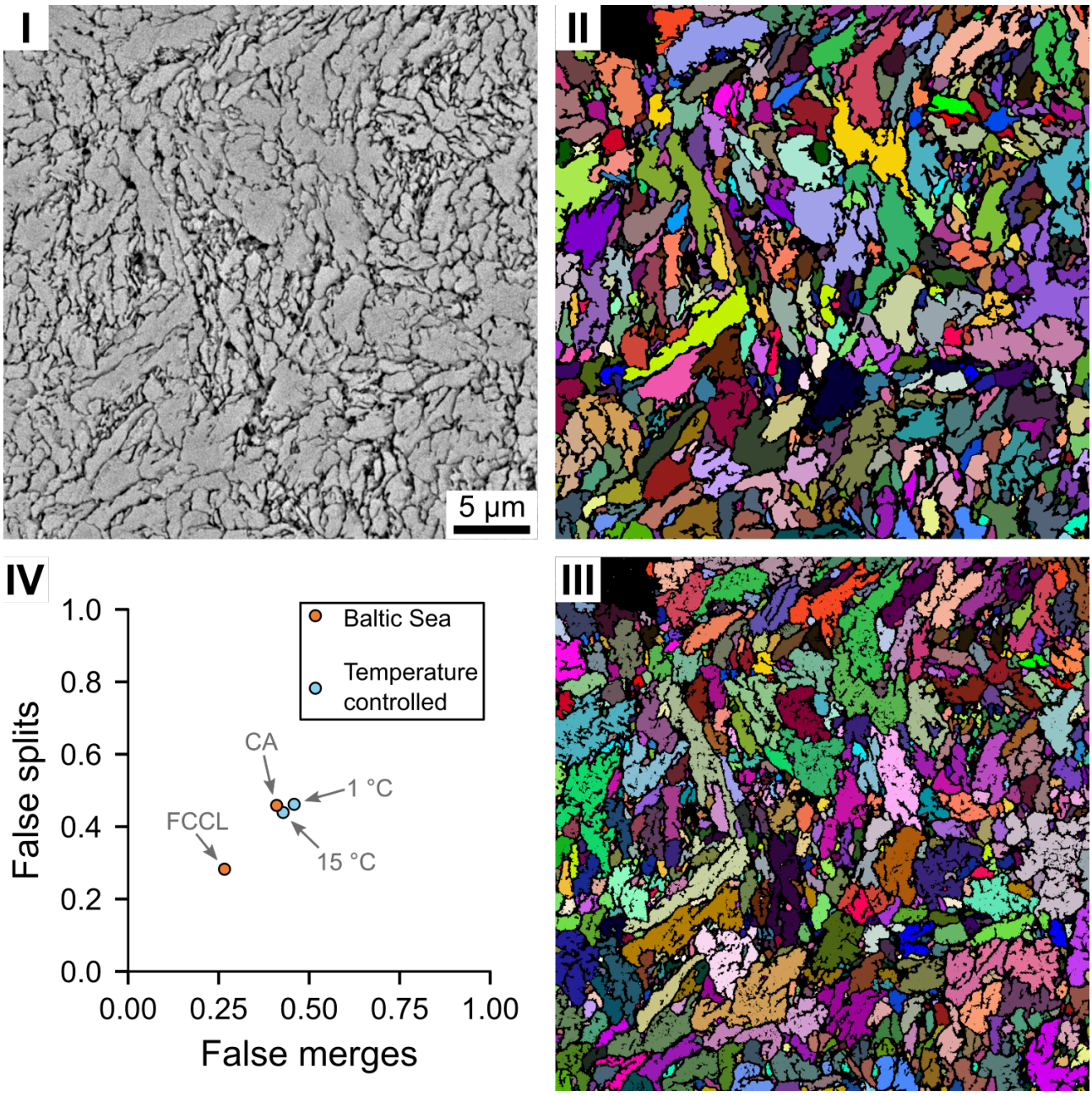

Figure S3.5 Comparison between manually and automatically segmented images. (I) SEM image of specimen Nioz-TC-15-A1R used for BMU size analysis. (II) Manual segmentation ('ground truth') of the SEM image. Individual BMUs are displayed in various colors. (III) Machine learning–based segmentation as used in the study. (IV) Plot of the VI (Meilă, 2007). The x-axis represents the entropy of false merges, whereas the y-axis represents the entropy of false splits. Smaller values imply less uncertainty, i.e., better segmentation performance (0 = identical to the 'ground truth').

References

Agbaje, O. B. A., Thomas, D. E., Dominguez, J. G., McInerney, B. V., Kosnik, M. A., and Jacob, D. E., 2019. Biomacromolecules in bivalve shells with crossed lamellar architecture. J. Mater. Sci. 54, 4952–4969.

Agbaje, O. B. A., Thomas, D. E., McInerney, B. V., Molloy, M. P., and Jacob, D. E., 2017a. Organic macromolecules in shells of *Arctica islandica*: comparison with nacroprismatic bivalve shells. Mar. Biol. 164, 208.

Asami, R., Yoshimura, N., Toriyabe, H., Minei, S., Shinjo, R., Hongo, C., Sakamaki, T., and Fujita, K., 2020. High-resolution evidence for Middle Holocene East Asian winter and summer monsoon variations: snapshots of fossil coral records. Geophys. Res. Lett. 47, e2020GL088509.

Ballesta-Artero, I., Janssen, R., van der Meer, J., and Witbaard, R., 2018a. Interactive effects of temperature and food availability on the growth of *Arctica islandica* (Bivalvia) juveniles. Mar. Environ. Res. 133, 67–77.

Barbin, V., Ramseyer, K., and Elfman, M., 2008. Biological record of added manganese in seawater: a new efficient tool to mark in vivo growth lines in the oyster species *Crassostrea gigas*. Int. J. Earth Sci. 97, 193–199.

Berg, S., Kutra, D., Kroeger, T., Straehle, C. N., Kausler, B. X., Haubold, C., Schiegg, M., Ales, J., Beier, T., Rudy, M., Eren, K., Cervantes, J. I., Xu, B., Beuttenmueller, F., Wolny, A., Zhang, C., Koethe, U., Hamprecht, F. A., and Kreshuk, A., 2019. ilastik: interactive machine learning for (bio)image analysis. Nat. Methods 16, 1226–1232.

Bevelander, G. and Nakahara, H., 1980. Compartment and envelope formation in the process of biological mineralization. In: The mechanisms of biomineralization in animals and plants. Ed. by M. Ōmori and N. Watabe. Tokai University Press, 19–27.

Böhm, C. F., Demmert, B., Harris, J., Fey, T., Marin, F., and Wolf, S. E., 2016. Structural commonalities and deviations in the hierarchical organization of crossed-lamellar shells: a case study on the shell of the bivalve *Glycymeris glycymeris*. J. Mater. Res. 31, 536–546.

Bonsdorff, E., 2006. Zoobenthic diversity-gradients in the Baltic Sea: Continuous post-glacial succession in a stressed ecosystem. J. Exp. Mar. Biol. Ecol. A Tribute to Richard M. Warwick 330, 383–391.

Brand, U. and Morrison, J. O., 1987. Paleoscene #6. Biogeochemistry of fossil marine-invertebrates. Geosci. Can. 14, 85–107.

Branson, O., Fehrenbacher, J. S., Vetter, L., Sadekov, A. Y., Eggins, S. M., and Spero, H. J., 2019. LAtools: A data analysis package for the reproducible reduction of LA-ICPMS data. Chem. Geol. 504, 83–95.

Butler, P. G., Richardson, C. A., Scourse, J. D., Wanamaker, A. D., Shammon, T. M., and Bennell, J. D., 2010. Marine climate in the Irish Sea: analysis of a 489-year marine master chronology derived from growth increments in the shell of the clam *Arctica islandica*. Quat. Sci. Rev. 29, 1614–1632.

Butler, P. G., Wanamaker, A. D., Scourse, J. D., Richardson, C. A., and Reynolds, D. J., 2013. Variability of marine climate on the North Icelandic Shelf in a 1357-year proxy archive based on growth increments in the bivalve *Arctica islandica*. Palaeogeogr. Palaeoclimatol. Palaeoecol. Unraveling environmental histories from skeletal diaries - advances in sclerochronology 373, 141–151.

Carré, M., Bentaleb, I., Bruguier, O., Ordinola, E., Barrett, N. T., and Fontugne, M., 2006. Calcification rate influence on trace element concentrations in aragonitic bivalve shells: evidences and mechanisms. Geochim. Cosmochim. Acta 70, 4906–4920.

Carstensen, J., Conley, D. J., Bonsdorff, E., Gustafsson, B. G., Hietanen, S., Janas, U., Jilbert, T., Maximov, A., Norkko, A., and Norkko, J., 2014. Hypoxia in the Baltic Sea: biogeochemical cycles, benthic fauna, and management. Ambio 43, 26–36.

Carter, J. G., Harries, P. J., Malchus, N., Sartori, A. F., Anderson, L. C., Bieler, R., Bogan, A. E., Coan, E. V., Cope, J. C. W., Cragg, S. M., García-March, J. R., Hylleberg, J., Kelley, P., Kleemann, K., Kříž, J., McRoberts, C. A., Mikkelsen, P. M., Pojeta Jr., J., Tëmkin, I., Yancey, T., and Zieritz, A.,

2012. Part N: Illustrated glossary of the Bivalvia. In: Treatise on Invertebrate Paleontology no. 48, Revised. Vol. 1. Chapter 31. Kansas: University of Kansas, 1–209.

Carter, J. G., 1990. Skeletal biomineralization: patterns, processes, and evolutionary trends. Vol. 1. New York: Van Nostrand Reinhold. 2 pp.

Casella, L. A., He, S., Griesshaber, E., Fernández-Díaz, L., Harper, E. M., Jackson, D. J., Ziegler, A., Mavromatis, V., Dietzel, M., Eisenhauer, A., Brand, U., and Schmahl, W. W., 2018. Assessment of hydrothermal alteration on micro- and nanostructures of biocarbonates: quantitative statistical grain-area analysis of diagenetic overprint. Biogeosciences Discuss.

Cauquoin, A., Werner, M., and Lohmann, G., 2019. Water isotopes - climate relationships for the mid-Holocene and preindustrial period simulated with an isotope-enabled version of MPI-ESM. Clim. Past 15, 1913–1937.

Clark, G. R., 1968. Mollusk shell: daily growth lines. Science 161, 800–802.

Conley, D. J., Carstensen, J., Aigars, J., Axe, P., Bonsdorff, E., Eremina, T., Haahti, B.-M., Humborg, C., Jonsson, P., Kotta, J., Lännegren, C., Larsson, U., Maximov, A., Medina, M. R., Lysiak-Pastuszak, E., Remeikaitė-Nikienė, N., Walve, J., Wilhelms, S., and Zillén, L., 2011. Hypoxia is increasing in the coastal zone of the Baltic Sea. Environ. Sci. Technol. 45, 6777–6783.

Crippa, G., Ye, F., Malinverno, C., and Rizzi, A., 2016. Which is the best method to prepare invertebrate shells for SEM analysis? Testing different techniques on recent and fossil brachiopods. Boll. Della Soc. Paleontol. Ital. 55, 111–125.

Cuif, J.-P., Dauphin, Y., Luquet, G., Medjoubi, K., Somogyi, A., and Perez-Huerta, A., 2018. Revisiting the organic template model through the microstructural study of shell development in *Pinctada margaritifera*, the Polynesian Pearl Oyster. Minerals 8, 370.

De Winter, N., Müller, I., Kocken, I., Thibault, N., Ullmann, C. V., Farnsworth, A., Lunt, D., Claeys, P., and Ziegler, M., 2020. First absolute seasonal temperature estimates for greenhouse climate from clumped isotopes in bivalve shells. [Preprint].

Dunca, E., Mutvei, H., Goransson, P., Morth, C.-M., Schone, B. R., Whitehouse, M. J., Elfman, M., and Baden, S. P., 2009. Using ocean quahog (*Arctica islandica*) shells to reconstruct palaeoenvironment in Öresund, Kattegat and Skagerrak, Sweden. Int. J. Earth Sci. 15.

Ehrenbaum, E., 1884. Untersuchungen über die Struktur und Bildung der Schale der in der Kieler Bucht häufig vorkommenden Muscheln. PhD thesis. Kiel, Germany: Kiel University.

Eiler, J. M., 2011. Paleoclimate reconstruction using carbonate clumped isotope thermometry. Quat. Sci. Rev. 30, 3575–3588.

Faÿ-Gomord, O., Soete, J., Davy, C. A., Janssens, N., Troadec, D., Cazaux, F., Caline, B., and Swennen, R., 2017. Tight chalk: characterization of the 3D pore network by FIB-SEM, towards the understanding of fluid transport. J. Pet. Sci. Eng. 156, 67–74.

Featherstone, A. M., Butler, P. G., Schöne, B. R., Peharda, M., and Thébault, J., 2019. A 45-year subannual reconstruction of seawater temperature in the Bay of Brest, France, using the shell oxygen isotope composition of the bivalve *Glycymeris glycymeris*. The Holocene, 1–10.

Fiebig, J., Bajnai, D., Löffler, N., Methner, K., Krsnik, E., Mulch, A., and Hofmann, S., 2019. Combined high-precision 48 and 47 analysis of carbonates. Chem. Geol. 522, 186–191.

Füllenbach, C. S., Schoene, B. R., Shirai, K., Takahata, N., Ishida, A., and Sano, Y., 2017. Minute co-variations of Sr/Ca ratios and microstructures in the aragonitic shell of *Cerastoderma edule* (Bivalvia) - Are geochemical variations at the ultra-scale masking potential environmental signals? Geochim. Cosmochim. Acta 205, 256–271.

Füllenbach, C. S., Schöne, B. R., and Branscheid, R., 2014. Microstructures in shells of the freshwater gastropod *Viviparus viviparus*: A potential sensor for temperature change? Acta Biomater. 10, 3911–3921.

Füllenbach, C. S., Schöne, B. R., and Mertz-Kraus, R., 2015. Strontium/lithium ratio in aragonitic shells of *Cerastoderma edule* (Bivalvia) — A new potential temperature proxy for brackish environments. Chem. Geol. 417, 341–355.

Geurts, P., Irrthum, A., and Wehenkel, L., 2009. Supervised learning with decision tree-based methods in computational and systems biology. Mol. Biosyst. 5, 1593–1605.

Gilbert, P. U., Bergmann, K. D., Myers, C. E., Marcus, M. A., DeVol, R. T., Sun, C.-Y., Blonsky, A. Z., Tamre, E., Zhao, J., Karan, E. A., Tamura, N., Lemer, S., Giuffre, A. J., Giribet, G., Eiler, J. M., and Knoll, A. H., 2017. Nacre tablet thickness records formation temperature in modern and fossil shells. Earth Planet. Sci. Lett. 460, 281–292.

Gillooly, J. F., Brown, J. H., West, G. B., Savage, V. M., and Charnov, E. L., 2001. Effects of size and temperature on metabolic rate. Science 293, 2248–2251.

Goldstein, J. I., Newbury, D. E., Michael, J. R., Ritchie, N. W., Scott, J. H. J., and Joy, D. C., 2017. Scanning electron microscopy and x-ray microanalysis. New York, USA: Springer.

Gotliv, B.-A., Addadi, L., and Weiner, S., 2003. Mollusk shell acidic proteins: in search of individual functions. ChemBioChem 4, 522–529.

Grefsrud, E. S., Dauphin, Y., Cuif, J.-P., Denis, A., and Strand, Ø., 2008. Modifications in microstructure of cultured and wild scallop shells (*Pecten maximus*). J. Shellfish Res. 27, 633–641.

Hansson, D. and Gustafsson, E., 2011. Salinity and hypoxia in the Baltic Sea since A.D. 1500. J. Geophys. Res. Oceans 116, C03027.

Höche, N., Peharda, M., Walliser, E. O., and Schöne, B. R., 2020. Morphological variations of crossed-lamellar ultrastructures of *Glycymeris bimaculata* (Bivalvia) serve as a marine temperature proxy. Estuar. Coast. Shelf Sci. 237, 106658.

Höche, N., Walliser, E. O., Winter, N. J. de, Witbaard, R., and Schöne, B. R., 2021b. Temperature-induced microstructural changes in shells of laboratory-grown *Arctica islandica* (Bivalvia). PLOS ONE 16, e0247968.

Ilett, M., Wills, J., Rees, P., Sharma, S., Micklethwaite, S., Brown, A., Brydson, R., and Hondow, N., 2020. Application of automated electron microscopy imaging and machine learning to characterise and quantify nanoparticle dispersion in aqueous media. J. Microsc. 279, 177–184.

Jaccard, P., 1912. The distribution of the flora in the alpine zone. New Phytol. 11, 37–50.

Jacob, A., Peltz, M., Hale, S., Enzmann, F., Moravcova, O., Warr, L. N., Grathoff, G., Blum, P., and Kersten, M., 2020. Simulating permeability reduction by clay mineral nanopores in a tight sandstone by combining μXCT and FIB-SEM imaging. Solid Earth Discuss. 1–28.

Jeffree, R. A., Markich, S. J., Lefebvre, F., Thellier, M., and Ripoll, C., 1995. Shell microlaminations of the freshwater bivalve *Hyridella depressa* as an archival monitor of manganese water concentration: experimental investigation by depth profiling using secondary ion mass spectrometry (SIMS). Experientia 51, 838–848.

Jochum, K. P., Nohl, U., Herwig, K., Lammel, E., Stoll, B., and Hoffmann, A., 2007. GeoReM: A new geochemical database for reference materials and isotopic standards. Geostand. Geoanalytical Res. 29, 333–338.

Jochum, K. P., Weis, U., Stoll, B., Kuzmin, D., Yang, Q., Raczek, I., Jacob, D. E., Stracke, A., Birbaum, K., Frick, D. A., Günther, D., and Enzweiler, J., 2011. Determination of reference values for NIST SRM 610–617 glasses following ISO guidelines. Geostand. geoanal. res. 35, 397–429.

Justine, D., Gwénaëlle, C., Pierre, P., Pascal, L., André, P., Laurent, C., Philippe, A., and Julien, T., 2020. Assessment of Ba/Ca in *Arctica islandica* shells as a proxy for phytoplankton dynamics in the Northwestern Atlantic Ocean. Estuar. Coast. Shelf Sci. 237, 106628.

Karney, G. B., Butler, P. G., Scourse, J. D., Richardson, C. A., Lau, K. H., Czernuszka, J. T., and Grovenor, C. R. M., 2011. Identification of growth increments in the shell of the bivalve mollusc *Arctica islandica* using backscattered electron imaging. J. Microsc.. 241, 29–36.

Karney, G. B., Butler, P. G., Speller, S., Scourse, J. D., Richardson, C. A., Schröder, M., Hughes, G. M., Czernuszka, J. T., and Grovenor, C. R. M., 2012. Characterizing the microstructure of *Arctica islandica* shells using NanoSIMS and EBSD. Geochem. Geophys. Geosystems 13, Q04002.

Krause-Nehring, J., Klügel, A., Nehrke, G., Brellochs, B., and Brey, T., 2011. Impact of sample pretreatment on the measured element concentrations in the bivalve *Arctica islandica*. Geochem. Geophys. Geosystems 12.

Kremling, K., 1983. The behavior of Zn, Cd, Cu, Ni, Co, Fe, and Mn in anoxic Baltic waters. Mar. Chem. 13, 87–108.

Kremling, K. and Petersen, H., 1978. The distribution of Mn, Fe, Zn, Cd and Cu in Baltic seawater; a study on the basis of one anchor station. Mar. Chem. 6, 155–170.

Lei, L., Seol, Y., and Jarvis, K., 2018. Pore-scale visualization of methane hydrate-bearing sediments with micro-CT. Geophys. Res. Lett. 45, 5417–5426.

Levi-Kalisman, Y., Falini, G., Addadi, L., and Weiner, S., 2001. Structure of the nacreous organic matrix of a bivalve mollusk shell examined in the hydrated state using cryo-TEM. J. Struct. Biol. 135, 8–17.

Liehr, G. A., Zettler, M. L., Leipe, T., and Witt, G., 2005. The ocean quahog *Arctica islandica* L.: a bioindicator for contaminated sediments. Mar. Biol. 147, 671–679.

Lohmann, G. and Schöne, B. R., 2013. Climate signatures on decadal to interdecadal time scales as obtained from mollusk shells (*Arctica islandica*) from Iceland. Palaeogeography, Palaeoclimatology, Palaeoecology. Unraveling environmental histories from skeletal diaries - advances in sclerochronology 373, 152–162.

Malchus, N., 2010. Shell tubules in Condylocardiinae (Bivalvia: Carditoidea). J. Molluscan Stud. 76, 401–403.

Marin, F., Le Roy, N., and Marie, B., 2012. The formation and mineralization of mollusk shell. Front. Biosci. S4, 1099–1125.

Markich, S. J., Jeffree, R. A., and Burke, P. T., 2002. Freshwater bivalve shells as archival indicators of metal pollution from a copper–uranium mine in tropical Northern Australia. Environ. Sci. Technol. 36, 821–832.

Meilă, M., 2007. Comparing clusterings—an information based distance. Journal of Multivariate Analysis 98, 873–895.

Mejri, W., Korchef, A., Tlili, M., and Amor, M. B., 2014. Effects of temperature on precipitation kinetics and microstructure of calcium carbonate in the presence of magnesium and sulphate ions. Desalination Water Treat. 52, 4863–4870.

Milano, S., Nehrke, G., Wanamaker, A. D., Ballesta-Artero, I., Brey, T., and Schöne, B. R., 2017a. The effects of environment on *Arctica islandica* shell formation and architecture. Biogeosciences 14, 1577–1591.

Milano, S., Schöne, B. R., Wang, S., and Müller, W. E., 2016. Impact of high pCO2 on shell structure of the bivalve *Cerastoderma edule*. Mar. Environ. Res. 119, 144–155.

Milano, S., Schöne, B. R., and Witbaard, R., 2017b. Changes of shell microstructural characteristics of *Cerastoderma edule* (Bivalvia) — A novel proxy for water temperature. Palaeogeogr. Palaeoclimatol. Palaeoecol. 465, 395–406.

Morrison, J. and Brand, U., 1988. An evaluation of diagenesis and chemostratigraphy of upper cretaceous molluscs from the Canadian Interior Seaway. Chem. Geol.: Iso. Geosc. sec. 72, 235–248.

Nishida, K., Ishimura, T., Suzuki, A., and Sasaki, T., 2012. Seasonal changes in the shell microstructure of the bloody clam, *Scapharca broughtonii* (Mollusca: Bivalvia: Arcidae). Palaeogeogr. Palaeoclimatol. Palaeoecol. 363–364, 99–108.

Nishida, K., Nakashima, R., Majima, R., and Hikida, Y., 2011. Ontogenetic changes in shell microstructures in the cold seep-associated bivalve, *Conchocele bisecta* (Bivalvia: Thyasiridae). Paleontol. Res. 15, 193–212.

Olson, I. C., Kozdon, R., Valley, J. W., and Gilbert, P. U. P. A., 2012. Mollusk shell nacre ultrastructure correlates with environmental temperature and pressure. J. Am. Chem. Soc. 134, 7351–7358.

Palmer, A. R., 1983. Relative cost of producing skeletal organic matrix versus calcification: evidence from marine gastropods. Mar. Biol. 75, 287–292.

Palmer, R. E., 1980. Observations on shell deformities, ultrastructure, and increment formation in the Bay scallop *Argopecten irradians*. Mar. Biol. 58, 15–23.

Penkman, K. E. H., Kaufman, D. S., Maddy, D., and Collins, M. J., 2008. Closed-system behaviour of the intra-crystalline fraction of amino acids in mollusc shells. Quat. Geochronol. 3, 2–25.

Pitts, L. C. and Wallace, G. T., 1994. Lead deposition in the shell of the bivalve, *Mya arenaria*: an indicator of dissolved lead in seawater. Estuar. Coast. Shelf Sci. 39, 93–104.

Price, G. D. and Pearce, N. J. G., 1997. Biomonitoring of pollution by *Cerastoderma edule* from the British Isles: a laser ablation ICP-MS study. Mar. Pollut. Bull. 34, 1025–1031.

Ramachandran, P. and Varoquaux, G., 2011. Mayavi: 3D visualization of scientific data. Comput. Sci. Eng. 13, 40–51.

Reynolds, D. J., Butler, P., Williams, S., Scourse, J., Richardson, C., Wanamaker, A., Austin, W., Cage, A., and Sayer, M., 2013. A multiproxy reconstruction of Hebridean (NW Scotland) spring sea surface temperatures between AD 1805 and 2010. Palaeogeogr. Palaeoclimatol. Palaeoecol. 386, 275–285.

Ropes, J. W., Jones, D., Murawski, S., Serchuk, F., and Jearld, A., 1984a. Documentation of annual growth lines in ocean quahogs, *Arctica islandica* Linné. Fish. Bull. 82, 1–19.

Ropes, J. W., Murawski, S., and Serchuk, F., 1984b. Size, age, sexual maturity, and sex-ratio in Ocean Quahogs, *Arctica Islandica* Linne, Off Long-Island, New-York. Fish. Bull. 82, 253–267.

Rueden, C. T., Schindelin, J., Hiner, M. C., DeZonia, B. E., Walter, A. E., Arena, E. T., and Eliceiri, K. W., 2017. ImageJ2: ImageJ for the next generation of scientific image data. BMC Bioinformatics 18, 529.

Sato, S. and Chiba, T., 2016. Structural changes in molluscan community over a 15-year period before and after the 2011 Great East Japan Earthquake and subsequent tsunami around Matsushima Bay, Miyagi Prefecture, Northeastern Japan. PLOS ONE 11, e0168206.

Schindelin, J., Rueden, C. T., Hiner, M. C., and Eliceiri, K. W., 2015. The ImageJ ecosystem: An open platform for biomedical image analysis. Mol. Reprod. Dev. 82, 518–529.

Schmidt, G. A., Annan, J. D., Bartlein, P. J., Cook, B. I., Guilyardi, E., Hargreaves, J. C., Harrison, S. P., Kageyama, M., LeGrande, A. N., Konecky, B., Lovejoy, S., Mann, M. E., Masson-Delmotte, V., Risi, C., Thompson, D., Timmermann, A., Tremblay, L.-B., and Yiou, P., 2014. Using palaeoclimate comparisons to constrain future projections in CMIP5. Clim. Past 10, 221–250.

Schneider, C. A., Rasband, W. S., and Eliceiri, K. W., 2012. NIH Image to ImageJ: 25 years of image analysis. Nat. Meth. 9, 671–675.

Schöne, B. R., 2013. *Arctica islandica* (Bivalvia): A unique paleoenvironmental archive of the northern North Atlantic Ocean. Glob. Planet. Change 111, 199–225.

Schöne, B. R., Dunca, E., Fiebig, J., and Pfeiffer, M., 2005a. Mutvei's solution: An ideal agent for resolving microgrowth structures of biogenic carbonates. Palaeogeogr. Palaeoclimatol. Palaeoecol. 228, 149–166.

Schöne, B. R., Freyre Castro, A. D., Fiebig, J., Houk, S. D., Oschmann, W., and Kröncke, I., 2004. Sea surface water temperatures over the period 1884–1983 reconstructed from oxygen isotope ratios of a bivalve mollusk shell (*Arctica islandica*, southern North Sea). Paleogeogr. Paleoclimatol. Paleoecol. 212, 215–232.

Schöne, B. R., Radermacher, P., Zhang, Z., and Jacob, D. E., 2013. Crystal fabrics and element impurities (Sr/Ca, Mg/Ca, and Ba/Ca) in shells of *Arctica islandica*—Implications for paleoclimate reconstructions. Palaeogeogr. Palaeoclimatol. Palaeoecol. Unraveling environmental histories from skeletal diaries - advances in sclerochronology 373, 50–59.

Shibata, M., 1979. Tubules found in the arcoid shell. Venus Jpn. J. Malacol. 38, 48–60.

Shirai, K., Schöne, B. R., Miyaji, T., Radarmacher, P., Krause, R. A., and Tanabe, K., 2014. Assessment of the mechanism of elemental incorporation into bivalve shells (*Arctica islandica*) based on elemental distribution at the microstructural scale. Geochim. Cosmochim. Acta 126, 307–320.

Soreghan, M. J. and Francus, P., 2004. Processing backscattered electron digital images of thin section. In: Image analysis, sediments and paleoenvironments. Ed. by P. Francus. Developments in paleoenvironmental research. Dordrecht: Springer Netherlands, 203–225.

Tan Tiu, A., 1988. Temporal and spatial variation of shell microstructure of *Polydesmoda carolini-ana* (Bivalvia: Heterodonta). Am. Malacol. Bull. 6, 199–206.

Tan Tiu, A. and Prezant, R. S., 1989. Temporal variation in microstructure of the inner shell surface of *Corbicula fluminea* (Bivalvia: Heterodonta). Am. Malacol. Bull. 7, 65–71.

Trofimova, T., Milano, S., Andersson, C., Bonitz, F. G. W., and Schoene, B. R., 2018. Oxygen isotope composition of *Arctica islandica* aragonite in the context of shell architectural organization: Implications for paleoclimate reconstructions. Geochem. Geophys. Geosyst. 19, 453–470.

Van de Velde, S. J., Hylen, A., Kononets, M., Marzocchi, U., Leermakers, M., Choumiline, K., Hall, P. O. J., and Meysman, F. J. R., 2020. Elevated sedimentary removal of Fe, Mn, and trace elements following a transient oxygenation event in the Eastern Gotland Basin, central Baltic Sea. Geochim. Cosmochim. Acta 271, 16–32.

Von Leesen, G., Beierlein, L., Scarponi, D., Schöne, B. R., and Brey, T., 2017. A low seasonality scenario in the Mediterranean Sea during the Calabrian (Early Pleistocene) inferred from fossil *Arctica islandica* shells. Palaeogeography, Palaeoclimatology, Palaeoecology 485, 706–714.

Waller, T. R., 1980. Scanning electron microscopy of shell and mantle in the order Arcoida (Mollusca: Bivalvia). Smithson. Contrib. Zool. 1–58.

Walliser, E. O., Lohmann, G., Niezgodzki, I., Tütken, T., and Schöne, B. R., 2016. Response of Central European SST to atmospheric pCO_2 forcing during the Oligocene – A combined proxy data and numerical climate model approach. Palaeogeogr. Palaeoclimatol. Palaeoecol. 459, 552–569.

Wanamaker, A. D. and Gillikin, D. P., 2019. Strontium, magnesium, and barium incorporation in aragonitic shells of juvenile *Arctica islandica*: Insights from temperature controlled experiments. Chem. Geol. Chemical sclerochronology 526, 117–129.

Wanamaker, A. D., Kreutz, K. J., Schöne, B. R., Maasch, K. A., Pershing, A. J., Borns, H. W., Introne, D. S., and Feindel, S., 2009. A late Holocene paleo-productivity record in the western Gulf of Maine, USA, inferred from growth histories of the long-lived ocean quahog (*Arctica islandica*). Int. J. Earth Sci. 98, 19.

Winter, J. E., 1969. Über den Einfluß der Nahrungskonzentration und anderer Faktoren auf Filtrierleistung und Nahrungsausnutzung der Muscheln *Arctica islandica* und *Modiolus modiolus*. Mar. Biol. 4, 87–135.

Witbaard, R., Franken, R., and Visser, B., 1997. Growth of juvenile *Arctica islandica* under experimental conditions. Helgoländer Meeresunters. 51, 417–431.

Xiang, L., Kong, W., Su, J., Liang, J., Zhang, G., Xie, L., and Zhang, R., 2014. Amorphous calcium carbonate precipitation by cellular biomineralization in mantle cell cultures of *Pinctada fucata*. PLOS ONE 9, e113150.

4 Microstructural mapping of *Arctica islandica* shells reveals environmental and physiological controls on biomineral size

Nils Höche[1], Eric O. Walliser[1,2], Bernd R. Schöne[1]

1. *Johannes Gutenberg-University, Mainz, Germany*
2. *Museum Wiesbaden, Hessisches Museum für Kunst und Natur, Wiesbaden, Germany*

N. Höche, E. O. Walliser, and B. R. Schöne, 2022. Microstructural mapping of *Arctica islandica* shells reveals environmental and physiological controls on biomineral size. Front. Earth Sci. 9

In this chapter, naturally-grown *Arcitca islandica* shells collected from different habitats were examined in order to assess the precision and reliability at which temperature information can be obtained using microstructural properties of the shells. While a clear influence of temperature on the microstructure of the shells was visible in fully marine habitats, the temperature signal can easily be obscured by physiologically-induced microstructural changes if the animal

is exposed to unfavorable growth conditions such as low and variable salinity or low dissolved oxygen content. This manuscript was published in the journal "Frontiers in Earth Science - Quaternary Science, Geomorphology and Paleoenvironment". My contributions were in conceptualization, data curation, formal analysis, investigation, methodology, validation, visualization, writing-original draft and writing-review and editing. Funding for this study was supplied by a DFG grant to BRS [SCHO793/20-1].

Author contributions:

NH Conceptualization, Data Curation, Formal analysis, Investigation, Methodology, Validation, Visualization, Writing-original draft, Writing-review and editing.

EOW Formal analysis, Investigation, Supervision, Validation, Writing-review and editing.

BRS Conceptualization, Funding acquisition, Investigation, Project administration, Resources, Supervision, Validation, Writing-original draft, Writing-review and editing.

Abstract

The shells of long-lived bivalves record environmental variability in their geochemical signatures and are thus used extensively in marine high-resolution paleoclimate studies. To possibly overcome the limitations of the commonly employed temperature proxy, the $\delta^{18}O_{shell}$ value, which requires knowledge of the seawater $\delta^{18}O$ signature and is prone to diagenetic overprint, the shell microstructures and the morphological properties of individual biomineral units (BMUs) recently attracted research interest as an alternative paleoclimate proxy. In shells of *Arctica islandica*, one of the most extensively used and best studied sclerochronological archives, the size of the BMUs increases in warmer temperatures under laboratory circumstances. This study assesses whether this relationship persists under natural growth conditions or whether additional environmental and physiological factors control the BMU size and bias temperature reconstructions. For this purpose, shells from the surface waters of NE Iceland and the Baltic Sea, as well as from deeper waters of the North Sea (100 and 243 m) were analyzed by means of SEM. The BMU sizes were measured by means of image processing software. Results demonstrate a strong effect of temperature on the BMU size at NE Iceland and in the North Sea at 100 m depth. At 243 m depth, however, temperature variability was likely too low (1.2 °C) to evoke a microstructural change. At the Baltic Sea, the BMUs remained small, possibly due to physiological stress induced by low salinity and/or hypoxia. Thus, the size of BMUs of *A. islandica* shells only serves as a relative temperature indicator in fully marine habitats, as long as seasonal temperature amplitudes exceed ca. 1 °C. Furthermore, BMU size varied through lifetime with the largest units occurring during age seven to nine. This pattern is possibly linked to the shell growth rate or to the amount of metabolic energy invested in shell growth.

4.1 Introduction

Bivalve shells are increasingly used to reconstruct past environmental conditions in aquatic settings with unprecedented temporal resolution (Reynolds et al., 2013; Walliser et al., 2016; de Winter et al., 2021). Such data are of great value to constrain climate models (Schmidt et al., 2014; Cauquoin et al., 2019; Asami et al., 2020). Environmental variations can be recorded by the stable oxygen isotope data ($\delta^{18}O_{shell}$; Weidman et al., 1994; Peharda et al., 2019; Reynolds et al., 2019), shell growth patterns (Kennish and Olsson, 1974; Witbaard, 1996; Wanamaker et al., 2009) and certain trace elements (Krause-Nehring et al., 2012; Schöne, 2013; Füllenbach et al., 2015). As more recently suggested, the microstructural properties of the shells can potentially serve as a proxy for environmental changes as well, specifically the size and shape of individual BMUs, the building blocks of the shell microstructure (Olson et al., 2012; Gilbert et al., 2017; Milano et al., 2017b). In contrast to geochemical properties which are sensitive to diagenetic processes (Cochran et al., 2010; Ritter et al., 2017), the shell microstructure may 'survive' slight diagenetic alternations (Brand and Morrison, 1987; Knoll et al., 2016) and still provide useful environmental proxy data as long as no recrystallization occurred. Furthermore, temperature reconstructions based on the shell microstructure might be less affected by other environmental factors than conventional proxies such as the $\delta^{18}O_{shell}$, which require knowledge of the $\delta^{18}O_{water}$ signature or salinity. Microstructural properties of the long-lived *Arctica islandica* have gained particular interest (Milano et al., 2017a; Höche et al., 2021b), because this bivalve species not only forms distinct annual shell growth patterns, but also attains a lifespan of several hundred years (Thompson et al., 1980a; Schöne et al., 2005b; Wanamaker et al., 2008; Butler et al., 2013) and has a broad biogeographic distribution in the northern North Atlantic (Dahlgren et al., 2000; Schöne, 2013), prerequisites for long-term and high-resolution paleoclimate reconstructions in a climatologically highly relevant part of the global ocean.

According to recent laboratory experiments the size of BMUs of *A. islandica* shells correlates with the water temperature (Höche et al., 2021b). However, it remains unclear whether the same relationship exists in naturally grown individuals permitting temperature reconstructions from microstructural properties. Although food availability and pCO_2 have demonstrably no effect on the shell microstructure (Hiebenthal et al., 2013; Stemmer et al., 2013; Milano et al., 2017a; Ballesta-Artero et al., 2018a), other environmental factors could potentially bias or overprint the temperature signal recorded by the shell microstructure by affecting physiological processes responsible for biomineralization. In addition, it is unknown whether the morphol-

ogy of the individual building blocks of the shells, i.e., shape, size and orientation of the BMU vary with ontogeny or shell growth rate. Finally, the different shell portions of *A. islandica* consist of different microstructure types, with the BMUs of each type shaped differently. Crossed-acicular (CA) microstructures have disordered, partially rounded, partially acute BMUs, while growth lines come with ISP (Fig. 4.1). In contrast, homogeneous microstructures consist of ordered, rounded BMUs, whereas FCCL microstructures are made of acute, elongated, bidirectionally oriented BMUs (Figure 1). These microstructures, however, are termed differently by different authors and their morphologies have never been quantitatively analyzed and compared to each other. Addressing these questions requires comprehensive, quantitative microstructural data from specimens belonging to different age classes collected from different habitats.

Here, we investigate the microstructure of *A. islandica* shells collected from different coastal and deeper water settings of the NE Atlantic. Some specimens were exposed to strong seasonal and inter-annual variations of temperature and food availability (Northeast Iceland and Baltic Sea), whereas others lived in calmer subsurface waters of the North Sea (Norwegian Trench and East Viking Bank). The size and shape of the BMUs were investigated in SEM images by means of machine learning-based image processing software. The present study focuses on the microstructure of the hinge plate, where a temperature influence was previously identified in laboratory-grown specimens. For comparison with data from the hinge portion, the microstructure of the outer shell layer of the ventral margin was also studied. The data were temporally aligned and shell growth rates reconstructed via shell growth pattern and stable oxygen isotope analysis according to established methods (Jones, 1980; Schöne et al., 2005c; Vihtakari et al., 2016). The microstructural data of each locality were compared with environmental and physiological data (growth rate, ontogenetic age) to determine possible controls on the shell microstructure and to assess how confident BMU-based environmental reconstructions can be.

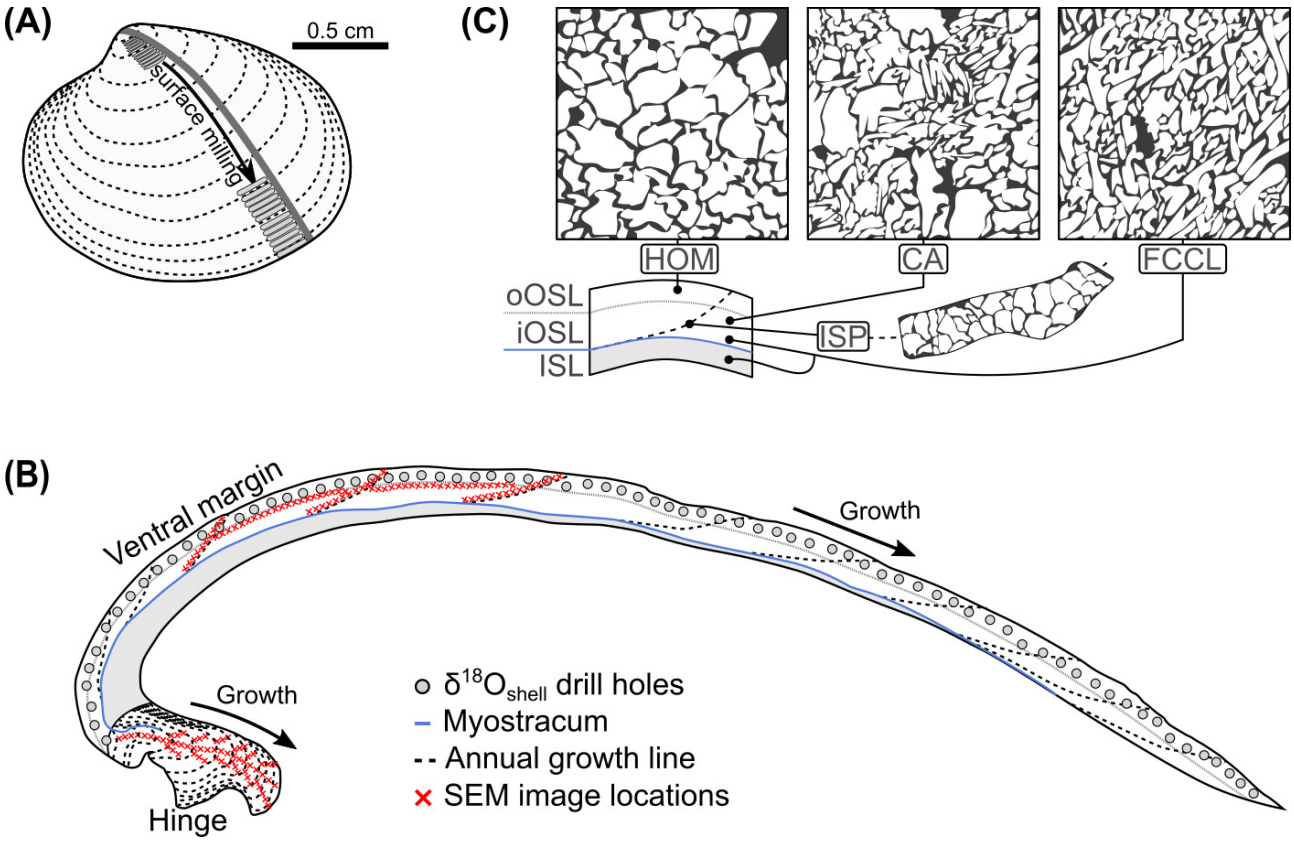

Figure 4.1 Sketch of *Arctica islandica* showing shell preparation, sampling strategy for stable oxygen isotope and SEM analysis, and microstructure. (A) Two slabs were cut from the valves along the axis of maximum growth (gray line). (B) Polished side of a shell slab; shell powder samples were obtained by surface milling (gray swaths, A), or by drilling in cross-sections (gray holes, B). The shell microstructure was studied under the SEM in the hinge plate and in the ventral shell portion (in the OSL). To assess spatial variation of BMU size within each of the respective shell portions, image transects were generated along contemporaneously formed regions in the OSL (following annual growth lines) and in transects away from the maximum growth axis of the hinge plate (B, specimen ICE06-6.2-A6R). (C) Sketches showing the homogeneous (HOM), crossed-acicular (CA) and fine compex-crossed lamellar (FCCL) microstructures, and where they are present within the ventral margin of the shell. oOSL: outer portion of the OSL; iOSL: inner portion of the OSL; ISL: inner shell layer.

4.2 Material and methods

The studied material comprises nine *A. islandica* shells collected alive from four localities across Northern Europe (Fig. 4.2A, Table 4.1). Three shells were collected in 2006 at a water depth of 6.6 m at Þistillfjörður, NE' Iceland (Marali and Schöne, 2015). Temperature data for this site were available from in situ measurements at Grímsey station (ca. 125 km NWW' the sampling site; Hanna et al., 2006) and remotely sensed chlorophyll a concentration data (used as a reference for food availability) were acquired from OceanColour (in 1 km distance to the sampling site; Sathyendranath et al., 2019). Three of the studied shells were collected at 24.8 m water depth in the Mecklenburg Bight, Baltic Sea (Schöne et al., 2021), an episodically hypoxic, stratified, eutrophic and polluted environment (Kremling et al., 1997; Karlson et al., 2002; Leipe et al., 2005; Conley et al., 2011; Hansson and Gustafsson, 2011; Carstensen et al., 2014). Here, temperature and chlorophyll a data were acquired from in situ measurements at marine station TF0012 operated by the Leibniz Institute for Baltic Sea Research Warnemünde (https://odin2.io-warnemuende.de/; accessed 14 Jul 2021). Furthermore, two specimens from the Viking Bank, collected at 92 and 100 m water depth (Ehrich, 2007), and one specimen from the Norwegian Trench (243 m depth, 1904) were studied. For these localities, remotely sensed monthly mean temperature data from the World Ocean Atlas (Boyer et al., 2020) were used, with data points (i.e., grid cell centers) located approx 33 km and 55.5 km away from the Viking Bank and Norwegian Trench, respectively. Depth-resolved monthly mean chlorophyll a data were acquired from EMODnet chemistry (Norwegian Marine Data Centre, 2019), located 3.2 km and 5.7 km away from the Viking Bank and Norwegian Trench, respectively. Differences in depth between the sampling sites and grid cell centers of the remotely sensed data were smaller than 7 m in all cases. From the sub-monthly temperature and chlorophyll a data of Iceland and the Baltic Sea, monthly means and standard deviations were calculated to allow comparisons with the Viking Bank and the Norwegian Trench, where such high-resolution data were not available (Fig. 4.2B+C, Supplement 4C).

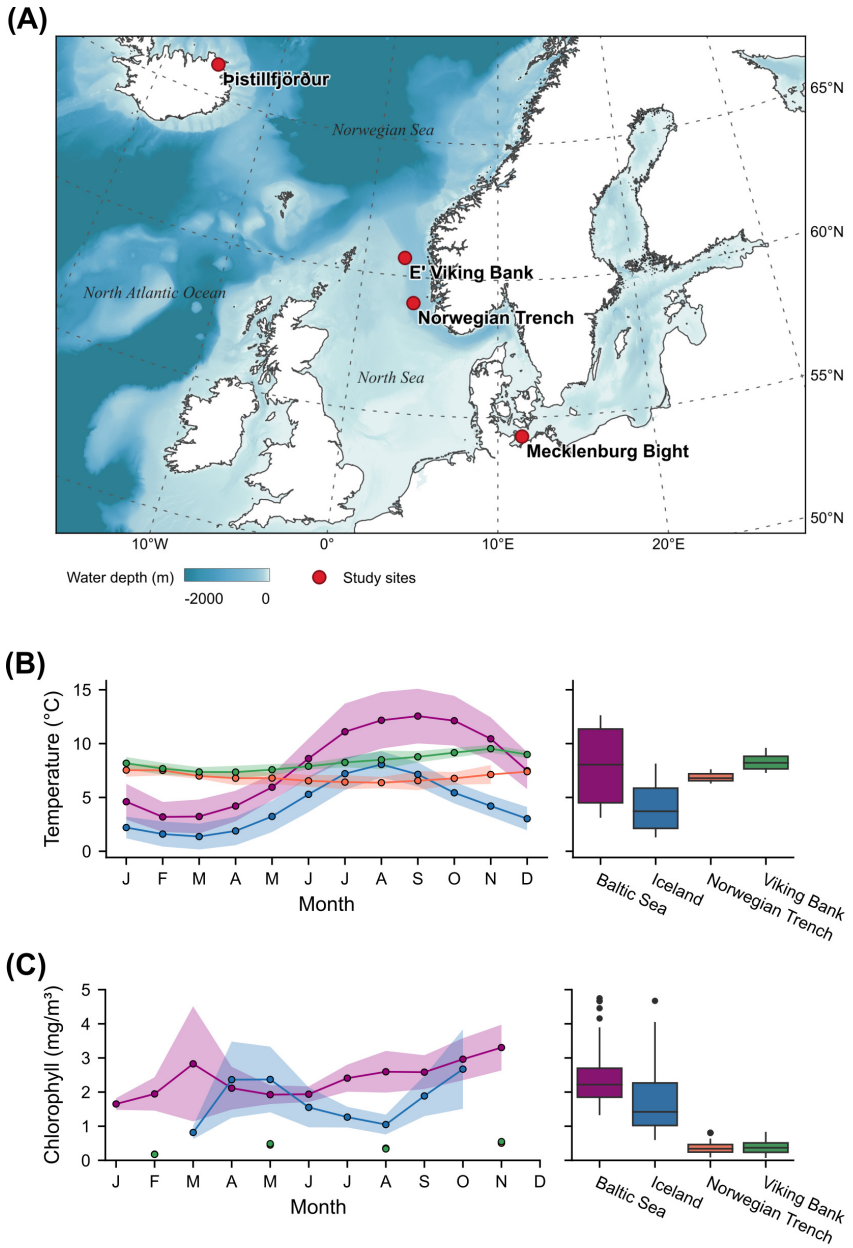

Figure 4.2 Shell (*Arctica islandica*) collection sites, temperature, and chlorophyll a data. (A) Map of Northern Europe showing the four shell collection sites of this study. Continent contours were taken from NaturalEarth (https://www.naturalearthdata.com/; last access 6 Jul 2021) and bathymetric data were acquired from EMODNet (http://www.emodnet-bathymetry.eu; last access 6 Jul 2021). Note that depths greater than 2000 m are displayed in the same color. (B) Water temperatures and (C) chlorophyll a concentrations shown as monthly averages (left side; solid line: mean; shaded area: ±one standard deviation) and annual ranges (right side) for each of the localities.

Table 4.1 Overview of the studied *Arctica islandica* shells.

Locality	Lon/lat	Water depth (m)	Date of collection	Specimen IDs	Ontogenetic age span covered by analysis	Time interval (year CE)	Ontogenetic age at death	# $\delta^{18}O_{shell}$ measurements	# BMU size measurements
Þistillfjöður, NE' Iceland	66° 10′ 45.06″ N 15° 21′ 23.76″ W	6.6	17 Aug 2006	ICE06-6.2-A6R	1-12	1995–2006	13	75	537
				ICE06-6.2-A11R	2–7	2001–2006	7	52	75
				ICE06-6.2-A16R	7–15	1997–2006	13	75	80
Mecklenburg Bight, Baltic Sea	54° 18′ 59.50″ N 11° 33′ 0.00″ E	24.8	25 Oct 2001	MLZ-St12-A4R	2–18	1986–2001	18	-	57
				MLZ-St12-A6R	2–15	1987–2000	16	-	37
				MLZ-St12-A9R	2–4	1995–1997	8	-	26
E' Viking Bank, North Sea	60° 40′ 0.00″ N 2° 60′ 0.00″ E	92.0	31 Jul 2007	WH302-804-BoxM-A1R	1–7	ca. 1972–1978	>50	72	35
		109.0		WH302-805-BoxM-A2R	3–8	ca.1950–1955	>50	67	31
Norwegian Trench, North Sea	59° 3′ 0.00″ N 4° 55′ 0.00″ E	243.0	15 May 1908	MOL8216_082V-A1	2–9	1905–1908	9	48	41

4.2.1 Shell preparation

From one valve of each shell, two 3 mm-thick slabs were cut out along the axis of maximum growth (Fig. 4.1A). For this purpose, the valves were glued to acrylic glass cubes using WIKO Multi Power 3 plastic welder and covered along the cutting axis with a protective layer of WIKO 05 metal epoxy resin. After air-curing, specimens were cut with a low-speed rotational saw (Buehler IsoMet 1000) equipped with a diamond-coated wafering thin blade (0.4 mm thickness; Buehler 15LC 11-4255) operated at 200 rpm. The shell slabs were manually ground on glass plates using F800 and F1200 SiC suspensions and subsequently polished with 1 µm Al_2O_3 on a Buehler MasterTex polishing cloth. After each preparation step, specimens were ultrasonically rinsed with tap water for six minutes. One of the slabs was affixed to a glass slide for growth pattern and stable oxygen isotope analysis, whereas the other slab was attached to a one-inch SEM sample holder with carbon stickers for microstructure analysis (Fig. 4.2B, Fig. S4.2).

4.2.2 Determination of timing and rate of shell formation

Bivalves grow their shells periodically, leading to the deposition of growth increments and lines (Clark, 1974; Clark, 1975). As in most other bivalves, prominent growth lines are formed annually in *A. islandica* (Thompson et al., 1980a; Ropes et al., 1984a; Karney et al., 2011). Growth line formation occurs ca. four weeks after the annual temperature maximum (Jones, 1980; Thompson et al., 1980a; Schöne et al., 2005b). The annual lines can therefore be used to determine the ontogenetic age of the animal and to place the shell record in temporal context. In order to analyze the growth patterns, shells were immersed in Mutvei's solution (12.5 % Glutaraldehyde, 0.5 % acetic acid, and 5 g L^{-1} alcian blue) and kept at 38 °C for 8 min under constant stirring, which stained and fixated the shell organics while gently etching the shell carbonate (Schöne et al., 2005a). After rinsing and air-drying, shells were imaged in sectoral (= one-quarter) dark-field illumination under a Leica Stemi 508 stereomicroscope equipped with a Canon EOS 600D DSLR camera. All sclerochonological measurements (i.e., distances between the annual growth lines, $\delta^{18}O_{shell}$ sampling spots and SEM images) were performed with the image processing software ImageJ (Schneider et al., 2012; Rueden et al., 2017).

Since most of the studied specimens lacked clearly defined sub-annual growth patterns, the $\delta^{18}O_{shell}$ method was used to place the shell record in temporal context. For this purpose, the paleothermometry equation by (Grossman and Ku, 1986) with the −0.27 ‰ PDB-SMOW scale correction (Gonfiantini et al., 1995; Eq. 4.1) was solved for $\delta^{18}O_{shell}$ (Eq. 4.2). Then, a pre-

dicted seasonal $\delta^{18}O_{shell}$(model) profile was computed for each locality based on the corresponding instrumental temperature (Fig. 4.2B) and $\delta^{18}O_{water}$ data taken from LeGrande and Schmidt (2006) using Eq. 4.2. Measured $\delta^{18}O_{shell}$ data were aligned to best fit the predicted seasonal $\delta^{18}O_{shell}$(model) profiles. This way, a precise calendar date could be assigned to each sample. Finally, these data were linearly interpolated to reconstruct the daily growth rate. In case of the Baltic Sea shells, an existing seasonal shell growth model was used (Schöne et al., 2021).

$$T = 20.6 - 4.34 \times (\delta^{18}O_{shell} - (\delta^{18}O_{water} - 0.27)) \tag{4.1}$$

$$\delta^{18}O_{shell}(model) = \frac{20.6 - 4.34 \times ((\delta^{18}O_{water} - 0.27) - T)}{4.34} \tag{4.2}$$

To measure the stable oxygen isotope composition of the shells, carbonate powder samples of ca. 60 µg were taken along the axis of maximum growth using a micro drill (Rexim Minimo KM11G) firmly attached to a binocular microscope equipped with a conical SiC drill bit (300 µm diameter at tip; Gebr. Brasseler GmbH & Co. KG, model no. H52.104.003). For most specimens, sampling was accomplished on the surface of the polished shell slabs, but in case of the thin shells from deeper settings, approx. 100 µm broad swaths were milled on the surface of the valves (surface milling; Fig. 4.1A). Carbonate powders were dissolved in He-flushed borosilicate exetainers at 72 °C by adding 99.9 % phosphoric acid and the released CO_2 gas was measured in continuous flow mode with a ThermoFisher MAT 253 isotope ratio mass spectrometer in coupled to a GasBench II. Stable isotope values were calibrated against an in-house Carrara marble standard ($\delta^{18}O$ [V-PDB] = −1.91 %) and are given relative to the V-PDB standard. Oxygen isotope values were not corrected for differences in acid fractionation factors between the calcite (Carrara marble) and aragonite (shell), because the source equation for Eqs. 4.1+4.2, i.e., the paleothermometry equation by Grossman and Ku (1986) is based on uncorrected $\delta^{18}O$ values (see Füllenbach et al., 2015, for more details). Measurement accuracy based on blindly measured reference materials of known isotopic composition (NBS-19) was better than 0.04 %.

4.2.3 Scanning electron microscopy

Since the contrast between shell carbonate and finely distributed intercrystalline organics in backscatter SEM is insufficient to analyze individual BMUs, they need to be revealed prior to morphometric analysis. This is typically accomplished by slight etching of the BMUs and/or removal

of the intercrystalline organic matrices, e.g., by immersion of the shells in weak acids, bleach or hydrogen peroxide (Crippa et al., 2016). This treatment, however, evokes a violent reaction (Lavkulich and Wiens, 1970), alters the original BMU shape (Höche et al., 2021b) and sometimes affects different materials of the shell heterogeneously. To overcome these problems, an ultrafine chemo-mechanical polishing step was instead employed in this study: shell slabs were polished for ten minutes on a rotational lap (Buehler MetaServ 2000) at 50 rpm using a Buehler Master-Tex polishing cloth and Buehler MasterMet polishing suspension. With a grain size of 60 nm, the colloidal silica particles of this suspension were small enough to mechanically erode the finely distributed organic phases, while its alkaline pH of ca. 10.1 aided in the gentle chemical removal of the organics. The resulting shell slab surface was polished very evenly and intercrystalline organics were removed thoroughly while keeping abrasion of the carbonate phase at a minimum (Fig. 4.3A).

As a previous study revealed a statistically significant relationship between the BMU size in the hinge plate of laboratory grown specimens and temperature (Höche et al., 2021b), the same shell portions were investigated here (953 images; Table 4.1). For comparison of BMU data in different contemporaneous portions of the shell, the OSL of the ventral margin was also studied (241 images; Table 4.1). Most images were taken in transects along the maximum growth axis to assess microstructural variation through time (Fig. 4.1B; Fig. S4.2). Additionally, images were taken along contemporaneously formed shell portions in the OSL of the ventral margin and in the hinge plate (in specimen ICE06-6.2-A6R) to assess the spatial variability of BMU sizes and to test the reproducibility of the BMU proxy method (Fig. **??**B).

Images used in BMU morphometry were generated with a Phenom Pro Desktop SEM (3rd generation) equipped with a CeB_6 electron source and backscatter electron detectors at 7700 × magnification and 10 keV. The images were subsequently processed with the machine-learning based image segmentation program Ilastik (Berg et al., 2019), which classifies each individual BMU as a unique shade of gray based on a prior training of the software. In a set of exemplary input images (randomly selected among the images of this study to cover a wide range of microstructural textures), labels were painted over the pixels to classify them as either BMU or intercrystalline space. Based on the characteristics (i.e., intensity, texture, contour sharpness) of these manually classified regions, the probability of being a BMU (p_{BMU}) was calculated for each remaining pixel. Individual BMUs were then detected in these probability maps by applying a two-step probability threshold (Canny, 1986; Condurache and Aach, 2005). Connected pixels with $p_{BMU} > 0.95$ were considered as the cores of individual BMUs and were assigned with a unique gray value. These

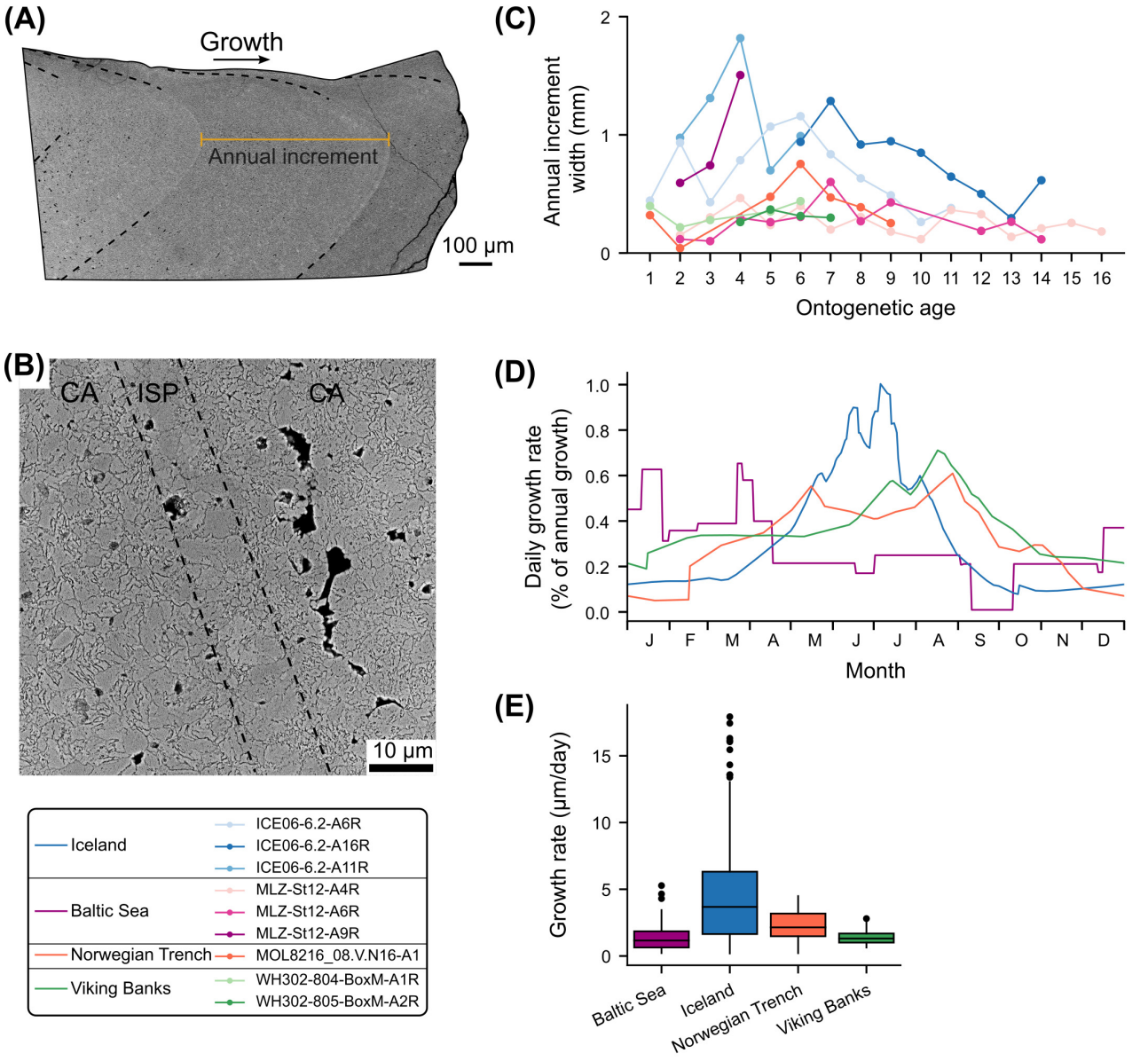

Figure 4.3 Hinge plate of *Arctica islandica*. (A) Overview of a hinge plate showing the growth direction, annual growth lines (dashed lines) and annual increment (orange). (B) Magnified annual growth line (SEM) showing the typical irregular simple prismatic (ISP) microstructure and the decrease in BMU size in the following crossed-acicular (CA) microstructures. Direction of growth is from lower left to upper right. (C) Annual growth increment curves of the studied specimens. (D) Seasonal growth models (daily resolution) for the studied sites based on the $\delta^{18}O_{shell}$ alignment technique (Fig. S4.1). Model for the Baltic Sea was obtained from (Schöne et al., 2021). (E) Daily shell growth rates of *A. islandica* at the different study localities.

areas were then expanded outward to include neighboring pixels of $p_{BMU} > 0.5$. This two-step hysteresis thresholding process allows for effective separation of adjoining BMUs, which would otherwise be considered as one entity. The segmented images were inspected visually, and all invalid results (= severe over- or under-splitting of the BMUs) arising from poor image quality due to sample drift or charging effects were discarded (217 of 1194 images). Finally, the size of each BMU in each correctly segmented image was automatically measured and its elongation estimated by fitting an ellipse using the programming language python and image processing library scikit-image (van der Walt et al., 2014). The scripts and classifier used in this study are available online (Höche et al., 2021a) and can be reused in future studies to batch process SEM images acquired under the same settings for BMU morphometry.

4.2.4 Statistical processing of the microstructural data

The BMU raw data comprise one entry for every BMU of each of the 1194 images, marking the need for data reduction techniques. Since previous studies revealed significant heterogeneity among BMU size values and determined a temperature relationship predominantly for the largest BMUs (Höche et al., 2021b), the same statistical measures were used herein. Of each image, the fifteen largest BMUs were selected and means and standard deviations were calculated for their size and elongation. The shell portion, microstructure type, ontogenetic age, and relative position within the annual growth increment corresponding to each image (i.e. BMU data point) were recorded.

To assess relationships between environmental, physiological and BMU morphological parameters at each locality, Pearson correlations (r) and corresponding significance values (p; significance threshold $\alpha = 0.05$) were computed. In addition, linear models between the BMU size and the environmental and physiological parameters were computed via least squares regression. Trends in BMU size through lifetime of the bivalves were estimated by locally weighted scatterplot smoothing (Cleveland, 1979) using a window size of one-third of the data to represent long-term developments and two years of data for the seasonal trends. All calculations were performed using python and the modules SciPy (Virtanen et al., 2020) and statsmodels (Seabold and Perktold, 2010).

4.3 Results

4.3.1 Shell formation: timing, rate and microstructure

Based on annual increment counts, the studied shell portions of the specimens formed before the age of seventeen (Table 4.1). In the hinge plate, annual increment widths ranged from 0.03 to 1.81 mm and were broadest at around age four to seven (Fig. 4.3C). According to the $\delta^{18}O_{shell}$-alignment (Fig. S4.1), studied bivalves formed annual growth lines a few weeks after the annual temperature maximum. Among the specimens from one locality, the timing and rate of shell growth were highly synchronized (Fig. S4.1), whereas they varied considerably between sampling sites (Fig. 4.3C+E). The Icelandic shells mainly grew from October until late August of the following year and attained maximum growth rates during spring and summer. In contrast, shells from the Viking Bank grew between February and December, with growth rate maxima during late August. The specimen from the Norwegian Trench grew its shell from April to February of the following year, with the fastest shell formation rates during early September (Fig. 4.3D).

The hinge plates were dominated by CA microstructure (occurring in 92.7 % of the images). Annual growth lines were easily identified, because they consisted of ISP microstructure (Figs. 4.1C+4.3B). In the CA microstructures following an annual line, much smaller BMUs were formed (Fig. 4.3B). These CA microstructures were occasionally replaced by FCCL. FCCL microstructures were also found in the most lateral regions of the hinge plate, i.e., in slower growing portions far away from the main growth axis. FCCL microstructures became more abundant with increasing age. Shells from the Baltic Sea consisted of a larger proportion of FCCL microstructures than those from the other localities (30.5 % of images vs. 1.7 % of images, respectively). Here, FCCL microstructures were not only found near the annual growth lines, but also in disturbance lines which frequently occurred during summer months.

The ventral margin of the shells was divided into an inner (ISL) and outer layer (OSL) separated by the myostracum (Fig. 4.1B). The outermost portion of the OSL consisted of homogeneous microstructures, which gradually transitioned into CA and FCCL microstructures towards the myostracum. Inner shell layers consisted of FCCL microstructures. Like the hinge plate, annual growth lines of the outer shell layer of the ventral margin consisted of ISP microstructures. These ISP microstructures were most defined in the oOSL, whereas they gradually disappeared toward the iOSL close to the myostracum.

4.3.2 Size of the biomineral units

The size of the BMUs differed distinctly between study localities (Fig. 4.4). Except for the Norwegian Trench and the Baltic Sea, this difference was statistically significant ($p < 0.05$). Specimens from Iceland formed the largest BMUs ($9.44 \pm 5.39\ \mu m^2$), followed by those from the Baltic Sea ($6.46 \pm 2.80\ \mu m^2$), while the BMUs were smallest in the deeper environments (Norwegian Trench $5.33 \pm 2.50\ \mu m^2$ and Viking Bank $3.72 \pm 1.47\ \mu m^2$). BMU size data were also heteroscedastic, i.e., size variance increased in portions with larger BMUs. In both the hinge plate and ventral margin, BMUs of FCCL microstructures were significantly smaller ($4.9 \pm 2.3\ \mu m^2$) than those of the CA microstructure ($8.7 \pm 5.1\ \mu m^2$) and also more elongated (2.41 ± 0.41 in FCCL and 1.97 ± 0.24 in CA; Fig. 4.4B).

Along the axis of maximum growth in the hinge plate, BMU sizes first increased and then decreased with ontogenetic age (Fig. 4.5). In all shells, BMUs reached their maximum size during age seven to nine. At large, BMU sizes of the hinge plate correlated with the annual growth rate. The broadest annual increments, however, occurred a few years earlier than the largest BMUs, i.e., between age four to seven (Fig. 4.3A). Furthermore, all shells, except those from the Baltic Sea, exhibited seasonal BMU size patterns (Fig. 4.5). This was most evident in the Icelandic shells: BMUs were smallest at the beginning of each growing season, shortly after the annual growth line. Thereafter, BMU size gradually increased, reaching a maximum at around 70–90 % of the annual growth increment and decreased toward the following annual line (Fig. 4.5). This intra-annual BMU size trend was not limited to the axis of maximum growth, but was likewise observed in transects away from that axis (Fig. 4.6). Specimens from the Viking Bank showed the same pattern as those from Iceland, yet with a smaller amplitude. The shell from the Norwegian Trench, in contrast, formed the largest BMUs about half way through the annual increments. In Baltic Sea specimens, BMU size variation was poorly synchronized among individuals and did not show a clear pattern over the course of each year. Note that 52 images of the shells from this locality had to be discarded because of problems during image segmentation (arising from highly irregular geometries of the interstitial spaces surrounding the BMUs), which obscured some portions of the shell growth records.

In the ventral margin, the size of BMUs of the iOSL was nearly identical to those formed contemporaneously in the hinge plate (Fig. 4.7A). Hinge plate and iOSL also exhibited similar seasonal BMU size patterns. The only exception was observed in specimens from the Norwegian Trench, in which BMUs of the iOSL attained largest sizes at the beginning of the growing

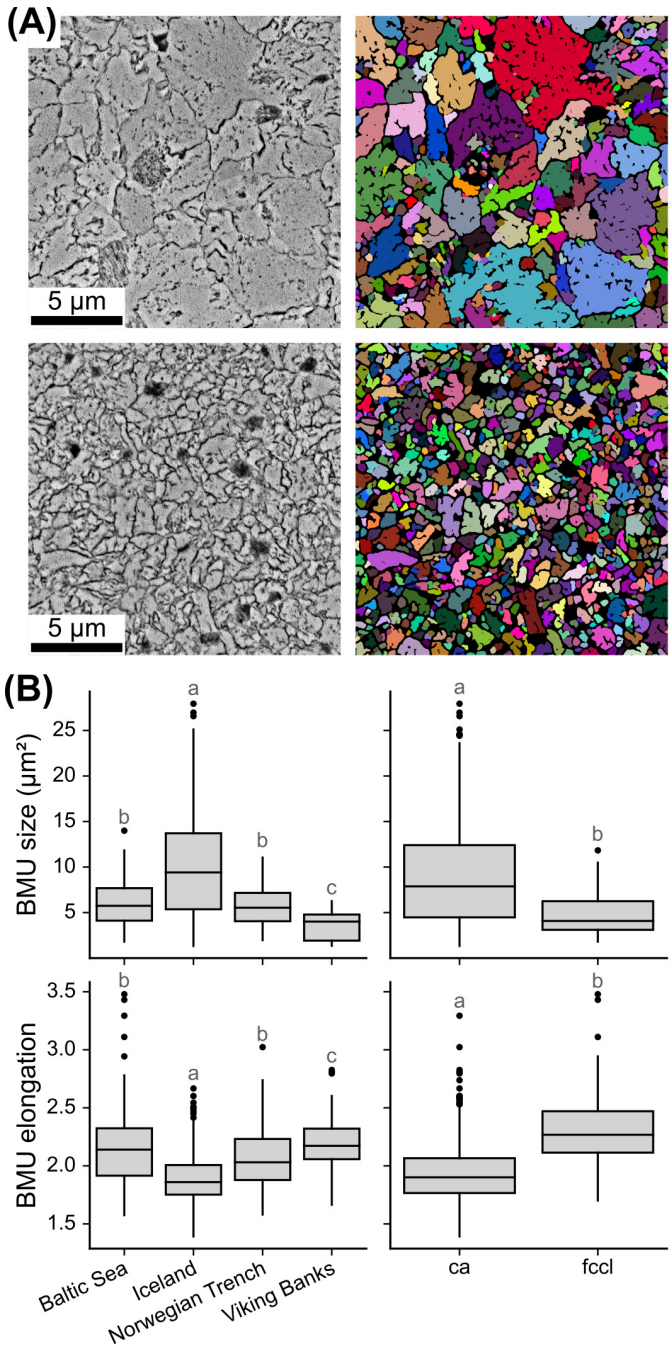

Figure 4.4 SEM image segmentation and BMU morphology data of *Arctica islandica*. (A) Two shell regions (left) with large and small BMUs, respectively, and their corresponding segmentations (right). For visualization purpose, individual BMUs are displayed in individual colors, whereas the intra- and intercrystalline space is represented in black. (B) Average size and elongation of the 15 largest BMUs of each image of the hinge plates as boxplots for each locality (left) and microstructure type (right). Statistically significantly different groups ($p < 0.05$) are marked with different letters.

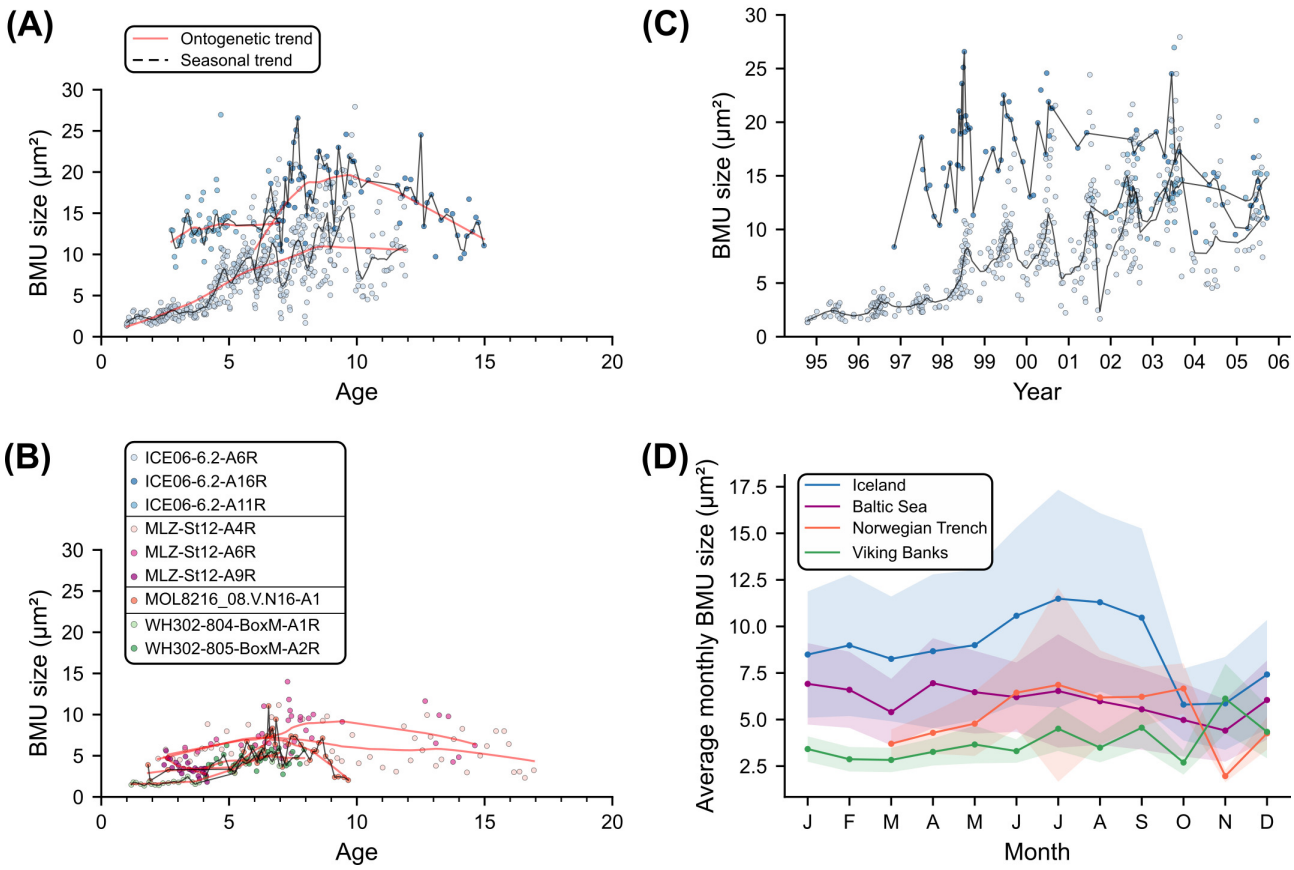

Figure 4.5 Temporal BMU size trends of the hinge plates of *Arctica islandica*. Ontogenetic BMU size curves for studied specimens from Iceland (A) and the remaining localities (B). At all localities, BMU size exhibited a parabolic trend over the lifetime of the animal (red lines), attaining maximum values at age seven to nine. In addition to this ontogenetic trend, all shells except those from the Baltic Sea exhibited seasonal variation of BMU size (black lines). (C) BMU data of the Icelandic specimens against calendar time. (D) Average monthly BMU sizes of each locality. Trend lines were calculated by locally weighted scatter plot smoothing (Cleveland, 1979) using a window size of one-third of the data for the long-term curves and two years of data for the seasonal curves.

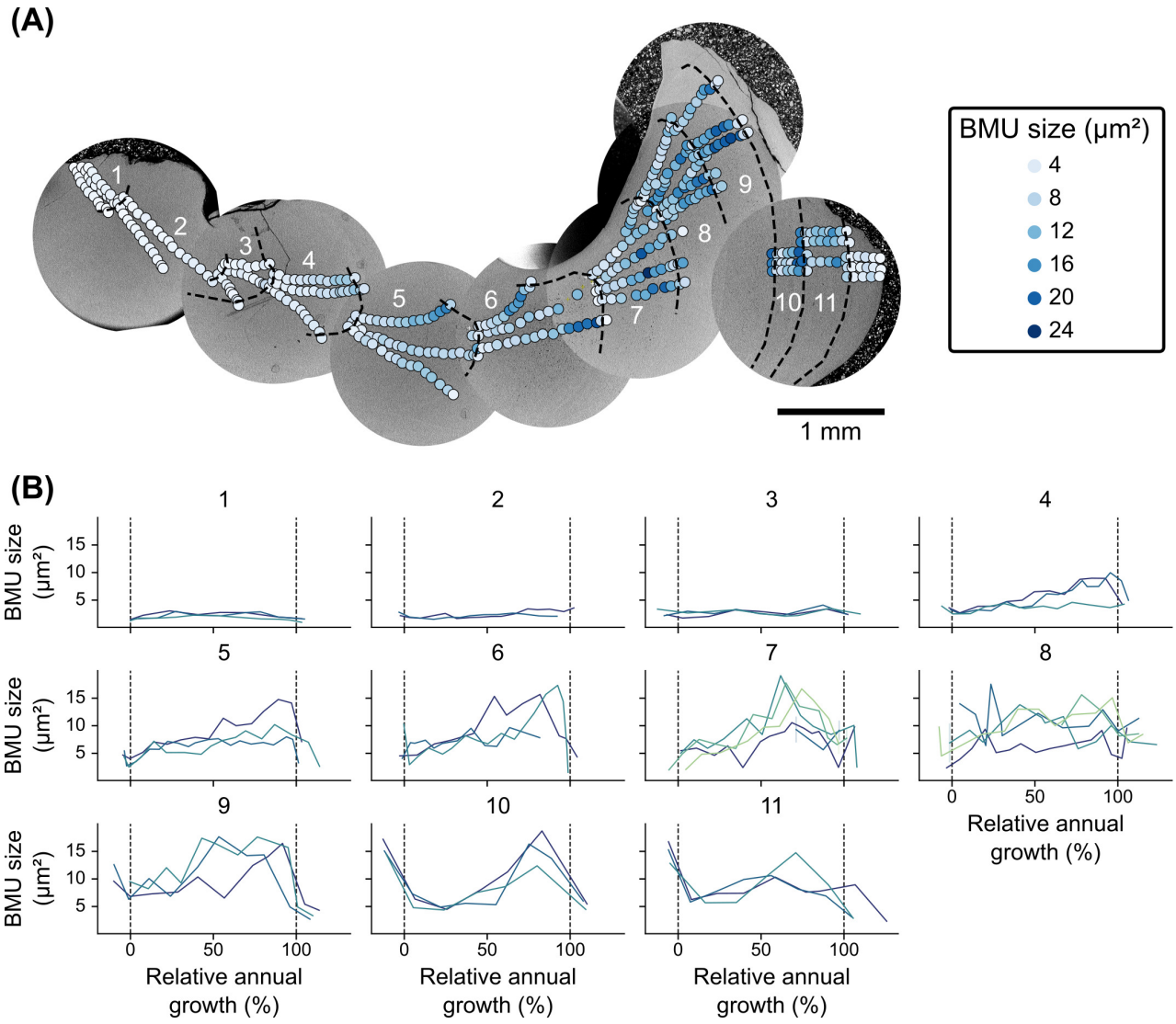

Figure 4.6 Spatial BMU size variability in the hinge plate of *Arctica islandica* specimen ICE06-6.2-A6R. (A) The BMU size varies strongly across and within the annual growth increments (labeled 1 through 11), but is largely similar in contemporaneously formed portions of the same annual increment. (B) Within each annual increment, the BMU sizes of different transects agree well with each other and show a sinusoidal pattern from age four onward. Merely increment seven and eight exhibited weaker correlation and less prominent seasonal patterns.

season. BMUs had a distinct size pattern from the outer shell surface to the myostracum (Fig. 4.7B). Relative to the average size of all BMUs in a vertical transect, values were smallest in the outermost homogeneous microstructures of the oOSL ($z \approx -1$; Eq. 4.3), but abruptly increased in size near the transition zone to the CA microstructures of the iOSL (to z of up to 3). Toward the myostracum, the BMU sizes decreased slightly (to $z \approx 0$) throughout the CA portion of the iOSL until at the transition to FCCL microstructures, a sharp size peak was developed (z of up to 3). Close to the myostracum, the BMUs of the FCCL microstructures remained at a moderate size ($z \approx 0$). The BMUs of CA microstructures were most variable in size, whereas FCCL BMUs had little size variation.

$$z\left(BMU_{area}\right) = \frac{BMU_{area} - \mu\left(BMU_{area}\right)}{\sigma\left(BMU_{area}\right)} \tag{4.3}$$

μ: mean

σ: standard deviation

The BMU morphology was only weakly correlated with the physiological and environmental parameters and did not reveal a common pattern for the studied localities. BMU sizes were weakly, but significantly positively correlated to water temperature at NE Iceland and the Viking Bank (Pearson $r = 0.24$ and 0.30, respectively; $p \geq 0.5$; Fig. 4.8A+E). The opposite, a significant negative correlation, was observed in specimens from the Baltic Sea ($r = -0.31$; $p = 0.05$). Linear regression models for BMU size and temperature, revealed similar slopes for Iceland and the Viking Bank (0.52 and 0.66 $\mu m^2\,°C^{-1}$) but their intercept differed (7.32 versus −1.76 °C; Fig. 4.8A). Chlorophyll a concentration and the BMU size were weakly positively correlated at the Viking Bank and Norwegian Trench ($r = 0.21$ and 0.32), but only the latter was statistically significant. In the specimens from the Baltic Sea and Iceland, in contrast, BMU size was significantly (negatively) correlated to the chlorophyll a concentration ($r = -0.19$ and 0.31; $p < 0.05$; Fig. 4.8B+E). Except for some specimens from the Baltic Sea, BMU size and shell growth (i.e., the annual increment widths and the reconstructed seasonal growth rates) was consistently positively correlated (Fig. 4.8C-E). Note, that BMU sizes in specimens from low-seasonality environments (Norwegian Trench, Viking Bank) were stronger correlated to the annual increment width than those of the environments with high seasonality (Iceland, Baltic Sea).

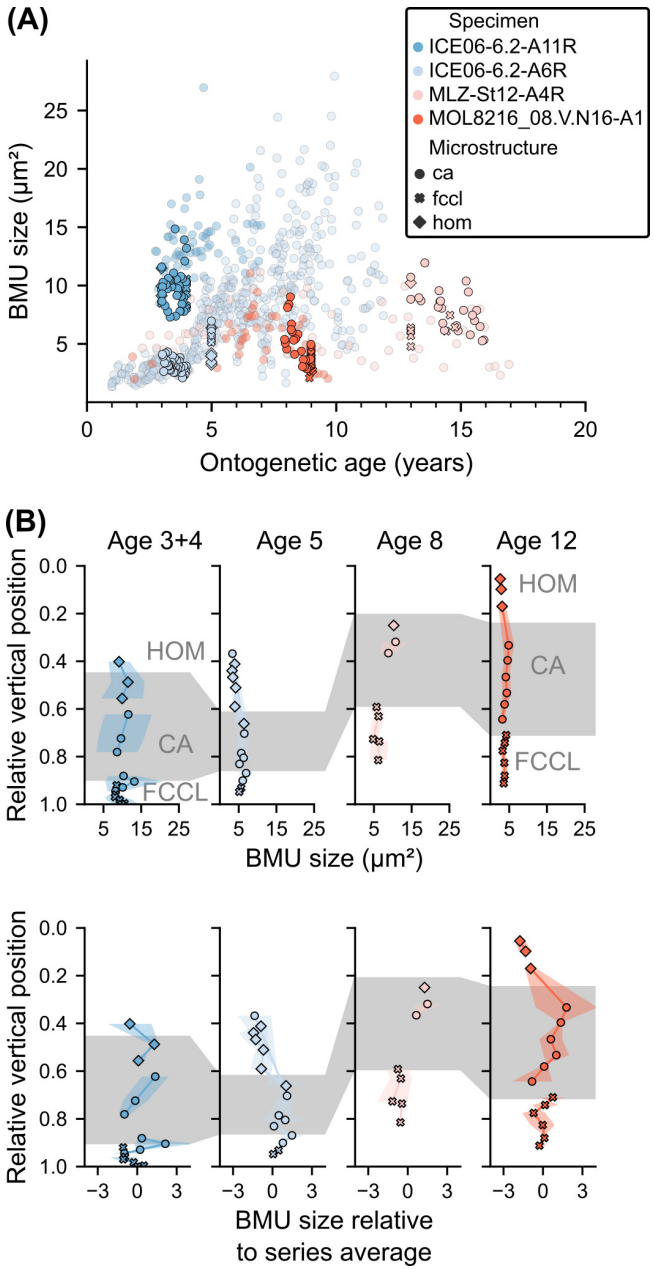

Figure 4.7 BMU sizes in the ventral margin of *Arctica islandica* shells. (A) BMUs of the ventral margin (solid colors) and the hinge plate (transparent) were almost identically sized and showed the same size patterns over time. (B) BMU sizes in vertical transects through the outer shell layer (OSL) as absolute and relative values. From the outer shell surface toward the myostracum (i.e., 1.0 relative vertical position; x-axis), BMUs were smallest in the HOM microstructures of the outer portion of the OSL, attained maximum sizes and largest size variances in the CA microstructures of the inner portion of the OSL, and decreased again toward average sizes in the FCCL microstructure near the myostracum.

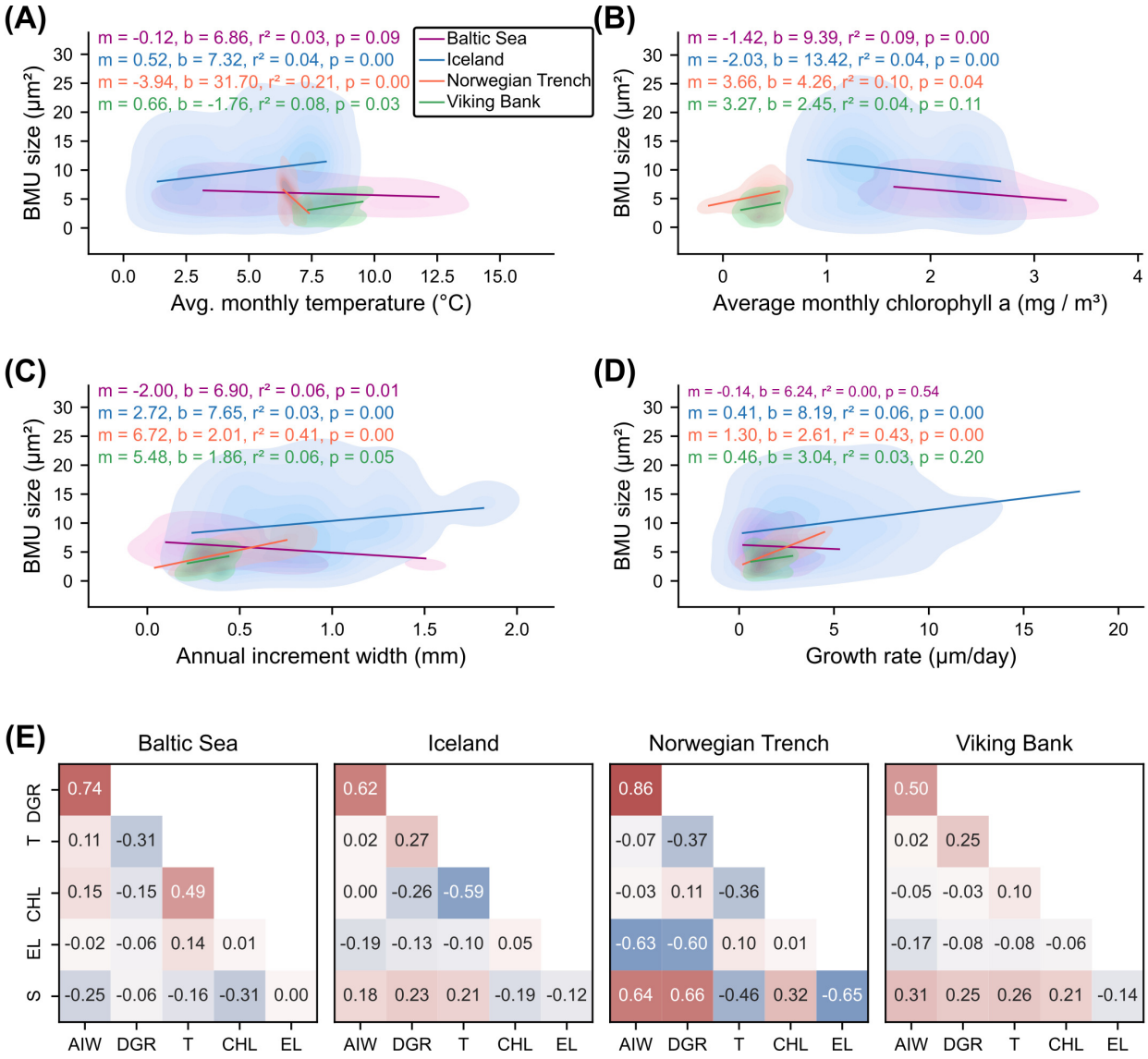

Figure 4.8 Correlation analysis between *Arctica islandica* hinge plate BMU sizes, shell growth rates, and environmental records. BMU size plotted against (A) average monthly temperature, (B) average monthly chlorophyll a concentration (C) annual increment width and (D) reconstructed daily growth rate at each study locality. Shaded areas represent the density of individual data points, and lines represent linear models. Model parameters are annotated in the plots. (E) Pearson correlation matrices of BMU size (S) and elongation (EL), environmental variables and shell growth parameters for each locality. DGR: daily growth rate; AIW: annual increment width; T: temperature; CHL: chlorophyll a.

4.4 Discussion

The BMU size range differed among sampling sites, with the largest BMUs occurring at NE Iceland and smallest at the Norwegian Trench (Fig. 4.4B). However, these differences in BMU size cannot be easily explained by environmental variables such as temperature and diet (Fig. 4.4B+4.8A). Firstly, correlations with environmental variables differed greatly among sites (Fig. 4.8). Secondly, microstructural data revealed a common ontogenetic trend in the BMU size (Fig. 4.5). Irrespective of environmental conditions, the largest BMUs were formed between age seven and nine. These BMU size patterns are examined more closely in the following in order to distinguish between environmental and biological processes which may have evoked them.

4.4.1 Environmental effects on the shell microstructure

At Iceland and the Viking Bank, BMU size covaried with the water temperature (Fig. 4.8A+E). As in other bivalve microstructures (Olson et al., 2012; Gilbert et al., 2017; Milano et al., 2017b), larger BMUs were formed in warmer waters, i.e., seasonal BMU size maxima coincided with the seasonal temperature maxima (Fig. 4.2B+4.5D). Moreover, seasonal BMU size amplitudes were larger at NE Iceland than at the Viking Bank, likely owing to the greater seasonal temperature range (Fig. 4.2B). At both localities, the temperature sensitivity of BMU size was similar (+0.52 and +0.66 $\mu m^2\,°C^{-1}$, respectively), and agreed well to findings of previous laboratory experiments using the same bivalve species (+0.50 $\mu m^2\,°C^{-1}$; Höche et al., 2021b). All this argues for a causal link between BMU size and temperature, which functions analogously to abiogenic systems, where rising temperature also leads to increased grain size of the precipitated carbonate (Mejri et al., 2014). In the Icelandic specimens, differences in BMU size between individuals of the same age could be explained by temperature differences. For example, specimen ICE06-6.2-A11R formed, during age three to five (corresponding to 2001–2003), BMUs on average 8.8 μm^2 larger than specimen ICE06-6.2-A6R at the same age (corresponding to 1997–1999, Figs. 4.5A+C), because temperatures were on average 1.1 °C warmer (5.34 and 4.19 °C, respectively; Supplement 4C). However, based on the previously determined relationship, this temperature difference would only account for ca. 0.6 μm^2 of the observed 8.8 μm^2. The intercepts of linear models between BMU size and temperature also differed strongly between specimens and sites (Fig. 4.8A). Furthermore, though statistically significant ($p < 0.05$), temperature was only weakly correlated to BMU size ($r = 0.28$–0.29; Fig. 4.8E) suggesting that other environmental and/or bi-

ological factors controlled the BMU sizes. In conclusion, BMU size in naturally grown specimens of *A. islandica* can only serve as a proxy for relative temperature changes.

In contrast to NE Iceland and the Viking Bank, the BMU size of the shell from the Norwegian Trench was negatively correlated to the water temperature, whereas BMU data of shells from the Baltic Sea showed no significant link with temperature (Fig. 4.8A). In case of the Norwegian Trench (243 m depth), this may partly be explained by the lack of high-resolution temperature data, i.e., only monthly average values were available. For comparison, at NE Iceland, the BMU size correlated stronger to the daily temperature data than to the monthly averages (r of 0.29 versus 0.21; r^2 of 0.09 versus 0.04). However, at the Viking Bank (100 m depth), BMU size was significantly linked with temperature even though monthly average water data were used. Hence, at the Norwegian Trench and the Baltic Sea, temperature effects on the shell microstructure were minor, and other, unknown factors played a larger role.

In the specimen from the Norwegian Trench, observed negative correlations between BMU size and water temperature were likely spurious, because seasonal minima or maxima of BMU size did not coincide with those of temperature (Figs. 4.2B+4.5D). A causal link also seems unlikely because all results published to date indicate the formation of larger BMUs at higher temperatures, rather than the opposite (Gilbert et al., 2017; Milano et al., 2017b). Perhaps, seasonal temperature variability at the Norwegian Trench (~1.2 °C; Fig. 4.2B) was insufficient to produce a seasonal BMU size pattern. However, in specimens from the Viking Bank, seasonal fluctuation of BMU sizes was clearly related to the seasonal temperature oscillation of approx. ±2.2 °C. Taken together, this could imply that temperature changes smaller than 1.2–2.2 °C may not visibly affect the shell microstructure of *A. islandica*.

Instead of temperature, dietary conditions could have controlled BMU size, because at the Norwegian Trench, BMU size was weakly positively correlated to the chlorophyll a concentration ($r = 0.32$, $r^2 = 0.04$; Fig. 4.8). For a variety of reasons, however, food availability was challenging to assess at the study sites. Firstly, as a deposit feeder, *A. islandica* can rely on various food sources (Winter, 1970; Cargnelli, 1999; Morton, 2011). Thus, a range of different indicators such as nutritional value of various primary producers in the water, particulate organic matter content, and hydrogeography, should ideally be used to assess food availability. These data, however, are not widely available, so that chlorophyll a concentration was used in this study. Secondly, chlorophyll a concentration does not always represent a good estimation of algal biomass (Kruskopf and Flynn, 2006). And lastly, in situ chlorophyll a data were only available for the Baltic Sea, whereas less precise, remotely sensed satellite data were used for all other localities. For example,

satellite data are likely less suitable to characterize the dietary conditions at the Viking Bank (100 m depth) and Norwegian Trench (243 m depth), which are both located well below the photic zone. Chlorophyll a data for NE Iceland were also less reliable, because satellite data are challenging in these optically highly complex coastal surface waters (IOCCG, 2000; Chen et al., 2013; Gholizadeh et al., 2016). Accordingly, quality and resolution of the chlorophyll a data were not sufficient to assess seasonal and interannual variations in food availability. Thus, positive correlations between BMU size and chlorophyll a at the Norwegian Trench and Viking Bank should be interpreted with care. Furthermore, at other localities, e.g., NE Iceland, the BMU sizes were negatively correlated to the chlorophyll a concentration (Fig. 4.8B). A link between food supply and BMU size thus seems highly unlikely, as has also been confirmed by recent laboratory experiments (Milano et al., 2017a; Ballesta-Artero et al., 2018a). At most, the deeper water of the Norwegian Trench could represent a special case in which the BMU size is more strongly linked to food availability than in surface waters. This scenario is supported by the fact that seasonal BMU size maxima occurred during autumn at this locality (Fig. 4.5D), the time at which the seasonal thermocline destabilizes and food items are transported to the bottom water (Pohlmann, 1996; Meyer et al., 2011; Rovelli et al., 2016).

Bivalves from the Baltic Sea, however, likewise did not show a significant correlation between BMU size and temperature (Fig. 4.8A) despite warm waters and highly variable temperatures (Fig. 4.2B). However, as demonstrated in laboratory experiments, under normal marine conditions, BMUs of *A. islandica* shells are larger in warmer waters (Höche et al., 2021b). Perhaps, the BMU size of specimens from the Baltic Sea is still weakly linked to temperature, but effects were overruled by those of other environmental stressors unique to this locality and absent under controlled conditions. These stressors could be low and variable salinity (Supplement 4C), episodic oxygen depletion and eutrophication (Gray et al., 2002; Karlson et al., 2002), high pCO_2 (acidification) or pollution (Kremling et al., 1997). pCO_2 was shown to leave the shell microstructure of *A. islandica* largely unaltered (Hiebenthal et al., 2013; Stemmer et al., 2013). Effects of the remaining environmental aspects on the microstructure are poorly studied. At dump sites polluted by trace metals, mortality of *A. islandica* increases (Kapp, 1980), and juveniles do not settle (Liehr et al., 2005). Polluted sediments thus appear to be unfavorable for this species (Leipe et al., 2005) and may negatively affect its biomineralization processes resulting in smaller BMUs. While *A. islandica* can survive low-oxygen conditions to some extent (Theede et al., 1969; Philipp et al., 2012), metabolic rates and ventilation rates decline substantially below dissolved oxygen (DO) concentrations of 5 mg L^{-1} (Taylor and Brand, 1975a,b). During hypoxia (i.e., DO <2 mg L^{-1}), res-

piration becomes anaerobic, so that body functions almost come to a complete halt (Oeschger, 1990; Strahl et al., 2011). The extrapallial fluid becomes increasingly acidified (Oeschger, 1990; Strahl et al., 2011), so that biomineralization stops. Since at the Baltic Sea, DO concentrations occasionally fell below 5 mg L^{-1}, but rarely below 2 mg L^{-1} (Supplement 4C), smaller BMUs may have been formed due to restricted body functions. Low and variable salinity likewise decreases shell growth rate (Hiebenthal et al., 2012) and shortens longevity (Begum et al., 2010). Hence, in the Baltic Sea, smaller BMUs may have been formed due to the low and variable salinity (approx. 19.2), when compared to that of all other studied localities (approx. 34.4; Supplement 4C). Even if the ultimate cause of the reduced BMU size at the Baltic Sea cannot be identified here, the smaller BMUs are likely the result of physiological stress.

To summarize, at Iceland and the Viking Bank, the BMU size was affected by changes in water temperature. The temperature sensitivity of BMU size was comparable among these localities (0.5–0.62 µm^2 °C^{-1}), suggesting that BMU-based temperature reconstructions can be completed in fully marine, unpolluted settings. The correlation between BMU size and temperature, however, was weak (Pearson r = 0.21–0.26 with monthly averages; 0.29 with daily temperature data) and did not occur at the other studied sites. In the deeper waters of the Norwegian Trench, temperature variability (approx. 1.2 °C) was likely too low to evoke significant microstructural changes, whereas at the Baltic Sea, temperature effects were probably overruled by environmental stressors such as the low and variable salinity and/or reduced dissolved oxygen content. BMU size ranges of individuals from the different sites did not reflect the temperature regimes in which they lived. This suggests, that BMU size is not solely controlled by temperature.

4.4.2 Physiological processes affecting BMU size

At all localities except the Baltic Sea, a weak positive link existed between BMU size and annual growth rate (Fig. 4.8C+D). BMU size ranges of specimens from the respective localities reflected shell growth rate ranges (Figs. 4.3E+4.4B). Moreover, in the hinge plate, BMU size and shell growth rate varied non-linearly through lifetime (Figs. 4.3C+4.5A,B). At first sight, this argues for a coupling between the shell growth rate and the BMU size. However, the following observations speak against this hypothesis. Firstly, the broadest annual increments were formed two to four years before the largest BMUs were produced (Fig. 4.9A). Secondly and more importantly, BMU sizes in the hinge plate were nearly the same as in the ventral margin (Fig. 4.7A), even though the latter grew about five times as fast (Höche et al., 2021a). Irrespective of whether a direct or

an indirect link exists, BMU size was evidently influenced by the physiology of the bivalve.

Perhaps, BMU size and shell growth are regulated by the same underlying biological processes, so that both parameters develop similar patterns over lifetime (Figs. 4.3C+4.5A,B) and are coupled to the same environmental variables (Fig. 4.8E). This hypothesis seems reasonable because both BMU size and shell growth are related to biomineralization performance. Bivalve biomineralization is controlled at many levels by the cellular activity of the organism, be it in production and secretion of the organic matrices, in the uptake and transport of carbonate precursor ions (i.e., Ca^{2+} and HCO_3^-), or in the establishment of the chemical boundary conditions necessary for mineralization (Wilbur and Saleuddin, 1983; Marin et al., 2012). Organic components, calcium ions and carbonate ions can be acquired via food uptake or filtration (Wilbur and Saleuddin, 1983; Marin et al., 2012), so that the supply of shell material is bound to the feeding and respiration activity of the bivalve as well as its assimilation efficiency (Winter, 1978). Furthermore, HCO_3^- ions can be hydrated from metabolized CO_2 (Marin et al., 2012), so that HCO_3^- supply is coupled to the metabolic rate. Metabolic energy also supports transmembrane Ca^{2+}-ATPase-pumps, which are required to transport Ca^{2+} ions (Carré et al., 2006) and to extrude them into the extrapallial fluid in order to reach supersaturation (Marin et al., 2012; Stemmer et al., 2019). Similar ATPase-pumps are also involved in the removal of H^+ from the calcification site for pH regulation (Marin et al., 2012; Stemmer et al., 2019). Since the bivalve metabolism supports these processes, improved metabolic rate ultimately results in accelerated shell growth and, perhaps, larger BMUs. This hypothesis seems plausible because numerous other proxy systems of biogenic carbonates are also influenced by metabolism. For example, it has been suggested that metabolism controls the Sr/Ca ratios and carbon stable isotope composition of aragonitic bivalve shells (Purton et al., 1999; Gillikin et al., 2005; Gillikin et al., 2007), including *A. islandica* (Schöne et al., 2011a; Wanamaker and Gillikin, 2019).

The increase of BMU size and shell growth rate during youth can be explained by changes in metabolic rate, as the latter increases with body mass following a power law (respiration = $a \times \text{mass}^{3/4}$; Fig. 4.9B; Kleiber, 1932; da Silva et al., 2006; Ballesteros et al., 2018). With increasing ontogenetic age, a larger amount of energy becomes available that could support the formation of larger BMUs and faster shell growth. However, BMU size and shell growth rate decrease after the age of ca. four to nine (Figs. 4.3C+4.5A,B), whereas metabolic rates of *A. islandica* do not seem to decline before the age of 100 (Begum et al., 2009; Basova et al., 2012). Moreover, while it was observed that *Mytilus edulis* down-regulate mitochondrial respiration, ATP production and pH regulation after ca. age five to six (Sukhotin and Pörtner, 2001; Sukhotin et al., 2020), this is likely

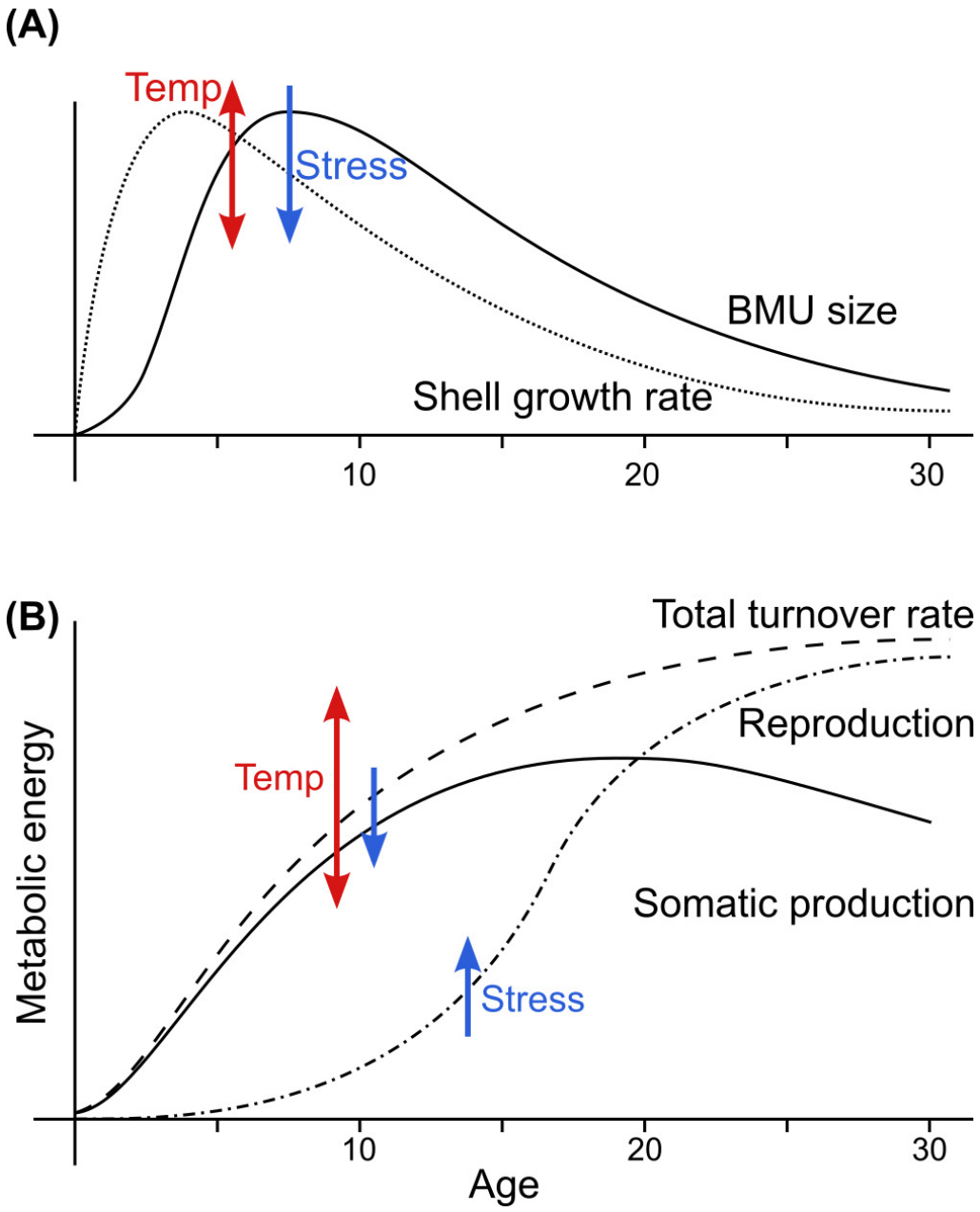

Figure 4.9 Interpretation of the coupling between the BMU size of *A. islandica* shells and early shifts in their metabolism. (A) Sketch of BMU size and shell growth rate patterns over lifetime observed in this study. Both parameters first increased then decreased over lifetime, with their maxima offset by two to four years. The levels of BMU size and shell growth rate as well as the amplitude of their changes over lifetime were increased by warmer temperature, whereas stressful environmental conditions led to a decrease. (B) Sketch of energetic developments during the early life stage of *A. islandica*, after Abele et al. (2008) and Begum et al. (2010). Somatic production (i.e., growth of shell and soft tissue) are prioritized at young age, causing the patterns seen in A. After reaching a sufficient size to escape predation, shell growth slows down because the metabolism prioritizes maturation and reproduction. For further explanations see text.

not the case in *A. islandica* (Begum et al., 2009). Decreases in BMU size and shell growth rate after age four and seven are thus not simply caused by a decrease in metabolic energy. Instead, according to dynamic energy budget models, during lifetime, *A. islandica* increasingly shifts its metabolic energy expenditure from shell production toward reproduction (Fig. 4.9B; Abele et al., 2008; Begum et al., 2010). Accordingly, ontogenetic patterns in BMU size and shell growth rate can reflect the amount of metabolic energy available for shell production, which reaches peak values during early stages of life (Begum et al., 2010; Ballesta-Artero et al., 2018b).

BMU size trends during the first ca. 20 years of life can thus correspond to the changing amount of energy available for shell growth. However, even if a direct link does not exist, an understanding of the early physiological developments of *A. islandica*, upon which the aforementioned metabolic budgets were based (Begum et al., 2010), can help to predict and detrend the 'ontogenetic bias' of the BMU sizes. Just after settlement of the larvae, metabolism and shell growth occur only at slow rate due to the small body size of the individuals (Fig. 4.9). However, during this early stage of life, shell growth also accelerates most rapidly, because it receives the largest proportion of the increasing metabolic power in order to improve individual survival chances (Kooijman and Kooijman, 2010; Ballesta-Artero et al., 2019). Accordingly, the shell of young *A. islandica* grows faster than its soft body (Murawski et al., 1982). Shell growth rate reaches a maximum already at around age four (Fig. 4.9). BMU sizes increase concurrently with the metabolic rate and shell growth rate, but formation of the largest BMUs is delayed by two to three years. Perhaps, larger BMUs can only form after the first few years of life, when lateral shell growth rates exceed a certain threshold. Once the shells are large enough to escape predation, shell growth becomes less important and metabolic priority shifts toward soft body growth and maturation (Fig. 4.9B; Kooijman and Kooijman, 2010). Accordingly, the maximum somatic production activity is attained after the formation of the largest BMUs. After maturation, shell growth reaches the negative asymptotic stage (Philipp and Abele, 2010) because the majority of available metabolic energy is now directed toward reproduction (Begum et al., 2010; Kooijman and Kooijman, 2010; Ballesta-Artero et al., 2019). However, the onset of sexual maturity varies greatly between localities and among specimens (Thompson et al., 1980b; Cargnelli, 1999; Thorarinsdottir and Steingrimsson, 2000), whereas BMU size maxima were always attained around age seven to nine (Fig. 4.5). Perhaps, not enough shells of each population were studied in order to portray the full temporal variation of the BMU size maxima. Still, ontogenetic BMU size patterns can be assessed relatively precisely by corresponding shell growth rates. Alternatively, the timing of ontogenetic BMU size changes can be assessed by habitat-specific models of metabo-

lic budgets or by estimates of longevity, age of maturation and shell size to escape the predation window.

Differences in BMU size range among individuals of the studied localities can also be explained by regional differences in shell growth and/or metabolic rate. At NE Iceland for example, BMUs were large and variable in size (Fig. 4.4A) and shells grew fast (Fig. 4.3C), due to the relatively warm and variable temperatures (Fig. 4.2B). Accordingly, the total metabolic throughput estimated for *A. islandica* of this locality is also quite large (approx. 43 700 kJ; Begum et al., 2010), because warmer temperatures increase metabolic performance (Gillooly et al., 2001). On the other hand, BMUs of specimens from the Baltic Sea were small despite substantial temperature variability (Figs. 4.2B+4.4B), which can be explained by the negative effects of low and variable salinity and/or DO content on the metabolism of *A. islandica* (Taylor and Brand, 1975b; Oeschger, 1990; Strahl et al., 2011; Basova et al., 2012; Hiebenthal et al., 2012), leading to slow shell growth and formation of smaller BMUs. Lower salinity and oxygen levels have also been found to impair metabolism and shell formation processes of other bivalve species (Sobral and Widdows, 1997; Sillanpää et al., 2020), supporting this hypothesis. Accordingly, estimated lifetime metabolic budgets of Baltic Sea populations are much lower than those of fully marine ones (~300 kJ at Kiel Bay, approx. 70 km NE' the site of this study; Begum et al., 2010). Mass-specific metabolic rates, filtration rates, and oxygen consumption rates, in contrast, are all enhanced under physiological stress (Taylor and Brand, 1975b; Basova et al., 2012). However, most of the excess metabolic energy is used for coping with stress and reproduction to ensure population survival (Begum et al., 2010), so that the amount of energy used for shell formation does not increase and BMUs remain small. Lastly, populations of low longevity show almost no metabolic reaction to warming (Begum et al., 2010; Basova et al., 2012) which could explain why Baltic Sea specimens lack a correlation between BMU size and temperature (Fig. 4.8A).

In summary, BMU size of *A. islandica* is strongly coupled to its physiology, which complicates temperature reconstructions based on the shell microstructure. Changes in BMU size during the first ca. 20 years of life corresponded to variations in shell growth rate and/or shifts in metabolic activity. This early stage of the shell growth record should thus be excluded in BMU-based proxy reconstructions in order to minimize ontogenetic bias. Suboptimal growth conditions, i.e., low salinity and/or low DO conditions, also prevented the formation of large BMUs, likely because physiological stress exerted a negative control on metabolism and shell growth. Hence, BMU size only serves as a temperature proxy in fully oxygenated, fully marine settings.

4.4.3 BMU size across different shell portions and microstructures

The different microstructure types formed BMUs of distinct size and shape. Under the same environmental conditions and at the same ontogenetic age, BMUs of homogeneous microstructure are comparatively small, FCCL BMUs are moderately sized with little size variation but highly elongated, and CA BMUs are larger and more variable in size and of moderate elongation (Figs. 4.4B+4.7B). Within one individual, BMUs of the same microstructure formed at the same time varied only slightly in size, regardless of shell portion (hinge and ventral margin) or position within the shell layer (Figs. 4.6+4.7), except for two increments of specimen ICE06-6.2-A6R. If BMU size is indeed coupled to the metabolism, the size heterogeneity within these increments might be caused by variations of metabolic rate in different portions of the mantle. A similar effect exists, for example, in Mytilus edulis, where at lateral margins, trace element incorporation into the shell is more strongly controlled by metabolism than along the ventral margin (Klein et al., 1996). However, only the seventh increment of the hinge plate of ICE06-6.2-A6R was substantially curved (Fig. 4.6A), whereas increment eight was not. Still, BMU sizes of different transects through increment eight correlated poorly, so that variations in shell curvature and associated changes in metabolism cannot explain the BMU size heterogeneity.

Baltic Sea specimens formed FCCL microstructures much more frequently than specimens of the other localities, at which CA was predominantly deposited. Since FCCL BMUs are smaller than those of CA microstructures (Fig. 4.4B), BMU size data of Baltic Sea specimens are generally lower than that of the remaining studied localities. Perhaps, correction factors can be applied to facilitate comparisons of BMU size data of different microstructures. Interestingly, FCCL microstructures were mostly formed after disturbance lines and annual lines, i.e., during times of slow shell growth and reduced biomineralization rate. This aligns with the hypothesis that physiological stress reduces metabolism and leads to the formation of small BMUs. Environmental stressors likely evoked the formation of an entirely different microstructure (FCCL instead of CA), as was previously postulated in other studies (Prezant et al., 1988; Tan Tiu and Prezant, 1989; Dunca et al., 2009).

To summarize, each microstructure type (homogeneous, crossed-acicular and fine complex crossed-lamellar) exhibits a specific BMU size range. In order to use BMU size as a proxy for temperature or other environmental or physiological variables, respective measurements should be completed in microstructurally identical shell portions (e.g., CA in iOSL and hinge plate). Otherwise, corrections may be needed. When selecting shell portions for BMU-based proxy recon-

structions, higher temporal resolution can be achieved in the ventral margin than in the hinge plate. However, due to microstructural gradation of the ventral margin of *A. islandica*, preparation quality varied more strongly and image targeting was more challenging to accomplish than in the hinge plate.

4.5 Conclusions

The BMU size of *A. islandica* shells increased with water temperature at NE Iceland and the Viking Bank. Temperature sensitivity of BMU size was comparably strong at these localities, but the size ranges at the two habitats did not reflect the regional temperature regimes, so that the BMU size may only serve as a proxy for relative temperature changes. Furthermore, in the Norwegian Trench, temperature variability (approx. 1.2 °C) was likely too low to trigger significant microstuctural changes, or BMU size was controlled more strongly by changes in food availability. In the Baltic Sea, BMUs did not grow significantly larger in warmer waters, despite strong temperature variation. Most probably, challenging environmental conditions encountered at the Baltic Sea, i.e., reduced and variable salinity and/or oxygen levels, led to significantly reduced biomineralization performance and significantly smaller BMUs. As such, the BMU size might only be used as a temperature proxy at undisturbed, fully marine sites.

Furthermore, the BMU size of all specimens changed similarly with age, with the largest units being formed at around age seven to nine. The ontogenetic changes in BMU size covary with those of the shell growth rate and metabolic energy used for shell production. BMU size patterns during the first ca. 20 years prevent the reconstruction of meaningful temperature information during this stage of life. Perhaps, shell growth rate data or metabolic models can be used to constrain the ontogenetic BMU size bias. Alternatively, temperature estimates without ontogenetic bias and with reasonable error ranges could be obtained if only BMUs from the mature stage of the shell growth record were considered.

This study highlights the value of quantitative microstructural mapping of biogenic carbonates to assess the interplay of environmental conditions and shell formation processes. Resource-efficient SEM imaging and user-friendly machine learning applications were able to enable a wide range of new applications in paleoclimatology and biomineralization research. Still, the development of three-dimensional imaging techniques with sub-µm resolution is desirable to overcome the limitations of two-dimensional SEM analysis.

4.6 Supplementary material

Supplement 4A - Sampling details

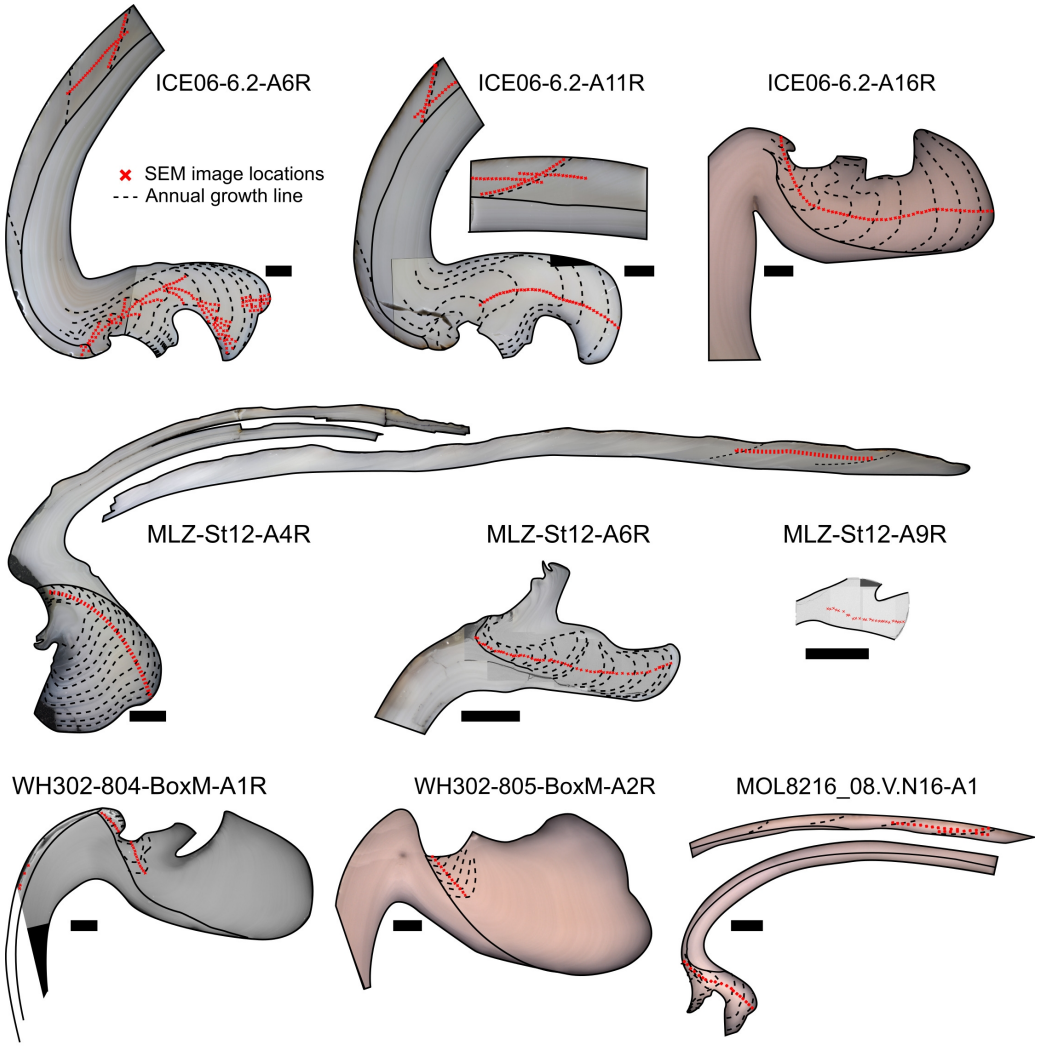

Figure S4.1 Studied shell material of *Arctica islandica*. Annual growth lines are shown as red dashed lines. Red crosses and trades indicate SEM image locartions. Scale bars are 1 mm.

Supplement 4B - Stable oxygen isotope-based intra-annual growth model

Table S4.1 Stable oxygen isotope based daily intra-annual growth model. Growth given as (% of annual growth).

Date	Iceland (10–20 m)		Norwegian Trench (242 m)		Viking Banks (100 m)		Baltic Sea (25 m)	
	daily growth rate	cumulative growth	daily growth rate	cumulative growth	daily growth rate	cumulative growth	daily growth rate	cumulative growth
2020-09-25	0.000	0.000	0.000	0.000	0.000	0.000	0.009	0.009
2020-09-26	0.000	0.000	0.000	0.000	0.000	0.000	0.009	0.017
2020-09-27	0.000	0.000	0.000	0.000	0.000	0.000	0.009	0.026
2020-09-28	0.000	0.000	0.000	0.000	0.000	0.000	0.009	0.034
2020-09-29	0.000	0.000	0.000	0.000	0.000	0.000	0.009	0.043
2020-09-30	0.000	0.000	0.000	0.000	0.000	0.000	0.009	0.051
2020-10-01	0.000	0.000	0.000	0.000	0.000	0.000	0.009	0.060
2020-10-02	0.000	0.000	0.000	0.000	0.000	0.000	0.009	0.068
2020-10-03	0.000	0.000	0.000	0.000	0.000	0.000	0.009	0.077
2020-10-04	0.000	0.000	0.000	0.000	0.000	0.000	0.009	0.085
2020-10-05	0.000	0.000	0.000	0.000	0.000	0.000	0.009	0.094
2020-10-06	0.000	0.000	0.000	0.000	0.000	0.000	0.009	0.102
2020-10-07	0.000	0.000	0.000	0.000	0.000	0.000	0.009	0.111
2020-10-08	0.000	0.000	0.000	0.000	0.000	0.000	0.009	0.119
2020-10-09	0.000	0.000	0.000	0.000	0.000	0.000	0.009	0.128
2020-10-10	0.000	0.000	0.000	0.000	0.000	0.000	0.043	0.171
2020-10-11	0.000	0.000	0.000	0.000	0.000	0.000	0.233	0.403
2020-10-12	0.000	0.000	0.000	0.000	0.000	0.000	0.233	0.636
2020-10-13	0.000	0.000	0.000	0.000	0.000	0.000	0.233	0.869

2020-10-14	0.000	0.000	0.000	0.000	0.000	0.000	0.233	1.101
2020-10-15	0.117	0.105	0.000	0.000	0.000	0.000	0.233	1.334
2020-10-16	0.115	0.208	0.000	0.000	0.000	0.000	0.233	1.567
2020-10-17	0.113	0.309	0.000	0.000	0.000	0.000	0.233	1.799
2020-10-18	0.111	0.408	0.000	0.000	0.000	0.000	0.233	2.032
2020-10-19	0.109	0.506	0.000	0.000	0.000	0.000	0.233	2.265
2020-10-20	0.107	0.602	0.000	0.000	0.000	0.000	0.233	2.497
2020-10-21	0.105	0.696	0.000	0.000	0.000	0.000	0.241	2.738
2020-10-22	0.103	0.789	0.000	0.000	0.000	0.000	0.241	2.979
2020-10-23	0.101	0.879	0.000	0.000	0.000	0.000	0.241	3.220
2020-10-24	0.099	0.968	0.000	0.000	0.000	0.000	0.241	3.460
2020-10-25	0.097	1.056	0.000	0.000	0.000	0.000	0.241	3.701
2020-10-26	0.095	1.141	0.000	0.000	0.000	0.000	0.241	3.942
2020-10-27	0.093	1.225	0.000	0.000	0.000	0.000	0.241	4.183
2020-10-28	0.093	1.309	0.000	0.000	0.000	0.000	0.241	4.424
2020-10-29	0.093	1.392	0.000	0.000	0.000	0.000	0.241	4.665
2020-10-30	0.092	1.475	0.000	0.000	0.000	0.000	0.241	4.905
2020-10-31	0.092	1.557	0.000	0.000	0.000	0.000	0.241	5.146
2020-11-01	0.092	1.640	0.000	0.000	0.000	0.000	0.241	5.387
2020-11-02	0.092	1.722	0.000	0.000	0.000	0.000	0.224	5.611
2020-11-03	0.092	1.805	0.000	0.000	0.000	0.000	0.224	5.834
2020-11-04	0.092	1.888	0.000	0.000	0.000	0.000	0.224	6.058
2020-11-05	0.092	1.970	0.000	0.000	0.000	0.000	0.224	6.281
2020-11-06	0.092	2.053	0.000	0.000	0.000	0.000	0.224	6.505
2020-11-07	0.092	2.136	0.000	0.000	0.000	0.000	0.224	6.728
2020-11-08	0.092	2.220	0.000	0.000	0.000	0.000	0.224	6.952
2020-11-09	0.092	2.303	0.000	0.000	0.000	0.000	0.224	7.175
2020-11-10	0.092	2.386	0.000	0.000	0.000	0.000	0.224	7.399
2020-11-11	0.093	2.470	0.000	0.000	0.000	0.000	0.224	7.623
2020-11-12	0.093	2.555	0.000	0.000	0.000	0.000	0.224	7.846
2020-11-13	0.094	2.639	0.000	0.000	0.000	0.000	0.224	8.070
2020-11-14	0.094	2.725	0.000	0.000	0.000	0.000	0.224	8.293
2020-11-15	0.095	2.811	0.000	0.000	0.000	0.000	0.224	8.517

2020-11-16	0.096	2.897	0.000	0.000	0.000	0.000	0.224	8.740
2020-11-17	0.096	2.984	0.000	0.000	0.000	0.000	0.224	8.964
2020-11-18	0.097	3.072	0.000	0.000	0.000	0.000	0.224	9.188
2020-11-19	0.097	3.160	0.000	0.000	0.000	0.000	0.224	9.411
2020-11-20	0.098	3.248	0.000	0.000	0.000	0.000	0.224	9.635
2020-11-21	0.098	3.337	0.000	0.000	0.000	0.000	0.224	9.858
2020-11-22	0.099	3.427	0.000	0.000	0.000	0.000	0.224	10.082
2020-11-23	0.100	3.517	0.000	0.000	0.000	0.000	0.224	10.305
2020-11-24	0.100	3.608	0.000	0.000	0.000	0.000	0.224	10.529
2020-11-25	0.101	3.699	0.000	0.000	0.000	0.000	0.224	10.753
2020-11-26	0.101	3.791	0.000	0.000	0.000	0.000	0.224	10.976
2020-11-27	0.102	3.883	0.000	0.000	0.000	0.000	0.224	11.200
2020-11-28	0.103	3.977	0.000	0.000	0.000	0.000	0.224	11.423
2020-11-29	0.103	4.070	0.000	0.000	0.000	0.000	0.224	11.647
2020-11-30	0.104	4.164	0.000	0.000	0.000	0.000	0.224	11.870
2020-12-01	0.105	4.259	0.000	0.000	0.000	0.000	0.224	12.094
2020-12-02	0.105	4.354	0.000	0.000	0.000	0.000	0.433	12.527
2020-12-03	0.105	4.450	0.000	0.000	0.000	0.000	0.433	12.959
2020-12-04	0.106	4.546	0.000	0.000	0.000	0.000	0.433	13.392
2020-12-05	0.106	4.642	0.000	0.000	0.000	0.000	0.433	13.824
2020-12-06	0.107	4.738	0.000	0.000	0.000	0.000	0.433	14.257
2020-12-07	0.107	4.835	0.000	0.000	0.000	0.000	0.433	14.690
2020-12-08	0.107	4.932	0.000	0.000	0.000	0.000	0.433	15.122
2020-12-09	0.108	5.029	0.000	0.000	0.000	0.000	0.433	15.555
2020-12-10	0.108	5.127	0.000	0.000	0.000	0.000	0.433	15.988
2020-12-11	0.108	5.225	0.000	0.000	0.000	0.000	0.375	16.363
2020-12-12	0.109	5.324	0.000	0.000	0.000	0.000	0.375	16.738
2020-12-13	0.109	5.422	0.000	0.000	0.000	0.000	0.375	17.114
2020-12-14	0.110	5.521	0.000	0.000	0.000	0.000	0.375	17.489
2020-12-15	0.110	5.621	0.000	0.000	0.000	0.000	0.375	17.865
2020-12-16	0.111	5.721	0.000	0.000	0.000	0.000	0.473	18.338
2020-12-17	0.111	5.821	0.000	0.000	0.000	0.000	0.473	18.811
2020-12-18	0.112	5.923	0.000	0.000	0.000	0.000	0.473	19.285

2020-12-19	0.113	6.025	0.000	0.000	0.000	0.000	0.473	19.758
2020-12-20	0.113	6.127	0.000	0.000	0.000	0.000	0.473	20.231
2020-12-21	0.114	6.231	0.000	0.000	0.000	0.000	0.424	20.656
2020-12-22	0.115	6.335	0.000	0.000	0.000	0.000	0.424	21.080
2020-12-23	0.116	6.439	0.000	0.000	0.000	0.000	0.424	21.504
2020-12-24	0.116	6.545	0.000	0.000	0.000	0.000	0.424	21.928
2020-12-25	0.117	6.651	0.000	0.000	0.000	0.000	0.424	22.353
2020-12-26	0.118	6.757	0.000	0.000	0.000	0.000	0.419	22.772
2020-12-27	0.118	6.864	0.000	0.000	0.000	0.000	0.419	23.191
2020-12-28	0.119	6.972	0.000	0.000	0.000	0.000	0.419	23.611
2020-12-29	0.120	7.081	0.000	0.000	0.000	0.000	0.419	24.030
2020-12-30	0.121	7.190	0.000	0.000	0.000	0.000	0.419	24.450
2020-12-31	0.121	7.300	0.000	0.000	0.000	0.000	0.563	25.012
2021-01-01	0.122	7.411	0.000	0.000	0.000	0.000	0.411	25.423
2021-01-02	0.123	7.522	0.000	0.000	0.000	0.000	0.411	25.834
2021-01-03	0.123	7.633	0.000	0.000	0.000	0.000	0.411	26.245
2021-01-04	0.124	7.745	0.000	0.000	0.000	0.000	0.411	26.656
2021-01-05	0.125	7.858	0.000	0.000	0.000	0.000	0.411	27.067
2021-01-06	0.125	7.972	0.000	0.000	0.000	0.000	0.505	27.572
2021-01-07	0.126	8.086	0.000	0.000	0.000	0.000	0.505	28.077
2021-01-08	0.126	8.200	0.000	0.000	0.000	0.000	0.505	28.582
2021-01-09	0.127	8.315	0.000	0.000	0.000	0.000	0.505	29.087
2021-01-10	0.128	8.431	0.000	0.000	0.000	0.000	0.593	29.680
2021-01-11	0.128	8.547	0.000	0.000	0.000	0.000	0.549	30.229
2021-01-12	0.129	8.664	0.000	0.000	0.000	0.000	0.549	30.778
2021-01-13	0.129	8.781	0.000	0.000	0.000	0.000	0.549	31.328
2021-01-14	0.130	8.899	0.000	0.000	0.000	0.000	0.549	31.877
2021-01-15	0.130	9.017	0.000	0.000	0.259	0.195	0.549	32.426
2021-01-16	0.131	9.135	0.000	0.000	0.261	0.391	0.514	32.940
2021-01-17	0.131	9.254	0.000	0.000	0.263	0.589	0.514	33.454
2021-01-18	0.132	9.373	0.000	0.000	0.266	0.789	0.514	33.968
2021-01-19	0.132	9.493	0.000	0.000	0.268	0.991	0.514	34.481
2021-01-20	0.133	9.613	0.000	0.000	0.271	1.194	0.514	34.995

2021-01-21	0.133	9.733	0.000	0.000	0.273	1.400	0.514	35.509
2021-01-22	0.133	9.854	0.000	0.000	0.275	1.607	0.514	36.023
2021-01-23	0.134	9.975	0.000	0.000	0.278	1.815	0.514	36.537
2021-01-24	0.134	10.096	0.000	0.000	0.280	2.026	0.514	37.051
2021-01-25	0.134	10.217	0.000	0.000	0.282	2.238	0.357	37.407
2021-01-26	0.135	10.339	0.000	0.000	0.285	2.452	0.357	37.764
2021-01-27	0.135	10.461	0.000	0.000	0.287	2.668	0.357	38.121
2021-01-28	0.135	10.583	0.000	0.000	0.289	2.885	0.357	38.477
2021-01-29	0.135	10.706	0.000	0.000	0.292	3.105	0.324	38.801
2021-01-30	0.136	10.828	0.000	0.000	0.294	3.326	0.324	39.124
2021-01-31	0.136	10.951	0.000	0.000	0.296	3.549	0.346	39.471
2021-02-01	0.136	11.073	0.000	0.000	0.299	3.773	0.346	39.817
2021-02-02	0.135	11.196	0.000	0.000	0.301	3.999	0.346	40.163
2021-02-03	0.135	11.318	0.000	0.000	0.303	4.227	0.346	40.510
2021-02-04	0.135	11.440	0.000	0.000	0.306	4.457	0.346	40.856
2021-02-05	0.135	11.562	0.000	0.000	0.308	4.689	0.346	41.202
2021-02-06	0.135	11.683	0.000	0.000	0.311	4.922	0.346	41.549
2021-02-07	0.135	11.805	0.000	0.000	0.313	5.157	0.346	41.895
2021-02-08	0.134	11.926	0.000	0.000	0.315	5.394	0.346	42.241
2021-02-09	0.134	12.046	0.000	0.000	0.318	5.633	0.346	42.587
2021-02-10	0.134	12.167	0.000	0.000	0.320	5.873	0.346	42.934
2021-02-11	0.135	12.288	0.000	0.000	0.322	6.115	0.478	43.412
2021-02-12	0.135	12.410	0.000	0.000	0.325	6.359	0.478	43.891
2021-02-13	0.136	12.532	0.000	0.000	0.326	6.604	0.478	44.369
2021-02-14	0.137	12.655	0.000	0.000	0.327	6.849	0.478	44.848
2021-02-15	0.138	12.780	0.202	0.180	0.328	7.096	0.478	45.326
2021-02-16	0.139	12.904	0.206	0.363	0.329	7.344	0.478	45.805
2021-02-17	0.139	13.030	0.210	0.550	0.331	7.592	0.478	46.283
2021-02-18	0.140	13.156	0.213	0.741	0.332	7.842	0.478	46.762
2021-02-19	0.141	13.283	0.217	0.934	0.333	8.092	0.478	47.240
2021-02-20	0.142	13.411	0.221	1.132	0.334	8.344	0.494	47.734
2021-02-21	0.143	13.540	0.225	1.333	0.336	8.596	0.408	48.142
2021-02-22	0.143	13.669	0.229	1.537	0.337	8.850	0.408	48.550

2021-02-23	0.144	13.799	0.233	1.745	0.337	9.103	0.408	48.957
2021-02-24	0.145	13.930	0.237	1.957	0.337	9.356	0.408	49.365
2021-02-25	0.146	14.062	0.241	2.172	0.337	9.609	0.408	49.773
2021-02-26	0.147	14.194	0.245	2.390	0.337	9.862	0.408	50.181
2021-02-27	0.147	14.327	0.249	2.612	0.337	10.115	0.408	50.589
2021-02-28	0.148	14.461	0.253	2.838	0.337	10.368	0.408	50.997
2021-03-01	0.149	14.596	0.257	3.067	0.337	10.620	0.408	51.404
2021-03-02	0.148	14.730	0.261	3.299	0.337	10.873	0.408	51.812
2021-03-03	0.147	14.862	0.265	3.535	0.338	11.125	0.408	52.220
2021-03-04	0.146	14.994	0.269	3.775	0.338	11.377	0.408	52.628
2021-03-05	0.145	15.124	0.273	4.018	0.338	11.629	0.408	53.036
2021-03-06	0.144	15.254	0.277	4.264	0.338	11.881	0.408	53.444
2021-03-07	0.143	15.382	0.281	4.514	0.338	12.133	0.333	53.776
2021-03-08	0.142	15.509	0.285	4.768	0.338	12.385	0.333	54.109
2021-03-09	0.141	15.635	0.289	5.025	0.338	12.637	0.333	54.442
2021-03-10	0.140	15.760	0.293	5.286	0.338	12.888	0.333	54.774
2021-03-11	0.140	15.886	0.295	5.548	0.338	13.140	0.266	55.040
2021-03-12	0.141	16.012	0.297	5.811	0.338	13.391	0.266	55.306
2021-03-13	0.142	16.139	0.298	6.076	0.338	13.642	0.266	55.572
2021-03-14	0.143	16.267	0.300	6.342	0.338	13.893	0.266	55.838
2021-03-15	0.143	16.396	0.302	6.610	0.338	14.144	0.266	56.103
2021-03-16	0.147	16.527	0.304	6.878	0.338	14.394	0.266	56.369
2021-03-17	0.150	16.661	0.306	7.149	0.338	14.644	0.266	56.635
2021-03-18	0.153	16.798	0.307	7.421	0.338	14.894	0.266	56.901
2021-03-19	0.157	16.938	0.309	7.694	0.337	15.144	0.266	57.167
2021-03-20	0.160	17.081	0.311	7.968	0.337	15.393	0.266	57.433
2021-03-21	0.164	17.228	0.313	8.244	0.337	15.642	0.398	57.830
2021-03-22	0.169	17.378	0.315	8.521	0.337	15.890	0.398	58.228
2021-03-23	0.174	17.533	0.316	8.800	0.336	16.138	0.398	58.626
2021-03-24	0.178	17.692	0.318	9.080	0.336	16.386	0.398	59.024
2021-03-25	0.183	17.855	0.320	9.362	0.336	16.634	0.398	59.422
2021-03-26	0.187	18.022	0.322	9.644	0.336	16.881	0.361	59.783
2021-03-27	0.192	18.193	0.324	9.929	0.335	17.128	0.361	60.144

2021-03-28	0.197	18.368	0.325	10.214	0.335	17.374	0.361	60.506
2021-03-29	0.201	18.547	0.327	10.501	0.335	17.621	0.361	60.867
2021-03-30	0.206	18.730	0.329	10.790	0.335	17.867	0.361	61.228
2021-03-31	0.211	18.917	0.331	11.079	0.335	18.113	0.361	61.589
2021-04-01	0.215	19.109	0.332	11.371	0.335	18.360	0.361	61.950
2021-04-02	0.220	19.304	0.334	11.663	0.336	18.606	0.271	62.221
2021-04-03	0.225	19.504	0.336	11.957	0.336	18.853	0.271	62.492
2021-04-04	0.230	19.708	0.338	12.252	0.336	19.100	0.271	62.763
2021-04-05	0.235	19.917	0.340	12.549	0.336	19.347	0.271	63.034
2021-04-06	0.240	20.129	0.341	12.847	0.336	19.594	0.271	63.305
2021-04-07	0.244	20.346	0.343	13.147	0.337	19.841	0.271	63.576
2021-04-08	0.249	20.567	0.345	13.448	0.337	20.088	0.271	63.847
2021-04-09	0.254	20.792	0.347	13.750	0.337	20.335	0.271	64.118
2021-04-10	0.259	21.022	0.349	14.054	0.337	20.582	0.271	64.389
2021-04-11	0.264	21.256	0.353	14.362	0.337	20.829	0.271	64.660
2021-04-12	0.269	21.494	0.358	14.674	0.337	21.077	0.271	64.931
2021-04-13	0.274	21.737	0.363	14.990	0.338	21.324	0.271	65.202
2021-04-14	0.279	21.984	0.368	15.311	0.337	21.572	0.271	65.473
2021-04-15	0.284	22.235	0.373	15.635	0.337	21.819	0.271	65.744
2021-04-16	0.289	22.491	0.377	15.964	0.337	22.066	0.179	65.923
2021-04-17	0.293	22.751	0.382	16.297	0.336	22.312	0.179	66.102
2021-04-18	0.298	23.015	0.387	16.635	0.336	22.559	0.179	66.280
2021-04-19	0.303	23.283	0.392	16.976	0.336	22.805	0.179	66.459
2021-04-20	0.308	23.555	0.397	17.322	0.336	23.051	0.179	66.637
2021-04-21	0.313	23.831	0.401	17.672	0.335	23.297	0.206	66.843
2021-04-22	0.317	24.112	0.406	18.026	0.335	23.543	0.206	67.049
2021-04-23	0.322	24.397	0.411	18.385	0.335	23.788	0.206	67.255
2021-04-24	0.327	24.686	0.416	18.747	0.335	24.033	0.206	67.461
2021-04-25	0.332	24.980	0.421	19.114	0.334	24.278	0.206	67.667
2021-04-26	0.337	25.277	0.425	19.485	0.334	24.523	0.206	67.873
2021-04-27	0.342	25.579	0.430	19.860	0.334	24.768	0.206	68.079
2021-04-28	0.347	25.885	0.435	20.240	0.333	25.012	0.206	68.285
2021-04-29	0.351	26.196	0.440	20.623	0.333	25.257	0.206	68.491

2021-04-30	0.356	26.510	0.445	21.011	0.333	25.501	0.206	68.697
2021-05-01	0.365	26.833	0.449	21.403	0.333	25.745	0.206	68.903
2021-05-02	0.374	27.164	0.457	21.802	0.332	25.988	0.206	69.110
2021-05-03	0.383	27.504	0.464	22.207	0.332	26.232	0.206	69.316
2021-05-04	0.395	27.854	0.472	22.619	0.332	26.475	0.206	69.522
2021-05-05	0.407	28.214	0.479	23.038	0.332	26.719	0.206	69.728
2021-05-06	0.418	28.585	0.487	23.463	0.332	26.962	0.206	69.935
2021-05-07	0.430	28.967	0.494	23.895	0.332	27.205	0.206	70.141
2021-05-08	0.442	29.359	0.501	24.334	0.332	27.449	0.206	70.347
2021-05-09	0.453	29.762	0.509	24.779	0.332	27.692	0.206	70.554
2021-05-10	0.465	30.176	0.516	25.231	0.332	27.936	0.206	70.760
2021-05-11	0.479	30.602	0.524	25.689	0.334	28.181	0.206	70.966
2021-05-12	0.493	31.041	0.531	26.154	0.336	28.427	0.206	71.172
2021-05-13	0.508	31.493	0.538	26.626	0.337	28.676	0.206	71.379
2021-05-14	0.522	31.958	0.546	27.105	0.339	28.926	0.206	71.585
2021-05-15	0.536	32.436	0.553	27.590	0.340	29.177	0.206	71.791
2021-05-16	0.550	32.927	0.545	28.067	0.342	29.430	0.206	71.997
2021-05-17	0.564	33.430	0.537	28.537	0.343	29.684	0.206	72.204
2021-05-18	0.579	33.946	0.529	28.999	0.345	29.940	0.206	72.410
2021-05-19	0.590	34.472	0.521	29.453	0.347	30.198	0.206	72.616
2021-05-20	0.601	35.008	0.513	29.900	0.348	30.457	0.206	72.823
2021-05-21	0.605	35.547	0.504	30.339	0.350	30.717	0.223	73.045
2021-05-22	0.609	36.090	0.496	30.770	0.351	30.979	0.223	73.268
2021-05-23	0.610	36.632	0.486	31.191	0.353	31.243	0.223	73.491
2021-05-24	0.597	37.163	0.475	31.603	0.354	31.508	0.223	73.713
2021-05-25	0.583	37.680	0.465	32.004	0.356	31.774	0.223	73.936
2021-05-26	0.574	38.189	0.464	32.404	0.357	32.042	0.223	74.159
2021-05-27	0.584	38.708	0.462	32.803	0.359	32.312	0.223	74.381
2021-05-28	0.595	39.235	0.461	33.200	0.360	32.583	0.223	74.604
2021-05-29	0.604	39.771	0.460	33.596	0.362	32.856	0.223	74.827
2021-05-30	0.614	40.316	0.459	33.990	0.363	33.130	0.223	75.049
2021-05-31	0.628	40.875	0.458	34.383	0.365	33.406	0.223	75.272
2021-06-01	0.643	41.447	0.456	34.775	0.366	33.683	0.223	75.495

2021-06-02	0.664	42.039	0.455	35.165	0.368	33.962	0.223	75.717
2021-06-03	0.677	42.642	0.454	35.554	0.370	34.242	0.223	75.940
2021-06-04	0.685	43.252	0.453	35.942	0.371	34.524	0.223	76.163
2021-06-05	0.693	43.869	0.452	36.328	0.373	34.807	0.223	76.386
2021-06-06	0.700	44.492	0.451	36.713	0.374	35.092	0.223	76.608
2021-06-07	0.718	45.132	0.449	37.096	0.376	35.378	0.223	76.831
2021-06-08	0.736	45.789	0.448	37.479	0.377	35.666	0.223	77.054
2021-06-09	0.755	46.462	0.447	37.859	0.379	35.955	0.223	77.276
2021-06-10	0.762	47.141	0.446	38.239	0.380	36.246	0.223	77.499
2021-06-11	0.814	47.871	0.445	38.616	0.382	36.539	0.389	77.888
2021-06-12	0.866	48.651	0.444	38.993	0.383	36.832	0.389	78.278
2021-06-13	0.877	49.441	0.442	39.367	0.388	37.130	0.389	78.667
2021-06-14	0.888	50.242	0.440	39.740	0.392	37.430	0.389	79.056
2021-06-15	0.899	51.052	0.438	40.110	0.397	37.735	0.389	79.446
2021-06-16	0.899	51.863	0.436	40.478	0.402	38.042	0.367	79.813
2021-06-17	0.898	52.673	0.434	40.846	0.406	38.353	0.367	80.180
2021-06-18	0.897	53.483	0.432	41.212	0.411	38.667	0.367	80.547
2021-06-19	0.788	54.185	0.430	41.577	0.418	38.987	0.367	80.915
2021-06-20	0.787	54.887	0.428	41.940	0.424	39.312	0.367	81.282
2021-06-21	0.774	55.578	0.427	42.302	0.431	39.643	0.174	81.456
2021-06-22	0.761	56.256	0.425	42.663	0.438	39.980	0.174	81.630
2021-06-23	0.747	56.922	0.423	43.022	0.445	40.321	0.174	81.805
2021-06-24	0.738	57.580	0.421	43.380	0.451	40.669	0.174	81.979
2021-06-25	0.729	58.230	0.419	43.737	0.458	41.021	0.174	82.153
2021-06-26	0.725	58.876	0.417	44.092	0.465	41.379	0.174	82.327
2021-06-27	0.721	59.517	0.415	44.446	0.472	41.743	0.174	82.502
2021-06-28	0.783	60.215	0.414	44.799	0.478	42.112	0.174	82.676
2021-06-29	0.850	60.972	0.412	45.150	0.485	42.487	0.174	82.850
2021-06-30	0.866	61.745	0.410	45.500	0.492	42.867	0.174	83.024
2021-07-01	0.882	62.531	0.410	45.850	0.499	43.253	0.214	83.238
2021-07-02	0.882	63.318	0.410	46.200	0.505	43.644	0.231	83.469
2021-07-03	0.883	64.104	0.411	46.551	0.512	44.041	0.231	83.700
2021-07-04	0.946	64.949	0.413	46.904	0.519	44.443	0.231	83.931

2021-07-05	1.003	65.847	0.415	47.259	0.526	44.850	0.231	84.162
2021-07-06	0.994	66.738	0.418	47.617	0.533	45.264	0.231	84.393
2021-07-07	0.986	67.622	0.420	47.976	0.539	45.682	0.231	84.624
2021-07-08	0.978	68.499	0.422	48.338	0.546	46.106	0.231	84.856
2021-07-09	0.970	69.370	0.425	48.702	0.553	46.536	0.231	85.087
2021-07-10	0.962	70.233	0.427	49.068	0.560	46.971	0.231	85.318
2021-07-11	0.959	71.095	0.429	49.437	0.566	47.411	0.231	85.549
2021-07-12	0.956	71.953	0.432	49.808	0.573	47.857	0.231	85.780
2021-07-13	0.827	72.691	0.434	50.181	0.575	48.306	0.231	86.011
2021-07-14	0.829	73.430	0.436	50.556	0.577	48.757	0.231	86.242
2021-07-15	0.831	74.170	0.439	50.933	0.572	49.204	0.231	86.473
2021-07-16	0.811	74.891	0.440	51.312	0.568	49.648	0.231	86.704
2021-07-17	0.788	75.591	0.442	51.691	0.563	50.087	0.231	86.935
2021-07-18	0.674	76.187	0.443	52.072	0.558	50.523	0.231	87.166
2021-07-19	0.621	76.735	0.445	52.453	0.554	50.955	0.231	87.397
2021-07-20	0.568	77.234	0.446	52.836	0.549	51.383	0.231	87.628
2021-07-21	0.563	77.729	0.448	53.220	0.544	51.807	0.231	87.859
2021-07-22	0.558	78.221	0.449	53.605	0.539	52.227	0.231	88.090
2021-07-23	0.553	78.708	0.451	53.991	0.535	52.644	0.231	88.321
2021-07-24	0.549	79.191	0.452	54.378	0.530	53.056	0.231	88.552
2021-07-25	0.537	79.665	0.453	54.765	0.525	53.465	0.231	88.783
2021-07-26	0.539	80.139	0.455	55.154	0.521	53.870	0.231	89.014
2021-07-27	0.541	80.615	0.456	55.544	0.516	54.271	0.231	89.245
2021-07-28	0.544	81.093	0.458	55.935	0.523	54.676	0.231	89.476
2021-07-29	0.551	81.577	0.459	56.327	0.530	55.084	0.231	89.707
2021-07-30	0.559	82.066	0.460	56.720	0.537	55.495	0.231	89.938
2021-07-31	0.566	82.561	0.466	57.117	0.545	55.911	0.231	90.169
2021-08-01	0.574	83.061	0.472	57.519	0.552	56.330	0.231	90.400
2021-08-02	0.585	83.571	0.477	57.925	0.563	56.755	0.217	90.618
2021-08-03	0.599	84.091	0.483	58.335	0.573	57.187	0.217	90.835
2021-08-04	0.587	84.602	0.488	58.749	0.584	57.626	0.217	91.053
2021-08-05	0.575	85.105	0.494	59.168	0.594	58.071	0.217	91.270
2021-08-06	0.563	85.599	0.499	59.591	0.605	58.522	0.217	91.487

2021-08-07	0.550	86.084	0.505	60.019	0.616	58.981	0.217	91.705
2021-08-08	0.538	86.560	0.510	60.451	0.626	59.446	0.217	91.922
2021-08-09	0.522	87.024	0.516	60.887	0.637	59.917	0.217	92.140
2021-08-10	0.505	87.475	0.521	61.328	0.647	60.395	0.217	92.357
2021-08-11	0.498	87.919	0.527	61.772	0.658	60.880	0.257	92.614
2021-08-12	0.491	88.357	0.532	62.222	0.669	61.371	0.257	92.871
2021-08-13	0.476	88.781	0.538	62.675	0.679	61.869	0.257	93.127
2021-08-14	0.461	89.190	0.543	63.133	0.690	62.374	0.257	93.384
2021-08-15	0.447	89.586	0.549	63.595	0.700	62.885	0.257	93.641
2021-08-16	0.430	89.967	0.554	64.061	0.711	63.403	0.257	93.898
2021-08-17	0.413	90.333	0.559	64.530	0.708	63.918	0.257	94.155
2021-08-18	0.399	90.686	0.564	65.003	0.705	64.432	0.257	94.411
2021-08-19	0.382	91.025	0.569	65.480	0.701	64.944	0.257	94.668
2021-08-20	0.365	91.349	0.574	65.960	0.698	65.453	0.257	94.925
2021-08-21	0.355	91.664	0.579	66.444	0.695	65.961	0.257	95.182
2021-08-22	0.344	91.969	0.584	66.931	0.685	66.461	0.257	95.439
2021-08-23	0.333	92.265	0.589	67.422	0.675	66.952	0.257	95.696
2021-08-24	0.321	92.552	0.594	67.917	0.665	67.434	0.257	95.952
2021-08-25	0.310	92.829	0.599	68.416	0.655	67.908	0.257	96.209
2021-08-26	0.299	93.096	0.604	68.918	0.645	68.374	0.257	96.466
2021-08-27	0.288	93.354	0.609	69.424	0.638	68.833	0.257	96.723
2021-08-28	0.276	93.602	0.596	69.919	0.632	69.286	0.257	96.980
2021-08-29	0.265	93.841	0.582	70.404	0.625	69.732	0.257	97.237
2021-08-30	0.254	94.071	0.568	70.878	0.618	70.173	0.257	97.493
2021-08-31	0.249	94.296	0.554	71.342	0.612	70.606	0.257	97.750
2021-09-01	0.244	94.517	0.540	71.796	0.603	71.033	0.257	98.007
2021-09-02	0.239	94.733	0.527	72.240	0.595	71.452	0.236	98.243
2021-09-03	0.234	94.944	0.513	72.673	0.587	71.863	0.238	98.481
2021-09-04	0.229	95.150	0.500	73.096	0.579	72.267	0.238	98.718
2021-09-05	0.224	95.352	0.486	73.510	0.570	72.663	0.238	98.956
2021-09-06	0.218	95.549	0.481	73.920	0.560	73.050	0.238	99.194
2021-09-07	0.212	95.739	0.477	74.326	0.549	73.429	0.238	99.431
2021-09-08	0.207	95.925	0.472	74.728	0.539	73.799	0.238	99.669

2021-09-09	0.201	96.106	0.467	75.127	0.529	74.160	0.203	99.872
2021-09-10	0.195	96.281	0.462	75.522	0.518	74.512	0.009	99.881
2021-09-11	0.190	96.451	0.457	75.914	0.515	74.862	0.009	99.889
2021-09-12	0.184	96.616	0.452	76.302	0.511	75.210	0.009	99.898
2021-09-13	0.179	96.776	0.447	76.687	0.507	75.555	0.009	99.906
2021-09-14	0.173	96.931	0.442	77.068	0.504	75.897	0.009	99.915
2021-09-15	0.168	97.081	0.438	77.445	0.500	76.237	0.009	99.923
2021-09-16	0.163	97.226	0.427	77.813	0.492	76.572	0.009	99.932
2021-09-17	0.158	97.367	0.416	78.173	0.484	76.902	0.009	99.940
2021-09-18	0.152	97.502	0.406	78.523	0.476	77.227	0.009	99.949
2021-09-19	0.147	97.633	0.395	78.865	0.468	77.547	0.009	99.957
2021-09-20	0.142	97.759	0.385	79.198	0.460	77.862	0.009	99.966
2021-09-21	0.138	97.881	0.375	79.523	0.452	78.172	0.009	99.974
2021-09-22	0.134	97.999	0.365	79.839	0.444	78.477	0.009	99.983
2021-09-23	0.130	98.114	0.355	80.147	0.436	78.776	0.009	99.991
2021-09-24	0.126	98.225	0.345	80.447	0.429	79.071	0.009	100.000
2021-09-25	0.122	98.333	0.335	80.738	0.421	79.361	0.000	100.000
2021-09-26	0.118	98.437	0.326	81.022	0.417	79.648	0.000	100.000
2021-09-27	0.117	98.540	0.316	81.296	0.413	79.932	0.000	100.000
2021-09-28	0.116	98.643	0.306	81.563	0.410	80.215	0.000	100.000
2021-09-29	0.115	98.744	0.296	81.821	0.406	80.495	0.000	100.000
2021-09-30	0.114	98.844	0.286	82.070	0.402	80.772	0.000	100.000
2021-10-01	0.111	98.942	0.285	82.320	0.399	81.047	0.000	100.000
2021-10-02	0.108	99.037	0.284	82.569	0.395	81.320	0.000	100.000
2021-10-03	0.105	99.129	0.283	82.818	0.391	81.590	0.000	100.000
2021-10-04	0.102	99.219	0.281	83.066	0.387	81.857	0.000	100.000
2021-10-05	0.099	99.306	0.280	83.314	0.383	82.122	0.000	100.000
2021-10-06	0.096	99.391	0.279	83.561	0.379	82.384	0.000	100.000
2021-10-07	0.093	99.473	0.277	83.808	0.376	82.644	0.000	100.000
2021-10-08	0.089	99.553	0.276	84.054	0.372	82.901	0.000	100.000
2021-10-09	0.087	99.630	0.275	84.300	0.368	83.156	0.000	100.000
2021-10-10	0.084	99.706	0.273	84.545	0.364	83.408	0.000	100.000
2021-10-11	0.083	99.781	0.272	84.790	0.359	83.656	0.000	100.000

2021-10-12	0.081	99.855	0.270	85.034	0.353	83.901	0.000	100.000
2021-10-13	0.080	99.928	0.269	85.278	0.348	84.143	0.000	100.000
2021-10-14	0.078	100.000	0.268	85.521	0.342	84.381	0.000	100.000
2021-10-15	0.000	100.000	0.266	85.764	0.337	84.615	0.000	100.000
2021-10-16	0.000	100.000	0.269	86.009	0.331	84.846	0.000	100.000
2021-10-17	0.000	100.000	0.271	86.256	0.326	85.073	0.000	100.000
2021-10-18	0.000	100.000	0.274	86.506	0.320	85.297	0.000	100.000
2021-10-19	0.000	100.000	0.277	86.759	0.315	85.517	0.000	100.000
2021-10-20	0.000	100.000	0.279	87.013	0.309	85.734	0.000	100.000
2021-10-21	0.000	100.000	0.282	87.271	0.304	85.947	0.000	100.000
2021-10-22	0.000	100.000	0.284	87.530	0.298	86.156	0.000	100.000
2021-10-23	0.000	100.000	0.287	87.792	0.293	86.362	0.000	100.000
2021-10-24	0.000	100.000	0.290	88.057	0.287	86.564	0.000	100.000
2021-10-25	0.000	100.000	0.292	88.324	0.282	86.763	0.000	100.000
2021-10-26	0.000	100.000	0.295	88.593	0.277	86.959	0.000	100.000
2021-10-27	0.000	100.000	0.295	88.862	0.271	87.150	0.000	100.000
2021-10-28	0.000	100.000	0.294	89.131	0.266	87.338	0.000	100.000
2021-10-29	0.000	100.000	0.294	89.399	0.260	87.523	0.000	100.000
2021-10-30	0.000	100.000	0.294	89.667	0.255	87.704	0.000	100.000
2021-10-31	0.000	100.000	0.294	89.935	0.253	87.884	0.000	100.000
2021-11-01	0.000	100.000	0.294	90.203	0.252	88.064	0.000	100.000
2021-11-02	0.000	100.000	0.288	90.465	0.251	88.242	0.000	100.000
2021-11-03	0.000	100.000	0.283	90.723	0.250	88.420	0.000	100.000
2021-11-04	0.000	100.000	0.277	90.975	0.249	88.596	0.000	100.000
2021-11-05	0.000	100.000	0.272	91.222	0.247	88.772	0.000	100.000
2021-11-06	0.000	100.000	0.266	91.463	0.246	88.946	0.000	100.000
2021-11-07	0.000	100.000	0.261	91.700	0.245	89.120	0.000	100.000
2021-11-08	0.000	100.000	0.255	91.931	0.244	89.293	0.000	100.000
2021-11-09	0.000	100.000	0.249	92.157	0.243	89.465	0.000	100.000
2021-11-10	0.000	100.000	0.244	92.378	0.242	89.637	0.000	100.000
2021-11-11	0.000	100.000	0.238	92.594	0.242	89.809	0.000	100.000
2021-11-12	0.000	100.000	0.233	92.805	0.242	89.980	0.000	100.000
2021-11-13	0.000	100.000	0.227	93.010	0.242	90.151	0.000	100.000

2021-11-14	0.000	100.000	0.222	93.211	0.242	90.322	0.000	100.000
2021-11-15	0.000	100.000	0.216	93.406	0.242	90.493	0.000	100.000
2021-11-16	0.000	100.000	0.207	93.592	0.242	90.664	0.000	100.000
2021-11-17	0.000	100.000	0.199	93.771	0.241	90.835	0.000	100.000
2021-11-18	0.000	100.000	0.190	93.941	0.241	91.005	0.000	100.000
2021-11-19	0.000	100.000	0.181	94.104	0.241	91.176	0.000	100.000
2021-11-20	0.000	100.000	0.172	94.257	0.241	91.346	0.000	100.000
2021-11-21	0.000	100.000	0.166	94.405	0.241	91.516	0.000	100.000
2021-11-22	0.000	100.000	0.159	94.548	0.241	91.686	0.000	100.000
2021-11-23	0.000	100.000	0.153	94.684	0.241	91.856	0.000	100.000
2021-11-24	0.000	100.000	0.147	94.815	0.241	92.025	0.000	100.000
2021-11-25	0.000	100.000	0.141	94.940	0.240	92.195	0.000	100.000
2021-11-26	0.000	100.000	0.134	95.059	0.240	92.364	0.000	100.000
2021-11-27	0.000	100.000	0.128	95.173	0.240	92.534	0.000	100.000
2021-11-28	0.000	100.000	0.122	95.280	0.240	92.703	0.000	100.000
2021-11-29	0.000	100.000	0.115	95.382	0.240	92.872	0.000	100.000
2021-11-30	0.000	100.000	0.109	95.478	0.239	93.040	0.000	100.000
2021-12-01	0.000	100.000	0.103	95.569	0.238	93.208	0.000	100.000
2021-12-02	0.000	100.000	0.102	95.658	0.238	93.375	0.000	100.000
2021-12-03	0.000	100.000	0.101	95.747	0.237	93.542	0.000	100.000
2021-12-04	0.000	100.000	0.100	95.834	0.236	93.709	0.000	100.000
2021-12-05	0.000	100.000	0.098	95.921	0.236	93.875	0.000	100.000
2021-12-06	0.000	100.000	0.097	96.006	0.235	94.040	0.000	100.000
2021-12-07	0.000	100.000	0.096	96.091	0.234	94.205	0.000	100.000
2021-12-08	0.000	100.000	0.095	96.175	0.233	94.369	0.000	100.000
2021-12-09	0.000	100.000	0.094	96.257	0.233	94.533	0.000	100.000
2021-12-10	0.000	100.000	0.093	96.339	0.232	94.696	0.000	100.000
2021-12-11	0.000	100.000	0.092	96.420	0.231	94.859	0.000	100.000
2021-12-12	0.000	100.000	0.091	96.500	0.230	95.021	0.000	100.000
2021-12-13	0.000	100.000	0.090	96.578	0.230	95.183	0.000	100.000
2021-12-14	0.000	100.000	0.089	96.656	0.229	95.344	0.000	100.000
2021-12-15	0.000	100.000	0.088	96.733	0.228	95.505	0.000	100.000
2021-12-16	0.000	100.000	0.087	96.809	0.227	95.665	0.000	100.000

2021-12-17	0.000	100.000	0.086	96.884	0.227	95.825	0.000	100.000
2021-12-18	0.000	100.000	0.085	96.958	0.226	95.984	0.000	100.000
2021-12-19	0.000	100.000	0.083	97.031	0.225	96.143	0.000	100.000
2021-12-20	0.000	100.000	0.082	97.104	0.225	96.301	0.000	100.000
2021-12-21	0.000	100.000	0.081	97.175	0.224	96.458	0.000	100.000
2021-12-22	0.000	100.000	0.080	97.245	0.223	96.615	0.000	100.000
2021-12-23	0.000	100.000	0.079	97.314	0.222	96.772	0.000	100.000
2021-12-24	0.000	100.000	0.078	97.382	0.222	96.928	0.000	100.000
2021-12-25	0.000	100.000	0.077	97.450	0.221	97.084	0.000	100.000
2021-12-26	0.000	100.000	0.076	97.516	0.220	97.239	0.000	100.000
2021-12-27	0.000	100.000	0.075	97.582	0.219	97.393	0.000	100.000
2021-12-28	0.000	100.000	0.074	97.646	0.219	97.547	0.000	100.000
2021-12-29	0.000	100.000	0.073	97.710	0.218	97.701	0.000	100.000
2021-12-30	0.000	100.000	0.072	97.772	0.216	97.853	0.000	100.000
2021-12-31	0.000	100.000	0.071	97.834	0.214	98.004	0.000	100.000
2022-01-01	0.000	100.000	0.069	97.894	0.213	98.154	0.000	100.000
2022-01-02	0.000	100.000	0.068	97.954	0.211	98.303	0.000	100.000
2022-01-03	0.000	100.000	0.067	98.013	0.209	98.451	0.000	100.000
2022-01-04	0.000	100.000	0.066	98.071	0.207	98.597	0.000	100.000
2022-01-05	0.000	100.000	0.065	98.127	0.206	98.743	0.000	100.000
2022-01-06	0.000	100.000	0.064	98.183	0.204	98.887	0.000	100.000
2022-01-07	0.000	100.000	0.063	98.238	0.202	99.030	0.000	100.000
2022-01-08	0.000	100.000	0.062	98.292	0.200	99.172	0.000	100.000
2022-01-09	0.000	100.000	0.061	98.345	0.199	99.313	0.000	100.000
2022-01-10	0.000	100.000	0.060	98.397	0.197	99.453	0.000	100.000
2022-01-11	0.000	100.000	0.059	98.448	0.195	99.591	0.000	100.000
2022-01-12	0.000	100.000	0.058	98.498	0.193	99.729	0.000	100.000
2022-01-13	0.000	100.000	0.057	98.547	0.192	99.865	0.000	100.000
2022-01-14	0.000	100.000	0.056	98.595	0.190	100.000	0.000	100.000
2022-01-15	0.000	100.000	0.054	98.642	0.000	100.000	0.000	100.000
2022-01-16	0.000	100.000	0.054	98.689	0.000	100.000	0.000	100.000
2022-01-17	0.000	100.000	0.053	98.735	0.000	100.000	0.000	100.000
2022-01-18	0.000	100.000	0.052	98.779	0.000	100.000	0.000	100.000

2022-01-19	0.000	100.000	0.051	98.823	0.000	100.000	0.000	100.000
2022-01-20	0.000	100.000	0.050	98.867	0.000	100.000	0.000	100.000
2022-01-21	0.000	100.000	0.050	98.910	0.000	100.000	0.000	100.000
2022-01-22	0.000	100.000	0.051	98.954	0.000	100.000	0.000	100.000
2022-01-23	0.000	100.000	0.051	98.998	0.000	100.000	0.000	100.000
2022-01-24	0.000	100.000	0.051	99.042	0.000	100.000	0.000	100.000
2022-01-25	0.000	100.000	0.051	99.086	0.000	100.000	0.000	100.000
2022-01-26	0.000	100.000	0.051	99.130	0.000	100.000	0.000	100.000
2022-01-27	0.000	100.000	0.051	99.174	0.000	100.000	0.000	100.000
2022-01-28	0.000	100.000	0.052	99.219	0.000	100.000	0.000	100.000
2022-01-29	0.000	100.000	0.052	99.264	0.000	100.000	0.000	100.000
2022-01-30	0.000	100.000	0.052	99.308	0.000	100.000	0.000	100.000
2022-01-31	0.000	100.000	0.052	99.353	0.000	100.000	0.000	100.000
2022-02-01	0.000	100.000	0.052	99.399	0.000	100.000	0.000	100.000
2022-02-02	0.000	100.000	0.052	99.444	0.000	100.000	0.000	100.000
2022-02-03	0.000	100.000	0.052	99.489	0.000	100.000	0.000	100.000
2022-02-04	0.000	100.000	0.053	99.535	0.000	100.000	0.000	100.000
2022-02-05	0.000	100.000	0.053	99.581	0.000	100.000	0.000	100.000
2022-02-06	0.000	100.000	0.053	99.627	0.000	100.000	0.000	100.000
2022-02-07	0.000	100.000	0.053	99.673	0.000	100.000	0.000	100.000
2022-02-08	0.000	100.000	0.053	99.719	0.000	100.000	0.000	100.000
2022-02-09	0.000	100.000	0.053	99.766	0.000	100.000	0.000	100.000
2022-02-10	0.000	100.000	0.054	99.812	0.000	100.000	0.000	100.000
2022-02-11	0.000	100.000	0.054	99.859	0.000	100.000	0.000	100.000
2022-02-12	0.000	100.000	0.054	99.906	0.000	100.000	0.000	100.000
2022-02-13	0.000	100.000	0.054	99.953	0.000	100.000	0.000	100.000
2022-02-14	0.000	100.000	0.054	100.000	0.000	100.000	0.000	100.000

Supplement 4C - Environmental time-series data

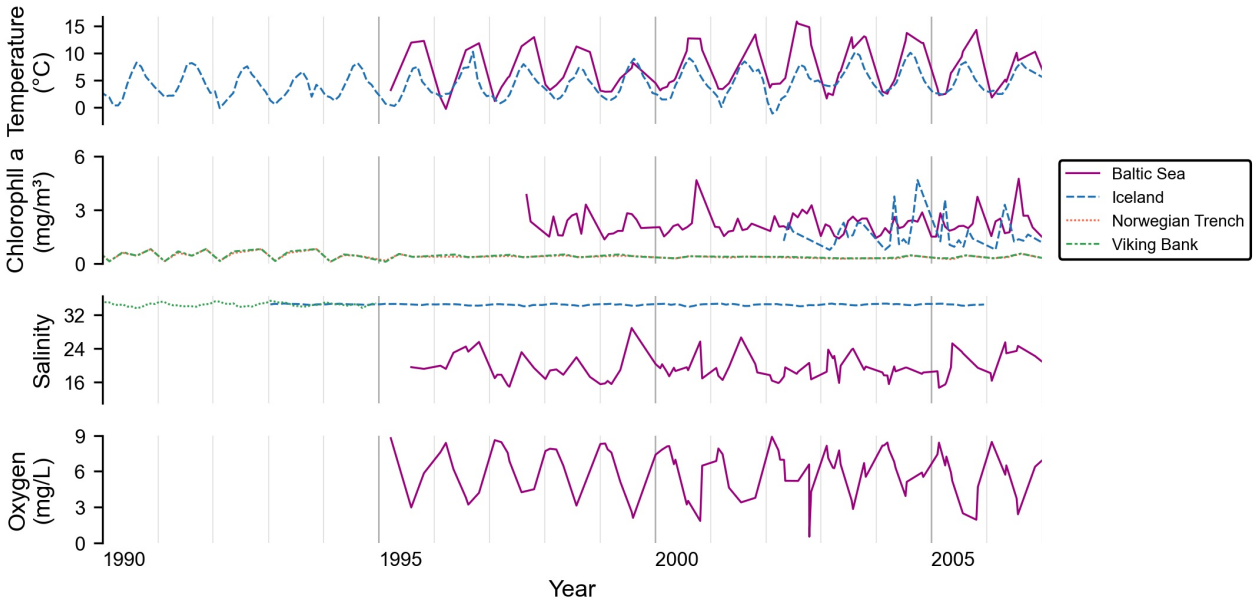

Figure S4.2 Temperature, chlorophyll a, and salinity time series data acquired for this study. For the Norwegian Trench and the Viking Bank, only monthly average temperature data were available. Salinity data were missing for the Norwegian Trench and dissolved oxygen data could only be acquired for the Baltic Sea.

Table S4.2 Sources of environmental data used in the study.

Locality	Temperature	Chlorophyll a	Salinity	DO
Baltic Sea	Station TF0012[1]	Station TF0012[1]	Station TF0012[1]	Station TF0012[1]
Iceland	(Hanna et al., 2006)	(Sathyendranath et al., 2019)	(Gaillard et al., 2016)	
Norwegian Trench	(Boyer et al., 2020)	(Norwegian Marine Data Centre, 2019)		
Viking Bank	(Boyer et al., 2020)	(Norwegian Marine Data Centre, 2019)	(Gaillard et al., 2016)	

[1] operated by the Leibniz Institute for Baltic Sea Research Warnemünde (https://odin2.io- warnemuende.de/; accessed 14 Jul 2021)

References

Abele, D., Strahl, J., Brey, T., and Philipp, E. E. R., 2008. Imperceptible senescence: Ageing in the ocean quahog *Arctica islandica*. Free. Radical Res. 42, 474–480.

Asami, R., Yoshimura, N., Toriyabe, H., Minei, S., Shinjo, R., Hongo, C., Sakamaki, T., and Fujita, K., 2020. High-resolution evidence for Middle Holocene East Asian winter and summer monsoon variations: snapshots of fossil coral records. Geophys. Res. Lett. 47, e2020GL088509.

Ballesta-Artero, I., Augustine, S., Witbaard, R., Carroll, M. L., Mette, M. J., Wanamaker Alan, D., and van der Meer, J., 2019. Energetics of the extremely long-living bivalve *Arctica islandica* based on a Dynamic Energy Budget model. J. Sea Res. Ecosystem based management and the biosphere: a new phase in DEB research 143, 173–182.

Ballesta-Artero, I., Janssen, R., van der Meer, J., and Witbaard, R., 2018a. Interactive effects of temperature and food availability on the growth of *Arctica islandica* (Bivalvia) juveniles. Mar. Environ. Res. 133, 67–77.

Ballesta-Artero, I., Zhao, L., Milano, S., Mertz-Kraus, R., Schöne, B. R., van der Meer, J., and Witbaard, R., 2018b. Environmental and biological factors influencing trace elemental and microstructural properties of *Arctica islandica* shells. Sci. Total Environ. 645, 913–923.

Ballesteros, F. J., Martinez, V. J., Luque, B., Lacasa, L., Valor, E., and Moya, A., 2018. On the thermodynamic origin of metabolic scaling. Sci. Rep. 8, 1448.

Basova, L., Begum, S., Strahl, J., Sukhotin, A., Brey, T., Philipp, E., and Abele, D., 2012. Age-dependent patterns of antioxidants in *Arctica islandica* from six regionally separate populations with different lifespans. Aquat. Biol. 14, 141–152.

Begum, S., Basova, L., Strahl, J., Sukhotin, A., Heilmayer, O., Philipp, E., Brey, T., and Abele, D., 2009. A metabolic model for the ocean quahog *Arctica islandica* — effects of animal mass and age, temperature, salinity, and geography on respiration rate. J. Shellfish Res. 28, 533–539.

Begum, S., Basova, L., Heilmayer, O., Philipp, E. E. R., Abele, D., and Brey, T., 2010. Growth and energy budget models of the bivalve *Arctica islandica* at six different sites in the Northeast Atlantic realm. J. Shellfish Res. 29, 107–115.

Berg, S., Kutra, D., Kroeger, T., Straehle, C. N., Kausler, B. X., Haubold, C., Schiegg, M., Ales, J., Beier, T., Rudy, M., Eren, K., Cervantes, J. I., Xu, B., Beuttenmueller, F., Wolny, A., Zhang, C., Koethe, U., Hamprecht, F. A., and Kreshuk, A., 2019. ilastik: interactive machine learning for (bio)image analysis. Nat. Methods 16, 1226–1232.

Boyer, T. P., Garcia, H. E., Locarnini, R. A., Zweng, M. M., Mishonov, A. V., Reagan, J. R., Weathers, K. A., Baranova, O. K., Seidov, D., and Smolyar, I. V., 2020. World Ocean Atlas 2018: Temperature. NOAA National Centers for Environmental Information.

Brand, U. and Morrison, J. O., 1987. Paleoscene #6. Biogeochemistry of fossil marine-invertebrates. Geosci. Can. 14, 85–107.

Butler, P. G., Wanamaker, A. D., Scourse, J. D., Richardson, C. A., and Reynolds, D. J., 2013. Variability of marine climate on the North Icelandic Shelf in a 1357-year proxy archive based on growth increments in the bivalve *Arctica islandica*. Palaeogeogr. Palaeoclimatol. Palaeoecol. Unraveling environmental histories from skeletal diaries - advances in sclerochronology 373, 141–151.

Canny, J., 1986. A Computational Approach to Edge Detection. IEEE Trans. Pattern Anal. Mach. Intell. PAMI-8, 679–698.

Cargnelli, L. M., 1999. Essential fish habitat source document. Ocean quahog, *Arctica islandica*, life history and habitat characteristics. Woods Hole, Massachusetts, USA: U.S. Department of Commerce.

Carré, M., Bentaleb, I., Bruguier, O., Ordinola, E., Barrett, N. T., and Fontugne, M., 2006. Calcification rate influence on trace element concentrations in aragonitic bivalve shells: evidences and mechanisms. Geochim. Cosmochim. Acta 70, 4906–4920.

Carstensen, J., Conley, D. J., Bonsdorff, E., Gustafsson, B. G., Hietanen, S., Janas, U., Jilbert, T., Maximov, A., Norkko, A., and Norkko, J., 2014. Hypoxia in the Baltic Sea: biogeochemical cycles, benthic fauna, and management. Ambio 43, 26–36.

Cauquoin, A., Werner, M., and Lohmann, G., 2019. Water isotopes - climate relationships for the mid-Holocene and preindustrial period simulated with an isotope-enabled version of MPI-ESM. Clim. Past 15, 1913–1937.

Chen, J., Zhang, M., Cui, T., and Wen, Z., 2013. A review of some important technical problems in respect of satellite remote sensing of chlorophyll-a concentration in coastal waters. IEEE J. Sel. Top. Appl. Earth Obs. Remote Sens. 6, 2275–2289.

Clark, G. R., 1974. Growth lines in invertebrate skeletons. Annu. Rev. Earth Planet. Sci. 2, 77–99.

Clark, G. R., 1975. Periodic growth and biological rhythms in experimentally grown bivalves. In: Growth rhythms and the history of the Earth's rotation. Ed. by G. D. Rosenberg and S. K. Runcorn. London: John Wiley & Sons, 103–117.

Cleveland, W. S., 1979. Robust locally weighted regression and smoothing scatterplots. J. Am. Stat. Assoc. 74, 829–836.

Cochran, J. K., Kallenberg, K., Landman, N. H., Harries, P. J., Weinreb, D., Turekian, K. K., Beck, A. J., and Cobban, W. A., 2010. Effect of diagenesis on the Sr, O, and C isotope composition of late Cretaceous mollusks from the Western Interior Seaway of North America. Am J Sci 310, 69–88.

Condurache, A.-p. and Aach, T., 2005. Vessel segmentation in angiograms using hysteresis thresholding. In: Proceedings of the ninth IAPR conference on machine vision applications. Tsukuba, Japan, 16–18.

Conley, D. J., Carstensen, J., Aigars, J., Axe, P., Bonsdorff, E., Eremina, T., Haahti, B.-M., Humborg, C., Jonsson, P., Kotta, J., Lännegren, C., Larsson, U., Maximov, A., Medina, M. R., Lysiak-Pastuszak, E., Remeikaitė-Nikienė, N., Walve, J., Wilhelms, S., and Zillén, L., 2011. Hypoxia is increasing in the coastal zone of the Baltic Sea. Environ. Sci. Technol. 45, 6777–6783.

Crippa, G., Ye, F., Malinverno, C., and Rizzi, A., 2016. Which is the best method to prepare invertebrate shells for SEM analysis? Testing different techniques on recent and fossil brachiopods. Boll. Della Soc. Paleontol. Ital. 55, 111–125.

Dahlgren, T. G., Weinberg, J. R., and Halanych, K. M., 2000. Phylogeography of the ocean quahog (*Arctica islandica*): influences of paleoclimate on genetic diversity and species range. Mar Biol 137, 487–495.

Da Silva, J. K. L., Garcia, G. J. M., and Barbosa, L. A., 2006. Allometric scaling laws of metabolism. Phys Life Rev 3, 229–261.

De Winter, N., Müller, I., Kocken, I., Thibault, N., Ullmann, C., Farnsworth, A., Lunt, D., Claeys, P., and Ziegler, M., 2021. Absolute seasonal temperature estimates from clumped isotopes in bivalve shells suggest warm and variable greenhouse climate. Commun. Earth Environ. 2, 121.

Dunca, E., Mutvei, H., Goransson, P., Morth, C.-M., Schone, B. R., Whitehouse, M. J., Elfman, M., and Baden, S. P., 2009. Using ocean quahog (*Arctica islandica*) shells to reconstruct palaeoenvironment in Öresund, Kattegat and Skagerrak, Sweden. Int. J. Earth Sci. 15.

Ehrich, S., 2007. „Walther Herwig III" Cruise 302. Cruise Report. Bundesforschungsanstalt für Fischerei, Institut für Seefischerei.

Füllenbach, C. S., Schöne, B. R., and Mertz-Kraus, R., 2015. Strontium/lithium ratio in aragonitic shells of *Cerastoderma edule* (Bivalvia) — A new potential temperature proxy for brackish environments. Chem. Geol. 417, 341–355.

Gaillard, F., Reynaud, T., Thierry, V., Kolodziejczyk, N., and von Schuckmann, K., 2016. In Situ–Based Reanalysis of the Global Ocean Temperature and Salinity with ISAS: Variability of the Heat Content and Steric Height. J. Clim. 29, 1305–1323.

Gholizadeh, M. H., Melesse, A. M., and Reddi, L., 2016. A comprehensive review on water quality parameters estimation using remote sensing techniques. Sensors 16, 1298.

Gilbert, P. U., Bergmann, K. D., Myers, C. E., Marcus, M. A., DeVol, R. T., Sun, C.-Y., Blonsky, A. Z., Tamre, E., Zhao, J., Karan, E. A., Tamura, N., Lemer, S., Giuffre, A. J., Giribet, G., Eiler, J. M., and Knoll, A. H., 2017. Nacre tablet thickness records formation temperature in modern and fossil shells. Earth Planet. Sci. Lett. 460, 281–292.

Gillikin, D. P., Lorrain, A., Meng, L., and Dehairs, F., 2007. A large metabolic carbon contribution to the $\delta^{13}C$ record in marine aragonitic bivalve shells. Geochim. Cosmochim. Acta 71, 2936–2946.

Gillikin, D. P., Lorrain, A., Navez, J., Taylor, J. W., André, L., Keppens, E., Baeyens, W., and Dehairs, F., 2005. Strong biological controls on Sr/Ca ratios in aragonitic marine bivalve shells. Geochem. Geophys. Geosystems 6.

Gillooly, J. F., Brown, J. H., West, G. B., Savage, V. M., and Charnov, E. L., 2001. Effects of size and temperature on metabolic rate. Science 293, 2248–2251.

Gonfiantini, R., Stichler, W., and Rozanski, K., 1995. Standards and intercomparison materials distributed by the International Atomic Energy Agency for stable isotope measurements (IAEA-TECDOC–825). IAEA.

Gray, J. S., Wu, R. S.-s., and Or, Y. Y., 2002. Effects of hypoxia and organic enrichment on the coastal marine environment. Mar. Ecol. Prog. Ser. 238, 249–279.

Grossman, E. L. and Ku, T.-L., 1986. Oxygen and carbon isotope fractionation in biogenic aragonite: Temperature effects. Chem. Geol. Iso Geosc Sec 59, 59–74.

Hanna, E., Jónsson, T., Ólafsson, J., and Valdimarsson, H., 2006. Icelandic coastal sea surface temperature records constructed: putting the pulse on air–sea–climate interactions in the northern North Atlantic. Part I: comparison with HadISST1 open-ocean surface temperatures and preliminary analysis of long-term patterns and anomalies of SSTs around Iceland. J. Clim. 19, 5652–5666.

Hansson, D. and Gustafsson, E., 2011. Salinity and hypoxia in the Baltic Sea since A.D. 1500. J. Geophys. Res. Oceans 116, C03027.

Hiebenthal, C., Philipp, E. E. R., Eisenhauer, A., and Wahl, M., 2012. Interactive effects of temperature and salinity on shell formation and general condition in Baltic Sea *Mytilus edulis* and *Arctica islandica*. Aquat. Biol. 14, 289–298.

Hiebenthal, C., Philipp, E. E. R., Eisenhauer, A., and Wahl, M., 2013. Effects of seawater pCO_2 and temperature on shell growth, shell stability, condition and cellular stress of Western Baltic Sea *Mytilus edulis* (L.) and *Arctica islandica* (L.) Mar. Biol. 160, 2073–2087.

Höche, N., Walliser, E. O., and Schöne, B. R., 2021a. Data for "Microstructural mapping of A. islandica shells reveals environmental and physiological controls on biomineral size". zenodo.

Höche, N., Walliser, E. O., and Schöne, B. R., 2022. Microstructural mapping of *Arctica islandica* shells reveals environmental and physiological controls on biomineral size. Front. Earth Sci. 9.

Höche, N., Walliser, E. O., Winter, N. J. de, Witbaard, R., and Schöne, B. R., 2021b. Temperature-induced microstructural changes in shells of laboratory-grown *Arctica islandica* (Bivalvia). PLOS ONE 16, e0247968.

IOCCG, 2000. Remote sensing of ocean colour in coastal, and other optically-complex, waters. Report. International Ocean Colour Coordinating Group (IOCCG).

Jones, D. S., 1980. Annual cycle of shell growth increment formation in two continental shelf bivalves and its paleoecologic significance. Paleobiology 6, 331–340.

Kapp, R. M., 1980. Distribution of recent mortalities of the Ocean Quahog, *Arctica Islandica*, at two Middle Atlantic Ocean dumpsites. M.S. United States – District of Columbia: American University. 44 pp.

Karlson, K., Rosenberg, R., and Bonsdorff, E., 2002. Temporal and spatial large-scale effects of eutrophication and oxygen deficiency on benthic fauna in Scandinavian and Baltic waters: a review. Oceanogr. Mar. Biol. Annu. Rev. 40, 427–489.

Karney, G. B., Butler, P. G., Scourse, J. D., Richardson, C. A., Lau, K. H., Czernuszka, J. T., and Grovenor, C. R. M., 2011. Identification of growth increments in the shell of the bivalve mollusc *Arctica islandica* using backscattered electron imaging. J. Microsc.. 241, 29–36.

Kennish, M. J. and Olsson, R. K., 1974. Effects of thermal discharges on the microstructural growth of *Mercenaria mercenaria*. Environ. Geol. 1, 44–64.

Kleiber, M., 1932. Body size and metabolism. Hildegardia 6, 315–353.

Klein, R. T., Lohmann, K. C., and Thayer, C. W., 1996. SrCa and $^{13}C^{12}C$ ratios in skeletal calcite of *Mytilus trossulus*: Covariation with metabolic rate, salinity, and carbon isotopic composition of seawater. Geochim. Cosmochim. Acta 60, 4207–4221.

Knoll, K., Landman, N. H., Cochran, J. K., Macleod, K. G., and Sessa, J. A., 2016. Microstructural preservation and the effects of diagenesis on the carbon and oxygen isotope composition of Late Cretaceous aragonitic mollusks from the Gulf Coastal Plain and the Western Interior Seaway. Am. J. Sci. 316, 591–613.

Kooijman, B. and Kooijman, S., 2010. Dynamic energy budget theory for metabolic organisation. Cambridge, United Kingdom: Cambridge university press.

Krause-Nehring, J., Brey, T., and Thorrold, S. R., 2012. Centennial records of lead contamination in northern Atlantic bivalves (*Arctica islandica*). Mar. Pollut. Bull. 64, 233–240.

Kremling, K., Tokos, J. J. S., Brügmann, L., and Hansen, H.-P., 1997. Variability of dissolved and particulate trace metals in the Kiel and Mecklenburg bights of the Baltic Sea, 1990–1992. Mar. Pollut. Bull. 34, 112–122.

Kruskopf, M. and Flynn, K. J., 2006. Chlorophyll content and fluorescence responses cannot be used to gauge reliably phytoplankton biomass, nutrient status or growth rate. New Phytol. 169, 525–536.

Lavkulich, L. M. and Wiens, J. H., 1970. Comparison of organic matter destruction by hydrogen peroxide and sodium hypochlorite and its effects on selected mineral constituents. Soil Sci. Soc. Am. J. 34, 755–758.

LeGrande, A. N. and Schmidt, G. A., 2006. Global gridded data set of the oxygen isotopic composition in seawater. Geophys. Res. Lett. 33, L12604.

Leipe, T., Kersten, M., Heise, S., Pohl, C., Witt, G., Liehr, G., Zettler, M., and Tauber, F., 2005. Ecotoxicity assessment of natural attenuation effects at a historical dumping site in the western Baltic Sea. Mar. Pollut. Bull. 50, 446–459.

Liehr, G. A., Zettler, M. L., Leipe, T., and Witt, G., 2005. The ocean quahog *Arctica islandica* L.: a bioindicator for contaminated sediments. Mar. Biol. 147, 671–679.

Marali, S. and Schöne, B. R., 2015. Oceanographic control on shell growth of *Arctica islandica* (Bivalvia) in surface waters of Northeast Iceland — Implications for paleoclimate reconstructions. Palaeogeogr. Palaeoclimatol. Palaeoecol. 420, 138–149.

Marin, F., Le Roy, N., and Marie, B., 2012. The formation and mineralization of mollusk shell. Front. Biosci. S4, 1099–1125.

Mejri, W., Korchef, A., Tlili, M., and Amor, M. B., 2014. Effects of temperature on precipitation kinetics and microstructure of calcium carbonate in the presence of magnesium and sulphate ions. Desalination Water Treat. 52, 4863–4870.

Meyer, E. M. I., Pohlmann, T., and Weisse, R., 2011. Thermodynamic variability and change in the North Sea (1948–2007) derived from a multidecadal hindcast. J. Mar. Syst. 86, 35–44.

Milano, S., Nehrke, G., Wanamaker, A. D., Ballesta-Artero, I., Brey, T., and Schöne, B. R., 2017a. The effects of environment on *Arctica islandica* shell formation and architecture. Biogeosciences 14, 1577–1591.

Milano, S., Schöne, B. R., and Witbaard, R., 2017b. Changes of shell microstructural characteristics of *Cerastoderma edule* (Bivalvia) — A novel proxy for water temperature. Palaeogeogr. Palaeoclimatol. Palaeoecol. 465, 395–406.

Morton, B., 2011. The biology and functional morphology of *Arctica islandica* (Bivalvia: Arcticidae) – A gerontophilic living fossil. Mar. Biol. Res. 7, 540–553.

Murawski, S. A., Ropes, J. W., and Serchuk, F. M., 1982. Growth of the ocean quahog, *Arctica islandica*, in the Middle Atlantic Bight. Fish. Bull. 80, 21–34.

Norwegian Marine Data Centre, 2019. Combined DIVA 4D 6-year analysis of water body chlorophyll-a 1983-2016 v2018, 18.

Oeschger, R., 1990. Long-term anaerobiosis in sublittoral marine invertebrates from the Western Baltic Sea: *Halicryptus spinulosus* (Priapulida), *Astarte borealis* and *Arctica islandica* (Bivalvia). Mar. Ecol. Prog. Ser. 59, 133–143.

Olson, I. C., Kozdon, R., Valley, J. W., and Gilbert, P. U. P. A., 2012. Mollusk shell nacre ultrastructure correlates with environmental temperature and pressure. J. Am. Chem. Soc. 134, 7351–7358.

Peharda, M., Walliser, E. O., Markulin, K., Purroy, A., Uvanović, H., Janeković, I., Župan, I., Vilibić, I., and Schöne, B. R., 2019. Glycymeris pilosa (Bivalvia) - A high-potential geochemical archive of the environmental variability in the Adriatic Sea. Mar. Environ. Res. 150, 104759.

Philipp, E. E. R. and Abele, D., 2010. Masters of longevity: Lessons from long-lived bivalves – a mini-review. GER 56, 55–65.

Philipp, E. E. R., Wessels, W., Gruber, H., Strahl, J., Wagner, A. E., Ernst, I. M. A., Rimbach, G., Kraemer, L., Schreiber, S., Abele, D., and Rosenstiel, P., 2012. Gene expression and physiological changes of different populations of the long-lived bivalve *Arctica islandica* under low oxygen conditions. PLOS ONE 7, e44621.

Pohlmann, T., 1996. Calculating the development of the thermal vertical stratification in the North Sea with a three-dimensional baroclinic circulation model. Cont. Shelf Res. 16, 163–194.

Prezant, R. S., Tiu, A. T., and Chalermwat, K., 1988. Shell microstructure and color changes in stressed *Corbicula fluminea* (Bivalvia: Corbiculidae). The Veliger 31, 236–243.

Purton, L. M. A., Shields, G. A., Brasier, M. D., and Grime, G. W., 1999. Metabolism controls Sr/Ca ratios in fossil aragonitic mollusks. Geology 27, 1083.

Reynolds, D. J., Butler, P., Williams, S., Scourse, J., Richardson, C., Wanamaker, A., Austin, W., Cage, A., and Sayer, M., 2013. A multiproxy reconstruction of Hebridean (NW Scotland) spring sea surface temperatures between AD 1805 and 2010. Palaeogeogr. Palaeoclimatol. Palaeoecol. 386, 275–285.

Reynolds, D. J., Hall, I. R., and Slater, S. M., 2019. An integrated carbon and oxygen isotope approach to reconstructing past environmental variability in the northeast Atlantic Ocean. Paleogeogr. Paleoclimatol. Paleoecol. 523, 48–61.

Ritter, A.-C., Mavromatis, V., Dietzel, M., Kwiecien, O., Wiethoff, F., Griesshaber, E., Casella, L. A., Schmahl, W. W., Koelen, J., Neuser, R. D., Leis, A., Buhl, D., Niedermayr, A., Breitenbach, S. F. M., Bernasconi, S. M., and Immenhauser, A., 2017. Exploring the impact of diagenesis on (isotope) geochemical and microstructural alteration features in biogenic aragonite. Sedimentology 64, 1354–1380.

Ropes, J. W., Jones, D., Murawski, S., Serchuk, F., and Jearld, A., 1984a. Documentation of annual growth lines in ocean quahogs, *Arctica islandica* Linné. Fish. Bull. 82, 1–19.

Rovelli, L., Dengler, M., Schmidt, M., Sommer, S., Linke, P., and McGinnis, D. F., 2016. Thermocline mixing and vertical oxygen fluxes in the stratified central North Sea. Biogeosciences 13, 1609–1620.

Rueden, C. T., Schindelin, J., Hiner, M. C., DeZonia, B. E., Walter, A. E., Arena, E. T., and Eliceiri, K. W., 2017. ImageJ2: ImageJ for the next generation of scientific image data. BMC Bioinformatics 18, 529.

Sathyendranath, S., Brewin, R. J. W., Brockmann, C., Brotas, V., Calton, B., Chuprin, A., Cipollini, P., Couto, A. B., Dingle, J., Doerffer, R., Donlon, C., Dowell, M., Farman, A., Grant, M., Groom, S., Horseman, A., Jackson, T., Krasemann, H., Lavender, S., Martinez-Vicente, V., Mazeran, C., Mélin, F., Moore, T. S., Müller, D., Regner, P., Roy, S., Steele, C. J., Steinmetz, F., Swinton, J., Taberner, M., Thompson, A., Valente, A., Zühlke, M., Brando, V. E., Feng, H., Feldman, G., Franz, B. A., Frouin, R., Gould, R. W., Hooker, S. B., Kahru, M., Kratzer, S., Mitchell, B. G., Muller-Karger, F. E., Sosik, H. M., Voss, K. J., Werdell, J., and Platt, T., 2019. An ocean-colour time series for use in climate studies: The experience of the Ocean-Colour Climate Change Initiative (OC-CCI). Sensors 19, 4285.

Schmidt, G. A., Annan, J. D., Bartlein, P. J., Cook, B. I., Guilyardi, E., Hargreaves, J. C., Harrison, S. P., Kageyama, M., LeGrande, A. N., Konecky, B., Lovejoy, S., Mann, M. E., Masson-Delmotte, V., Risi, C., Thompson, D., Timmermann, A., Tremblay, L.-B., and Yiou, P., 2014. Using palaeoclimate comparisons to constrain future projections in CMIP5. Clim. Past 10, 221–250.

Schneider, C. A., Rasband, W. S., and Eliceiri, K. W., 2012. NIH Image to ImageJ: 25 years of image analysis. Nat. Meth. 9, 671–675.

Schöne, B. R., 2013. *Arctica islandica* (Bivalvia): A unique paleoenvironmental archive of the northern North Atlantic Ocean. Glob. Planet. Change 111, 199–225.

Schöne, B. R., Dunca, E., Fiebig, J., and Pfeiffer, M., 2005a. Mutvei's solution: An ideal agent for resolving microgrowth structures of biogenic carbonates. Palaeogeogr. Palaeoclimatol. Palaeoecol. 228, 149–166.

Schöne, B. R., Fiebig, J., Pfeiffer, M., Gleβ, R., Hickson, J., Johnson, A. L., Dreyer, W., and Oschmann, W., 2005b. Climate records from a bivalved Methuselah (*Arctica islandica*, Mollusca; Iceland). Palaeogeogr. Palaeoclimatol. Palaeoecol. 228, 130–148.

Schöne, B. R., Houk, S. D., Freyre Castro, A. D., Fiebig, J., Oschmann, W., Kröncke, I., Dreyer, W., and Gosselck, F., 2005c. Daily growth rates in shells of *Arctica islandica*: Assessing subseasonal environmental controls on a long-lived bivalve mollusk. PALAIOS 20, 78–92.

Schöne, B. R., Huang, X., Zettler, M. L., Zhao, L., Mertz-Kraus, R., Jochum, K. P., and Walliser, E. O., 2021. Mn/Ca in shells of *Arctica islandica* (Baltic Sea) – A potential proxy for ocean hypoxia? Estuar. Coast. Shelf Sci. 107257.

Schöne, B. R., Wanamaker, A. D., Fiebig, J., Thébault, J., and Kreutz, K., 2011a. Annually resolved $\delta^{13}C_{shell}$ chronologies of long-lived bivalve mollusks (*Arctica islandica*) reveal oceanic carbon dynamics in the temperate North Atlantic during recent centuries. Palaeogeogr. Palaeoclimatol. Palaeoecol. Reconstructing mid- to high-latitude marine climate and ocean variability using bivalves, coralline algae, and marine sediment cores from the Northern Hemisphere 302, 31–42.

Seabold, S. and Perktold, J., 2010. statsmodels: Econometric and statistical modeling with python. In: 9th python in science conference. Austin, Texas.

Sillanpää, J. K., Cardoso, J. C. d. R., Félix, R. C., Anjos, L., Power, D. M., and Sundell, K., 2020. Dilution of seawater affects the Ca^{2+} Transport in the outer mantle epithelium of *Crassostrea gigas*. Front. Physiol. 11.

Sobral, P. and Widdows, J., 1997. Influence of hypoxia and anoxia on the physiological responses of the clam *Ruditapes decussatus* from southern Portugal. Marine Biology 127, 455–461.

Stemmer, K., Brey, T., Gutbrod, M. S., Beutler, M., Schalkhausser, B., and De Beer, D., 2019. in situ measurements of pH, Ca^{2+} and DIC dynamics within the extrapallial fluid of the ocean quahog *Arctica islandica*. J. Shellfish Res. 38, 71–78.

Stemmer, K., Nehrke, G., and Brey, T., 2013. Elevated CO_2 levels do not affect the shell structure of the bivalve *Arctica islandica* from the Western Baltic. PLOS ONE 8, 9.

Strahl, J., Dringen, R., Schmidt, M. M., Hardenberg, S., and Abele, D., 2011. Metabolic and physiological responses in tissues of the long-lived bivalve *Arctica islandica* to oxygen deficiency. Comp. Biochem. Physiol. A. Mol. Integr. Physiol. 158, 513–519.

Sukhotin, A. A. and Pörtner, H. .-., 2001. Age-dependence of metabolism in mussels *Mytilus edulis* (L.) from the White Sea. J Exp Mar Biol Ecol 257, 53–72.

Sukhotin, A., Kovalev, A., Sokolov, E., and Sokolova, I. M., 2020. Mitochondrial performance of a continually growing marine bivalve, *Mytilus edulis*, depends on body size. J. Exp. Biol. 223.

Tan Tiu, A. and Prezant, R. S., 1989. Temporal variation in microstructure of the inner shell surface of *Corbicula fluminea* (Bivalvia: Heterodonta). Am. Malacol. Bull. 7, 65–71.

Taylor, A. C. and Brand, A. R., 1975a. A comparative study of the respiratory responses of the bivalves *Arctica islandica* (L.) and *Mytilus edulis* L. to declining oxygen tension. Proc. R. Soc. Lond. B Biol. Sci. 190, 443–456.

Taylor, A. C. and Brand, A. R., 1975b. Effects of hypoxia and body size on the oxygen consumption of the bivalve *Arctica islandica* (L.) J. Exp. Mar. Biol. Ecol. 19, 187–196.

Theede, H., Ponat, A., Hiroki, K., and Schlieper, C., 1969. Studies on the resistance of marine bottom invertebrates to oxygen-deficiency and hydrogen sulphide. Mar. Biol. 2, 325–337.

Thompson, I., Jones, D. S., and Dreibelis, D., 1980a. Annual internal growth banding and life history of the Ocean Quahog *Arctica islandica* (Mollusca: Bivalvia). Mar. Biol. 57, 25–34.

Thompson, I., Jones, D. S., and Ropes, J. W., 1980b. Advanced age for sexual maturity in the Ocean Quahog *Arctica islandica* (Mollusca: Bivalvia). Mar. Biol. 57, 35–39.

Thorarinsdottir, G. G. and Steingrimsson, S. A., 2000. Size and age at sexual maturity and sex ratio in ocean quahog, *Arctica islandica* (Linnaeus, 1767), off northwest Iceland. J. Shellfish Res. 19, 943–948.

Van der Walt, S., Schönberger, J. L., Nunez-Iglesias, J., Boulogne, F., Warner, J. D., Yager, N., Gouillart, E., and Yu, T., 2014. scikit-image: image processing in Python. PeerJ 2, e453.

Vihtakari, M., Renaud, P. E., Clarke, L. J., Whitehouse, M. J., Hop, H., Carroll, M. L., and Ambrose, W. G., 2016. Decoding the oxygen isotope signal for seasonal growth patterns in Arctic bivalves. Palaeogeogr. Palaeoclimatol. Palaeoecol. 446, 263–283.

Virtanen, P., Gommers, R., Oliphant, T. E., Haberland, M., Reddy, T., Cournapeau, D., Burovski, E., Peterson, P., Weckesser, W., Bright, J., van der Walt, S. J., Brett, M., Wilson, J., Millman, K. J., Mayorov, N., Nelson, A. R. J., Jones, E., Kern, R., Larson, E., Carey, C. J., Polat, İ., Feng, Y., Moore, E. W., VanderPlas, J., Laxalde, D., Perktold, J., Cimrman, R., Henriksen, I., Quintero, E. A., Harris, C. R., Archibald, A. M., Ribeiro, A. H., Pedregosa, F., and van Mulbregt, P., 2020. SciPy 1.0: fundamental algorithms for scientific computing in Python. Nat. Methods 17, 261–272.

Walliser, E. O., Lohmann, G., Niezgodzki, I., Tütken, T., and Schöne, B. R., 2016. Response of Central European SST to atmospheric pCO_2 forcing during the Oligocene – A combined proxy data and numerical climate model approach. Palaeogeogr. Palaeoclimatol. Palaeoecol. 459, 552–569.

Wanamaker, A. D. and Gillikin, D. P., 2019. Strontium, magnesium, and barium incorporation in aragonitic shells of juvenile *Arctica islandica*: Insights from temperature controlled experiments. Chem. Geol. Chemical sclerochronology 526, 117–129.

Wanamaker, A. D., Heinemeier, J., Scourse, J. D., Richardson, C. A., Butler, P. G., Eiríksson, J., and Knudsen, K. L., 2008. Very long-lived mollusks confirm 17th century AD tephra-based radiocarbon reservoir ages for North Icelandic shelf waters. Radiocarbon 50, 399–412.

Wanamaker, A. D., Kreutz, K. J., Schöne, B. R., Maasch, K. A., Pershing, A. J., Borns, H. W., Introne, D. S., and Feindel, S., 2009. A late Holocene paleo-productivity record in the western Gulf

of Maine, USA, inferred from growth histories of the long-lived ocean quahog (*Arctica islandica*). Int. J. Earth Sci. 98, 19.

Weidman, C., Jones, G., and Lohmann, K. C., 1994. The long-lived mollusk *Arctica islandica* - a new paleoceanographic tool for the reconstruction of bottom temperatures for the continental shelves of the northern-North Atlantic Ocean. J. Geophys. Res.-Oceans 99, 18305–18314.

Wilbur, K. M. and Saleuddin, A. S. M., 1983. 6 - Shell Formation. In: The Mollusca. Ed. by A. S. M. Saleuddin and K. M. Wilbur. Academic Press, 235–287.

Winter, J. E., 1970. Filter feeding and food utilization in *Arctica islandica* L. and *Modiolus modiolus* L. at different food concentrations. Mar. Food Chains, 196–206.

Winter, J. E., 1978. A review on the knowledge of suspension-feeding in lamellibranchiate bivalves, with special reference to artificial aquaculture systems. Aquaculture 13, 1–33.

Witbaard, R., 1996. Growth variations in *Arctica islandica* L. (Mollusca): a reflection of hydrography-related food supply. ICES J. Mar. Sci. 53, 981–987.

5 Summary and outlook

The goal of this thesis was to explore and calibrate bivalve shell microstructures as a potential high-resolution paleotemperature proxy. Recent publications have demonstrated a link between the size of BMUs of the shells and the ambient water temperature, but only for two microstructure types and for relatively short-lived bivalve species (Gilbert et al., 2017; Milano et al., 2017b). Here, the microstructural properties of *Glycymeris bimaculata* and *Arctica islandica* were analyzed to assess whether the link between water temperature and BMU size is a widespread phenomenon among bivalves. The studied taxa can live for several decades to centuries, have a rich fossil record, a wide biogeographic distribution, and consist of commonly occurring microstructures, making them a perfect target for analysis. Investigation of specimens collected from various different environmental regimes and raised in the lab allowed to individually assess the influences of each environmental factor (i.e., temperature, food conditions and salinity). Analyses were performed at various ontogenetic stages and in different shell portions in order to assess potential biological and physiological controls over the shell microstructure. These experiments were prerequisite for reliable paleotemperature reconstructions based on the shell microstructure and significantly advanced our understanding of bivalve microstructure morphogenesis. The main results of this project comprise:

In Manuscript 1, *Glycymeris bimaculata* was investigated — a bivalve species that is long-lived, widely distributed in coastal areas of temperate seas, and forms aragonitic, crossed-lamellar microstructures. Image processing and analysis methods were developed to automatically measure the size and shape of BMU in SEM images. These techniques were used to assess morphological variation of the crossed-lamellar microstructure through time. In three specimens collected alive at the Croatian coast of the Adriatic Sea, the size of the BMUs correlated strongly with the ambient water temperature. This relationship can be used to infer temperature information with up to 2.3 °C precision. Since the crossed-lamellar microstructure occurs frequently in aragonitic bivalves, microstructural temperature reconstructions might be applicable in many bivalve taxa. However, effects of other environmental factors on the BMU size could not be excluded. This is

because the temperature, chlorophyll a concentration and the salinity of the water at the sampling site were linked to each other, and hence, to the BMU size. This demonstrated an urgent need for experiments using specimens raised in the lab under controlled conditions, so that temperature effects on the shell microstructure could be studied without further influences.

To resolve this issue, in Manuscript 2, lab-raised specimens of *Arctica islandica*, an extremely long-lived bivalve species routinely used for paleoclimatological reconstructions, were studied. These specimens were grown in aquaria kept at different temperatures (1, 3, 6, 9, 12 and 15 °C) but constant salinity and food conditions. The microstructure of the shells was analyzed by means of SEM and image analysis. The methods developed for BMU morphometry of crossed-lamellar microstructures could not be easily applied to the HOM, CA and FCCL microstructures formed by *A. islandica*, because their BMUs are much more variable in shape and lack a hierarchical arrangement into larger structural units. However, the use of machine learning assisted image segmentation enabled processing of the chaotically organized and nearly structureless microstructures. This way, it could be shown that also in *A. islandica*, BMU size is controlled by water temperature. In addition, pores of unknown function are present within the shells of *A. islandica*, whose size also correlated strongly with the water temperature. The temperature sensitivity of BMU size was comparable for *A. islandica* and *G. bimaculata*, hinting at an overarching mechanism in marine mollusks. This promising paleotemperature proxy should be further tested and calibrated in natuirally grown shells.

Thus, Manuscript 3 studied several *A. islandica* specimens collected at different localities in the Northern European Seas using SEM to test whether BMU size of naturally grown *A. islandica* shells also change with the water temperature. In addition, it was evaluated whether the shell microstructure shows the expected changes in different temperature regimes, or whether other physiological and environmental influences obscure temperature reconstructions. The results revealed that the shell microstructure is not solely influenced by temperature. Unfavorable environmental conditions such as low DO content and/or suboptimal salinity, caused the formation of smaller BMUs and disturbance lines. In addition, the BMU size values varied systematically throughout life, likely due to physiological changes during early life stages of the bivalves such as variations in growth rate and/or metabolic rate. This complicates temperature reconstructions based on the shell microstructure. BMUs of different shell portions (hinge and ventral margin) but of the same microstructure and formed at the same time (i.e., under the same environmental conditions) had highly similar size ranges. Different microstructures, however, possess unique BMU size ranges. Comparisons between different microstructure types can likely be

accomplished by applying correction factors.

In conclusion, these investigations demonstrated a consistent influence of water temperature on the size of BMUs in bivalve shells. In natural habitats, however, further environmental influences and physiological processes of the bivalve overprint the link between water temperature and BMU size. Accordingly, the potential of paleoclimate proxies based on shell microstructures remains limited. Still, the studies provided new insights on the coupling of environmental parameters to bivalve biomineralization processes. The methods developed within this thesis promise to open new applications in biomineralization research not only for bivalves, but also for many other organisms forming tessellated calcareous microstructures.

Future studies should identify the effects of other environmental parameters on the shell microstructure by investigating specimens reared under constant temperature while varying, e.g., salinity, food availability and dissolved oxygen content. This way, the effects of these parameters on the microstructure can be studied individually, facilitating the identification of further proxy relationships of the microstructure and/or the removal of biases that overprint the temperature signal. Furthermore, additional bivalve species should be investigated which form shells of the same microstructure types as those from this thesis (i.e., crossed-lamellar, homogeneous, crossed-acicular). By that it can be determined whether temperature sensitivity of BMU size is consistent across multiple species, and target taxa can be identified whose microstructural characteristics may vary less throughout lifetime or are less affected by additional environmental parameters. Lastly, the reliability and precision of the analytical methods methods for microstructure analysis developed in this thesis should be further refined.

References

Gilbert, P. U., Bergmann, K. D., Myers, C. E., Marcus, M. A., DeVol, R. T., Sun, C.-Y., Blonsky, A. Z., Tamre, E., Zhao, J., Karan, E. A., Tamura, N., Lemer, S., Giuffre, A. J., Giribet, G., Eiler, J. M., and Knoll, A. H., 2017. Nacre tablet thickness records formation temperature in modern and fossil shells. Earth Planet. Sci. Lett. 460, 281–292.

Milano, S., Schöne, B. R., and Witbaard, R., 2017b. Changes of shell microstructural characteristics of *Cerastoderma edule* (Bivalvia) — A novel proxy for water temperature. Palaeogeogr. Palaeoclimatol. Palaeoecol. 465, 395–406.